Advances in Solar Radiometry

Dissertation
zur
Erlangung der naturwissenschaftlichen Doktorwürde
(Dr. sc. nat.)

vorgelegt der
Mathematisch-naturwissenschaftlichen Fakultät
der
Universität Zürich

von
MARKUS SUTER
von
Zürich ZH

Promotionskomitee
Prof. Dr. Ulrich Straumann (Vorsitz)
Dr. Wolfgang Finsterle (Leitung der Dissertation)
Dr. Thomas Kentischer
Prof. Dr. Werner Schmutz

Zürich, 2015

Zusammenfassung

Die totale Solare Irradianz (TSI) ist ein zentraler Parameter für den Energiehaushalt und das Klimasystem der Erde. Fortwährende und verlässliche Messungen, sowie präzise Absolutmessungen, sind deshalb unerlässlich für das Verständnis, die Rekonstruktion und schliesslich die Vorhersage des Klimas.

Die Messung des absoluten Wertes der TSI hat sich in der Vergangenheit als schwierig erwiesen. Mit Hilfe von Irradianz Standards wie der World Radiometric Reference (WRR) oder des kryogenen SI Labor Standards wurden Radiometer kalibriert. Zudem wurden Radiometer auch direkt in SI Grundeinheiten charakterisiert. Auf Grund der Implementierung dieser verschiedenen Standards und der gleichzeitigen Unterschätzung der Unsicherheiten, sowie unglücklich gewählter Nomenklatur kam es in der Geschichte der solaren Radiometrie immer wieder zu Verwirrungen beim Vergleich von Messdaten. So ist die Frage nach dem "wahren" Wert der TSI letztendlich eine Frage der Verwendung des "richtigen" Massstabs.

Das Physikalisch-Meteorologische Observatorium Davos und Weltstrahlungszentrum (PMOD/WRC) hat eine lange Tradition im Entwickeln von solaren Radiometern. 2009 wurde mit der Entwicklung eines neuen Prototypen für Weltraumanwendungen, dem Digital Absolute Radiometer (DARA) begonnen. Dabei wurden die neusten Erkenntnisse in der Radiometrie, sowie auch die Trends in der Satellitentechnologie hin zu leichteren und kompakteren Instrumenten und Satelliten berücksichtigt. Radiometer des Typs DARA werden die Unsicherheiten auf den absoluten Wert der TSI, verglichen mit der Vorgängergeneration (PMO6), signifikant reduzieren. Durch die geringen Abmessungen und die kleine Masse wird es öfter möglich sein eine Mitfluggelegenheit, auch auf kleineren Satelliten, zu finden. Zukünftige Missionen wo diese Radiometer eingesetzt werden sind das CLARA Radiometer auf dem NORSAT-1 Satellit und die PROBA-III Mission, wo ebenfalls ein DARA-Typ Radiometer eingesetzt wird.

In dieser Arbeit wird der DARA Prototyp getestet und charakterisiert. Mit Hilfe der Charakterisierung kann eine instrumenteigene Skala (in W/m^2) implementiert werden, welche sich auf die SI Grundeinheiten bezieht. Diese instrumenteigene Skala ist daher unabhängig von einem Irradianz-Kalibrierstandard. Die relative 1-Sigma Unsicherheit dieser Skala wird auf 200 ppm (parts per million) geschätzt. Die Charakterisierung des DARA Prototyps beinhaltet die Kontroll- und Datenerfassungselektronik, die Blendenfläche, die Absorbtivität der Kavitäten, der Wärmefluss durch elektrische Leitungen, die Beugungseffekte an der Blende, die nicht-Äquivalenz, und die thermischen Eigenschaften der Kavitäten. Diese Komponenten werden theoretisch und experimentell untersucht. Zudem wird wird DARA gegen die gängigen Irradianz Standards WRR und kryogener SI Labor Standard verglichen. Die instrumenteigene DARA Skala stimmt innerhalb der Unsicherheiten mit dem kryogenen SI Labor Standard überein, während zwischen der instrumenteigenen Skala und dem WRR Standard ein signifikanter Unterschied von 0.31 % besteht.

Um die experimentellen Möglichkeiten im Bereich Radiometrie am PMOD/WRC zu erweitern wurde ein neuer Heliostat konzipiert und gebaut. Das Design des Heliostat ist für die Bedürfnisse von radiometrischen Experimenten (grosses Gesichtsfeld, korrekte Strahlgeometrie) optimiert worden. Der Heliostat wurde Ende 2013 erfolgreich in Betrieb genommen. Probleme bestehen noch mit einem Lager das eine grössere Reibung als erwartet aufweist. Dies reduziert die Genaugkeit der Spiegelnachführung und hat noch Verbesserungspotenzial. Nach der Inbetriebnahme ist der Heliostat für die experimentelle Untersuchung der Beugungseffekte im DARA verwendet worden.

Abstract

Total solar irradiance (TSI) is a key input parameter for the climate system on earth. Continuous and reliable monitoring as well as the knowledge of the absolute TSI value is therefore crucial for understanding, reconstructing and eventually forecasting our climate on earth.

The determination of the absolute value of TSI has not been a straightforward task in the past. Irradiance standards, such as the World Radiometric Reference (WRR) or the SI cryogenic laboratory standard, have been used to calibrate radiometers. Additionally some radiometers have been characterised in terms of SI base units. Implementations of different standards and underestimated uncertainties of characterised radiometers have led to much confusion. Recent findings revealed that the question of the "true solar constant" is eventually a question of using the proper scale.

The Physikalisch-Meteorologisches Observatorium Davos and World Radiation Centre (PMOD/WRC) has a longtime experience in building radiometers to measure TSI. Starting in 2009 a new prototype for satellite based measurements, the Digital Absolute Radiometer (DARA) has been developed. The development includes the recent insights in radiometry, as well as the trend in satellite applications towards lighter and more compact instruments and satellites. DARA type radiometers will reduce the uncertainty of absolute TSI value significantly compared to previously operated PMO6 radiometers. Due to the low mass and dimensions it will be easier to find flight opportunities even on small satellites. Future missions are the CLARA radiometer on the NORSAT-1 satellite and a DARA type radiometer on the PROBA-III satellite.

Within this work the DARA prototype has been tested and characterised in detail. DARA has a native Irradiance scale (in W/m^2) implemented, that is directly linked to the SI base units and is therefore independent of any irradiance standards. This native scale has a relative uncertainty of 200 parts per million (ppm) at the 1-sigma level. The characterisation of the DARA instrument covers the control and readout electronics, the apertures, the absorptivity of the cavities, the lead heating, the diffraction effects, the non equivalence and the thermal properties of the cavities. These components are studied in theory and experimentally. Furthermore DARA is compared against the WRR and the SI cryogenic laboratory standard. The DARA native scale is found in good agreement with the SI laboratory standard, while there is a difference of 0.31% between the DARA native Scale and the WRR standard.

In order to extend PMOD/WRCs capabilities for radiometric experiments, a new heliostat has been designed and built. The design is optimised for specific needs like a large field of view and a natural (unfocussed) solar radiation field. The heliostat has been successfully installed and commissioned. However a friction problem in the bearing, affecting the tracking accuracy will need further improvement. The heliostat has then first been used to study diffraction effects at the DARA aperture.

Preface

The Sun! A truly fascinating object. It not only wakes us in the morning, gives us our daily rhythm, but is after all the source of all life on earth. In ancient times worshipped as a deity, and now possibly more adored by sunbathers, its positive effects on our minds is undeniable. It is therefore no surprise that the sun has become an object of studies in academic circles long before the present days. And it remains fascinating today. Despite of all "scientific" motivation given in the following pages, the true driver of investigating the sun, and maybe this is true for science in general, is mainly curiosity, fascination and amazement. I am very grateful that the society in Switzerland and in particular the Swiss National Science Foundation is supporting aesthetic, non applied science without a having a direct profit, but rather cultivate old traditions of advanced civilisations, which eventually are a benefit to all of us.

When I came to work at the Observatory in Davos for the first time, in August 2005, I would never have thought to write this lines nine years later. Back then I was a young civilian service employee and had the luck to experience the International Pyrheliometer Comparison in 2005 and was immediately fascinated by this very special community that the IPC brought together and the team spirit of the PMOD staff during this event. Also the technical aspects and especially the Ångström radiometer had fascinated me, and to be honest of course the mountains around Davos always attracted me. Not to forget the sun that was frequently shining these days. It should not have been the last time in Davos and so I finally ended up writing this work, still enjoying the beautiful view towards the Tinzenhorn.

It has been a great pleasure to write this thesis. Especially the fact of writing a book has appealed to me and motivated me a lot. Apart from the writing process, the project itself was not always so pleasant and straightforward. The situation concerning the infrastructure during the renovation of the institute building was quite difficult, the management of the heliostat project was very challenging and demanding a lot of patience. Nevertheless it offered me the opportunity of managing an infrastructure project for which I was definitely not qualified for by education and thus gaining experience that might indeed become valuable. Regular use of the milling machines and other tools in the workshop and the electronics laboratory allowed me to maintain the technical skills.

I hope that this work will contribute to the better understanding of radiometry in general and particularly to the understanding of PMOD's new generation of radiometers. Solar radiometry has a long tradition at PMOD and used to be the core competence of the institute for decades. Together with the preceding work by André Fehlmann this work will hopefully keep this tradition up and strengthen the solar radiometry at PMOD.

I wish to thank the "Promomtionskomitee": U. Straumann, W. Schmutz, W. Finsterle and T. Kentischer for their support, and for making this project possible. Furthermore I am indebted to G. Kopp for the fruitful collaboration and for hosting me at LASP and to E. Shirley for discussing the diffraction effects in the DARA. Of course this project would not have been possible without the help and support of many of the current and former PMOD/WRC staff. Last but not least my thanks goes to the Swiss Conferderation and to our society who is supporting and financing such scientific projects with no direct return, but rather in the belief that a developed society should have philosophers of different kind who are free to think about the state of the world and our nature.

Markus Suter, Davos, September 2014

Contents

Chapter 1

Introduction

This work is about measuring solar radiation with high precision. On the one hand reliable data is a need of the climatology community, on the other hand the metrological aspect, the art of the measurement itself is an important driver. The Physikalisch-Meteorologisches Observatorium Davos (PMOD) has a long history in developing radiometers and a record of measurements of more than 100 years.

Starting in 2009 a prototype for a new generation of solar radiometers, the Digital Absolute Radiometer (DARA) was developed. Within this work the DARA prototype is described and characterised in detail.

In this introduction, motivation for this work is give, metrological concepts are introduced as background information is provided. The last sections of this introductory chapter describe the goal of this work in more detail.

1.1 Motivation

Total Solar Irradiance (TSI) is a key input parameter for the earth climate system. The earth's energy balance is in the first place determined by incoming and outgoing electromagnetic radiation [1].

Climate change is one of the major challenges the world faces today. The scientific community, under the roof of the Intergovernmental Panel on Climate Change (IPCC), is putting a lot of effort into the understanding of climate mechanisms. With better understanding of the climate and the rising accuracy of climate models, the demand is high for precise data [2].

1.1.1 Solar Influence on Earth Climate in the Past

The sun, and in particular TSI, is varying at different time scales from minutes to millions of years [3], of which the 11-year solar cycle is probably the most prominent. In connection with climate history solar variability on longer time scales, from decades to millennia are most interesting.

Solar influence on earth climate has been discussed widely. Today's consensus is that while the sun is not responsible for the recent climate change and rise in global temperature in the past 30 years, the sun has been important for climate effects in the past [4]. A good review has been published by Solanki et al. in 2013 [3]. A very prominent example for solar influence on climate is the so called Maunder minimum, a period of low solar activity (low sunspot numbers) and very low temperatures in Europe during the second half of the

17th century. While the record of satellite based TSI measurements dates only back to 1978 (Section 1.4.2), a record of sunspot numbers is available back to about 1600. The sunspots are associated with magnetic fields and therefore a measure of magnetic activity of the sun. The historical sunspot record is described in detail by Eddy [5].

TSI values for the past have been reconstructed on the base of sunspot number (back to the 17th century) and cosmogenic isotope production rates (for the last 10'000 years or more). The next section describes the TSI reconstruction in more detail.

1.1.2 Reconstruction and Forecasting of Solar Activity

Solar activity has been reconstructed, analysing the isotope concentration of ^{14}C and ^{10}Be in natural archives such as tree trunks or ice sheets. These isotopes are formed in the atmosphere by nuclear reactions between cosmic rays and particles of the earth's atmosphere. The flux density of cosmic rays is dependent on the level of solar activity. If the sun is more active, solar magnetic fields shield the earth better from the cosmic rays. Thus the production rate of ^{14}C and ^{10}Be is lower if the sun is more active. The isotopes get stored in natural archives such as tree rings (^{14}C) and ice sheets (^{10}Be) where their concentrations can be extracted and time series can be reconstructed. The relationship between ^{14}C concentration and solar activity has been proposed already in 1961 by Stuiver [6]. As the variations in production rates are small, only improved decay counting equipment led to the unambiguous detection of the correlation between solar activity and the ^{14}C production rates in the late 1970s [7]. Reliable reconstruction of solar magnetic activity based on ^{10}Be concentrations became only later possible with more precise measurements of ^{10}Be isotope concentration by means of accelerator mass spectrometry in the 1980s. In this ^{10}Be time series even the 11-year solar cycle could be resolved [8], which was later also possible with the ^{14}C data [9]. The progress in isotope concentration measurements fell into the same era as the early satellite measurements of TSI that led to the discovery of the correlation between TSI and magnetic activity (sunspots) [10, 11]. This led in turn to the reconstruction of TSI based on proxies like sunspot number and isotope concentrations. Recently several solar irradiance reconstructions have been published that, in addition to the proxies, relay on the now 35 year record of satellite based TSI measurements as well as on solar models. A good overview and comparison between the TSI reconstructions can be found in Solanki et al. [3]. More details on techniques involving cosmogenic radionuclides can be found in the recently published book by Beer et al. [12].

Figure 1.1 shows the results of different TSI reconstructions. In the last 400 years three periods of low solar activity have been identified: Maunder-($\approx$ 1645 to 1715), Dalton-($\approx$ 1790 to 1830), and Gleissberg-($\approx$ 1900) minimum. According to the definition used by Usoskin et al. [13] that relies on the sunspot number, the Maunder-minimum is classified as a grand minimum in which the sun is considered to be in a low activity state. The period in the second half of the 20th century, where the TSI values are comparably high, is classified as a grand maximum [13].

Not only reconstruction of solar activity, but also predictions of the future activity have been published recently. Steinhilber and Beer [14] presented a prediction for solar activity for the next 500 years. The study is based on the idea that the solar activity will vary with the same periodicities as it did in the past. It predicts a steep decrease in solar activity in the next fifty years and a grand minima for the second half of the present century. Such predictions are however quite controversial.

1.1.3 Solar Influence on Earth Climate in the Future

Thinking of global warming and climate change, the occurrence of a new grand minimum is of course a "hot" topic. Could a possible grand minimum stop global warming? Is

the sun saving our climate? Such questions have been raised, and several articles have recently been published on the subject. These studies use climate models with standard scenarios for anthropogenic influence and volcanic activity while varying the solar forcing component. It has been found that an upcoming grand minimum (comparable to the Maunder minimum) could reduce the predicted increase in global surface temperature (2 to 4 K) by roughly 0.3 K [15, 16]. According to these studies, reduced solar forcing could not compensate global warming, but it can have a considerable effect on earth surface temperature.

1.1.4 Detection of a Possible Grand Minima

From an observational point of view, the challenge is to detect such an upcoming grand minimum as early as possible. If the prediction of Shapiro et. al. [17] is correct then a detection is possible in an early stage of a grand minimum, otherwise already the detection of a grand minimum as a whole is challenging. Therefore accurate and reliable measurements, and a continuous record of TSI are crucial.

Recently an article by Kopp [18] has been published that addresses the accuracy requirements for future TSI experiments in order to detect a grand minimum comparable to the Maunder minimum. It concludes that either an absolute accuracy of less than 0.01%, or by a continous measurement series with a long term stability better than 0.001% per year. Similar estimates are also published in the *Review of NOAA Working Group Report on Maintaining the Continuation of Long-term Satellite Total Solar Irradiance Observation* [19], this estimates are based on considerations at the timescales of antropogenic climate change and separating the solar influence from antropogenic influence at acertain confidence level.

It shall be noted that the considerations by Kopp [18] are based on TSI reconstructions as shown in Figure 1.1 but don not include the extreme case by Shapiro et al. [17], but a minimum that is 0.05% to 0.1% lower compared to the present TSI value.

Comparable requirements on TSI measurements have also been proposed by Fox et al. [20], that are also based on TSI reconstructions and past TSI variability.

1.1.5 Requests from the United Nations Global Climate Observing System

Global Climate Observing System (GCOS) is a joint undertaking of the World Meteorological Organisation and further United Nations agencies in order to provide comprehensive information on the climate system. It defines so called *Essential Climate Variables* that are crucial to observe, to provide international climate research programmes and initiatives e.g. the Intergovernmental Panel on Climate Change (IPCC) with high quality datasets. TSI is one of these essential climate variables, GCOS points out the importance of an uninterrupted TSI record, and makes requirements of 1 Wm^{-2} on absolute accuracy and 0.3 Wm^{-2} per decade in stability [21]. These requirements are given for the final data products and do not directly relate to the uncertainty of an individual instrument, but can be considered in the same order of magnitude as the requirements given in the previous section.

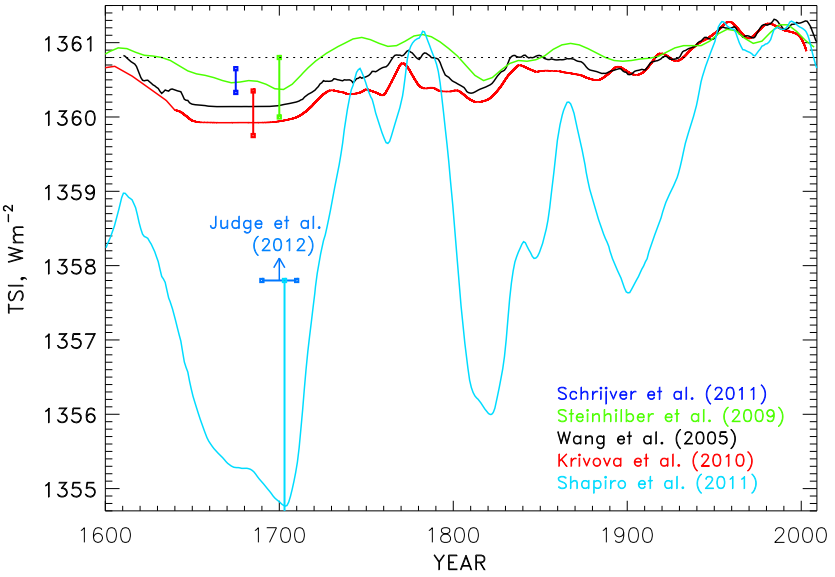

Figure 1.1: TSI reconstructions (1600 to present): The period of lower irradiance in the second half of the 17th century is the maunder minimum. While most models suggest a difference in TSI between Maunder minimum and present of roughly one watt per square meter, Shapiro et al. [17] suggest a much higher TSI (long-term) variability. (Figure from Solanki et al. [3])

1.2 Direct Solar Radiation and Total Solar Irradiance (TSI)

Electromagnetic radiation originating from the sun is measured and studied in different fields of science, that ranges from astronomy to medicine, biology and climatology. In this work the focus lies on the metrological, the meteorological/climatological, and the astronomical aspect. Different user groups are of course interested in different aspects of the radiation. Therefore some terminology is introduced to have a consistent vocabulary.

Generally what is measured with a radiometer like DARA is an electromagnetic flux density, measured in W/m^2. However depending on the application there are some more specific definitions:

- **Direct Solar Radiation:** The meteorological community, represented by the World Meteorological Organisation (WMO) defines *Direct Solar Radiation* as the observable parameter in their *Guide to Meteorological Instruments and Observation* [22]. According to the WMO, Direct Solar Radiation is measured with a pyrheliometer, that has a well defined field of view centred at the sun (described in Section 2.4.2). As meteorological measurements are usually ground based, this implies that not only radiation that comes directly from the sun is measured, but also radiation that originates from or is scattered by the earth's atmosphere.

- **Total Solar Irradiance:** From an astronomical point of view the relevant parameter is the *Total Solar Irradiance (TSI)*. Total solar irradiance is defined as the solar electromagnetic radiation at the top of the atmosphere on a plane area, normal to the incident radiation. It is integrated over all wavelengths and normalised to the mean distance of the earth from the sun (1AU). This quantity is independent of the earth atmosphere. Of course this astronomical property is also very relevant for weather and climate on earth, especially for the earth radiation budget, and is therefore widespread in climatology as well.

The function of metrology on the other hand is to study the measurement process itself. Its interest lies in the methodology of the measurement, in the realisation of and relations between scales and their uncertainty.

1.3 How to Measure Solar Irradiance

Generally electromagnetic radiation is measured with a *radiometer*. A radiometer that measures direct solar radiation is also called a *pyrheliometer*. Its name is derived from the Greek words πῦρ (= fire) and Ἥλιος (= sun). In order to measure radiation quantitatively, a scale must be implemented in the radiometer. This can be done in different ways that are described in this Section. A radiometer that is characterised (i.e. that has a native scale implemented, Section 1.3.5) is called an *absolute* radiometer.

1.3.1 Implementation of a Scale: Characterisation and Calibration

I order to measure Irradiance with an radiometer in a certain unit (e.g. W/m^2), it must be calibrated. In the following sections we will further distinguish between a *characterisation* and a *calibration*:

- **Characterisation:** A characterisation of an instrument is a component level calibration of a radiometer. Each component, for example the data acquisition, or the size of the aperture is calibrated individually. The result of an instrument characterisation is a *native* scale.

- **Calibration:** Within this work the term calibration will be used for so called end to end calibrations. An end to end calibration is a procedure where an instrument is directly calibrated for the target dimension e.g W/m^2 for a radiometer. Technically the radiometer to calibrate is compared to a reference radiometer (representing a standard) that is measuring the irradiance of the same source.

1.3.2 The International System of Units (SI)

The Convention of the Metre from 1875 is an international agreement on units of measurement. It is the base for coherent measurements worldwide. Based on the Metre Convention, in 1960 the 11th General Conference on Weights and Measures established the International System of Units (SI), that is based on seven base units. These are the metre, kilogram, second, ampere, kelvin, mol and candela [23].

The Convention of the Metre also set up the Bureau International des Poids et Mesures (BIPM) in Paris. This institute is responsible for the consistency of the SI units. It hosts for example the international prototype of the kilogram, which is the standard of the kilogram. On the other hand the institute also recommends how standards should be realised based on natural constants [23].

Besides the BIPM there are the national metrology institutes that work closely together with BIPM to ensure accuracy of measurements within their country. For Switzerland this is the Eidgenössisches Institut für Metrologie (METAS) .

1.3.3 Irradiance in the International System of Units

Physically the measured property is an energy flux passing through an area. Thus the obvious unit is the W/m^2. This is also the official unit for irradiance according to the international system of units (SI)[23]. Considering SI base units, algebraically this reduces to kg/s^3. This would mean that in principle only two of the SI base units, the kilogram and the second are effectively necessary to measure total solar irradiance. Practically however it seams unavoidable to use some kind of length unit.

From a philosophical point of view it is interesting to think if it is possible to measure the radiation directly in the (mechanical) unit kilograms. It seems indeed possible if one is thinking about the radiation pressure that is acting on a defined area, for example a solar sail, while at the same time the sail is attracted by the solar gravity. Thus radiation pressure could be measured via the Newtonian gravitational constant. This would require accurate knowledge of the mass of the sun, the Newtonian gravitational constant and the sun-sail distance, as well as the sail size. An accurate way to measure lengths is needed in order to compare sail size and distance to the gravitational constant. In practice, rather than to use the gravitational constant (Γ) and the mass of the sun ($m_\odot$) separately, the product $\Gamma \cdot m_\odot$ would be used instead, as Γ is a natural constant with a comparatively high uncertainty (150 ppm) [24, 25] whereas the the product $\Gamma \cdot m_\odot$ is known with a very low relative uncertainty of 10^{-10} [24].

1.3.4 Realisation of Units

The SI base units are realised by the national metrology institutes based on their definition. For practical reasons, units that are *derived units* in the sense of SI nomenclature e.g. the watt are sometimes derived via natural constants or other derived units rather than from the base units. Within DARA the derived units volt and ohm are used to realise the watt. According to the SI [23] the volt is derived via the Josephson effect and the Josephson constant that links the volt to the second, rather than using the definition of the base units ampere, kilogram, metre and second. Likewise the ohm is realised using the quantum hall

effect and the Klitzing constant. Both effects and their application for reference standards can be found in Taylor & Witt [26] and references therein.

These effects depend on the fundamental natural constants electron mass e and the Planck constant h, and are therefore very reliable concerning long term stability. The numerical value of the Josephson constant (e/h) and the Klitzing constant (h/e^2) have been determined precisely in SI base units. Based on these results, the BIPM brochure [23] recommends standard values for these constants. This allows now to use them to accurately realise the volt and the ohm with respect to the SI base units, while officially volt and ohm are still defined by the definition of the base units. Technically the volt and ohm realised in this manner are *conventional* standards because they are based on a convention (recommended values) rather than on the base unit definition[23].

Technically the volt and ohm are realised by the national metrology institutes. These institutes distribute then these standards via transfer instruments e.g. standard resistors. It is important that every step in this realisation and distribution chain is traceable and repeatable within stated uncertainties.

In the future the current definitions of ampere (force between parallel wires) and kilogram (kilogram prototype), as well as the kelvin and mole will be replaced by a definition that is based on defined natural constants (Planck constant, elementary charge, Boltzmann constant, Avogadro constant), like the metre (speed of light). Thus also the volt and the ohm would be directly defined via the natural constants. To keep the impact of such a paradigm change as small as possible it is of great importance that new conventions and definitions are consistent with existing definitions. More details on the *new SI* can be found in Mills et al. [27] and references therein.

1.3.5 The DARA Native Scale

Figure 1.2 shows schematically the realisation of the necessary standards to build the DARA native scale. The DARA native scale is the scale that is finally used to measure solar irradiance with DARA. It is based directly on SI base and derived units, as provided by the metrology institutes. The standard volt, the standard ohm and the standard metre are the base for the realisation of the DARA native irradiance scale in watts per square metre. In case of DARA, the area of the aperture (in m^2) is directly measured at the METAS, the Swiss metrology institute, while the volt and the ohm are provided via transfer instruments.

The DARA native scale can then be used to measure solar irradiance in W/m^2. Measurements based on this scale are traceable to the SI base units. In order to ensure a high accuracy of the scale, the radiometer (DARA) needs to be characterised in detail, in order to compensate for negative effects that can influence the measurement. Furthermore the uncertainty of the native scale with respect to the SI base units needs to be estimated.

1.3.6 Irradiance Scales

Besides the native scale (Section 1.3.5) there are other scales that can be implemented in a radiometer by calibration. These scales are based directly on a comparison to existing irradiance standards, rather than on standards of different units. These standards are:

- WRR Standard (WMO/SI)
- SI-Cryogenic Laboratory Standard for Radiant Power and Irradiance
- Cryogenic Solar Absolute Radiometer (CSAR) Standard

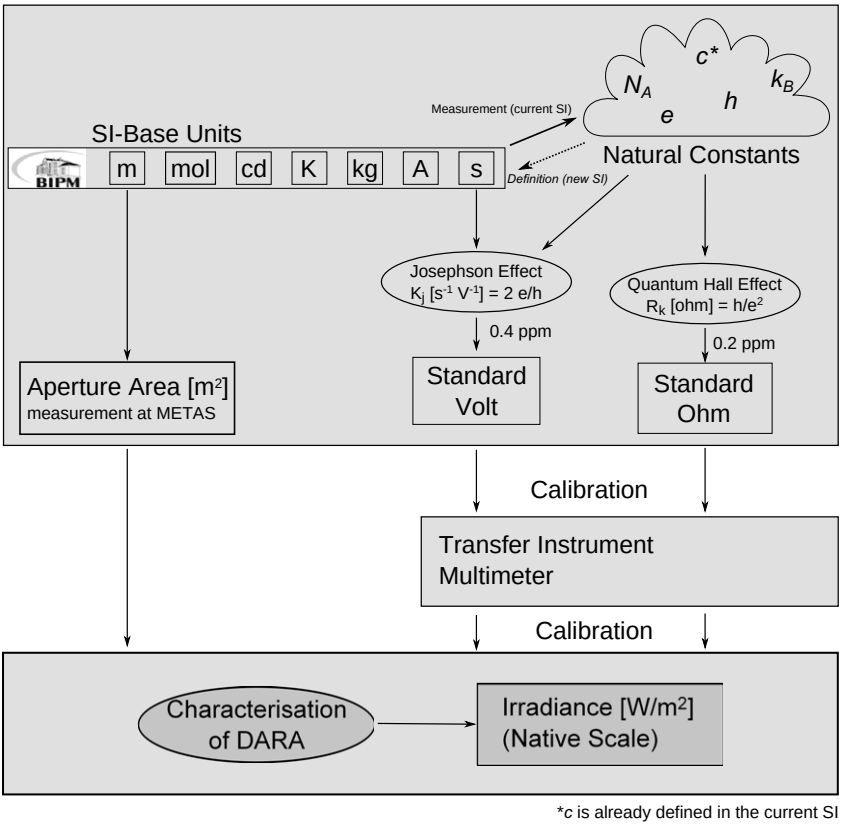

Figure 1.2: Realisation of Derived SI Units for DARA: The Diagram shows the realisation of the necessary units for the radiometer from the SI base units as a flow chart. The realisation of the standard volt and standard ohm is based on the natural constants: elementary charge (e) and the Planck constant (h). According to the current paradigm, the value of the natural constants (with the exception of c) is based on the definition of the SI base units. These constants have been measured with high precision with respect to the SI base units. Based on these measurements, conventional values for the Josephson constant $K_j = 2e/h$ and the Klitzing constant $R_K = h/e^2$ are recommended by BIPM, to guarantee consistency. In the future the "new SI" will define the values of the natural constants and thus the SI units will depend on the values of the natural constants. The realisation of the units (upper box) is done by the national metrology institutes. These institutes ensure traceability to the SI unit system.

Figure 1.3 schematically shows the possible implementation of different scales to the DARA instrument, with the corresponding uncertainties of the standard itself and the calibration of an instrument to this standard.

The WRR Standard

The World Radiometric Reference (WRR) standard is an artefact based (*conventional*) standard that has been introduced in the late 1970s in order to homogenise the measurements worldwide [28], see also Section 1.4. The WRR standard is based on a World Standard Group (WSG) of instruments that are situated at the World Radiation Centre (WRC) in Davos. The WRR standard has been adopted by the WMO as the official reference standard for solar irradiance measurements in 1979. Furthermore the WRR standard is also recognised by the SI as a conventional standard for solar irradiance measurements. The uncertainty of the WRR standard with respect to the SI base units is estimated to be 0.3% [28].

SI Cryogenic Laboratory Standard for Radiant Power and Irradiance

The SI cryogenic laboratory standard for radiant power and irradiance is a technology based standard, meaning that the standard is directly traceable to the SI base units. It is realised with cryogenic radiometers in a similar way as the DARA native Scale. Working at cryogenic temperatures however allows much higher accuracy compared to the characterisation of DARA. The cryogenic radiometers that represent the SI cryogenic laboratory standard for radiant power and irradiance can only be operated in a laboratory environment inside a vacuum chamber. To ensure stability and homogeneity of this standard, the standards of the different institutes are compared in key comparisons [29, 30].

While most of these cryogenic radiometers are only able to measure radiant power in watts, the Total Irradiance Radiometer Facility (TRF) at the Laboratory for Atmospheric and Space Physics (LASP) in Boulder, USA, offers also a standard for irradiance (in W/m^2). The uncertainty of the cryogenic standard at the TRF with respect to SI base units is 0.014% (2σ) which is very low compared to the uncertainty of the WRR standard [31].

The CSAR Standard

The third possibility is to integrate a scale based on the Cryogenic Solar Absolute Radiometer (CSAR) . Unlike the above mentioned cryogenic radiometers, CSAR can operate outdoors and is designed to measure direct solar irradiance. CSAR uses the advantages of the cryogenic radiometers while maintaining the possibility to directly measure solar irradiance. Of course this is a compromise meaning a slightly lower accuracy with respect to SI base units and a higher effort to characterise CSAR. For example CSAR needs a window where light can enter the vacuum tank. The transmission of this window then needs to be known very accurately. CSAR was built as a joint project of PMOD, METAS and the National Physics Laboratory (NPL) in London. NPL is the national metrology institute of the UK. CSAR is described by Winkler [32] and Fehlmann [33].

1.3.7 Artefact Versus Technology Based Standards

In the previous sections different irradiance standards have been described. An important difference between these standards is the fact that the WRR standard is an artefact based (conventional) standard, while the other two standards are technology based. Symptomatic for an artefact based standard is the fact, that the calibration uncertainty is smaller than the uncertainty of the standard itself with respect to SI base units. On the other hand,

when calibrating against one of the technology based standards the main uncertainty originates from the calibration itself. This is illustrated in Figure 1.3.

Technology based standards are independent of any particular realisation (instrument) thus, a technology based standard always represents "true SI" in the sense of the base units with a certain uncertainty. When using the artefact based WRR standard as a representation for "true SI" the uncertainty of the WRR with respect to SI base units of 0.3 % must always be considered. In reality this does not make much sense, as the WRR standard had been established to improve the homogeneity of irradiance measurements. The artefact based standard has been found very reliable and traceability to the WRR standard allows consistent measurements with much lower uncertainty with respect to WRR than the uncertainty of WRR with respect to SI base units. Therefore it is absolutely necessary to identify a measurement, taken with respect to WRR as such. Otherwise if a mesurement is reported in SI units without indication of the WRR standard, the uncertinty of the WRR itself needs to be added.

Inconsistency in these notations and improper handling have led to much confusion in the past. A proper solution would have been to give the measurements according to the WRR standard a distinct unit. Such a unit would have avoided the problem of measuring with different scales without noticing it. Conversion factors between the units could then be used to convert between the units.

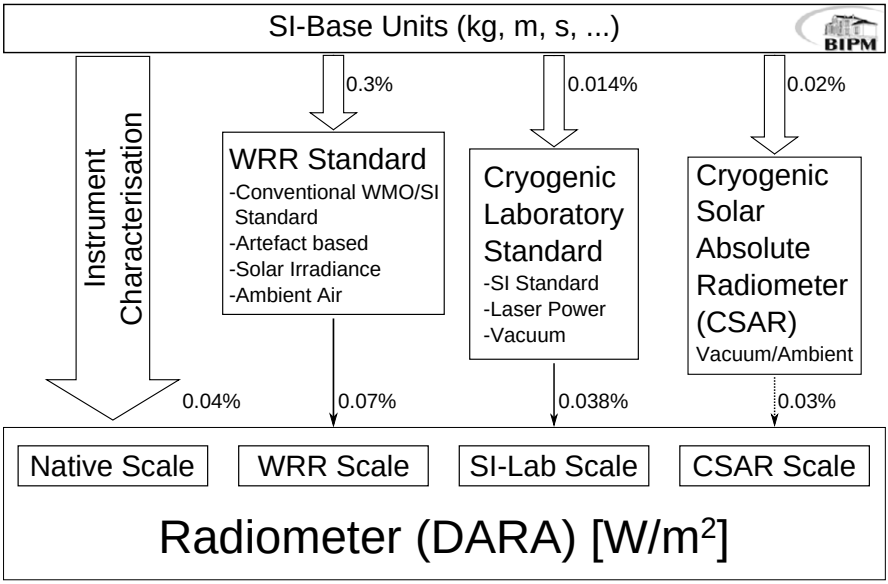

Figure 1.3: Implementation of different SI-traceable scales in a radiometer. All scales are ultimately based on the SI base units. Each wide arrow describe a characterisation with respect to SI base units. The narrow arrows describe a calibration. To each arrow the corresponding approximate relative uncertainty (2σ) is noted. The CSAR instrument is the latest development in terms of radiometric standards. It has not been implemented to another instrument so far.

1.4 History of Solar Radiation Measurements

The History of solar radiometry dates back to the 1830s when Claude S. M. Pouillet developed the first radiometer and published his measurements in 1938 [34]. Since then instruments have improved and more accurate measurements became possible.

A major step in the history of solar radiometry had been the development of the famous Ångström compensation pyrheliometer by Knut Johann Ångström in the 1890s [35]. It was the first radiometer that substituted the solar power with electrical power and so derived the solar irradiance from the measurement of the electrical power. This principle is still the base for the modern cavity radiometers that were developed first in the late 1960s and are still in use today. More details on the history of early solar radiometry can be found in Fröhlich [28].

Ground based irradiance measurements led reasonable estimates of the "Solar Constant" varying by only a few percent from the present value. In the 1960s the first measurements of solar irradiance from air planes and high altitude balloons have been carried out, these programs continued and partly overlapped with the satellite area that started in the 1970s. Despite all efforts and improvements in accuracy, it was not before continuous satellite based measurements were available, that the 11-year solar cycle could be detected in TSI. Since 1978 there are continuous satellite based TSI observation, which are described in Section 1.4.2. An extensive overview on TSI measurements prior to 1980 can be found in the book by Kmito [36]. The need for a worldwide standard for irradiance measurements became evident in the early 20th century and remains an issue until the present days. The next section describes the history of these standardisation in more detail.

1.4.1 Historical Irradiance Standards

In order to homogenise measurement data of different stations and instruments, in the early 20th century the first reference standards (or scales in their terminology) have been introduced. These were based on a specific instrument type. Until 1956 the *Ångström Scale* and the *Smithsonian Scale* were in use. These standards however differed by almost 5 % from each other. Therefore the common *International Pyrheliometer Scale* (IPS56) had been introduced in 1956. In 1979 the WRR standard had been established as a standard for solar irradiance. The WRR is based on the characterisation of several modern instruments. The uncertainty compared to SI-base units was estimated to be 0.3 % which was almost an order of magnitude better than the earlier standards [28]. See also Section 1.3.6.

Studying the history of these standards, used in solar radiometry, it can be seen that it is not straightforward to compare standards, or to adapt data from one standard to another. Different standards, and the task to establish a newer and better standard has often led to confusion in the past [28]. Some of these problems emerged again when comparing different measurements in the satellite age as described in the next sections.

1.4.2 Satellite based TSI Measurements

In the late 1970s satellite based TSI measurements have started. Numerous radiometers have been brought into space since then and have contributed to the now about 35 year record of TSI. This measurements not only established a value for the "Solar Constant", but also revealed the TSI variability with the 11 year cycle of the sun that is in the order of 0.1%. Figure 1.4 shows the results of different measurements of TSI. The origin of these data is summarised in Table 1.1. The TSI data record has been discussed in many publications, the most recent are by Yeo et al. [37], Kopp [18] and Zacharias [38].

The experiments that are further discussed in this work are:

- VIRGO/SOHO - Variablilty of the Solar Irradiance and Gravity Oscillations on board the Solar and Heliospheric Observatory (PMOD/WRC and IRMB Instruments) [39, 40]

- TIM/SORCE - Total Irradiance Monitor on board the Solar Radiation and Climate Experiment Satellite (LASP Instrument)[41]

- PREMOS/PICARD - Precision Monitoring Sensor on board the PICARD satellite (PMOD/WRC Instrument)[42, 43]

- TCTE/STPSat-3 - Total Solar Irradiance Calibration Transfer Experiment on board the STPSat-3 satellite (LASP Instrument) [18, 44]

Satellite	Experiment	Instrument type	Data version/date	References
Nimbus-7	ERB	HF	download: 14 July 2014	[45]
SMM	ACRIM I	ACRIM-type	ACRIM1_V1_89	[46, 47, 48]
ERBS	ERBE	adapted ACRIM	download: 14 July 2014	[49]
UARS	ACRIM II	ACRIM-type	ACRIM2_V3_0110	[48, 50]
SOHO	VIRGO	PMO6/DIARAD	virgo: d_v6_004_1402	[40]
ACRIMSAT	ACRIM III	ACRIM-type	Version 03/13	[50]
SORCE	TIM	TIM	Version 16 Level 3	[41, 51]
PICARD	PREMOS	PMO6	Feb. 2014	[33, 43]
STPSat-3	TCTE	TIM	Version 1 Level 3	[44]

Table 1.1: Overview of the TSI experiments and data that are shown in Figure 1.4. All data with the exception of TCTE has been downloaded through the ISSI homepage [52].

1.4.3 Inconsistency of the Satellite Data

As can be seen in Figure 1.4 the data of the different experiments are not consistent to each other with respect of the absolute value. Especially when the TIM instrument on board the SORCE satellite became operational in 2003 and reported a lower value (by 0.35% compared to VIRGO) [41, 53] the discussion on the true TSI value arised anew[1]. The problem was then investigated further. It was proposed to build an indoor laboratory calibration facility to campare the flight spare units on ground [55]. This faciltity, the Total Solar Irradiance Radiometer Facility (TRF) was then built at LASP in Boulder USA. [31]

Comparisons between the instruments on ground revealed the same differences as in space. Some of the differences could be explained by traceability to either the WRR standard or to the SI base units, or simply by the fact that the native scale (characterisation) of some instrument was not as accurate as stated in the respective uncertainty. Further investigation on the causes of inconsistency are described by Kopp et al [54].

The PMO6-PREMOS instrument was the first experiment calibrated at TRF that was to measure TSI from a satellite in 2010. Thus PREMOS was the first instrument that brought the SI cryogenic laboratory scale to space. PREMOS carried out the most accurate (300 ppm, 1σ) measurement to date (in terms of the absolute value traceable to SI base units), and confirmed the measurements of TIM/SORCE within the uncertainty of the implemented SI cryogenic laboratory scale [33, 43]. A comparison between the WRR and the SI-cryogenic laboratory standard for irradiance (as represented by TRF) was also carried out with data from the PREMOS calibration. Fehlmann et al. [33, 56]

[1] The absolute value of ACRIM III has been changed form $\approx$1365 W/m^2 to $\approx$1362 W/m^2 after a flight spare intrument had been calibrated against the SI cryogenic laboratory scale at TRF in 2010/2011 [54, 50].

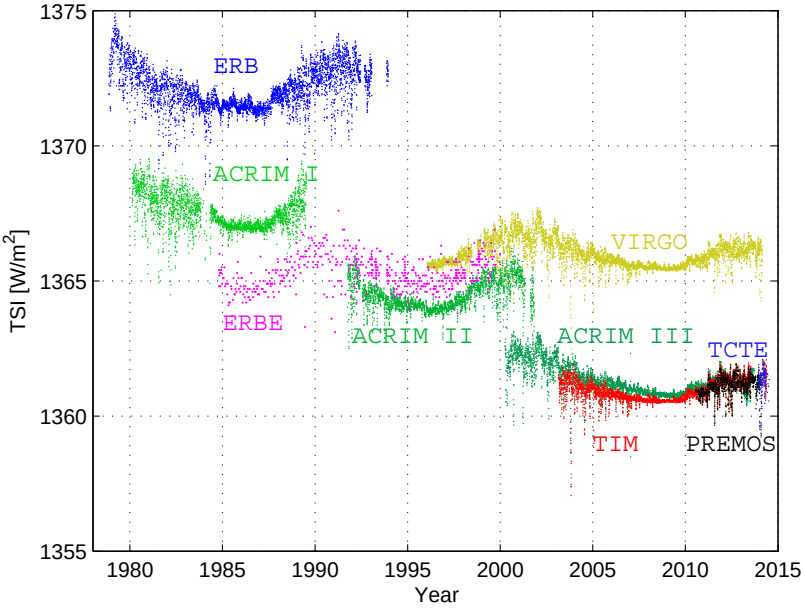

Figure 1.4: TSI satellite data from different experiments. The different datasets are listed in Table 1.1

found a difference between the standards that can explain the discrepancy between the measurements in space by VIRGO and TIM.

The latest TSI experiment, the TCTE, launched in late 2013 is also in good agreement with TIM and PREMOS [44]. The "new" lower value of TSI is now widely accepted and adopted by the IPCC Report 2013 [1].

TSI Composites

Different attempts have been made to homogenise the different datasets in order to generate a complete TSI time-series from 1978 to present days. Mainly three such TSI composites have been widely spread. These are the ACRIM-, IRMB- and PMOD-composite. A comparison of these three composites, as well as further references can be found in Solanki et al. [3] and Zacharias [38]. These composites are based on a different combination of data, and consequently suffer from the same inconsistencies as the original instrument data.

A new initiative to establish a homogeneous TSI time-series has been started at the International Space Science Institute (ISSI) in Bern. A working group, led by G. Kopp, is currently re-analysing TSI data in order to establish a new common TSI composite. The group consists of members of all major TSI experiment teams [52, 18, 38].

1.4.4 Future of Satellite Measurements

To date several instruments are planned to be launched in near the future. These are:

- CLARA/NORSAT-1 - Compact Lightweight Absolute Radiometer, on the Norwegian microsatellite NORSAT-1 (PMOD/Norwegian Space Agency). Launch is foreseen in early 2016. [57]
- TSIS/ISS - Total Solar Irradiance Sensor on the International Space Station (LASP/ NASA). Launch is foreseen in 2017 [2].
- DARA/PROBA3 - DARA on ESA's PROBA3 satellite (PMOD/ESA). Launch is foreseen in 2018 [3].

In order to have consistent and accurate data in the future it is important to carefully characterise and calibrate the instruments before launch, as well as having overlap between the measurement periods of the different instruments.

1.5 Goal of this Work

Although the inconsistencies mentioned in Section 1.4.3 have been partly resolved, there are still some unsolved problems. The tendency for TSI measurements is to be traceable to the SI base units with as high accuracy as possible. This can be achieved either with calibration of space radiometers against a cryogenic radiometer (SI cryogenic laboratory standard) or by implementing an accurate native scale to the space radiometer by fully characterising it. While the first possibility is nowadays much easier to do, only the characterisation of the instrument stimulates new insights and understanding of the radiometer. To date only the characterisation of the TIM instrument has a relatively high accuracy (on orbit uncertainty: 350 ppm 1σ [18], characterisation uncertainty: 200 ppm 1σ [58]). The PMO6 characterisation of Brusa & Fröhlich [59], dating from from the early 1980s, has an uncertainty of 0.11%, but is in principle also compatible with the SI cryogenic laboratory standard. The characterisation of PREMOS by Fehlmann [33] however is incomplete (no reflectivity measurements) and there is no consistency between the individual PREMOS radiometers.

1.5.1 Characterisation of DARA

With the new development of DARA, where the consolidated findings of the last decade have been implemented, the need for an accurate characterisation arised. In this work DARA will be characterised and irradiance scales based on the SI standards (Section 1.3.6) will be implemented. Thus the understanding of DARA will be stimulated. Besides the aesthetic aspect of this work, upcoming space radiometers CLARA and DARA/PROBA3 as well as the new generation of ground based radiometers can benefit from new insights. The aspect of ground based radiometry is very important from the point of view of the WRC as it is responsible for maintaining the WRR and ensure the world wide homogeneity of ground based solar irradiance measurements.

Note to the Uncertainties

An important aspect within this work are estimations of uncertainties, especially within the characterisation of DARA. Generally we follow the *Guide to the Expression of Uncertainty*

[2] Personal communication with Greg Kopp (LASP)
[3] Personal communication with Wolfgang Finsterle (PMOD)

in Measurement (GUM) [60] and the *Guide to GUM* [61]. Instead of using the GUMs coverage factor k, the uncertainties are marked as 1σ or 2σ uncertainties which would correspond to a coverage factor of k=1 or k=2 respectively. This is done in order to avoid confusion with other quantities labelled k. Thus a 1σ uncertainty corresponds to the standard uncertainty, and a 2σ uncertainty corresponds to the expanded standard uncertainty with a coverage factor k=2.

Within the DARA characterisation, most corrections and subcomponents are in simple multiplicative relation to the result. Therefore, when combining uncertainties, their relative uncertainties squared can be summed up. If not otherwise stated, this is the standard procedure to calculate the combined standard uncertainty.

1.5.2 The Heliostat

For many radiometric experiments some sort of light source is needed. Depending on the specific application such a light source can be a laser, a lamp, an LED or the sun itself. The solar light has the advantage, that it is the light source for which solar radiometers are designed for. It has the right geometry, spectrum and power level. On the other hand, such experiments with sun light normally need to take place outdoors, where there are numerous environmental influences, such as wind, temperature variations, etc. A solution that allows to benefit from the advantages of the solar light and to avoid the downsides is a heliostat. A heliostat is a system of two mirrors that guides solar light on to a fixed target in the laboratory.

PMOD/WRC used to have such a system in the past, but this system had to removed in the course of the renovation of the PMOD/WRC institute building. Therefore it was considered to build a new heliostat. This new heliostat should provide a higher quality beam and offer versatile applications that were not possible with the old system. In the frame of this work a new heliostat has been planned and realised. A first application of the heliostat was to visualise and characterise diffraction effects in the DARA radiometer (Section 3.6.

The design and the construction of the heliostat is described within this work (Sections 5, 6 and 7).

Chapter 2

The Digital Absolute Radiometer (DARA): Instrument Description

2.1 Introduction

DARA is a radiometer to measure direct solar radiation in W/m^2. It was developed at PMOD/WRC in 2009/2010 as a prototype for a new generation of solar radiometers for space and ground based applications.

The measurement principle is based on the previous generation of PMOD's radiometers, the PMO6 developed by Brusa & Fröhlich [59]. However the design of DARA is almost completely new and includes the latest insights in radiometry and trends in satellite technology. To be able to fly on small, low budget satellite missions the radiometer must be lightweight and compact.

The DARA instrument was originally planned as a prototype for the Sun Monitor space experiment that was foreseen to fly on ESA's PROBA3 satellite. Unfortunately the PROBA3 mission has been postponed several times. To date the project is continuing again, aiming for a launch date in 2018. However the TSI experiment on PROBA3 will no longer be called Sun Monitor, but DARA (like the prototype) instead. If not indicated otherwise, the term DARA will be used for the prototype throughout this work.

As the PROBA3 mission had been on hold for several years, the DARA prototype served more as a general prototype of a new generation of radiometers for space and ground based use. The first actual flight instrument within the new DARA generation will be the CLARA radiometer on the NORSAT-1 satellite.

The development of DARA could benefit from the MITRA instrument [33, 62], that was built at the same time. Joint efforts have been made for the development of the heat sink, cavity and thermometer of the two instruments.

2.2 General Properties

DARA consists of a detector head and a control and data acquisition unit, which are both mechanically connected in one case. DARA has three cavities (detectors) with separate data acquisition channels.

The main features and design updates include:

- 3 measurement cavities for degradation tracking and redundancy, any two can be operated simultaneously

- Inverse aperture geometry (compared to the PMO6) to eliminate stray light
- New cavity and heat sink design with reduced non-equivalence
- Measurement cadence of 30 s
- Digital controller loop with feed forward system
- Pulse width modulated heater power application
- Size: 241 x 142 x 151 mm (box), Weight: approx. 3.4 kg

2.3 Measurement Principle

DARA is a so called electrical substitution radiometer, it means the principle of measurement is based on the substitution of solar radiant power with electrical power, that can relatively easy be measured. The following paragraphs describe the method in more detail. The principle of electrical substitution has also been described in numerous articles, starting with Ångström [35] in 1899. A recent discussion can be found in Fox and Rice [29].

Each of the three cavities (detectors) of the DARA instrument is equipped with an electrical heater and an absorptive coating for solar radiation. The cavities are connected to a common heat sink via a heat link with a precise thermal resistance. Figure 2.1 illustrates the measurement principle. One cavity (on the right) is operated as the reference cavity. It is permanently shaded from the sun and heated electrically with a constant power. The active cavity is heated by absorption of solar radiation and additional electrical power, so that the heat flux between cavity and heat sink is equal for both cavities. This is done by comparing the two temperature differences (ΔT_A and ΔT_R) and controlling the electrical heater power for the active cavity accordingly. For the heat flow at the reference cavity the incoming flux is equal to the outgoing flux:

$$P_{A_{Electrical}} + P_{Sun} = P_A \tag{2.1}$$

In order to determine the radiant power P_{Sun} the P_A needs to be determined. Therefore the active cavity is completely shaded (e.g. the shutter is closed) at regular intervals. If the shutter is closed $P_{A_{Electrical}}$ is equal to P_A. Thus follows:

$$P_{sun} = P_{closed} - P_{open} \tag{2.2}$$

where P_{closed} is the electrical power in closed shutter state and P_{open} is the electrical power in open shutter state. The radiant power of the sun is the difference in electrical power between closed and open shutter state. This is how the radiant power is determined.

The reason to have a reference cavity supplied with a constant power, rather than just controlling ΔT_A to a fixed value, is to compensate for temperature drifts. If for example the temperature of the environment changes, cavity and heat sink temperature will drift and influence the measurement. Using an identical cavity as a reference, suppresses these effects.

In order to calculate solar irradiance, solar power has to be multiplied by the *Complete Radiometric Constant* C (Equation 2.3). C is the result of the instrument characterization (Chapter 3). In first order C approximately equal to the inverse of the aperture opening area ($\widetilde{C}$), its unit is m^{-2}. Within this work $\widetilde{C}$, the inverse of the aperture opening area, is named the *Basic Radiometric Constant* . In practice $\widetilde{C}$ is for example implemented in

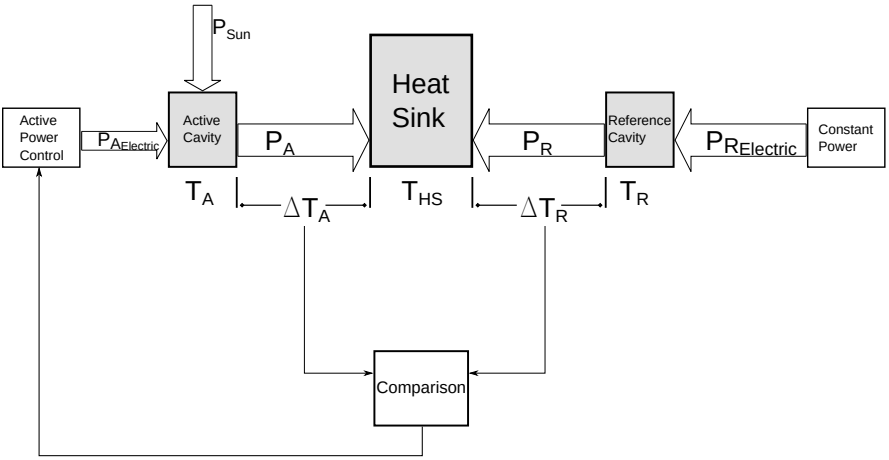

Figure 2.1: Illustration of the DARA measurement principle: The broad arrows represent heat flows between different components. The reference cavity on the right is electrically heated with a constant power. The active cavity on the left is heated by the sun and an electrical heater. The electrical heater power is adjusted to balance the temperature of the two cavities.

the data evaluation software, so that the necessary correction factors (Chapter 3) can be applied separately, depending on the environmental conditions.

$$I_{sun} = C(P_{closed} - P_{open}) \tag{2.3}$$

In practice the shutter is opened and closed at a certain period (e. g. 30s). For a given open shutter measurement the corresponding closed shutter measurement is interpolated from the closed period before and after the open shutter cycle.

DARA features three cavities. The third cavity can be operated as a second active cavity (simultaneously to the first active cavity), using the same reference cavity. Furthermore the cavities are interchangeable, so that each cavity can be set as reference cavity.

2.4 Detector Head

Figure 2.2 shows the cross section of the DARA radiometer. The blue structure is the heat sink, the core of the radiometer, the cavities are directly attached to it. The individual elements of the detector head are described in more detail in the next few sections.

Table 2.1 lists some geometrical properties corresponding to the cross-section (Figure 2.2).

2.4.1 Precision Apertures

In front of the instrument are the precision apertures. They are fixed to the front plate. The apertures are made of tungsten carbide (RGS 50). They have a nominal diameter of 5 mm, the exact diameters are listed in section 3.1. These apertures define the m^2 in the irradinace unit (W/m^2).

2.4.2 Optical Path and Field of View

The light entering the precision aperture (front) is passing through a black tube, and through the view limiting aperture into the cavity. The system of the two apertures defines the instruments field of view. Table 2.1 lists the dimensions of this system and Figure 2.4 illustrates the situation. While the radius (or diameter) of the precision aperture defines the m^2 of the irradiance unit, the parameters d_d and R_d define the field of view. The field of view can also be described by means of angles as illustrated in Figure 2.4: The slope angle defines areas that can be seen from everywhere on the detector, whereas the limit angle defines the outer limit of the instruments field of view. The World Meteorological Organisation (WMO) defines standard values for these parameters [22]. The WMO standard is 1° for the slope angle, and 2.5° for the nominal field of view. DARA has a slope angle of 1° and a nominal field of view of 3.65°. DARA thus has a limit angle of 6.28°, which is larger than the WMO standard. This means that the DARA instrument can see more of the sky (and sky radiation) than a WMO standard instrument. This needs to be considered when calibrating the instrument on the ground, using the sun as a source.

Figure 2.5 shows the so called penumbra function. It describes the relative amount of light originating from a certain angle can enter the cavity through the two apertures. It is needed for the estimation of a possible correction for circumsolar radiation (Section 4.2).

The design of the optical path is inspired by the design of the TIM instrument [63]. The TIM instrument was the first radiometer to have a geometry where the precision aperture is in front, and the view limiting aperture in the back, close to the cavity. Previous radiometer designs, e. g. the PMO6 [59] had an inverted geometry, that means the view limiting aperture is in front and the precision aperture is behind, close to the cavity. The new design as implemented with DARA and TIM has two major advantages. First, the new design reduces stray light effects. The precision aperture lets only the amount of light (originating from the sun) passing into the instrument, that is actually meant to be measured. The muffler tube and the view limiting aperture only have to absorb stray light originating from the sky (which is non existent in space). With the old design however the view limiting aperture lets pass three to four times as much sun-light into the muffler, than passes through the precision aperture. This means that the muffler gets illuminated intensively. This illumination then leads to enhanced stray light effects. Such stray light has been found a major source of uncertainty in the PMO6-PREMOS instruments [33, 56]. The second advantage is that problems in connection with the warming up of the precision aperture can be avoided. In PMO6 radiometers the precision aperture gets heated up during the measurement phase by absorbing solar radiation. Because the precision aperture is so close to the cavity an additional heat flow from the aperture to the cavity biases the measurement by roughly 100 to 200 ppm [33, 64].

2.4.3 Cavities

The DARA detector head features three conical cavities. The cavities are made of silver (130µm) and coated with a gold layer (5µm) on the outside. The cavity is attached to the heat link aluminium structure using ultrasonic welding technique. The advantage of this technique is that there is no solder necessary, which would add to the thermal mass of the cavity.

The reason for making the cavities out of silver is the high thermal conductivity and the comparable low heat capacity. This makes the heat distribution within the cavity as homogeneous as possible.

Inside the cone a heater on a polyimide foil is attached. On top of the Heater foil there is a layer of black paint (Aeroglaze Z302) [65].

Four meters of very thin (⌀=30µm) copper wire is wound around the cavity at the

cylindrical part. These copper wires are used as thermometers to sense the temperature of the cavity. The same type copper wire is also wound around the heat sink. The electrical resistance of these wires changes by $3.9 \cdot 10^{-3}$ K^{-1} [66].

Figure 2.6 shows the cross section of the configuration. The thermometer wires are not illustrated in the figure.

2.4.4 Thermal Resistance and Heat Sink

The heat sink is made out of aluminium (AW 6082) and attached to the front plate. The whole heat sink and heat link structure is machined from one solid piece of aluminium. This ensures a good thermal conduction. The thermal resistance of the heat link is realized by a fine aluminium labyrinth. The structure is spark eroded. Figure 2.3 shows a 3D view of the heat sink structure and the cavities. Thermal simulations have been carried out to optimize the design of the heat sink.

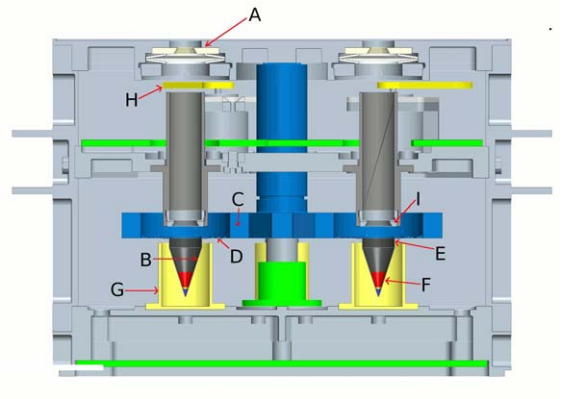

A Precision Aperture
B Cavity
C Heat Sink
D Heat Link
E Thermometer
F Electrical Heater
G Radiation Shield
H Shutter
I View Limiting Aperture

Figure 2.2: Cross section of the DARA instrument

Symb	Description	Value
d_d	Distance between precision (defining) and view limiting aperture	54.1 mm
R	Diameter of the precision aperture	5.0 mm
R_d	Diameter of the view limiting aperture	6.9 mm

Table 2.1: Geometrical data

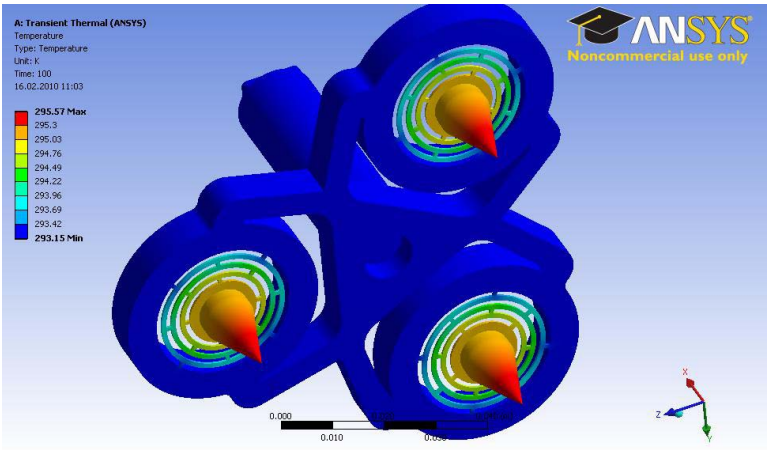

Figure 2.3: DARA heat sink with cavities, thermal simulation: 40 mW heater power is applied to the cavities, to simulate the thermal configuration. It can be seen that the main temperature drop (2°C) occurs across the heat link (labyrinth) structure.

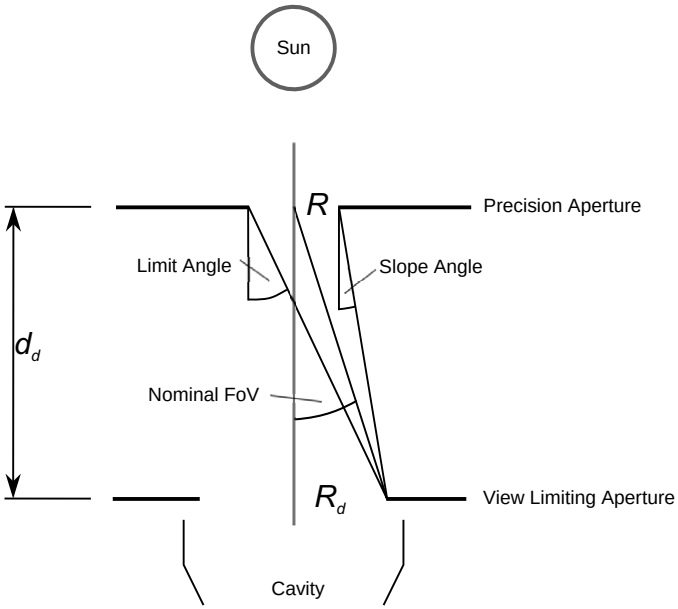

Figure 2.4: Illustration of the field of view

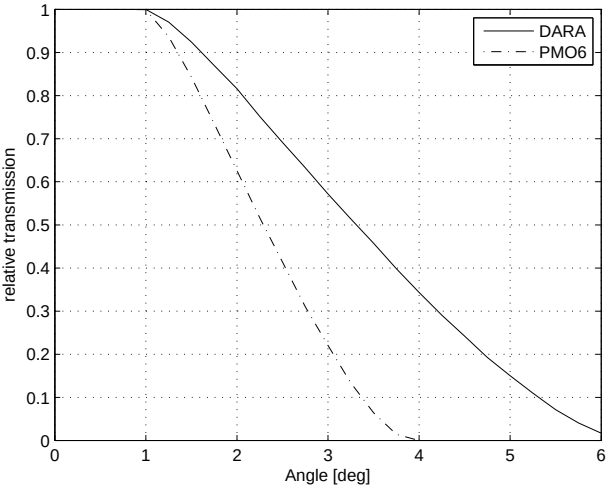

Figure 2.5: Penumbra function of DARA and PMO6 (WMO standard geometry) radiometers

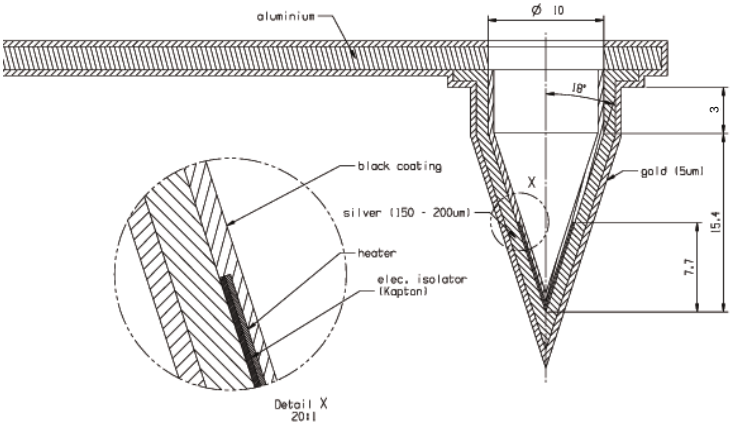

Figure 2.6: Cross section of the cavity, courtesy of Ricco Soder

2.5 Electronics

The electronics consists of a two channel digital controller loop, a data acquisition system and a communication interface. The next sections describes these components in detail. The radiometer is controlled by a 68332-CPU (Motorola 68k-family, 32-bit), which is also available as a radiation hard space version.

2.5.1 Controller Loop

The controller loop is responsible for keeping the active and the reference cavity in thermal balance. The realisation of the controller loop is schematically drawn in Figure 2.7. The reference cavity is electrically heated with a constant DC power, while the heater power of the active cavity is pulse width modulated. The duty cycle of the pulse width modulated power is proportional to the power dissipated in the cavity. In order to thermally balance the active and the reference cavity, four thermometer wires are connected in an AC-measurement bridge. The AC-measurement bridge generates an error signal, if the cavities are not thermally balanced, which is processed by the digital control unit. The digital controller unit adjusts the duty cycle for the active cavity power accordingly.

An advantage of the digital controller loop over analogue systems is the feed forward system. In the moment when the shutter is operated the controller can directly apply the necessary power for the situation, by restoring the last known power setting for the corresponding state. For example when the shutter is closed the controller will immediately apply the duty cycle value (power) from the last closed shutter cycle. This use of memory ensures that the cavities are never much out of balance, which in turn allows to run much faster shutter cycles than would be possible with an analogue controller. Fast shutter cycles are especially valuable if the radiometer operates in a thermally unstable environment (see Section 3.9). A good description of such a feed forward system, including a illustrative figure can be found in Fox and Rice [29]. A similar system is also included in the TIM instrument [63].

The controller is able to control two cavities simultaneously. Therefore a second measurement bridge is implemented (not shown in Figure 2.7).

2.5.2 Data Acquisition

Analogue to digital converters are used to sample the error signals as well as the voltage over the heaters. These values plus the values of the duty cycle as generated by the controller, are continuously logged at a sampling rate of 20 Hz. Housekeeping signals, for example temperatures and pointing sensor data, are read at a lower rate (10s). Additionally there is also system data that reports on the status of CPU and memory.

All data are stored on board until they are down linked in packages. Table 2.2 gives an overview of these data. The total data rate is about 720kb per hour.

2.5.3 Communication and Data Transfer

The Electrical Ground Support Equipment (EGSE) is an interface to receive the data from the instrument. The EGSE consists of a computer and the EGSE software. As the DARA instrument is only a prototype, the instrument is connected to the EGSE via an RS485 serial connection. The measurement data is downlinked from the radiometer to the EGSE using a Kermit protocol. The data is formatted in a special binary data format. This is described in detail in the Software Design Document (see Section 2.10).

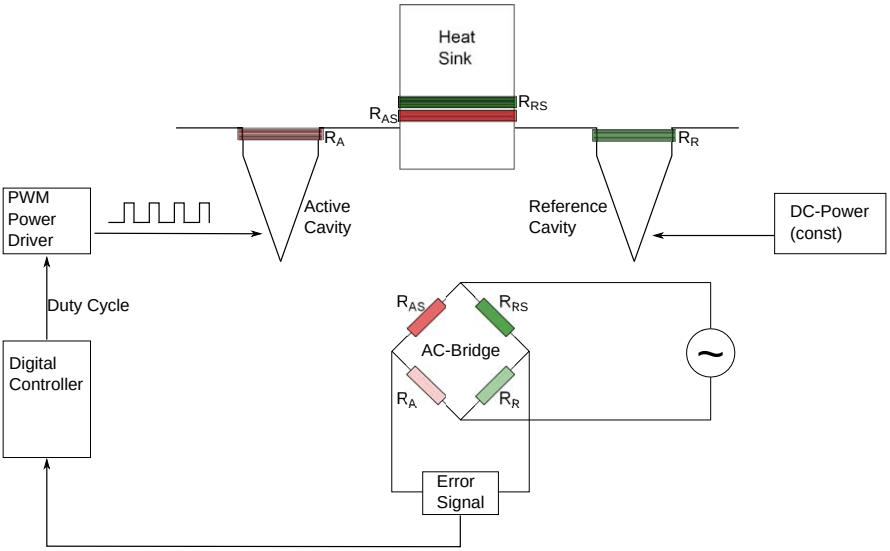

Figure 2.7: Function diagram of the controller loop

Parameter	Bits	No of channels	Sampling rate/period	Data rate [bytes/s]
Time stamp (signal)	32	1	20 Hz	80
Error signal	24	2	20 Hz	120
PWM signal	24	2	20 Hz	120
Voltage (power) signal	24	3	20 Hz	180
Time stamp (irradiance)	32	3	30 s	0.4
Level1 irradiance	24	6	30 s	0.6
Time stamp (HK)	32	1	10 s	0.4
Housekeeping data	16	45	10 s	9
Time stamp (system)	32	1	30 s	0.13
System data	16	22	30 s	1.5
Total data rate				**512**

Table 2.2: Overview of the downlinked data and data rate

2.6 Operation Modes

All three cavities can be used as active cavities. However one of the three cavities is always used as a reference cavity. This means the instrument can operate with a single active cavity, two active cavities in parallel or two cavities operating with inverted shutter cycles. This design offers redundancy in case one of the cavity would fail. Furthermore it allows better tracking of the degradation of the sensors, as all three cavities can be used in active mode.

2.7 Package Design

The DARA instrument package consists of a detector housing and a electronics housing, that are attached to each other. The detector is facing the sun, whereas the electronics is located in the back. The front plate of the instrument acts as a sun shield mirror. It has a high reflectivity in the visible range and is a crucial part in the thermal design. Figure 2.8 shows the DARA instrument partly opened.

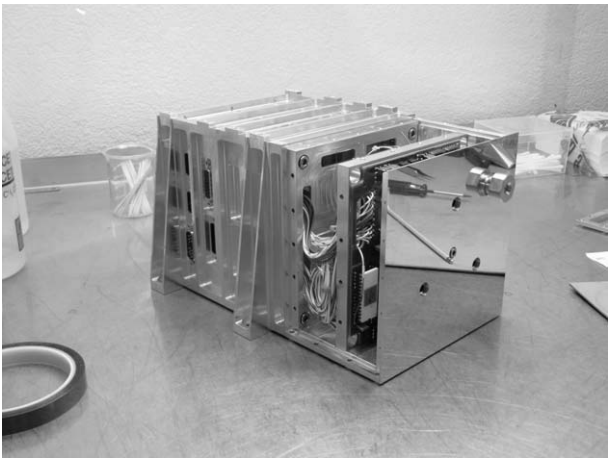

Figure 2.8: DARA package with front shield and entrance apertures

2.8 Data Evaluation

The DARA on board software does an on-line processing of the data and calculates irradiance values. However the complete raw data is downlinked to allow more sophisticated data evaluation, corrections and diagnostics. These corrections involve the estimation of the current in the cavity heater, based on temperature, as well as temperature dependent corrections to the analogue to digital converters. Furthermore the exact aperture size and further parameters of the characterisation (Chapter 3) are included in the external data evaluation process.

The data evaluation is based on formula 2.3. When calculating the difference between P_{closed} and P_{open}, the difference can be built between the two values of the duty cycle

(open and closed phase) while the voltage and current remain the same in both phases. So formula 2.3 expands to (where D_{PWM} is the pulse width modulation value, that represents the duty cycle $0 < D_{PMW} < 1$):

$$I_{sun} = C \cdot U \cdot I \cdot (D_{PWM_{closed}} - D_{PWM_{open}}) \tag{2.4}$$

While PWM_{open} is the PWM value at the end of an open phase, integrated over typically 5 to 10 s, the corresponding closed phase PWM value is a linear interpolation of two such measurements at the end of the closed phases. This is done in order to find the best estimate of the hypothetical closed power value at the time of the open phase measurement. This reduces the impact of a slightly changing power level over a measurement cycle. The uncertainty caused by this linear interpolation when having non-linear drifts in the power signal, is addressed in the characterisation chapter (Section 3.9.5). Figure 2.9 shows an example of the power signal ($U \cdot I \cdot D_{PWM}$) versus time.

Note to Phase Sensitive Data Evaluation Methods

An alternative to the analysis in the time domain as described in the previous paragraph and illustrated in Figure 2.9, is the so called phase sensitive analysis in the frequency domain. This method had been applied to the TIM data to reduce noise, non equivalence effects and thermal drift effects [63, 29].

The availability of the complete raw data would allow to perform such an analysis, and in principle, the on board controller is also capable of performing a phase sensitive evaluation. The philosophy of DARA is however to run fast shutter cycles (30 s versus 100 s by TIM) to reduce thermal drift problems (Section 3.9.5). The shutter cycles are therefore not optimised to a frequency were noise levels are particularly low. Furthermore studies with an upgraded PMO6 radiometer have shown that the phase sensitive evaluation is extremely sensitive to small wiggles of the controlled signal that can occur directly after the shutter transition, especially if the shutter cycle is short. This leads to a problem, when PID parameters need to be adjusted, or unexpected transition wiggles occur as experienced at TRF (Appendix B).

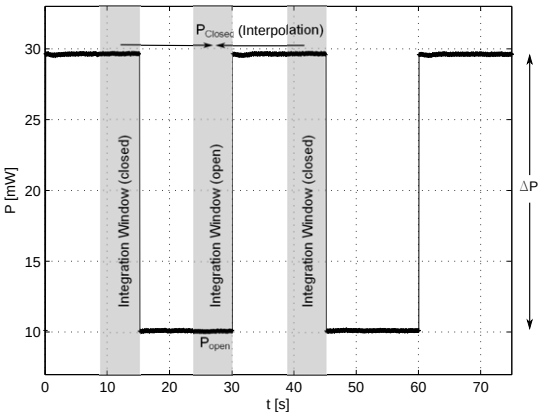

Figure 2.9: Signal of the electrical heater power $U \cdot I \cdot D_{PWM}$ versus time, the integration windows at the end of each period are shaded in grey.

2.9 Design Improvements

The air to vacuum ratio of PMO6 radiometer [67] has been causing a high uncertainty, when transferring a WRR calibration from ambient air conditions into space (vacuum). This is a problem when WRR-calibrating instruments for satellite use, as well as when comparing an instrument for ground based use to a SI cryogenic laboratory standard. (Cryogenic standard radiometers are operated in vacuum, where as the WRR is operated in ambient pressure.)

The new heat sink and the cavities have been designed to reduce the air to vacuum ratio. This goal could be reached, although there still exists a difference in sensitivity. The air to vacuum ratio and the measurement thereof is described in detail in section 3.7.

The second major improvement is the implementation of the digital controller. It allows much faster and more robust operation. This is a clear advantage if temperature drifts are present. These temperature drifts are unavoidable if the instrument is light weight, and therefore has a lower thermal mass.

Other improvements like the inverse aperture geometry have already been implemented in the TIM radiometer [63] and are therefore not really new. Also TIM uses an digital controller circuit and pulse width modulated power control, however TIM is not designed to operate with fast shutter cycle, nor is it a light weight instrument.

2.10 Technical Documents

There are several technical documents that describe details on the implementation of software and electronics hardware. These are listed in Table 2.3.

Title	Author	Revision	Date
On Board Software - Test Report	R. Cerny	0.1	15. 3. 2010
On Board Software - Final Report	R. Cerny	0.1	15. 3. 2010
On Board Software - Hardware Specification	R. Cerny	0.1	22. 10. 2009
On Board Software - Software User Manual	R. Cerny	0.1	14. 04. 2010
On Board Software - Software Design Document	R. Cerny	0.1	9. 11. 2009
EGSE Developpement - Software Design Document	R. Cerny	0.1	1. 12. 2009
EGSE Developpement - Final Report	R. Cerny	0.1	15. 3. 2010
EGSE Developpement - Software Use Manual	R. Cerny	0.1	11. 12. 2009

Table 2.3: Technical Documents

Chapter 3

Characterisation of the DARA Instrument

In order to measure solar irradiance in SI units (W/m^2) the instrument needs to be characterized. First of all, the components that define the *metre* and the *watt* need to be known in detail. These components are:

- Aperture size
- Control and readout electronics

In addition there are several corrections that need to be applied to raw measurement data. These are:

- Imperfect absorptivity of the cavity
- Lead heating
- Diffraction
- Non equivalence of electrical and radiative heating, or air to vacuum ratio

All of these components are to be characterized experimentally with the exception of the diffraction effects that are treated numerically in order to obtain a correction factor. Additionally the experimental approaches are supported by theoretical model calculations and diffraction effects are visualised in addition to the numerical treatment. The following sections describe in detail the characterisations of these components and corrections.

Additionally the following characteristics are also reviewed in order to better understand the instrument performance:

- Time constants of the cavities
- Balance of the thermometers

3.1 Aperture

The area of the aperture directly defines the m^2 of the irradiance unit [W/m^2]. As the optical power is measured in W, the radiometric constant (as used in equation 2.4) is the inverse of the aperture area.

The apertures are made out of cemented tungsten carbide (RGS 50). The opening of the apertures have been measured at the national metrology institute of Switzerland (METAS) at a temperature of 20°C. These values are listed in Table 3.1.

Cavity	Serial No	Aperture area	Measurement uncertainty (2σ)	Basic radiometric constant[1] ($\widetilde{C}$)
A	06/2010	19.6140 mm^2	$\pm$ 0.0011 mm^2	51131.9 m^{-2}
B	07/2010	19.6144 mm^2	$\pm$ 0.0015 mm^2	51130.9 m^{-2}
C	11/2010	19.6172 mm^2	$\pm$ 0.0010 mm^2	51123.6 m^{-2}

Table 3.1: Measured aperture sizes and radiometric constants of the DARA instrument

3.1.1 Thermal Expansion

RGS50 consists of tungsten carbide and cobalt (15%). Similar to metals, there is thermal expansion. Unfortunately data on coefficients of thermal expansion for such carbide metals are not very consistent.

The dependence of the expansion of the aperture area on the linear expansion coefficient is shown in Equation 3.1. A is the aperture area, r is the radius, and α is the linear expansion coefficient.

$$\frac{dA}{dr} = 2\pi r \Rightarrow dA\frac{1}{A} = 2\frac{dr}{r} \Rightarrow \frac{dA}{A} = 2\alpha dT \tag{3.1}$$

The aperture area correction factor $c_\alpha(T)$ is defined as follows:

$$c_\alpha(T) = \left[\frac{A + \Delta A}{A}\right]^{-1} = [1 + (2\alpha \cdot \Delta T)]^{-1} \tag{3.2}$$

where ΔT is the difference between the Temperature where the area has been measured ($T_0 = 20^o$C) and the actual temperature T:

$$\Delta T = T - T_0 \tag{3.3}$$

The value of the expansion coefficient α is not very consistent in the literature. Therefore a rather large uncertainty is assumed. The value used here is taken from the *Designer's Guide to Tungsten Carbide* [68]. The expansion coefficient is listed in Table 3.2.

Linear expansion coefficient α	$6 \pm 1 \cdot 10^{-6}$ K^{-1}

Table 3.2: Thermal expansion coefficient for cemented tungsten carbide (15% Co)

[1] The basic radiometric constant is implemented in the DARA evaluation software. Further corrections need to be applied separately, see Section 3.10

Uncertainty of the Thermal Expansion Correction

The uncertainty of the thermal expansion correction arises from the fact that the temperature of the precision aperture is not known very accurately and furthermore also the linear expansion coefficient comes along with a certain uncertainty.

According to GUM (propagation of uncertainty) [60, 61], the combined relative standard uncertainty for the correction factor c_α can be expressed:

$$\frac{u_c}{c_\alpha}(T) = \frac{1}{c_\alpha}\sqrt{\left(\frac{2\alpha}{c_\alpha^{-2}}\cdot u_{\Delta T}\right)^2 + \left(\frac{2\Delta T}{c_\alpha^{-2}}\cdot u_\alpha\right)^2} = \frac{1}{1+2\alpha\Delta T}\sqrt{(2\alpha\cdot u_{\Delta T})^2 + (2\Delta T\cdot u_\alpha)^2} \tag{3.4}$$

Thus the uncertainty is a function of T. It increases with ΔT and the size of the correction itself. Figure 3.1 shows the dependence. For the the uncertainty $u_{\Delta T}$ an uncertainty of 2°C (1σ) is assumed. The relevant contribution to the uncertainty results from the fact that the temperature of the aperture is not directly measured but assumed to be equal to the heat sink temperature. It is however a rough guess as the aperture can get warmer than the heat sink, by absorbing radiation, or cooler, if there is strong wind coupling. The temperature of the heat sink thermistor itself (type YSI) is more accurate (±0.1°C).

For the temperature range between 10 and 30°C the maximum uncertainty is 31 ppm (1σ) this value will be taken into account for the overall uncertainty budget of the DARA native scale.

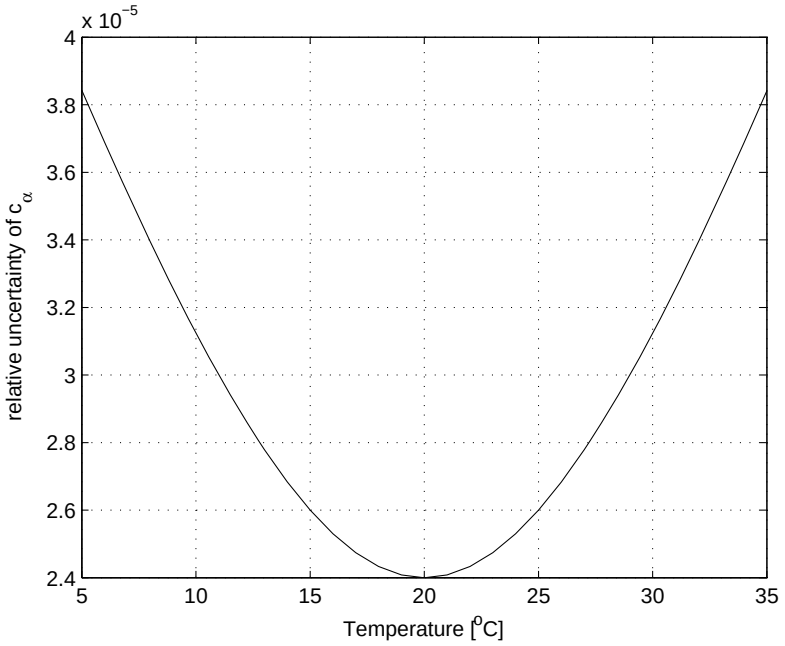

Figure 3.1: Relative standard uncertainty of the thermal expansion correction (1σ)

3.1.2 Combined Uncertainty

Table 3.3 lists the uncertainty contributions for the aperture area. The combined relative standard uncertainty of the aperture area is between 40 and 50 ppm. The contributions from the measurement and the thermal expansion correction are of the same order.

In case of higher variation of the thermal configuration, for example on a satellite, the uncertainty of the thermal expansion would increase. In this case it would be an advantage to attach a thermometer directly at the aperture, that would reduce the uncertainty on the actual aperture temperature.

	Aperture A	Aperture B	Aperture C
Relative measurement uncertainty	0.000028	0.000038	0.000025
Relative uncertainty of expansion corr.	0.000031	0.000031	0.000031
Combined uncertainty	**0.000042**	**0.000049**	**0.000040**

Table 3.3: Uncertainty budget for the aperture area (all uncertainties are relative uncertainties, 1σ)

3.2 Calibration of the Readout Electronics

The Readout electronics is responsible for the measurement of the radiant power in watts. The radiant power is substituted with electrical power as described in Chapter 2. Therefore the readout electronics needs to be able to measure electrical power in SI-traceable watts. The internal SI-watt scale is realised with a voltage reference and a precision resistor. Thus having a standard V and a standard Ω it is possible to measure in W (V^2/Ω).

3.2.1 Realisation of the Watt

In reality the realisation of the power measurement in W is more complicated than just setting up a voltage reference and a precision resistor.

The DARA Cavity heaters are powered by a pulse width modulated signal (PWM), the heater power applied to the cavity can be written the following way:

$$P = U \cdot I \cdot (D_{PWM} + S) \tag{3.5}$$

where D_{PWM} is the duty cycle of the PWM signal and S is a shape offset of the PWM signal. The circuit is designed to keep the current level I constant. This is done by keeping a fixed voltage (nominal 2.1 V) over a precision shunt resistor (nominal 90 Ω). The voltage U over the cavity heater however is not constant and is measured with an analogue to digital converter ADC. Figure 3.2 illustrates the electrical circuit.

Both components, the current I as well as the measurement of U have a temperature dependence, that needs to be accounted for. Therefore both components are to be calibrated against the temperature on the electronics board. The temperature of the electronics board is continuously sampled when operating DARA. The next section describes how the two components I and U are calibrated.

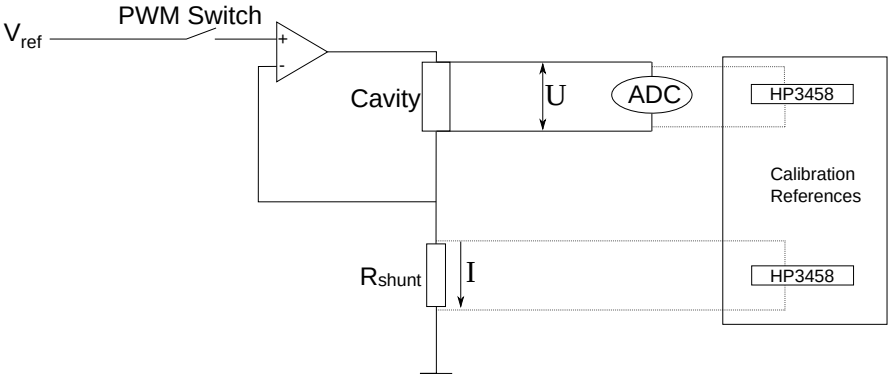

Figure 3.2: Simplified schematic of the electrical measurement circuit

3.2.2 Measurement Set-up

The basic idea is to compare the internal data acquisition system to an external reference data acquisition system.

Therefore sense wires for the voltage measurement are soldered to the internal sense wires. To measure the current (voltage drop across the precision shunt resistor), sense

wires are soldered to the precision shunt resistors directly. In this configuration both, voltage and current are measured simultaneously.

In the DARA software, the channel (cavity) to be calibrated is chosen as reference cavity. This is because then, the cavity is powered with a DC current. The current level of the reference cavity (ucr parameter) is set to the level of the active cavities (nominal 2.1 V at 90 Ω). Having set this parameter, a dark measurement is initiated (eg: 'start radio msr R:A'). For the external power measurement, two HP3458 multimeters [69] are used to ensure high accuracy over a wide temperature range.

The DARA is placed in a vacuum chamber, inside a temperature controlled cage. The measurements are performed under vacuum as well as at ambient pressure. The reason for measuring under these two pressure conditions is mainly that the temperature distribution at the electronics board is not necessary identical for these two situations. Furthermore the instrument is generally on a higher temperature when measuring in vacuum, due to less efficient cooling.

3.2.3 Calibration Data Application

Optical power of the sun is determined according to equation 3.6. It is linear in $U \cdot I$ which means that corrections for U and I can directly be applied as a multiplicative factor to P_{sun}.

$$P_{sun} = (P_{closed} - P_{open}) = (D_{closed} - D_{open}) \cdot U \cdot I \tag{3.6}$$

The correction term C_{UI} consists of the following components:

$$C_{UI}(T) = C_U(T) \cdot C_I(T) \tag{3.7}$$

where C_U is a correction factor for the U measurement and C_I is the correction factor for the nominal I. The actual implementation is described in further detail in the Appendix A.2.

3.2.4 Calibration Data Evaluation

The calibration raw data are split into U correction data ($[U_{internal}/U_{external}](T)$) and I data respectively ($[I_{external}/I_{nominal}](T)$). Figures A.1, A.2 and A.3 in the Appendix give an overview of these data. All data are evaluated against T_{PA} (on-board temperature), this temperature has been found to be the most reliable temperature sensor, in terms of stability and data quality, on the data acquisition electronics board. A polynomial fit of degree 2 has been applied for $I(T)$ and the ratio between $U_{internal}$ and $U_{external}$.

In order to fit the polynomial, the data are binned to one data bin per degree C. The mean value of each bin containing more than 10 data points is then used for the fit. This ensures that all temperature regions have the same weight on the fit. The voltage data are fitted for combined vacuum and ambient pressure data, where for the current, separate fits for vacuum and ambient pressure are performed. This is due to the fact that the current data of ambient pressure and vacuum do not correspond that well. This is also the reason to do a separate calibration for vacuum and ambient pressure.

The polynomial coefficients are also noted in Figures A.1, A.2 and A.3 in the appendix. These are also the coefficients implemented in the data evaluation software. The calibration measurements were done in November/December 2011 (between TRF and WRR comparison).

	Cavity A	Cavity B	Cavity C
Resistance [Ω]	89.99845	89.99445	89.99765
Uncertainty [Ω]	0.0029	0.0029	0.0029
$R/R_{nominal}$	0.999983	0.999938	0.999974
Uncertainty	0.000032	0.000032	0.000032

Table 3.4: Measured values of the precision resistors

3.2.5 Calibration Check in 2014

In order to investigate long term stability of the readout electronics, calibration measurements, similar to the 2011 measurements have been performed in February 2014. These measurements have been compared to the original calibration curves from 2011 (Figures A.4, A.5 and A.6). Channel A shows differences of 40 to 50 ppm between 2011 and 2014. Channel B and C show slightly less deviation. Considering the calibration uncertainty (22 ppm) and the long term stability uncertainty (29 ppm) at 1 sigma level (Section 3.2.8), this is still within the specification.

3.2.6 Correction for the Precision Resistor

The current is measured as a voltage drop over a precision resistor. The nominal resistance is 90 Ω and the specified tolerance is 100 ppm. Therefore the resistance is also measured. Table 3.4 shows the result of these measurements. The measurements have been performed with a HP3458 Multimeter in 4 Wire configuration.

3.2.7 Quality of the PWM Signal

The shape of the PWM signal has been monitored to ensure that the PWM signal has a nice rectangular shape. Figure 3.3 shows the rising and falling edge of the PWM signal at test point 19. The PWM has a period of 50 ms. A duty cycle between 1 % and 99 % is possible. This ensures that there is always enough time to include the rise time. Figure 3.3 shows the rising and falling edge of the PWM signal. The average rise/falling time is around 2 µs, which is about 40 ppm of the period. This is valid for all three channels.

Accuracy of the PWM

The time resolution for the PWM generation is 16 bit or 65536 steps at 20 Hz. The corresponding time resolution is then 0.77 µs. Therefore the error, generated by the resolution limit of the PWM is assumed to be distributed rectangular thus the corresponding σ is 0.22 µs. In this case for the closed-open duty cycle difference the accuracy is around 0.31 µs. Assuming the closed-open duty cycle difference is around 17 ms (one third of a period), the relative uncertainty is roughly 18 ppm. This holds for a single PWM value. If each PWM value was independent and the resolution limit (18 ppm) is the uncertainty of each value, integrating over 5 seconds (100 readings) would yield a reduction by $\sqrt{100}$ to 1.8 ppm. As the PWM value tends to correct for the previous adjustment error (due to the resolution limit) this value might even be overestimated. A value of 2 ppm is taken into the uncertainty budget its influence is negligible.

Due to fact that the value for further processing is a difference between two PWM values, and the fact that the PWM is usually operated in the range between 20% and 80% possible offsets and nonlinearities at extreme values should not introduce furter uncertainties.

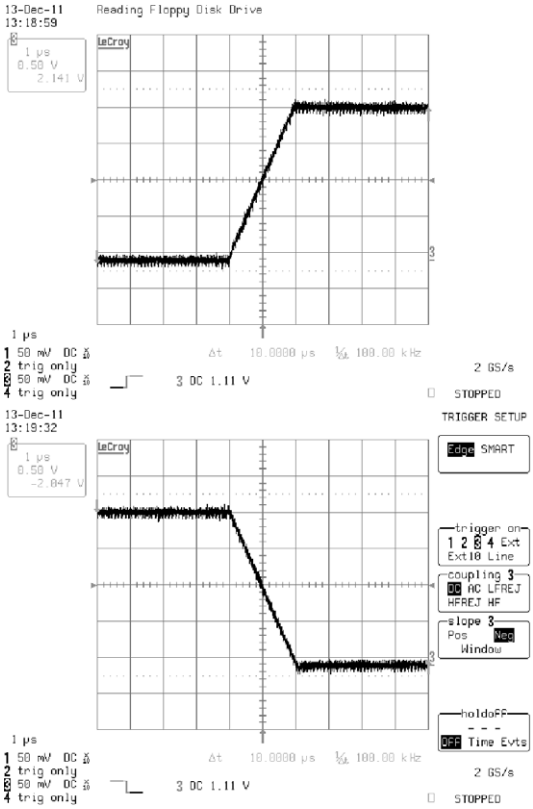

Figure 3.3: Rising and falling edge of the PWM signal (Channel A at TP19)

3.2.8 Uncertainty Estimation

The power signal consists of the following components:

$$P = C_U(T) \cdot U_{heater} \frac{C_I(T) \cdot U_I}{R} \cdot \Delta D_{PWM} \tag{3.8}$$

Where C_U and C_I are the calibrations, U_{heater} and U_I the respective hardware (ADC and voltage reference) and R is the precision resistor. As this is a simple multiplicative relation the square of the relative uncertainties can be summed up. The uncertainties of the individual components are listed in Table 3.5. The uncertainties originate from the specification/calibration of the HP3458 multimeters [69] and the data sheets of the components [70, 71]. They are treated as type B uncertainties according to the GUM [61].

Certainly these uncertainties are by no means the technical limits that can be achieved. Improvements either on the quality/stability of the used electronics components itself or the calibration could be improved. For example the use of pre aged voltage sources could enhance the long term stability, as drifts in voltage sources tend to flatten out with time [72]. Furthermore traceability of the reference multimeters used, could be improved with a more recent calibration of the reference multimeter.

To significantly reduce the overall uncertainty of the electronics all the uncertainties of the subcomponents need to be reduced accordingly, otherwise one of the subcomponents will become dominant.

Component	Uncertainty (1σ)	Remark/subcomponents (1σ)
R	46 ppm	Absolute accuracy (32), long term stability (29), thermal drift (17)
$C_U(T)$	24 ppm	Uncertainty of the calibration (21), measurement statistics (12)
U_{heater}	29 ppm	Long term stability specification (29),
$C_I(T)$	22 ppm	Uncertainty of the calibration(21), measurement statistics (6)
U_I	29 ppm	Long term stability specification
ΔD_{PWM}	2 ppm	PWM duty cycle uncertainty
Total	**70 ppm**	Combined standard uncertainty

Table 3.5: Uncertainty budget of the electrical calibration

3.2.9 Electrical Resistance of the Cavity Heater

The resistance of the electrical cavity heater changes with temperature. If the behaviour of the cavity heater resistance is known accurately enough it would be possible to determine the electrical power without the voltage measurement. This is also discussed in Section 3.2.10. The behaviour of the resistance will be determined from a dedicated experiment over a wide temperature range, as well as from the electronics calibration data.

Resistance Measurement of the Cavity Heater

An experiment is set up in order to determine the behaviour of the heater resistance due to temperature changes. A heater foil is bonded to a piece of copper, and equipped with two leads at each connector as it would be in a cavity. So that a current can be fed through and the voltage drop across the heater can be measured. A YSI thermistor is also integrated in the copper to measure accurately the temperature. The set-up is placed in the climate chamber, where the resistance is measured for a temperature range from -30 to 50 °C. The

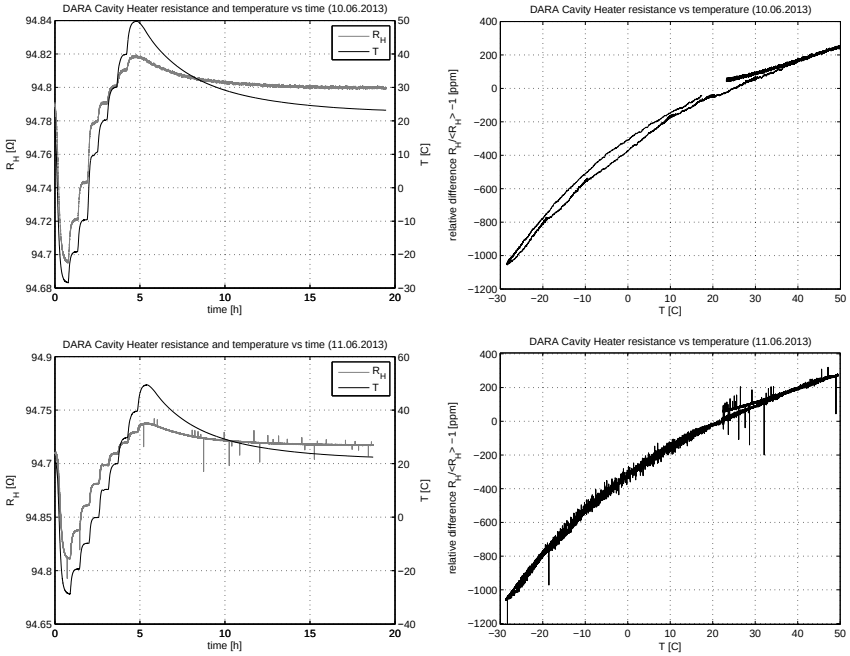

Figure 3.4: Resistance of the cavity heater: On the left the measurement data (temperature and resistance of the cavity heater) are plotted against time. The figures on the right show the dependency of the resistance on the temperature. The top figures show the measurements taken with a constant heater current of 20 mA, while the bottom figures show the measurements taken with a low current (4 wire configuration of the HP3458 DMM).

measurement is performed in two different configurations: first, using a precision source with 20 mA and the HP3458 as a Voltmeter, and second using the HP3458 directly in four wire ohm-meter mode.

Figure 3.4 shows the results from this measurement. It can be seen that the resistance varies roughly 0.12 Ω or 0.12 % over the whole temperature range from -30 to 50 °C. The curve is steeper in the lower temperature area and flatter in the higher temperature area. The derivative varies from 0.001 Ω/°C or 10 ppm/°C to 0.0025 Ω/°C or 25 ppm/°C.

While heating with 40 mW (20 mA mode) the hysteresis of the curve is higher, than with the low current mode. This might be explained by the fact that the heater produces a temperature gradient between the heater and the thermistor in the copper socket. Another issue is the absolute value of the resistor. It varies slightly between the two measurements (in the order of 100 to 200 ppm).

A equivalent measurement in the 4 wire configuration with the HP3458, has confirmed the data shown in Figure 3.4.

Results from the Calibration Data

The resistance of the cavity heater can also be determined, using the data from the electrical calibration (used throughout Section 3.2). The resistance is determined by simply dividing U/I. The exact temperature of the heater is not known in that case, however the heat sink temperature is used and a constant offset is assumed. This can be justified, as the stabilised heat flow between cavity and heat sink ensures a constant temperature difference.

This evaluation leads to a variation of roughly 0.10 $\Omega/°C$ or 10 ppm/°C in the temperature range between 20 °C and 30 °C. This is in good agreement with the result from the dedicated experiment.

3.2.10 Possible Improvements of the Data Acquisition

If the measurement regime is maintained, the following points should be considered:

- A continuous internal calibration of the ADC could improve the data accuracy substantially. Therefore the hardware should be able to feed a precise reference voltage (at the operating point) into the measurement chain. This would allow to trace all measurements to one voltage reference. In addition this reference could be characterized. Preferably the corrections/calibrations are implemented in the software rather than in the ADC register. Also it would be desirable in the test phase to have the calibration values stored for later analysis.

- In order to monitor the current rather than just estimate it, a similar data acquisition chain as for the voltage could be implemented. Including sample/hold and calibration capability. However if it is possible, reliable current source with good long term stability (e.g. 10 ppm) is preferable.

- For calibration purposes, as well as for monitoring and testing, it would be an advantage if the radiometer could transmit voltage and current data to the terminal, instead of sending just the power signal as it is implemented now.

Operation Mode Without Direct Measurements

Another possible measurement option is to keep the current constant, and estimate the resistance (and if necessary the current) from the actual temperature of the heat sink (and voltage reference) and take no direct measurements at all. In this case it must be considered that the resistance of the heater changes not insignificantly with temperature (Section 3.2.9). Therefore the behaviour of the heater must be well known, as it goes linearly into the calculation of the power $P = I^2R \cdot D_{PWM}$. In order to know the absolute value of the resistance more accurately, it would be worthwhile to investigate the impact of a higher resistance on the relative uncertainty of the resistance. Especially if the solder joint would cause the uncertainty, a higher heater resistance would reduce the influence of the solder joint.

3.3 Absorptivity of the Cavities

Ideally the cavity (detector) would absorb all of the incoming radiation. In reality there is no ideal absorber material. With a geometrical arrangement (cavity shape) the absorptivity of a detector can be further enhanced, but it will never become perfect. The remaining reflected light needs to be determined experimentally in order to correct the measurement of the radiometer. The absorption correction is a multiplicative factor to the measured solar irradiance.

In order to achieve a high absorptivity the cavity has a conical shape (see also Section 2.4.3). The angle of the cone is chosen so that the light will need 5 reflections in order to back reflect out of the cone (Figure 3.5). The black coating (Aeroglaze Z302, [65]) is a glossy coating, meaning that the light that is not absorbed (5% per reflection) will scatter forward and thus follow a known ray path. Theoretically this would lead to a very low reflectivity of 0.3 ppm ($= 0.05^5$). In reality there is also a small component of diffuse reflection, which leads to higher reflectivities of the cavities. This is described by Fox and Rice [29] who used a similar coating for the cavity of cryogenic radiometers. With PMO6 cavities reflectivities of several hundered ppm have been measured [59]. Altough the PMO6 cavities have an inverted cone the idea of the five reflections is the same.

The reflectivity of the DARA cavities as well as of some selected PMO6 cavities will be measured for comparison.

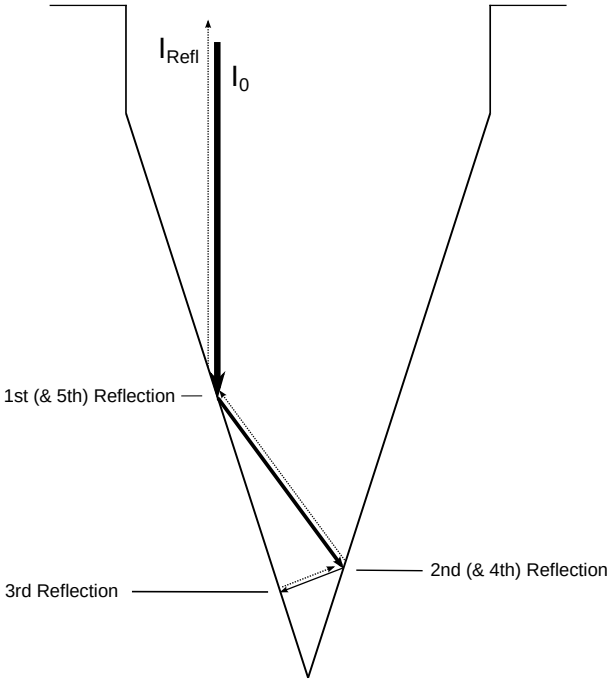

Figure 3.5: Multiple reflections in the DARA cavities: The cavity is designed so that the incoming ray needs to reflect 5 times in order to get reflected back out of the cavity

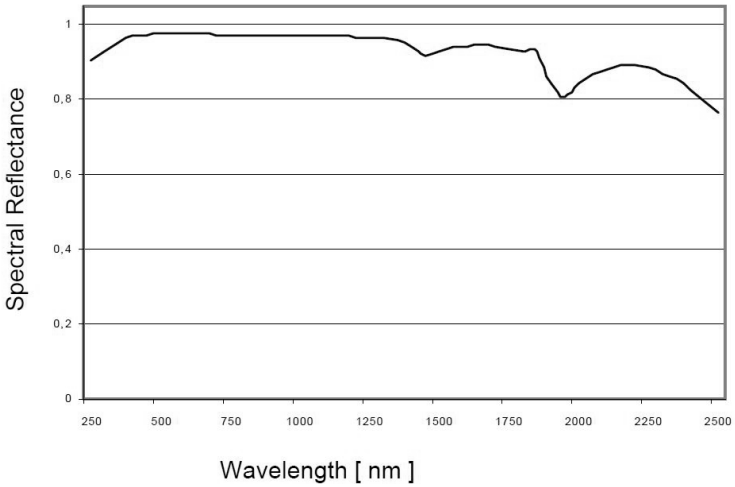

Figure 3.6: Reflectivity as a function of wavelength for the $BaSO_4$ coating inside the integrating sphere according to the manufacturer [3]

3.3.1 Theory of Integrating Spheres

In order to measure the reflectivity of the cavity, an integrating sphere is used. An integrating sphere is a standard set up for such a measurement. A short introduction to the theory of integrating spheres is given here. This theory is taken from the *Technical Guide* from Labsphere [73].

The integrating sphere used here is a metal sphere of 210 mm diameter, coated with $BaSO_4$ on the inside. The $BaSO_4$ coating is a material with high diffuse reflectance in the visible range of 97% (Figure 3.6). The sphere has three ports: entrance port, sample port and detector port (Figure 3.8).

The idea of the integrating sphere is that the light within the sphere is equally distributed and every infinitesimal area dA_1 of the sphere is exchanging the same amount of radiation with every other area dA_2. In order to understand the measurements taken with the integrating sphere, some parameters need to be considered.

Radiance and the Sphere Multiplier

The radiance within the sphere depends on the input radiation, the size of the sphere, the reflectivity of the coating and the relative area covered by the ports. The radiance originating from a certain point in the sphere (equal to the radiance reaching the point) can be written as:

$$L_s = \frac{\Phi_i}{\pi A_s} \cdot \underbrace{\frac{\rho}{1-\rho(1-f)}}_{M:SphereMultiplier} \tag{3.9}$$

[3] http://www.gigahertz-optik.de/101-0-ODP97+Bariumsulfatbeschichtung.html

where Φ_i is the initial incoming flux, A_s is the Area of the sphere, ρ is the reflectivity of the coating, and f is the port fraction (area of the ports as a fraction of the sphere area). This equation is valid in the case that all ports are open. The second fraction in equation 3.9 is the so called sphere multiplier. It characterises the light amplification of the sphere due to multiple reflection. The term $\rho(1-f)$ can also be replaced by $\rho_{effective}$.

Direct Reflectance Measurements

When measuring the reflectance of the DARA cavities a laser beam is pointed through the entrance port onto the target on the opposite side of the sphere (Figure 3.8). The reflected light is distributed within the sphere. The measurement is performed once with a reference sample and once with the cavity at the sample port. Comparing the two measurements the following equation applies:

$$\frac{L_1}{L_2} = \frac{\rho_1}{\rho_2} \cdot \frac{M_1}{M_2} = \frac{\rho_1}{\rho_2} \cdot \frac{1-\rho_{eff2}}{1-\rho_{eff1}} \tag{3.10}$$

where ρ_1 and ρ_2 are the sample reflectivity and the ρ_{eff} are the effective reflectivity of the whole sphere in the respective setting. It means that the ratio of the irradiances at the detector is not equal to the ratio of the reflectivity. The influence of the sphere multiplier needs to be estimated. In our case the maximal ρ_{eff} will occur when the reflectivity sample (1% in the visible range) is in place at the target opening. The minimal ρ_{eff} on the other hand will ocour when no sample is in place. Therefore the sphere muliplier term for these two extreme cases is studied. The effective reflectivities for these cases are listed in Table 3.6. It can be seen that the effective reflectivity does not change up to the fifth digit. Comparing these two $(1-\rho)$ values, the relative difference is less than 0.1%. The influence of the sphere multiplier can therefore be neglected in the data analysis.

Symbol	Quantity	Value	Unit
D_S	Diameter	210	mm
A_S	Total Area	1.39e5	mm^2
ρ_0	Coating reflectivity	0.97	-
D_D	Diameter of detector port	10	mm
D_T	Diameter of the target opening	10	mm
D_E	Diameter of the entrance opening	12 (10 or 24)	mm
f	Port fraction	0.002	-
M	Sphere Multiplier	approx 30	-
ρ_{eff0}	Effective reflectivity of the sphere with target port open	0.96834	-
ρ_{eff1p}	Effective reflectivity of the sphere with 1% reflectivity at target port	0.96834	-
A_{30}	Area of the cavity reflection cone on the sphere surface.	9280	mm^2

Table 3.6: Parameters of the integrating sphere

Losses Through the Entrance Hole

The reference sample for the reflectivity is considered a lambertian radiator [74]. However the DARA cavity is not. The geometrical distribution of the reflection is limited by the cavity geometry. This can be seen best in the illustration in Figure 3.7. This implies that

in the case of the cavity, a higher fraction of the reflected light is escaping directly out the entrance hole than in the lambertian case. In order to get an idea of the order of this effect the sizes of the different (illuminated) areas are compared.

The Area of the 30° cone on the sphere surface (A_{30}: blue area in Fig. 3.7) is 0.067 of the sphere surface. This means that the illumination at the entrance hole (D_E=12 mm), originating from the first reflection (in the cavity tip) is 15 times higher compared to the lambertian case, assuming a uniform distribution within A_{30}

The entrance opening covers about 1% of the area A_{30}, while comparing the entrance hole to the whole sphere surface a ratio of 0.0008 is obtained. Thus in the lambertian case the loss through the entrance hole can be neglected. In case of the cavity this quantity should be further investigated. Assuming a forward peaking reflection the direct loss through the hole could be higher than the estimated 1%.

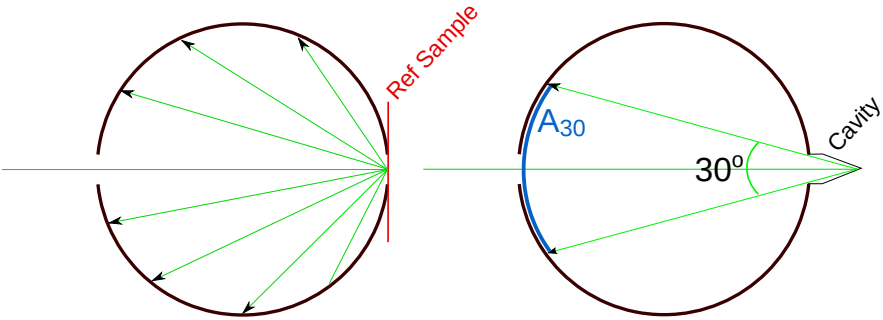

Figure 3.7: First reflections: lambertian case and cavity

Measurement of the Losses Through the Entrance Hole

In a dedicated experiment, the effect of the losses through the entrance hole is further investigated. Therefore in the usual set-up (Section 3.3.2) the laser beam is directed to the centre of the cavity where most of the (non lambertian) reflections take part. Then the aperture is exchanged, while the cavity stays in place at the sphere. Thus it is guaranteed that the illumination of the cavity is equal for two consecutive measurements. The black iris aperture (see Figure 3.8) that is narrower than the entrance apertures guarantees that the beam entering the sphere is identical. For every measurement a background measurement is also taken.

When substituting the aperture the sphere multiplier M in Equation 3.9 will change. Changing the aperture size from D_E=12 mm to D_E=6 mm the sphere multiplier increases by 2%.

Using equation 3.10 an apparent ratio of the reflectivity ρ can be calculated.

$$\frac{\rho_{6mm}}{\rho_{12mm}} = \frac{L_{6mm}}{L_{12mm}} \frac{M_{12mm}}{M_{6mm}} \tag{3.11}$$

This apparent difference in ρ is explained by the losses through the entrance hole, caused by the first back reflection from the tip of the cavity. A correction factor can thus be introduced. Therefore it is assumed, that the losses on the area covered by the 6 mm aperture but not by the 12 mm aperture are equal (per area) at the opening of the 6 mm

L_6/L_{12}	$1.056 \pm 0.007(1\sigma)$	Measurement Result
M_6/M_{12}	$1.02 \pm 0.007(1\sigma)$	Theoretical Value
ρ_6/ρ_{12}	$1.035 \pm 0.01(1\sigma)$	Apparent ratio of the reflectivity
C_{loss06}	$1.012 \pm 0.003(1\sigma)$	Correction factor for 6 mm sphere aperture
C_{loss12}	$1.047 \pm 0.013(1\sigma)$	Correction factor for 12 mm sphere aperture

Table 3.7: Results from the aperture hole loss experiment

aperture. The results of the measurements and the derived correction factors are listed in Table 3.7. The correction for a D_E=12 mm aperture is around 5%.

3.3.2 Reflectivity Maps of the Cavities

In order to get a qualitative (as well as quantitative) impression of the reflectivity, a reflectivity scan of the cavities is performed. This data allows to visualize the homogeneity and to localize spots of high reflectivity.

Experimental Set-Up

The experimental set-up, is schematically shown in Figure 3.8. It consists of a chopped laser beam, a beam-splitter, a lens, an integrating sphere with an Si photo diode detector, and a monitor-diode. The integrating sphere will collect the reflected light from the cavity, which is measured by the photo diode. There are three available lasers at 372 nm, at 532 nm and at 633 nm wavelength. Measurements are taken with a Si photo diode that is connected to a lock-in amplifier. The integrating sphere is moved in two directions perpendicular to the laser beam on motorised stages. This set-up allows to scan each point of the cavity individually. To make a full scan the cavity is scanned line by line with a line/point interval of 0.2 mm. As the width of the light spot is wider than the grid interval it ensures that every part of the cavity is contributing to the final result.

In order to make a reflectivity map, three scans are performed. A zero scan, with no target attached to the sphere, a reference scan with a NIST traceable spectralon® sample from Labsphere Inc. and a scan of the cavity is performed.

Data Processing

The measurement data is processed according to Equation 3.12. The zero or dark scan is subtracted from both, cavity and reference, measurements. This zero scan measures stray light that contributes a constant offset. Then the corrected cavity map is divided by the mean value of the reference scan in order to normalise the measurement. Then, the calibration factor of the reference Sample ($C_{Reference}$) is applied in order to get the relative reflectance of the cavity.

$$R_{Reflected} = \frac{V_{Cav} - V_{Zero}}{\langle V_{Reference} - V_{Zero} \rangle} C_{Reference} \tag{3.12}$$

Reflectivity Maps of the DARA Cavities

Figures 3.9,3.10 & 3.11 show reflectivity maps for the three DARA cavities scanned with a 633 nm and 532 nm Laser respectively. It can be seen that the tip of the cavity has a high reflectivity compared to the rest of the cavity. The blue area corresponds to roughly 500

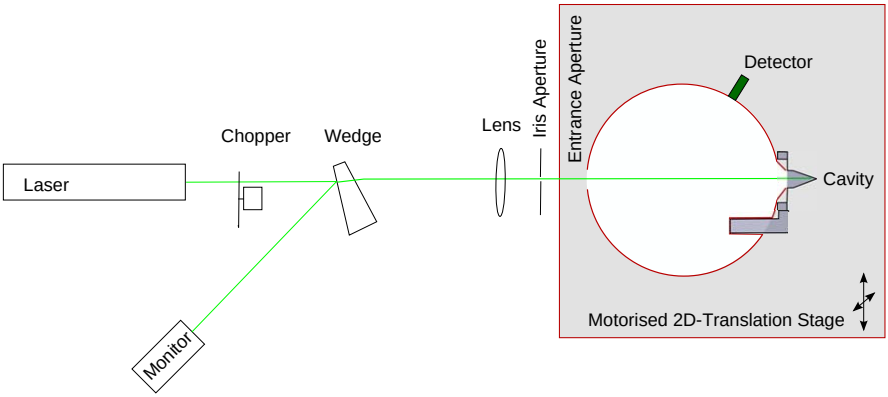

Figure 3.8: Reflectivity scan set-up: The cavity is attached to the integrating sphere. A fine spot of the cavity is illuminated by the focussed laser beam, the reflected light is measured with a silicon diode. The whole sphere can be moved in two directions to scan the entire cavity. The front aperture of the sphere has a diameter of 12 mm. Using a chopped beam (113 Hz) and a lock-in amplifier to process the diode signal, spurious light, not originating from the laser can be filtered out. The monitor ensures laser power stability. The monitor signal is also processed with a lock in amplifier.

ppm reflectivity. The reflectivity can be integrated (averaged) over the illuminated area. These integrated values are listed in Table 3.8.

The map does not give a true reflectivity image, that is limited by the resolution. In fact the map is a convolution of the laser beam profile and the true reflectivity. Therefore the geometry of the two tips looks slightly different at the two wavelength. This artefact is very likely introduced by the beam profile.

Reflectivity Maps of the PMO6 Cavity

In order to compare the spatial reflectivity distribution of the DARA cavities to the inverted cone cavities used hitherto in PMO6-type instruments, a measurement with the PMO6-10 cavity is performed. The PMO6-10 radiometer belongs to the group of radiometers characterised by Brusa & Fröhlich [59]. Thus the new results can be compared to the Brusa & Fröhlich measurements. Because Brusa & Frölich only measured spatially integrated reflectivity, it is only possible to compare these values. Additionally a PMO6 cavity has been measured by Beck [75]. This cavity was a spare from the PMO6-SOVIM radiometer manufactured in 2004. This cavity has never been exposed to direct sunlight.

Figure 3.12 shows the reflectivity of the PMO6-10 and the PMO6-SOVIM cavities. The PMO6-10 measurement does not cover the full illuminated area therefore the overall reflectivity is determined by averaging over the measured area and setting values outside the measurement range to 0.12 (corresponds to the dark areas within the measured area). A reflectivity of about 1900 ppm is found. This is in contradiction to the result by Brusa [67] who found a value of roughly 300 ppm in 1980 (see Table 3.9). However the cavity might have degraded over time. Brusa [67] already observes changes in reflectivity between 1978 and 1980 for some PMO6 instruments, although not for PMO6-10. It must further be noted that the black coating is a different kind than that used in DARA.

Cavity	scan 372nm	scan 532nm	scan 633nm	TRF Spot	TRF Ring
DARA A	743 ppm	942 ppm	1110 ppm	3696 ppm	618 ppm
DARA B	879 ppm	963 ppm	942 ppm	3895 ppm	733 ppm
DARA C	859 ppm	974 ppm	1026 ppm	4408 ppm	576 ppm
PMO6-10			1900 ppm		
PMO6/SOVIM			390 ppm *		

Table 3.8: Spatially integrated reflectivity of different cavities (data is corrected for losses through sphere aperture). * This measurement of the PMO6 cavity from the 2004/SOVIM series has been made by Ivo Beck [75]

	367 nm	458 nm	514 nm	647 nm	797 nm
PMO6-9	341 ppm	326 ppm	446 ppm	184 ppm	286 ppm
PMO6-10	337 ppm	304 ppm	332 ppm	201 ppm	254 ppm
PMO6-11	284 ppm	271 ppm	253 ppm	225 ppm	212 ppm

Table 3.9: Reflectivity measurements of PMO6 Radiometers taken by Brusa 1980 [67]

The reflectivity of the PMO6-SOVIM spare cavity (Figure 3.12 right) is however significantly lower than the PMO6-10 and the DARA cavities. It contains no such extreme reflecting dust particles, only very faint areas of slightly higher reflectivity.

3.3.3 Overall Values of the Reflectivity

Table 3.8 shows the overall reflectivity of the 3 DARA cavities as well as selected PMO6 cavities in the measured wavelengths. The numbers are derived by averaging the scans shown in Figures 3.9,3.10 & 3.11. A correction for the losses through the entrance aperture is applied. Table 3.9 shows the measurements for PMO6 instruments by Brusa in 1980 [67].

It can be seen that the PMO6-10 instrument has degraded by a considerable amount. Looking at the reflectivity map (Figure 3.12) it looks like there is some contribution of dust particles. However the degradation can not be explained by dust particles only, as the reflectivity in between the dust particles is also higher than the Brusa measurements. Comparing the measurement of a new PMO6 cavity by Beck [75] to the Brusa measurements from 1980 it is found that these two measurements agree much better.

3.3.4 Weighting with Solar Spectrum

In order to get a correction that is applicable for measurements of solar irradiance, the measurements are weighted with a solar spectrum (terrestrial and extraterrestrial). Figure 3.13 illustrates the weighting process. The results for the terrestrial and extraterrestrial spectrum differ by less than a percent, therefore no distinction is made in further evaluation.

3.3.5 Correction Factors

The correction factors that need to be applied to DARA measurements in order to correct for imperfect absorptivity of the cavity are listed in Table 3.10. To calculate these values from the raw data, the correction for losses through the sphere aperture has been included (Section 3.3.1), and spectral weighting has been performed.

	Cavity A	Cavity B	Cavity C
Correction factor (Solar)	1.00103	1.00094	1.00100
Uncertainty (solar)(1σ)	0.00016	0.00016	0.00016
Correction factor (532 nm)	1.00094	1.00096	1.00097
Uncertainty (532 nm)(1σ)	0.00012	0.00012	0.00012
Correction factor TRF spot	1.00371	1.00391	1.00443
Uncertainty (TRF spot)(1σ)	0.00060	0.00063	0.00069
Correction factor TRF ring	1.00062	1.00073	1.00058
Uncertainty (TRF ring)(1σ)	0.00010	0.00012	0.00010

Table 3.10: Correction factors for imperfect absorptivity

The correction factors have been calculated for different situations: For solar irradiance measurements and for measurements at TRF. The TRF measurements are made at 532 nm wavelength, the beam profile can be varied, to either simulate an irradiance field, to only illuminate the centre of the cavity (1.5 mm diameter), or to illuminate a ring (2.5 mm diameter) around the tip of the cavity. These special corrections need to be applied for comparisons to the SI cryogenic laboratory standard in power mode. (Section 4.3)

3.3.6 Uncertainties

The following effects are considered to contribute to the combined uncertainty of the correction factors, the numerical values (for irradiance) are listed in Table 3.11:

- Cut out uncertainty: Within the data analysis the centre of the cavity (e.g. the bright tip) is selected. Then the circular area with diameter=5mm, centred around the tip is used to determine the reflectivity. The sensitivity of the mean reflectivity to the tip selection is evaluated. The cut out uncertainty becomes higher for the spot and ring pattern because the total pixel taken into account is considerably smaller so that the sensitivity to pixel selection is higher. For the spot and the ring pattern an uncertainty of 0.1 is determined, rather than the value listed in Table 3.11 for irradiance.

- As a correction for the losses through the entrance aperture of the sphere is applied to the measured reflectivity values, an uncertainty is also associated with this correction (Section 3.3.1).

- The manufacturer of the reference sample gives an uncertainty for the calibration of the sample.

- Repeatability: This uncertainty contribution covers a range of effects. It is determined by comparing the measurements of the reference samples that were conducted before and after the cavity scan. These two measurements should ideally be equal. From the difference in these measurements an estimation of uncertainty is concluded by taking half of the difference between the two measurements as a control sample for the statistics. This includes laser and detector stability as well as the homogeneity of the reference sample.

- Spectral flatness: The weighting process described in Section 3.3.4 is based on the assumption that the absorptivity above 633 nm stays constant. This assumption is critical for the wavelength integrated values. The assumption to estimate the

cut out uncertainty	0.03
losses through aperture correction	0.013
calibration uncertainty of the reference sample	0.05
repeatability (set-up uncertainty)	0.1
spectral flatness	0.1
Total (Solar)	**0.16**
Total (@532 nm)	**0.12**

Table 3.11: Uncertainty budget for reflectivity correction factors determined by the laser scan method, (relative uncertainty 1σ) for irradiance measurements

uncertainty of this extrapolation is that the deviation at longer wavelength is in the order of the variance of the three measurements at 372 nm, 532 nm and 633 nm. This uncertainty is only relevant when measuring solar irradiance.

3.3.7 Discussion

In all three DARA cavities the tip is bright and accounts for most of the overall reflectivity. The tip reflects several times more than the tip of a PMO6 radiometer. That is a disadvantage of the DARA design. It is obvious that in the region of the tip, the concept of the 5 reflections does not hold. Due to the surface tension of the coating the tip will not be an ideal tip but rather a round edge. a small area will therefore back reflect the incoming radiation directly (reflection of the coating is 5%)

To reduce the reflectivity in future instruments, mechanically squeezing of the tip should be considered. So that the reflecting surfaces at the tip could be reduced.

Besides the absolute value of the absorptivity or the reflectivity the important question is about the stability of the coating. From previous space based TSI experiments with PMO6 radiometers it is known, that the instrument degrades over time. It is thought that degradation is introduced by a change in the optical properties of the cavity coating. Either by a loss of gloss or a by a reduced absorptivity of the coating itself [77]. The topic of degradation is also discussed in Chapter 8.

The uncertainty of the absorptivity correction is large compared to the other uncertainties of the DARA characterisation. To reduce the overall uncertainty of the DARA native scale, it is necessary to improve the absorptivity measurement. Therefore the stability of the set up (repeatability) and the wavelength coverage need to be improved.

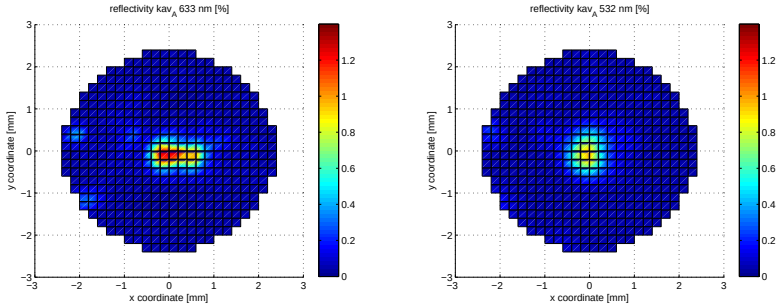

Figure 3.9: Reflectivity map of DARA cavity A at 633 nm (left) and 532 nm (right)

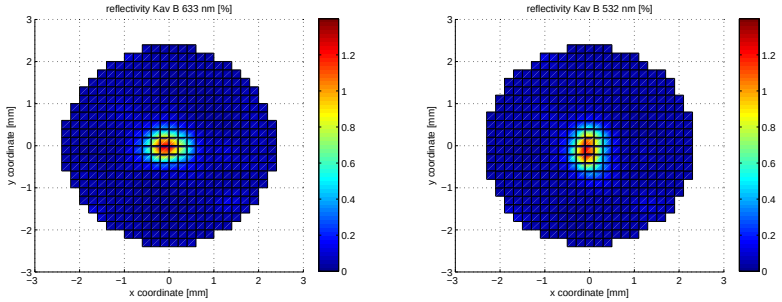

Figure 3.10: Reflectivity map of DARA cavity B at 633 nm (left) and 532 nm (right)

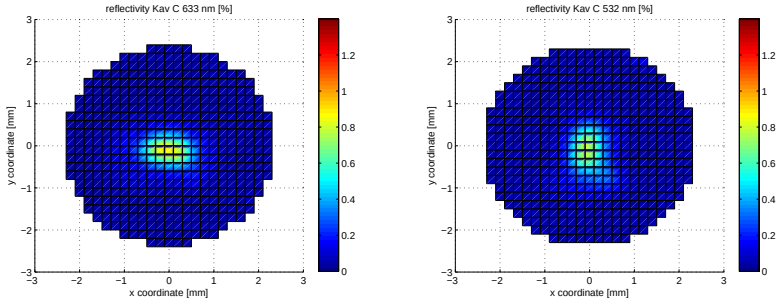

Figure 3.11: Reflectivity map of DARA cavity C at 633 nm (left) and 532 nm (right)

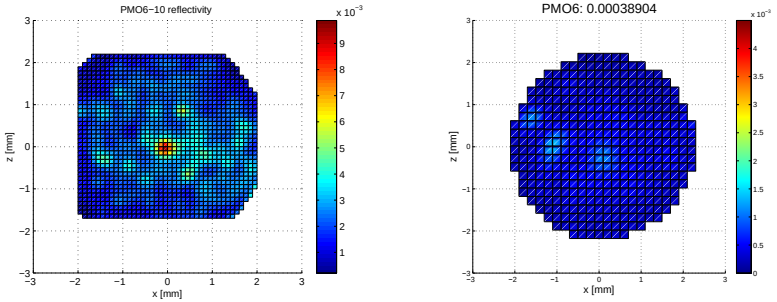

Figure 3.12: Reflectivity map of the PMO6-10 cavity normalized to the reference sample (1% reflectivity) (left) and a newer PMO6 cavity that has never been exposed to the sun (right, courtesy Ivo Beck). The left map does not cover the full illuminted cavity area, but it clearly shows a very high overall reflectivity compared to the newer PMO6 cavity. It should also be noted that the scales are not identical.

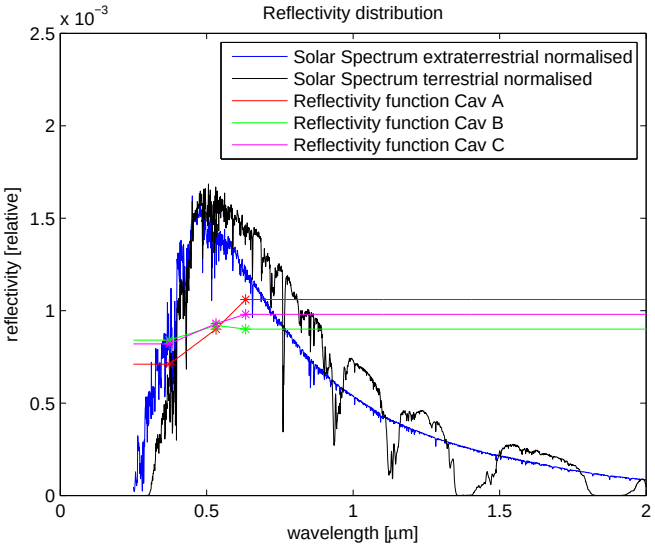

Figure 3.13: Spectral weighting of the reflectivity: The asterisks represent the laser measurements in three wavelengths. The reflectivity is interpolated linearly between the data points, and extrapolated with a constant value. The spectra are normalised and used to weight the reflectivity function. The extraterrestrial spectrum is from Kurucz [76] and the terrestrial spectrum is computed with LibRadtran for a zenith angle of 55° and an average water vapour content for Davos. More details on these spectra can be found in Sections 3.5.3 and 3.5.4.

3.4 Lead Heating

A spurious heat flow from the cavities to the heat sink is passing through the wires of the cavity heater. As long as this heat flow is equal in the open and closed states these wires act like an additional heat link in parallel to the actual heat link. Due to internal heat generation in the wires, caused by the electrical current passing through, the heat flow in the open state differs from the heat flow in the closed state. This effect is called the lead heating effect. It has been discussed for PMO6 radiometers by Brusa and Fröhlich [59], and Fehlmann [33].

The lead heating effect will first be analysed with a model, in order to understand the physical process and to justify the planned experiments. Then the lead heating effect will be determined experimentally, and a correction factor is introduced to correct for this effect.

3.4.1 The Model

A numerical model based on the heat transfer equation and the conservation of energy, is built to compute the temperature distribution and the heat flow in the leads. The one dimensional wire is divided into a number of segments. In each segment heat is generated according to the electrical current in the wire. Each segment point is connected with its two neighbouring points via the 1D heat transfer equation:

$$\frac{dQ}{dt} = \sigma_T \frac{dT}{dx} \Longrightarrow \frac{dT}{dt}\Delta m \cdot c = \sigma_T \frac{dT}{dx} \tag{3.13}$$

where dQ/dt is the heat flow, Δm is the mass of the segment, c the specific heat capacity and σ_T is the thermal conductivity between two segment points. The status of all the segments is represented in the vector $\vec{T}$ that represents the temperature of each segment. The time evolution of $\vec{T}$ is represented in Equation 3.14. The matrix $\mathbf{M}$ is the time evolution operator according to Equation 3.13. $\vec{P}$ represents the heat generated by the electrical current (Eq 3.15). To find the final equilibrium state, Equation 3.14 is iteratively solved in time steps until the solution converges.

$$\frac{d\vec{T}}{dt} = \mathbf{M}\vec{T} + \vec{P} \tag{3.14}$$

$$\mathbf{M} = \begin{pmatrix}
0 & 0 & \cdot & \cdot & \cdot & \cdot & \cdot & \cdot & 0 \\
\frac{\sigma_T}{\Delta mc} & \frac{-2\sigma_T}{\Delta mc} & \frac{\sigma_T}{\Delta mc} & 0 & \cdot & \cdot & \cdot & \cdot & 0 \\
0 & \frac{\sigma_T}{\Delta mc} & \frac{-2\sigma_T}{\Delta mc} & \frac{\sigma_T}{\Delta mc} & 0 & \cdot & \cdot & \cdot & 0 \\
0 & 0 & \frac{\sigma_T}{\Delta mc} & \frac{-2\sigma_T}{\Delta mc} & \frac{\sigma_T}{\Delta mc} & 0 & \cdot & \cdot & 0 \\
\cdot & \cdot & \cdot & \ddots & \ddots & \ddots & \cdot & \cdot & \vdots \\
\cdot & \cdot & \cdot & \cdot & \ddots & \ddots & \ddots & \cdot & \vdots \\
\cdot & \cdot & \cdot & \cdot & \cdot & \ddots & \ddots & \ddots & 0 \\
\vdots & \vdots & \cdot & \cdot & \cdot & 0 & \frac{\sigma_T}{\Delta mc} & \frac{-2\sigma_T}{\Delta mc} & \frac{\sigma_T}{\Delta mc} \\
0 & 0 & 0 & 0 & \cdot & \cdot & 0 & 0 & 0
\end{pmatrix}$$

$$\vec{P} = \begin{pmatrix} \frac{\Delta P_{ElHeating}}{\Delta m \cdot c} \\ \vdots \\ \frac{\Delta P_{ElHeating}}{\Delta m \cdot c} \end{pmatrix} \tag{3.15}$$

The numerical values of the parameters can be found in Table 3.13 where the model input parameters are described.

Once the temperature distribution is known, the heat flow can easily be determined by multiplying the temperature gradient along the wire with the heat conductivity of the wire.

3.4.2 Model Solution (DARA)

Figures 3.14 & 3.15 show the temperature distribution and the heat flow distribution along the copper wire. The boundary condition sets the cavity at 25 ^{o}C and Heat sink at 23 ^{o}C. This temperature difference refers to the DARA cavities in normal operation. From the difference in heat flow at the point x=0 that represents the cavity, the lead heating effect can be estimated.

In Figure 3.15 it can be seen that the heat flowing from the cavity into the wire decreases as more heat is generated in the wire itself. Table 3.12 shows the output of the model calculations. The output is given for the three situations (heater power) also shown in Figures 3.14 & 3.15. When dividing the difference in heat flow $\Delta(dQ/dt)$ by the amount of power applied to the cavity it is found that the lead heating effect per wire is 340 ppm of the applied cavity power. This function is linear. It means that for normal cavity operation, the lead heating effect is 340 ppm of the difference in applied power (open/closed phase). So it can be directly applied to the measured irradiance.

As the cavity has two current-carrying leads the amount of lead heating for one cavity needs to be doubled to 680 ppm.

Heater power (HP) applied	0 mW	20 mW	40 mW
dQ/dT flow from cavity to wire	0.2096 mW	0.2027 mW	0.1959 mW
Heat generated in wire	0 mW	0.0136 mW	0.0272 mW
$\Delta dQ/dt$ =dQ/dt(0mW) - dQ/dt	-	0.0069 mW	0.0137 mW
$(\Delta dQ/dt)/P_{Heater}$ (Lead heating per wire, fraction of HP)	-	0.00034	0.00034

Table 3.12: Output of the lead heating model

Constant Name	Value	Remarks
Length of leads (DARA)	30 mm	approximate value
Length of leads (PMO6)	20 mm	approximate value
Radius of lead wire	0.05 mm	manufacturers specification
Temperature difference (DARA) Δ T	2 K	corresponds to a heater power of 40 mW
Temperature difference (PMO6) Δ T	1 K	corresponds to a heater power of 40 mW
Specific heat capacity c of the wire	383 J $kg^{-1}K^{-1}$	heat capacity of copper
Heat conductivity of copper (σ_T)	400 W $m^{-1}K^{-1}$	approximate value for copper
Electrical conductivity of copper	$5.9 \cdot 10^7$ A $V^{-1}m^{-1}$	
Nominal heater resistance	95 Ω	

Table 3.13: Input parameters for the lead heating model

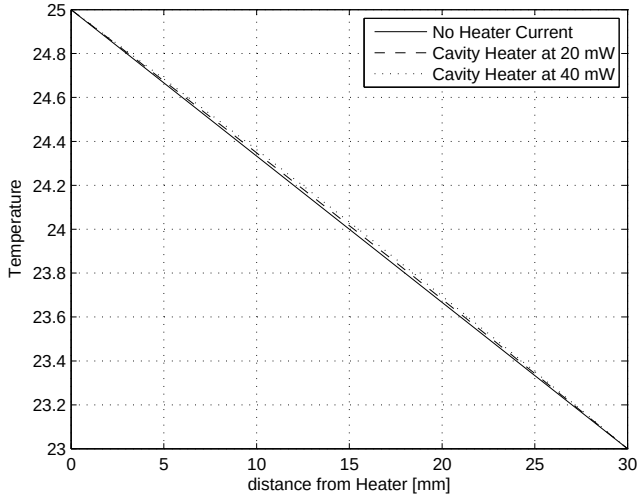

Figure 3.14: Temperature distribution along the wire for different amounts heater power applied

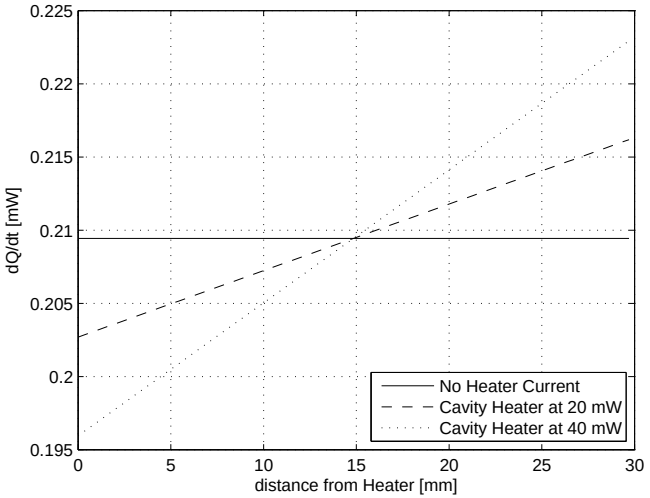

Figure 3.15: Heat flow distribution Along the wire for different amounts of heater power applied

3.4.3 Model Solution (PMO6)

The model has also been solved for the PMO6 radiometer. In contrast to the DARA case there is a lower temperature difference between heat sink and cavity of 1 degree Celsius. The length of the wire is estimated to be only 20 mm. The exact kind of wire is only known for the late-built PMO6 radiometers including PREMOS.

For the PMO6 the model is solved also for the case when the heat sink and the cavity are at equal temperature. This corresponds to the experiment performed by Brusa and Fröhlich [59] and Fehlmann [33]. With their experiment the rise in temperature at the cavity, when a current is circulating through the lead wires, but not trough the heater was measured. From this temperature rise, the lead heating contribution was estimated.

Figure 3.16 shows the result for the PMO6 radiometer. Here the lead heating contribution is approximately 500 ppm. This is in good agreement with Fehlmann who measured between 400 and 500 ppm for PREMOS Radiometers [33]. Furthermore from the situation illustrated in Figure 3.16 at the bottom, that corresponds to the Brusa and Fröhlich experiment, it can be seen that the behaviour in terms of heat flow is the same for the situation with and without temperature difference between cavity and heat sink.

3.4.4 Model Conclusion

The absolute value calculated here might not be as accurate as it depends on many assumptions such as exact wire length and diameter or ideal thermal contacts, that cannot be verified with high precision. However important things can be learned form the model: The effect of lead heating is proportional to the power dissipated in the leads. This means the contribution of the lead heating to the cavity heating is proportional to the actual heater power. Both scale with the square of I. As an additional illustration, Figure 3.17 shows the situation for DARA, when artificially doubling the lead heating current, as done in the experimental set up (Section 3.4.5).

Furthermore the lead heating contribution is independent from the actual temperature difference between cavity and heat sink. Thus it can be measured in the way Brusa and Fröhlich [59] did, while the cavity is not heated. Nevertheless the new method, using the controller loop as described in Section 3.4.5 is thought to yield more reliable results, because the lead heating power is directly measured and a calibration of the error signal from the bridge, which could introduce another uncertainty, is unnecessary.

The model describes the mechanism behind the effect very well and it is very helpful to understand the formation of the effect. But it can only give a rough estimation of the lead heating effect. Therefore the lead heating correction factor is determined experimentally. The model is in this case used as justification of the experimental set up. The next sections describe the experimental determination of the lead heating effect.

Model DARA	Model PMO6	Measurement PMO6 (Brusa [59])	Measurement PMO6-PREMOS [33]
680 ppm	500 ppm	200 ppm	400-500 ppm (vacuum)

Table 3.14: Lead heating estimation (model) and older measurements

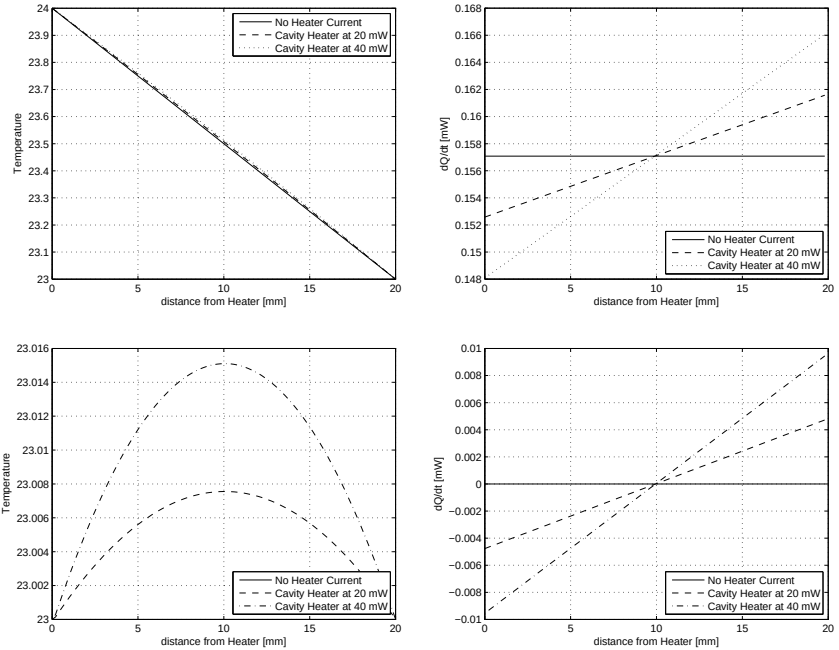

Figure 3.16: Temperature distribution (left) and corresponding heat flow distribution (right) for the PMO6 radiometer. The top situation is equivalent to the simulation discussed for the DARA instrument. The bottom situation corresponds to the experiments conducted by Brusa [59] and Fehlmann [33] with PMO6 Radiometers. The differences between the heat flows (20 mW and 40 mW curve) at the cavity end of the wire are identical for both situations.

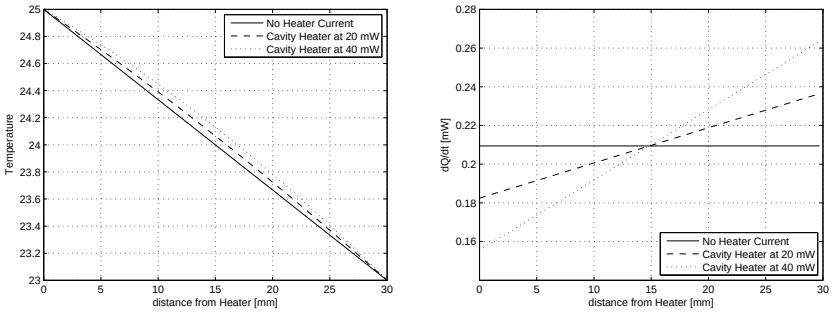

Figure 3.17: The figures show the situation for DARA when the lead current is artificially doubled (compared to Figures 3.14 & 3.15). The heat flow scales with the square of I (linear with heater power).

3.4.5 Experimental Set-up and Calculation

For the lead heating measurements an analogue PID controller is used so that all currents are DC currents. This facilitates the measurements. Using a voltage sensing wire, an additional current is fed through the sense- and the corresponding power lead wire, while the controller loop is active. Observing the controlled heater current, the effect of the additional (lead heating) current can be determined.

Figure 3.18 illustrates the measurement set up. Technical details are described later in Section 3.4.6. First the Calculation is discussed in detail.

In normal operation of the radiometer the heater current I_H is flowing through the lead high wire, through the cavity heater R_C and through the lead low wire. The heating power applied to the cavity consists of power dissipated in the cavity heater and of a lead heating contribution. If the shutter is closed and the control circuit operational, the total heating power is constant:

$$P_{TotalCavityHeating} = const = I_H^2 \cdot R_C + P_{LeadHeating} \tag{3.16}$$

The lead heating is expressed with the symbols $R_{L_{High}}$ and $R_{L_{Low}}$, they represent the lead heating contribution of the respective wire. This is not identical to the ohmic resistances of the wires, because heat generated in the wire is not fully transported to the cavity. Nevertheless $R_{L_{High}}$ and $R_{L_{Low}}$ are proportional to the actual ohmic resistance of the wire, and the lead heating effect is proportional then to I_H^2 (see Section 3.4.2).

Therefore in normal operation the lead heating effect is:

$$P_{NormalLeadHeating} = I_H^2 R_{L_{High}} + I_H^2 R_{L_{Low}} \tag{3.17}$$

In the experiment an additional lead heating current I_{Batt} is introduced. This current is feed into the system from a battery via the sense low lead (see Figure 3.18). This additional current is flowing through $R_{S_{Low}}$ and $R_{L_{Low}}$. If this additional current is present, equation 3.17 expands to:

$$P_{TotalLeadHeating} = \widetilde{I}_H^2 R_{L_{High}} + (\widetilde{I}_H + I_{Batt})^2 R_{L_{Low}} + I_{Batt}^2 R_{S_{Low}} \tag{3.18}$$

If the current I_{Batt} is switched on and off the cavity heater will react to the enhanced or reduced contribution of the lead heating and compensate for it by adjusting I_H to keep the total heating power constant. This can be written, using Equation 3.16 and some rearranging:

$$P_{TotalLeadHeating} - P_{NormalLeadHeating} = (I_H^2 - \widetilde{I}_H^2) \cdot R_C \equiv \Delta P_{CavityHeater} \tag{3.19}$$

where I_H is the heater current when no additional lead heating current is present ($I_{Batt} = 0$) and $\tilde{I}_H$ is the heater current when the additional current I_{Batt} is switched on.

Substituting $P_{TotalLeadHeating}$ and $P_{NormalLeadHeating}$ with their definitions above leads to:

$$(I_H^2 - \widetilde{I}_H^2) \cdot R_C = (\widetilde{I}_H^2 - I_H^2) \cdot R_{L_{High}} + \left[(\tilde{I}_H + I_{Batt})^2 - I_H^2\right] R_{L_{Low}} + I_{Batt}^2 R_{S_{Low}} \tag{3.20}$$

this can be rearranged to:

$$(R_C + R_{L_{High}}) \cdot (I_H^2 - \tilde{I}_H^2) = R_{L_{Low}} \left[(\widetilde{I}_H + I_{Batt})^2 - I_H^2\right] + R_{S_{Low}} I_{Batt}^2 \tag{3.21}$$

$R_{L_{High}}$ is small compared to R_C [4] and is therefore neglected in this equation, thus it simplifies to:

$$R_C(I_H^2 - \widetilde{I}_H^2) = R_{L_{Low}}\left[(\widetilde{I}_H + I_{Batt})^2 - I_H^2\right] + R_{S_{Low}} I_{Batt}^2 \tag{3.22}$$

In Equation 3.22 there are two unknown parameters, namely $R_{L_{Low}}$ and $R_{S_{Low}}$. In order to determine these parameter a second equation is necessary to have a linear system of equations that determines these two parameters. Therefore in the experimental set up the wires *Lead Low* and *Sense Low* (see Figure 3.18) are swapped. This leads to a second equation. Then a linear system of two equations and two unknown parameters $R_{L_{Low}}$ and $R_{S_{Low}}$ can be written:

$$\begin{array}{lll} R_C(I_H^2 - \widetilde{I}_H^2) & = R_{L_{Low}}\left[(\widetilde{I}_H + I_{Batt})^2 - I_H^2\right] & +R_{S_{Low}} I_{Batt}^2 \\ R_C(\hat{I}_H^2 - \widetilde{\hat{I}}_H^2) & = R_{L_{Low}} \hat{I}_{Batt}^2 & +R_{S_{Low}}\left[(\widetilde{\hat{I}}_H + \hat{I}_{Batt})^2 - \hat{I}_H^2\right] \end{array} \tag{3.23}$$

where the second equation represents the experiment with the inverted wires. $\hat{I}$ represents the current for the inverted wires set up.

This system can be solved for $R_{L_{Low}}$ and $R_{S_{Low}}$. The relevant parameter for the lead heating correction is $R_{L_{Low}}$, because in normal operation no current is flowing through the *Sense Low* wire.

The same procedure is repeated similarly on the *high* side of the cavity in order to determine $R_{L_{High}}$.

In order to create a multiplicative correction factor for the lead heating, not the absolute values of $R_{L_{Low}}$ and $R_{L_{High}}$ are relevant, but the values relative to R_C. This is illustrated in the next equation that is formed by inserting Equation 3.17 into Equation 3.16:

$$P_{TotalCavityHeating} = I_H^2(R_C + R_{L_{Low}} + R_{L_{High}}) = I_H^2 R_C \underbrace{\left(1 + \frac{R_{L_{Low}}}{R_C} + \frac{R_{L_{High}}}{R_C}\right)}_{Correction\ factor\ C_{LH}} \tag{3.24}$$

The right part splits the cavity heating power into the measured power I^2R_C and a correction term C_{LH} that consists of the determined $R_{L_{Low}}$ and $R_{L_{High}}$ values, relative to the cavity heater resistance R_C.

3.4.6 Measurement and Data Evaluation

During the measurements the selected cavity is controlled with the 'analogue 3-cavity controller'. An additional lead heating current is supplied by a 12 V auto-mobile battery, that can be tuned with a tunable resistor. Measurements are taken with I_{Batt}=14mA and I_{Batt}=20mA. This additional power is switched on and off every 30 seconds. The additional lead heating current is measured using a reference resistor (R_{ref} in Figure 3.18) of 200 Ohms and a battery-powered Fluke 177 voltmeter.

The radiometer current I_H is continuously measured with a HP3458 voltmeter, using the internal reference resistor (10 ohms) in the radiometer controller. The measurement points of the last 15 s of a 30 s period is integrated and used for further evaluation.

[4] $R_{L_{High}}$ is about 300 ppm of R_C, while the uncertainty on R_C due to temperature sensitivity is in the same order of magnitude. The evaluation of the experiment has also been performed by mulitplying a factor 1.0003 to R_C without significant effect on the result.

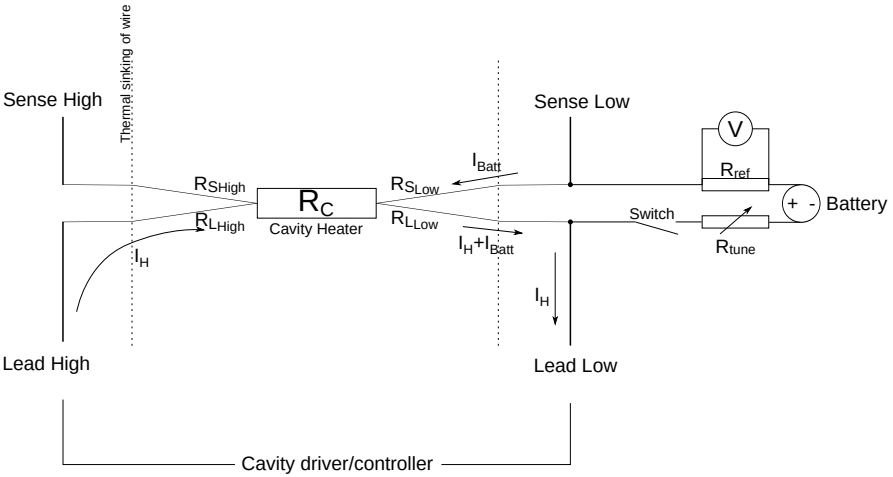

Figure 3.18: Schematic of the measurement set up

The measurements are performed at ambient air conditions as well as in a vacuum chamber at 10^{-3} Pa. The data is treated the following way: the quantity $I_H^2 - \tilde{I}_H^2$ is determined for each on/off/on interval of the additional current. Out of these values an average is taken for the further processing. The other parameters of Equation 3.23 are mean values of the measured series.

3.4.7 Measurement Results

Table 3.15 shows the results of the lead heating measurements. As a measurement with 14 mA and at 20 mA additional lead heating current is performed there are two results for each situation. The difference in these results is used to estimate the repeatability of the measurements (Section 3.4.8).

In Table 3.16 the average lead heating correction factors for each cavity is listed for vacuum and ambient pressure conditions. It is also noted that there is no significant difference between the measurements in the vacuum and the measurement at ambient pressure.

3.4.8 Uncertainty Estimation

The systematic type B uncertainty (based on the uncertainty of the individual measurements, e.g. accuracy of voltmeter etc.), for the single results is computed according to the GUM [61]:

$$u^2 = \left[r_1 \left\{ \frac{\partial C_{LH}}{\partial x_1} x_1 \right\} \right]^2 + \cdots + \left[r_n \left\{ \frac{\partial C_{LH}}{\partial x_n} x_n \right\} \right]^2 \tag{3.25}$$

where $r_1 \cdots r_n$ are the relative uncertainties of the input parameters. The coefficients in the curly brackets are computed numerically during the data evaluation. Example coefficients (Cav A) are listed in Table 3.17. The relative uncertainties are the same for all measurement series, whereas the coefficients are dependent of the measurement series.

Cavity	Pressure	I_{LH} [mA]	$R_{L_{High}}/R_C$	$R_{L_{Low}}/R_C$	Combined (sum)	Uncertainty (1σ)
A	ambient	14	0.000237	0.000259	0.000497	0.000036
A	ambient	21	0.000235	0.000265	0.000500	0.000036
A	vacuum	14	0.000299	0.000224	0.000523	0.000036
A	vacuum	21	0.000246	0.000224	0.000469	0.000036
B	ambient	14	0.000308	0.000332	0.000640	0.000036
B	ambient	21	0.000269	0.000329	0.000598	0.000036
B	vacuum	14	0.000298	0.000313	0.000611	0.000036
B	vacuum	21	0.000332	0.000332	0.000664	0.000036
C	ambient	14	0.000275	0.000228	0.000503	0.000036
C	ambient	21	0.000232	0.000275	0.000507	0.000036
C	vacuum	14	0.000251	0.000249	0.000501	0.000036
C	vacuum	21	0.000252	0.000288	0.000539	0.000036

Table 3.15: Lead heating results for DARA cavities

	Cavity A	Cavity B	Cavity C
Ambient	1.00050	1.00062	1.00051
Vacuum	1.00050	1.00064	1.00052
uncertainty (1σ)	0.000025	0.000025	0.000025

Table 3.16: Correction factors C_{LH} (mean values) of the lead heating correction for the DARA cavities

	$R_C(I_H^2 - \hat{I}_H^2)$	I_B	$\hat{I}_B$	I_H & $\hat{I}_H$	Repeatability
coefficient	0.000475	-0.000434	0.000105	-0.000186	1
relative uncertainty r	0.002	0.01	0.01	0.005	0.000025

Table 3.17: Uncertainty propagation coefficients for measurement DARA A pin24/25

As can be seen in Table 3.15 in columns R_{High}/R_{Cavity} and R_{Low}/R_{Cavity} the results for the 14 mA and 21 mA do not agree within the systematic type B uncertainties that would only be about 20 ppm (2σ). Therefore a repeatability error is introduced. The repeatability error is computed by taking the difference of the associated 14 mA and 21 mA measurements. The standard deviation of the distribution of these differences is taken as an estimate of the uncertainty due to the repeatability of the experiment. The 1σ uncertainty of a single measurement is then the standard deviation of the distributions of the difference divided by the square root of 2. The uncertainties of the combined high and low lead heating components is computed according to Equation 3.25. The repeatability component is dominating the combined uncertainty of the lead heating correction.

3.4.9 Comparison with the Brusa Method

The Lead Heating effect is also measured for a PMO6 radiometer that has already been characterized by Brusa [67]. This is done in order to compare the two methods. The

instrument used is the PMO6-11, that has been fully characterized in the early 1980s. The measurements are carried out in the same way as the measurement with the DARA cavities. However the measurements are only made in ambient air, like the Brusa measurements. For the uncertainties the repeatability component for the DARA measurements have also been used to estimate the uncertainties of this measurement. Table 3.18 shows the results of the 2012 as well as the Brusa measurements. The Measurements show good agreement within the uncertainties.

Brusa did not measure the reaction in heater power directly. He disconnected the heater and measured the change in the error signal of the controller loop. He then calibrated the error signal using the cavity heater in order to estimate the lead heating effect. The response of the measurement bridge that generates the error signal is not necessarily linear, and not such a precise measure. Therefore the agreement of both methods is a good result.

Measurement	R_{High}/R_{Cavity}	R_{Low}/R_{Cavity}	combined (sum)	uncertainty (2σ)
2012 14mA	0.000174	0.000098	0.000272	$\pm$0.000072
2012 20mA	0.000172	0.000098	0.000270	$\pm$0.000072
2012 Combined			0.000271	$\pm$0.000050
Brusa(1982)			0.000240	$\pm$0.000066

Table 3.18: Lead heating effect for the PMO6-11 radiometer

3.4.10 Discussion

A model has been set up that improved the understanding of the lead heating effect. Reasonable agreement has been found between the model calculation and the measurement although the model can not be considered very accurate. The measurements led to a determination of the lead heating correction factor with a comparable low standard uncertainty of 25 ppm. It is important to note, that the key condition for keeping the lead heating effect under control (and apply corrections), is that the wires are thermally connected to the heat sink, before they are connected to an electronics board. Otherwise the temperature gradient in the wire is not well defined, and the effect of lead heating becomes unpredictable and thus can not be correctly compensated for.

3.5 Diffraction

Due to the fact that electromagnetic radiation propagates as a wave, the radiation does not follow exactly the path one would assume from purely geometrical optics. The wave nature of the radiation creates diffraction effects at the front aperture of the instrument. This reduces the amount of power reaching the detector, compared to what is expected by geometrical optics. Therefore a correction factor for diffraction will be introduced in this section. Besides the mathematical formulation and calculation of the diffraction effect, the influence of the solar spectrum on the diffraction correction is discussed.

The subject of diffraction has been studied since the 19th century, by J. Fraunhofer, A. J. Fresnel and E. Lommel. While the first two prepared the terrain, Lommel solved the diffraction problem for a point source on a circular aperture in 1884 [78]. Lommel's solution (a combination of Bessel functions) is the base of most of the subsequent work on the topic. In modern times of radiometry E. Shirley has contributed many articles on diffraction effects in radiometry [79, 80] that are the base for the calculation of the diffraction correction in this work. A extensive list of further publications can be found in [79].

3.5.1 Mathematical Formulation

Lommel's solution $\alpha(u, v)$ gives the distribution of light on the detector plane, behind a circular aperture, considering a point source. The mathematical problem that needs to be solved is the integration of Lommel's solution $\alpha(u, v)$ over the detector area and the source area(equation 3.26). This can be done because the sun is an incoherent source and can be treated as an ensemble of independent point sources. Integrating Lommel's solution gives the Flux Φ_λ that is reaching the detector:

$$\Phi_\lambda = \frac{L_\lambda}{(d_s + d_d)^2} \int_{Source} dr_s^2 \int_{Detector} dr_d^2 \times \alpha(u, v) \tag{3.26}$$

where

$$u = \frac{2\pi}{\lambda} R^2 (\frac{1}{d_d} + \frac{1}{d_s}),\ v_s = \frac{2\pi}{\lambda} \frac{r_s R}{d_s},\ v_d = \frac{2\pi}{\lambda} \frac{r_d R}{d_d},\ v_0 = max(v_s, v_d) \tag{3.27}$$

Where L_λ is the luminosity of the point source at the considered wavelength, u, v_s, v_d, v_0 are geometrical variables, normalised by the wavelength. The various forms of v can be considered as measure of the angle, they are all used in order to evaluate Lommel's solution, the exact implementation will be shown later in this Section. r_d and r_s are the integration parameters (detector and source). The geometrical layout, illustrating the geometrical quantities is shown in Figure 3.19. The values are listed in Table 3.19.

The challenge is to evaluate Lommel's solution as well as to solve the Integrals. Shirley [79, 80] has shown an elegant solution to substitute Equation 3.26 by a single, one dimensional integral:

$$\Phi_\lambda = \frac{2\pi R_s^2 R_d^2 L_\lambda(\lambda)}{(d_s + d_d)^2} \int_{-1}^{1} dx \frac{\{(1 - x^2)[(2 + \sigma x)^2 - \sigma^2]\}^{1/2}}{1 + \sigma x} \times I(u, v_0, 1 + \sigma x) \tag{3.28}$$

with the parameter $\sigma = min(v_s, v_d)/max(v_s, v_d)$, and only one integration parameter (x) instead of r_d and r_s. The introduced function $I(u, v, 1 + \sigma x)$ is the fraction of the flux that is incident on the aperture and is subsequently falling on the detector (substitute for $\alpha(u, v)$). To evaluate this function that is based on Bessel function (similar to Lommel's solution) there are different approaches in the literature. For the calculation of the DARA diffraction correction two approximations are be used. The approximation from Steel et

al. [81] which is presented in a better form in [80] and Wolf's formula [82] for integrated flux which are both also used by Shirley [79, 80] in combination with Equation 3.28. The integral is then evaluated numerically, using these formulas for $I(u, v, 1 + \sigma x)$. The difference in the result, when using the two formulas, is found to be less than 1 ppm. Therefore for the final results, only Wolf's formula is used.

Calculations have also been made by Eric Shirley from the National Institute of Standards and Technology (NIST) who is the author of many publications on diffraction effects [79, 80]. Shirley's result differs less than 1 ppm, over the whole wavelength range, from calculations presented in this work[5].

Losses due to diffraction

The ultimate aim is not an absolute amount, received at the detector, but rather the ratio between the flux including diffraction effects and the flux predicted by geometrical optics. Geometrical optics predicts the following flux on the detector:

$$\Phi_{geom} = \frac{R_s^2 \pi_\lambda}{d_s^2} R^2 \pi = \frac{\pi^2 R_s^2 R_d^2 L_\lambda}{(d_s + d_d)^2} \cdot \frac{u^2}{v_0^2} \tag{3.29}$$

To get the correction factor that is applied to the measurement we write:

$$C_{Diffraction} = \frac{\Phi_{geom}}{\Phi_\lambda} \tag{3.30}$$

Looking at Equation 3.28 and 3.29 it can be seen that the scaling factors are equal for both fluxes, and will therefore vanish at the division in Equation 3.30.

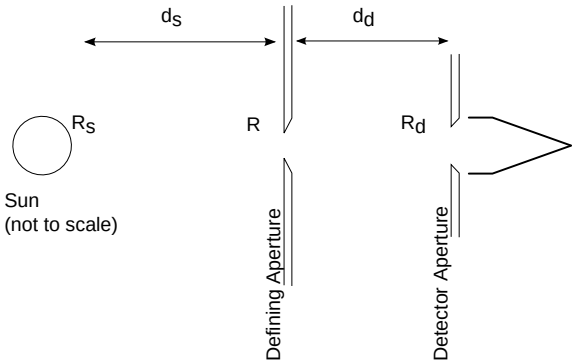

Figure 3.19: Layout of the source-aperture-detector geometry

3.5.2 Spectral Weighting of the Diffraction Effects

As diffraction is wavelength dependent, it is calculated for the spectral region from 250 to 10'000 nm. The wavelength dependent correction is then weighted with the respective solar spectrum (terrestrial or extraterrestrial). Thus the correction factors are obtained.

[5] Personal communication with Eric Shirley (NIST)

Solar radius	R_s	$6.75 \cdot 10^5$	km
Sun earth distance	d_s	$1.5 \cdot 10^8$	km
Defining aperture radius	R	2.5	mm
Aperture detector distance	d_d	54.1	mm
Detector aperture radius	R_d	3.45	mm

Table 3.19: Geometrical properties for the diffraction calculation

The wavelength region has been chosen so that a extension of the region does not change the correction factor by more than a few ppm. In order to compute the correction for an extraterrestrial spectrum, different common spectra have been evaluated (Section 3.5.3) .

For terrestrial measurement it is not so straight forward to find an appropriate spectrum. The accuracy of the diffraction calculation itself calls for accurate knowledge of the spectrum. Therefore the variations of the solar spectrum in Davos and its influence on diffraction will be studied in more detail in (Section 3.5.4).

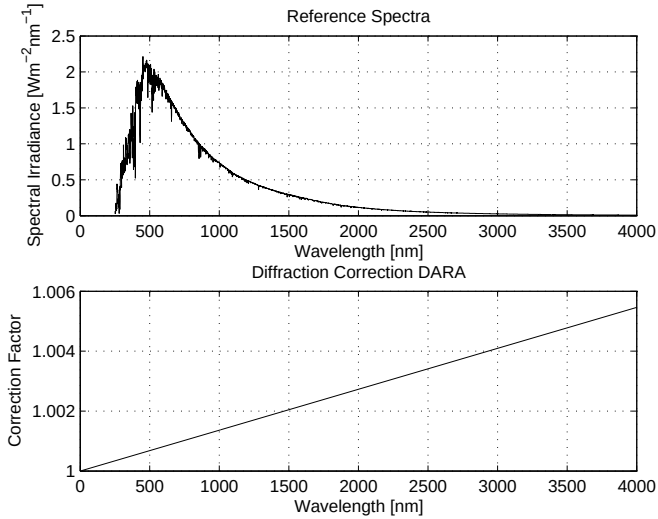

Figure 3.20: The wavelength dependent diffraction effect (bottom) is weighted with an extraterrestrial (Kurucz [76]) solar spectrum (top)

3.5.3 Extraterrestrial Spectra

Figure 3.20 shows the wavelength dependent diffraction correction and the extraterrestrial (Kurucz [76]) spectrum. The effect of diffraction increases almost linearly with wavelength.

Since there are differences between the different reference spectra in use [83, 84], the diffraction correction is computed for four different spectra. Table 3.20 shows the results for these four spectra. The agreement between the results from Kurucz and WRC spectra

Spectrum	Correction Factor	deviation from Kurucz
Kurucz [76]	1.0012788	–
WRC [85]	1.0012791	+0.3 ppm
Gueymard [86]	1.0012740	−4.8 ppm
ASTM 490 [87]	1.0012852	+6.4 ppm

Table 3.20: Diffraction correction factors for different extraterrestrial solar spectra

is better than 1 ppm, while the other two results differ by 5 to 6 ppm. The Kurucz spectrum, is taken as the reference in order to calculate the diffraction correction, whereas the difference between the result from Kurucz to ASTM and Gueymard is taken into the uncertainty budget. The Kurucz spectrum also serves as the input for the radiative transfer calculations in the next section.

3.5.4 Spectral Influence on Diffraction on Ground

In order to compute terrestrial solar spectra for Davos the radiative transfer software LibRadtran [88] is used. Spectra have been calculated and validated against spectroradiometer data obtained at the Davos site during winter season 2013/2014. Regarding diffraction it has been found that the relevant input parameters for the diffraction effect are the solar zenith angle and the integrated water vapour. The solar zenith angle determines the amount of Rayleigh scattering which reduces the blue/green part drastically compared to the red part of the spectrum. The water vapour on the other hand has the highest impact on the larger wavelengths. The overall diffraction effect is sensitive to changes in the ratio of the longer wavelengths to the shorter wavelengths. The contribution of aerosols has also been considered, but found negligible.

Figure 3.21 shows the diffraction correction versus the solar zenith angle based on spectra calculated with LibRadtran. Two different standard model atmospheres are used, as well as a winter atmosphere with minimal integrated water vapour and a summer atmosphere with maximal integrated water vapour. The integrated water vapour is taken from the Davos record from 2001 to present. These data are from the STARTWAVE database [89] and are based on GPS data [90].

It can be seen that for large solar zenith angles the diffraction correction increases about 50 ppm (of the correction factor) or 4% (relative of the correction) compared to low zenith angles. The dependence on the integrated water vapour is of the same order of magnitude, it varies by approximately 80 ppm between the extremes. Typically the highest integrated water vapour values occur during summer while the lowest values correspond to dry and cold winter periods.

Figure 3.22 shows the diffraction correction as a function of the season for a fixed solar zenith angle of 55°. The uncertainties originate from the uncertainty of the integrated water vapour. Figure 3.23 shows the seasonal trends in integrated water vapour. Data from 2001 to 2013 has been evaluated. There is a distinct seasonality in the water content of the atmosphere, however the distribution is quite broad as the water content can vary from day to day. Thus a seasonally dependent correction is certainly an improvement to a constant correction, but depending on the accuracy needed, an individual correction is an even better option.

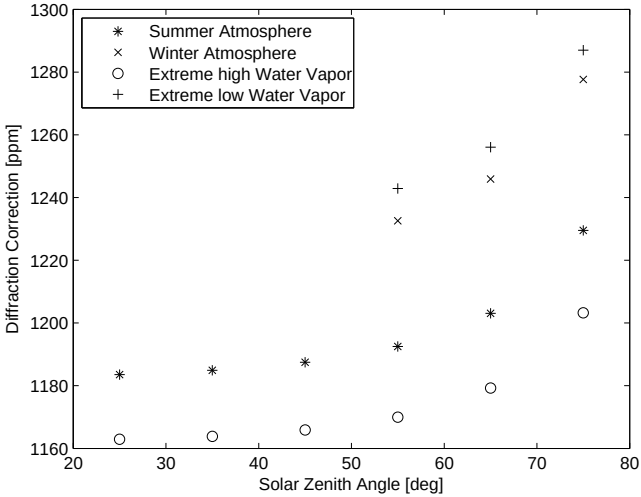

Figure 3.21: Diffraction effect versus solar zenith angle for different model atmospheres for Davos (spectra calculated with LibRadtran). "Summer" and "Winter" are LibRatran standard atmospheres, while the "Extreme" cases are based on the Davos water vapour climatology.

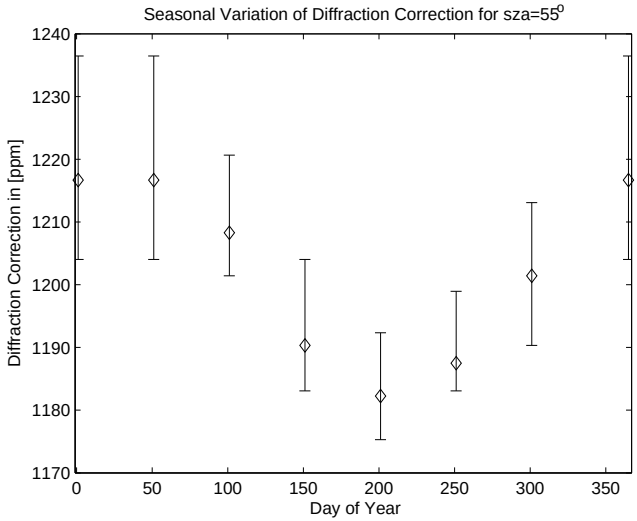

Figure 3.22: Seasonal influence on the diffraction correction, with 1σ uncertainties, based on Davos water vapour data.

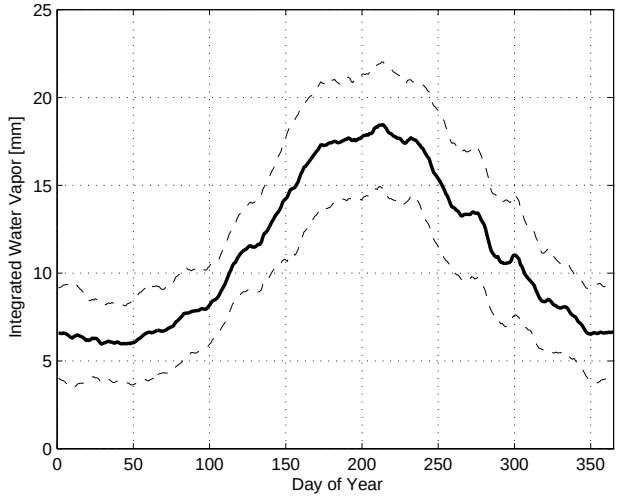

Figure 3.23: Seasonal variation of integrated water vapour for Davos with σ band showing the width of the distribution

Overall Correction Factor (fixed value)

A simple approach is to correct diffraction with one fixed overall value. This had also been done by Brusa [67] to correct the PMO6 Radiometer for diffraction. This value however is associated with a rather large uncertainty. From the data shown in Figure 3.21 an overall value of 1220 ppm and a standard (1σ) uncertainty of 36 ppm is deduced. This uncertainty is larger than the uncertainty of the diffraction calculation itself (Section 3.5.7). For aesthetic reasons this is not satisfactory. However the main real application of this factor is the comparison of DARA to the WRR standard, respectively the implementation of a WRR scale to DARA (Section 4.2). Comparing the uncertainties associated with a WRR calibration to the uncertainty of a fixed diffraction correction the contribution of the fixed diffraction correction seems small and therefore justifies the application of a fixed correction factor.

Seasonal Modulation of TSI Measurements

The seasonal variability of the integrated water vapour modulates the measurements taken with DARA (and other solar radiometers). Furthermore this effect is enhanced by the dependence on solar zenith angle, as in winter the sun does not rise high over the horizon, thus having always large zenith angles. Especially when comparing a Radiometer with DARA-type geometry to a PMO6-type radiometer (geometry inverted) that has an opposite diffraction correction, the seasonal modulation effect will double.

Therefore a seasonally and zenith angle dependent correction factor could be introduced. From the calculation shown in Figure 3.22 it can be seen that the 1σ uncertainty is smaller than 20 ppm in the worst case which is an improvement compared to the overall correction factor.

Individual Diffraction Correction Based on Environmental Data

In principle the diffraction effect can be calculated individually for every data point that is taken with the radiometer. Input data such as integrated water vapour, solar zenith angle and further parameters such as AOD, etc. could in principle be fed into radiative transfer models (e.g. LibRadtran) to find the appropriate spectrum. Another possibility would be to measure the solar spectrum in situ with a spectrometer. Using such an approach is possible to reduce the rather large uncertainty that is inevitable when using a fixed overall value. The accuracy of the calculated spectra suggests that for individual calculations an uncertainty that is smaller than the uncertainty of the diffraction calculation seems realistic.

Especially when aiming at higher accuracy with future instruments such an individual correction might become necessary. A candidate instrument for such a correction could be the Cryogenic Solar Absolute Radiometer (CSAR) [32, 33] that aims at very high accuracy. Winkler [32] also discusses diffraction effects for the CSAR instrument and finds a variability of up to 200 ppm for the diffraction correction factor between different terrestrial solar spectra.

3.5.5 Correction Factors

Table 3.21 shows the obtained correction factors for the different situations. The ratio of the terrestrial value and the value at 532 nm is used when comparing measurements against TRF with measurements against the WSG. The Extraterrestrial value is listed for completeness. It will not be used further in this work.

	Terrestrial(Davos)	Extraterrestrial	532 nm	C_{terr}/C_{532}
Correction factor	1.001220	1.001279	1.0007244	1.000485
Uncertainty (1σ)	0.000043	0.000025	0.000024	0.000036

Table 3.21: Correction factors for diffraction losses

3.5.6 Calculations for TIM and CLARA Geometries

The calculations are also performed for the TIM [63, 58] design in order to validate the results of the calculations presented here. Furthermore the calculations are carried out for the CLARA geometry. Table 3.22 shows the geometrical properties of these instruments.

Table 3.23 shows the results of the calculations. The values have been calculated using the Kurucz [76] spectrum The difference between the result for the TIM geometry and the values from the literature are 8 respectively 10 ppm. This is well within the uncertainties and could be explained by different spectra, used for weighting and different wavelength ranges considered.

		TIM [79]	CLARA[6]	unit
Solar radius	R_s	$6.75 \cdot 10^5$	$6.75 \cdot 10^5$	km
Sun earth distance	d_s	$1.5 \cdot 10^8$	$1.5 \cdot 10^8$	km
Precision aperture radius	R	3.9894	2.5	mm
Aperture detector distance	d_d	101.6	50.8	mm
Detector aperture radius	R_d	7.62	4.2	mm

Table 3.22: Geometrical properties for the diffraction calculation (TIM, CLARA)

Instrument	Extraterrestrial	at 532 nm
CLARA	1.000716	1.000406
TIM	1.000440	1.000249
TIM (Literature) [58]	1.000430	-
TIM (Literature) [79]	1.000432	-

Table 3.23: Diffraction correction factors for the TIM and CLARA instruments, calculated with Wolf's formula and comparison values from the literature

3.5.7 Uncertainty

As every component of the characterisation of the radiometer, also the diffraction correction brings an uncertainty into the budget. In contrast to the experimentally determined components of the characterisation, the uncertainty of the diffraction can not be so easily determined from the experiment as the correction factor is determined numerically. The uncertainty is also not a consequence of numerical precision, but rather limitations of the diffraction theory itself as well as imperfect knowledge of the environmental conditions. The problem of estimating the uncertainty of diffraction calculations has been investigated by Shirley et al. [91]. Their approach was to compare the diffraction calculations to experimental data with known measurement uncertainties. Out of this comparison they conclude an uncertainty for the theory behind the calculation. According to this work an uncertainty of 1.8% (1σ) can be concluded. This leads to 22 ppm for the 1σ uncertainty for the diffraction calculation. An additional contribution to the uncertainty of the calculation

[6] Personal communication with Silvio Koller (PMOD)

	Extraterrestrial	Terrestrial (fixed value)	Terrestrial (seasonal correction)	at 532 nm (TRF)
Calculation	0.000022	0.000022	0.000022	0.000022
Geometry	0.000009	0.000009	0.000009	0.000009
Spectrum	0.000006	0.000036	0.000020	–
Combined	0.000023	0.000043	0.000031	0.000024

Table 3.24: Uncertainty budget

originates from the geometrical input parameters (Table 3.19). An uncertainty (type B) for R_d (0.025 mm) and d_d (0.1 mm) is assumed. This leads to an uncertainty contribution of 9 ppm (1σ). Variations due to the sun earth distance parameter that is not constant over the year, have also been studied. The influence on the correction factor is less then 1 ppm and therefore neglected.

The second contribution to the uncertainty is the uncertainty originating from the spectra. For the extraterrestrial spectrum an uncertainty contribution of 6 ppm (1σ)is assumed, while for the terrestrial value in Davos the uncertainty is considerably higher for reasons explained in Section 3.5.4. For the value given in Table 3.21 the uncertainty contribution of the spectra is 36 ppm (1σ).

With a seasonal and solar zenith angle dependent correction the spectral contribution to the uncertainty lowers to 20 ppm (1σ). This leads to a standard uncertainty of 31 ppm for the seasonal diffraction correction.

Individually calculated spectra for each data point could further reduce the uncertainty contribution of the spectra and the diffraction correction. This depends of course on how accurate the spectra can be modelled, but the accuracy of the diffraction correction will still be limited by the uncertainty of the diffraction calculation itself. All uncertainty components are listed in Table 3.24.

3.5.8 Diffraction at the TRF

The TSI Radiometer Facility (TRF) [31], where DARA is compared against the SI cryogenic laboratory standard (Section 4.3), is generating an irradiance field by a moving laser beam that fills up the desired area with a continuous movement. At the TSI Workshop in December 2010, the question has been raised, if the diffraction effects at TRF are similar to the effects occurring when irradiating the aperture with sunlight (at equal wavelength). Whereupon Eric Shirley from NIST investigated the problem further and concluded that the difference is probably very small[7]. However no final conclusion on the subject has been published so far, and the proper mathematical treatment seams not that clear. For further calculations within this work it is assumed that there is no relevant difference between the two situations, and no further uncertainty is taken into account. In Section 4.3 the problem is discussed further in the context of the TRF comparison.

The topic remains an interesting field of study. An experiment, similar to the diffraction experiment described in Section 3.6, but using a moveable laser beam seems a possible approach from the experimental side, therewith the assumption that the diffraction is approximately equal for both cases of illumination could be verified.

[7] Eric Shirley, Seminar held at PMOD, 11 July 2011

3.5.9 Discussion

The numerical disagreement between the different calculations has been found very small, in the order of a ppm. It can be concluded that the calculations are numerically solid. The uncertainty of the calculation is determined by the limits of the theory, which is described in the literature. While the uncertainty of the correction factor (terrestrial) origins mainly from the uncertainty of the terrestrial solar spectrum.

In principal the correction can be calculated individually for each data point with a higher accuracy. Taking into account solar zenith angle and integrated water vapour.

For measurements at TRF it is assumed that the diffraction correction is equal to the calculated value with the sun as a source. The correct treatment of diffraction at TRF remains an open question.

3.6 Aperture Edge Scatter and Diffraction Experiment

An imaging experiment of the precision aperture is carried out for two purposes: First, it allows to check the quality of the aperture and second diffracted light can be measured and compared against calculations. Such an experiment had already been carried out by Harber et al. [92] with the TIM instrument. The experiment described here closely follows the the work by Harber et al. [92].

There is however an important difference: Sunlight from the heliostat beam is used to illuminate the aperture, rather than an artificial light source. This guarantees the correct geometrical properties of the incident light, it has however the downside of introducing spectral dependencies. Furthermore, due to the smaller dimensions of DARA the whole optical set-up is scaled down. Downscaling the experiment also makes it necessary to position the camera behind the image plane, whereas Harber et al. have it in front.

This experiment is not measuring the losses through diffraction as discussed in Section 3.5, but it illustrates nicely the nature of diffraction and enhances the understanding. The measured values are the part of the diffracted light that would enter the cavity and thus is not directly the object of interest. Nevertheless it can be compared to calculations and to some extend validate the theoretical discussion.

3.6.1 Experimental Set-up

A schematic of the experimental set-up is shown in Figure 3.24. The solar light beam is provided by the heliostat. The light gets diffracted at the aperture and is captured by a lens (f=30 mm) that images the diffracted light in the image plane of the aperture (60 mm behind the lens). The sun is however imaged in a plane 30 mm behind the lens, where the light is blocked by a beam block. The sensitivity of the camera can be calibrated by taking out the beam block and have the full beam on the camera. Moving the camera behind the image plane, the sharp edge of the image (Figure 3.25 on the left) separates into two rings (Figure 3.25 on the right) which originate from the inward and outward diffracted light respectively.

The illuminated precision aperture where the diffraction takes place is the DARA aperture A. At a distance of 54 mm behind the aperture a field of view aperture with a diameter of 11 mm is mounted. This diameter is larger than the original DARA field of view aperture in order to enhance the outward diffracted signal. Two different beam blocks have been used: A $\varnothing$=1.5 mm and a $\varnothing$=2 mm block. The beam blocks are held in place with four very thin threads.

3.6.2 Data Evaluation and Interpretation

The pixels of the image get binned according to their distance to the centre, thus a radial profile can be extracted (Figure 3.26). Pixels that are shaded by the thread, that hold the beam block in place, are compensated. In order to eliminate stray light originating from the lens and the beam block, a background subtraction is performed next. Different fitting routines and constraints have been applied in order to evaluate its influence on the final result. The background subtracted data is then binned as a function of angle. Figure 3.27 shows the radial integral over the inward diffraction peak as a function of angle. The shades of the threads are clearly visible. Furthermore the distribution has a sinusoidal shape that is due to a slight misalignment of the beam block [92]. A sine is therefore fitted to the data. The mean value of the sine is then taken for further evaluation, that is basically an integration over all angles and a normalisation, using a reference image (taken with no beam block present).

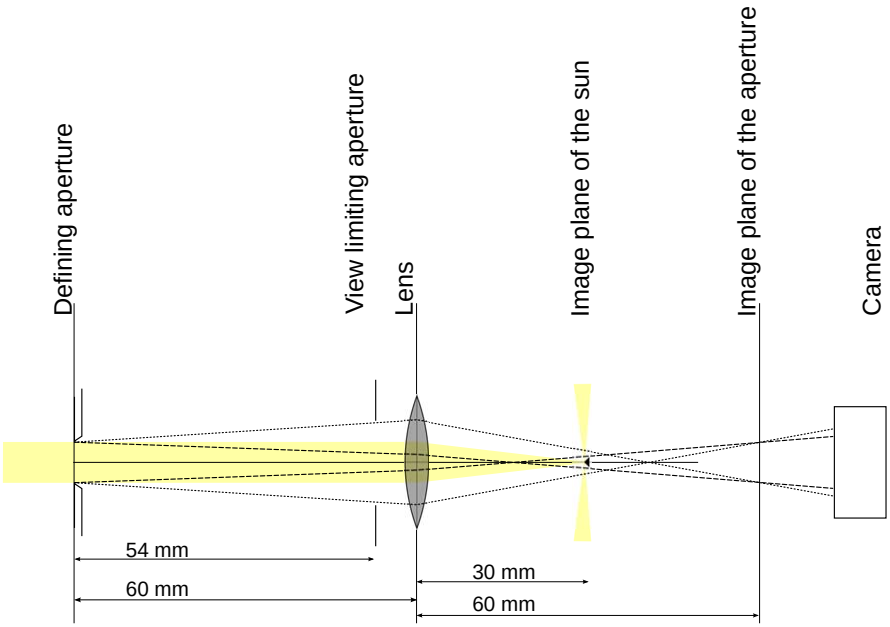

Figure 3.24: Schematic of the diffraction experiment: The light from the heliostat passes the precision aperture, where diffraction effects take place. The main beam (yellow) passes the view limiting aperture and gets focussed on the beam block where it is reflected away. The diffracted light from the aperture can pass the beam block and forms an image in the image plane of the aperture. Moving the camera behind the image plane allows to distinguish between the inward (dashed) and outward (dotted) diffraction.

It can be seen that in the region of 20° to 70°, which corresponds to the lower left in Figure 3.25 (right image), the data is very noisy. The origin of this effect in not quite clear. On the one hand it seems indeed to originate from the aperture as it is visible in the inward and outward diffracted light. On the other hand the effect is not visible in all of the diffraction images taken (same aperture). Possibly the effect is extremely alignment sensitive, thus slightly enhanced irradiation from the side onto the edge could cause this scatter. On average however the values in the selected region are equal to the regions with no such scatter present.

3.6.3 Comparison of the Measurements to Calculations

Figure 3.28 shows the results of the measurements for inward and outward diffraction portions for the two block sizes used. The lines are the expected effects based on calculations. These calculations are based on the formulas given in the appendix of Harber et al.[92] and also include the sensitivity of the CMOS-camera set-up as well as the solar spectrum measured with a spectro-radiometer and the losses at the heliostat mirrors (Section 5.5.4).

The uncertainties of the measurement points in the x-axis result from the uncertainty of the block size and on the y axis from the statistical distribution of different measurements

and from a systematic component that is associated to the background subtraction. The component associated to the background subtraction is assessed by analysing the effect of different constraints on the fit. Thus combined standard uncertainties of the measurements between 18 ppm and 45 ppm are obtained. The expanded (3σ) uncertainties are indicated in Figure 3.28.

Also the diffraction calculation contains an uncertainty, which is arising from the inaccurate knowledge of the spectrum, the camera response and the exact geometrical set-up. An upper boundary for the uncertainty has been established for the spectral dependency by assuming a flat spectrum as the solar input to the system and comparing this result to the result obtained with the calculation with the proper spectrum. Similar effects are expected if another component such as if the camera responsivity was improperly described. The thus estimated uncertainty is in the order of 2 % (1σ) for the spectral component. The non linearity of the camera is account for with 1% (1σ). Furthemore an uncertainty due to geometrical misalignment is found to be 3% (1σ) originating from the uncertainty of the field of view aperture (outward diffraction only) and 3.5% for inaccurate placements of the components in the z-direction. This results in a combined standard uncertainty (1σ) of 4% for the inward diffraction calculation and of 5% for the outward diffraction calculation respectively.

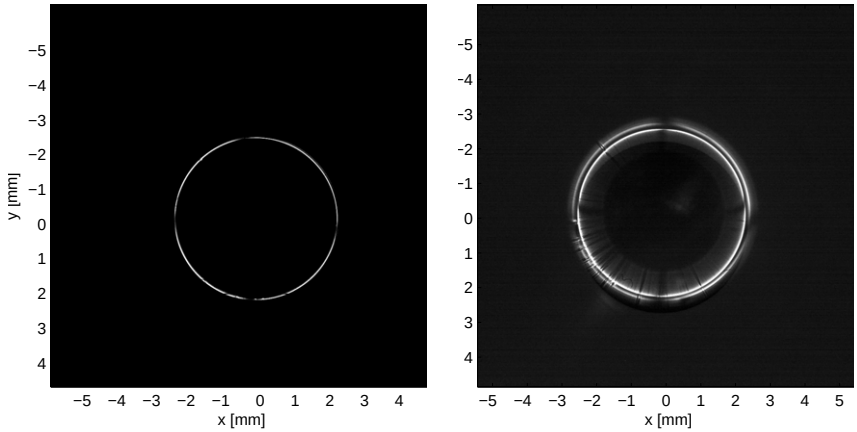

Figure 3.25: Image of diffracted light: The image on the left is taken with the camera in the image plane of the aperture. The diffracted light forms an image of the aperture. The image on the right is taken with the camera behind the image plane. The inner ring is the inward diffracted light, and the outer ring the outward diffracted light.

3.6.4 Discussion

The experiment provides a nice visualisation and allows to experimentally quantify diffraction effects. There is good agreement between measurement and calculations within the uncertainties. The uncertainties are significantly larger than the uncertainty obtained by Harber et al.[92]. This has on one hand to do with the fact that a broad band light source

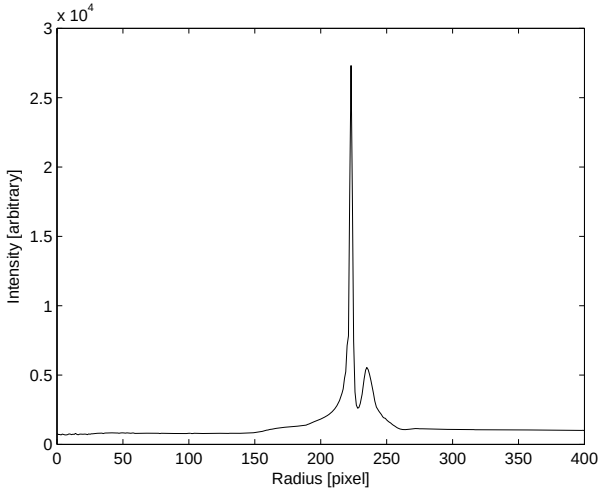

Figure 3.26: Radial profile of the diffraction image (Figure 3.25 right)

has been used and thus the spectral dependencies of all the components play a roll. On the other hand the issue of background stray light subtraction brings in a high uncertainty. Nevertheless the uncertainties of the experiment is in the order of the uncertainty of the terrestrial diffraction correction. The findings are compatible with the assumption that there is no stray light from the aperture edge that is significantly enhancing DARA's sensitivity.

The experiment reveals the potential for stray light measurements in PMO6 mufflers, which has been underestimated in the first place [33, 56]. A similar experiment could image the muffler instead of the aperture and thus identify sources of stray light within the muffler.

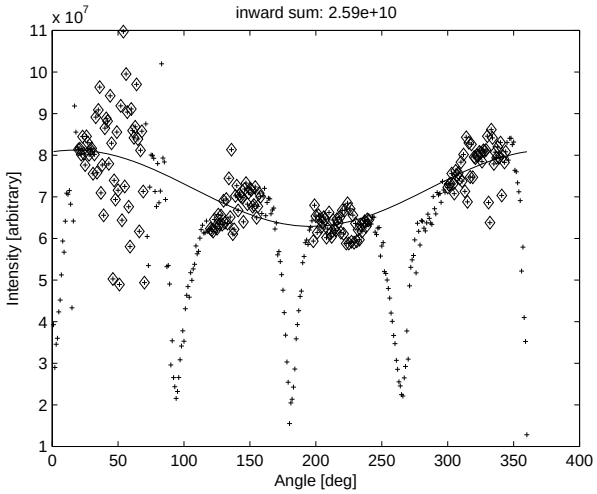

Figure 3.27: The figure shows the angular dependence of the diffraction signal. The four threads that hold the beam block are clearly visible. The diamond framed markers are the data that is used for evaluation. A sine is fitted to the data.

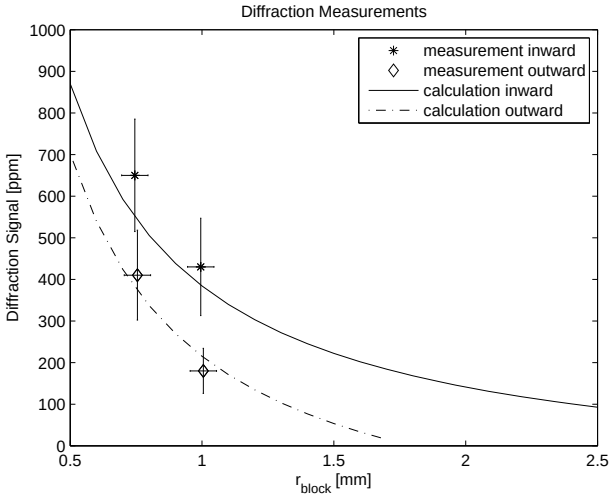

Figure 3.28: Measurable diffraction effects as a function of beam block size. The lines are calculated values, the measurements are marked with indicators that correspond to a 3σ uncertainty.

3.7 Non Equivalence

Non equivalence effects are caused by a slightly different thermal configuration of the active cavity in the measurement/calibration (open/cosed) phases. A different thermal configuration can cause spurious heat flows (e.g. through the surrounding air, or radiation) that are not exactly equal. This effects must be corrected for. With PMO6-type radiometers this has been a rather large correction [67, 59, 33], these corrections are listed in Table 3.25. It means for PMO6 type instruments as well as for DARA, that the readings (at ambient pressure) are too low due to this effect.

To identify the causes of this effect it will be treated theoretically and with a numerical model approach first. For operation in vacuum (or space application) non equivalence is considered negligible as justified in the model approach (Section 3.7.2). The non equivalence correction for operation at ambient air pressure is then derived from the air to vacuum ratio of the DARA's sensitivity. This ratio is experimentally determined by taking measurements in a vacuum chamber on the solar tracker.

PMO6-09	3100 ± 340 ppm
PMO6-11	1800 ± 340 ppm
PMO6-PREMOS 01	5710 ± 500 ppm
PMO6-PREMOS 02	6709 ± 600 ppm

Table 3.25: Non equivalence corrections for PMO6-type radiometers with uncertainties (2σ) [33, 59]

3.7.1 Non Equivalence of PMO6 and DARA Cavities

PMO6 Non Equivalence

The non equivalence of PMO6 radiometers is explained by a spurious heat flow through the air from the cavities cylindrical part to the radiation shield [67, 59, 33]. Figure 3.29 illustrates the origin of the non equivalence in PMO6 radiometers. The incoming radiation is partly heating the cylindrical part of the cavity. During the closed shutter phase, the electrical heater only heats the conical part of the cavity, thus the cylindrical part is at a slightly lower temperature than in the open shutter phase. The spurious heat flow from the cylindrical part of the cavity outwards to the radiation shield is therefore slightly higher during the open shutter phase. This leads to an underestimation of the radiative heating.

Because the thermal conductivity of air is temperature dependent [93] the non equivalence effect is therefore thought to be slightly temperature dependent. For that reason a lower non equivalence is also of high interest for ground based radiometry.

DARA Non Equivalence

The DARA cavity has been designed with the non equivalence problem of the PMO6 radiometers in mind. Therefore the cone has been inverted and the radiation shields have been placed further apart from the critical parts of the cavity. However it has not been considered in the design phase that due to reflection (5% of the incomming radiation) more energy will be absorbed in the central part of the cavity. Figure 3.30 illustrates these reflections. From geometrical arguments the surface of the cone can be devided into 3 different areas. These areas differ from each other in the amount of radiation they absorb. In the large outer area only direct light is absorbed. This light comes directly from the sun and 95% of this radiation is absorbed in the coating. Most of the remaining 5% of

the radiation is reflected in the forward direction (like on a mirror) towards the center of the cone. This is due to the gloss of the coating. In the inner areas this additional light coming from the outer area adds to the direct illumination. The geometrical concentration of this reflected light leeds to a considerable enhancement of the absorbed energy in the inner area of the cone. Figure 3.31 shows the distribution of the absorbed energy in the cavity with respect to the radius. In the inner radius the absorbed energy per area is more than a third higher than in the outer part.

A further cause for non equivalence, is a slight misplacement of the heater element, which makes the difference in the temperature distribution even larger. The exact position of the heater element is therefore very crucial to reduce the non equivalence effect. As the cavity is essentially hand crafted it is expected to be slightly imperfect. So there will be a contribution from this origin also.

3.7.2 Simple Model Calculation for the DARA Cavity

With a simple numerical approach the problem of non equivalence caused by the beam concentration efect has been studied in further detail. The model is based on the different energy input scenarios shown in Figure 3.31. The two dimensional structure of the cavity is reduced to a one dimensional model along the symmetry axis using the appropriate geometrical factors. Of course this model does not claim to be very sophisticated nor will it yield precise quantitative analysis of the non equivalence effect. But it will help to understand the thermal situation in the cavity and the physical processes.

The one dimensional model is divided into finite elements or grid points. The grid points are connected through the heat transfer equation similar to the model described in Section 3.4.1. Additionally a heat flux input (solar radiation or electrical heater) can be introduced to selected grid points. To all grid points a heat loss to the surrounding air can be introduced. This heat loss is proportional to the temperature difference between the point on the cavity and the surrounding air temperature. The heat transmission coefficient is scaled so that approximately 25 % of the total applied power is lost to the air. This is done due to the results from the cavity temperature measurements in Section 3.8.2. There it is shown that the cavity temperature is roughly 30% lower if air is surrounding the cavity, compared to vacuum conditions though some loss will also occour at the heat link. The resulting heat transmission coefficient (solid to air) of 5 W m^{-2} K^{-1} is compatible with estimations made according to the literature [94].

An additional parameter is introduced to represent the imperfect position of the heater. The manufacturing process is very challenging, especially the bonding of the heater element to the cavity. The correct position of the heater element cannot be achieved with a higher accuracy than a few tenths of a mm.

The input parameters and the output of the model is listed in Table 3.26.

Simple Model Results

Figure 3.32 shows the resulting temperature distribution. At the left side of the graph is the cavity tip and on the right side is the position of the thermometer. The thermometer grid point is fixed to 20 °C.

It can be seen that in the region of the cavity's tip there is a temperature increase of about 0.01 °C. Considering a difference between cavity tip and heat sink of about 1.6 °C, this is as large as 0.6%. This is valid of course for the very tip only. But it already shows the potential for the non equivalence.

From the amount of heat loss from the cavity to the air the non equivalence effect can be estimated by comparing the case of the open phase to the closed phase. From the

Thickness of the silver cone	0.13	mm
Thermal conductivity silver	430	W m^{-1} K^{-1}
Heat transmission coefficient cone to air	5	W m^{-2} K^{-1}
Total heat input	19.6	mW
Misplaced heater parameter (imperfect cavity)	0.3	mm (along cone)
Heat loss to the air approx	4.97	mW
Non equivalence (perfect cavity) approx	250	ppm
Non equivalence (misplaced heater) approx	950	ppm

Table 3.26: Input coefficients and output of the non equivalence model

model calculations the non equivalence is estimated to be between 200 and 300 ppm for a perfectly placed heater foil.

The evaluation of the influence of the misplacement parameter shows that misplacement of the heater element has a high impact on the non equivalence. In case of a misplacement of the heater element by 0.3 mm (upwards along the cone wall) the non equivalence increases to roughly 1000 ppm. This dependency explains why the actual measurements of the non equivalence are significantly higher than the estimate for the perfect cavity.

Heat transfer by means of radiation is not directly implemented the model. However some estimation is made to justify this simplification. The overall energy exchanged by the outer (gold) side of the cavity is less than a ppm (difference between open and closed shutter phase) and is therefore negligible. Also the absolute radiative loss (radiation exchange between the gold side of the cavity and the environment) that would affect the temperature of the cavity is in the order of 0.06 mW and therefore not crucial.

The radiation losses on the inside of the cavity (black coating) however are considerably higher. If the area of the cavity was a plane radiator against the environment, the heat loss would be in the order off 10 % of the incoming power. Considering the calculated temperature profile in Figure 3.32 the difference in radiative losses between open and closed state would be in the order of 25 ppm of the incoming power. This holds of course for a plane radiator only. The view factors of points inside the cavity towards the environment are reduced due to the cavity's geometry. For every relevant point of the cavity this view factor is well below 0.25. This means that 7 ppm could be set as an upper limit for vacuum non equivalence, assuming the same thermal environment for the open and closed shutter state. For measurements on ground non equivalence in vacuum is therefore neglected. In space the assumption of the same "thermal environment" does not hold, for that reason so called deep space calibrations are carried out to determine the radiative losses of the cavity.

Possible Improvements for the next Generation of Radiometers

For the next generation cavities new heater elements have been designed. These new elements consider the inhomogeneous energy absorption in the cavity (Figure 3.31). This will help to make the temperature distribution in both measurement phases as similar as possible.

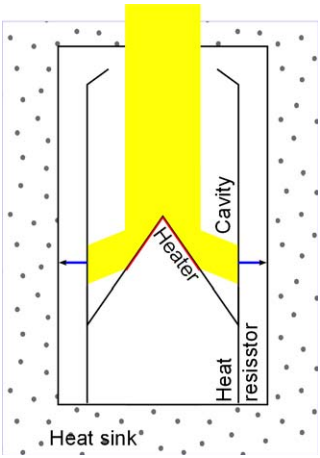

Figure 3.29: Illustration of non equivalence at the PMO6 cavity. The cylindrical part is only heated (optically) in the measurement phase and not by the electrical heater (red). Spurious heat flow (blue) from the cylindrical part is therefore enhanced in the open phase of a measurement cycle.

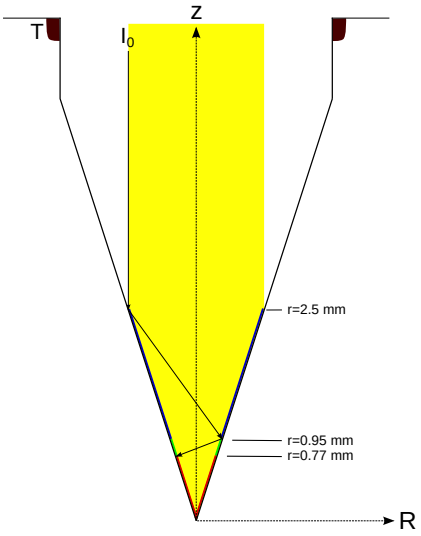

Figure 3.30: Illustration of the reflections inside the cavity. The absorbed optical power density increases with contributions from reflected light. Blue: area with direct illumination only, green: area with direct and 1 indirect illumination, red: area with direct and 2 indirect illuminations.

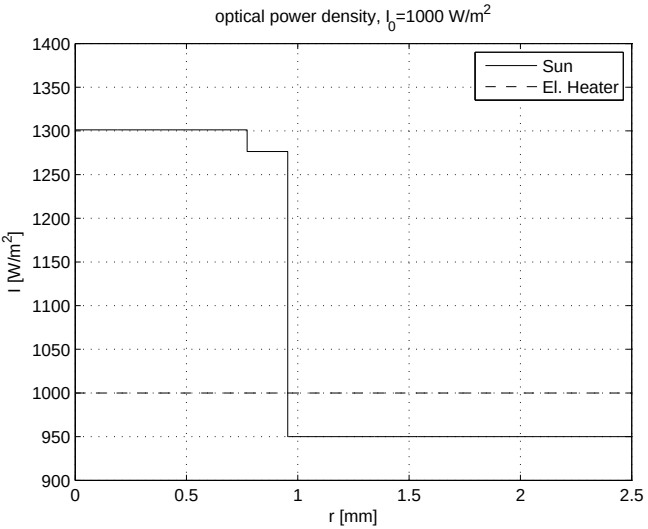

Figure 3.31: Distribution of the absorbed energy in the cavity due to reflected light

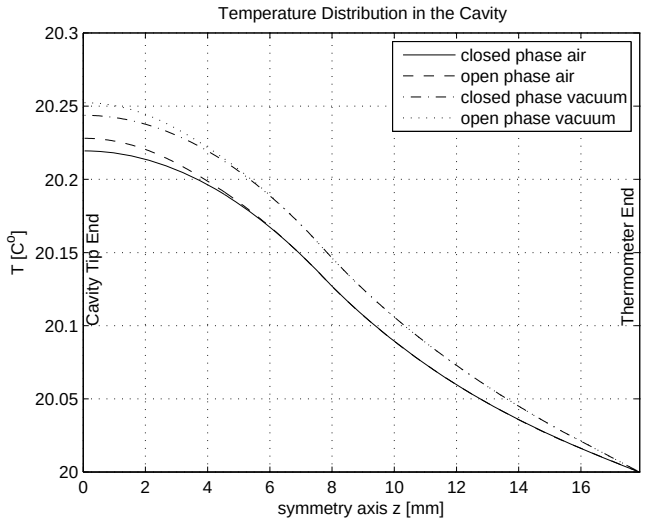

Figure 3.32: Distribution of temperatures in the cavity for the open and closed phase respectively in air and vacuum

3.7.3 Experimental Set-up

To determine the air to vacuum ratio, the DARA instrument is placed in the vacuum chamber that is mounted on to the solar tracker. This vacuum chamber has a window that is placed in front of one of the DARA apertures.The window is inclined by 4 degrees to avoid backscatter from the front plate via the window into the cavity. This has been reported as a problem by Fehlmann [33].

A PMO6 radiometer is mounted next to the vacuum chamber to act as reference instrument. A similar window to the one at the vacuum chamber is mounted onto the PMO6 Radiometer.

The DARA instrument is now operated in vacuum for 1.5 hours, then the vacuum chamber is filled with nitrogen to ambient pressure. The next 1.5 hours the instrument is operated in ambient pressure conditions, afterwards the chamber gets evacuated again. This cycle is then repeated until the end of a measurement day. DARA is operated with a 30s/30s shutter cycle.

The 1.5 hours timespan is selected, so that the instrument can adjust to the conditions for half an hour. After half an hour the instrument is in acceptable thermal equilibrium. Then data can be taken without being influenced by large thermal drifts for approximately on hour.

Losses due to Window Reflections

The window of the vacuum chamber generates losses in the incoming light due to reflections at the window surfaces. These reflections depend on the changes in the refracting index when the beam enters/exits the window material. This means that this loss in intensity when operating in vacuum slightly differs from the case when operating in nitrogen. Therefore an estimation of this effect is made.

Figure 3.33 shows schematically the situation at the window. The incoming light beam I_0 hits the window at the angle φ. The light is refracted and passes the glass at an angle $\varphi\prime$. A part of the light gets reflected back (R1). This refraction/reflection process is polarising both the reflected and the refracted beam. Therefore the two polarisation components need to be treated separately. After passing through the window, the beam is refracted and partly reflected (R2) at the back surface of the window. For the purpose of the experiment it is important to know the difference in R2 relative to the transmitted beam I' .

An estimation based on the Fresnel formulas (including polarisation) is performed. Details can be found in [95] (Chapter 10). The input parameters, intermediate results and the estimation are listed in Table 3.27. A value of 39 ppm is found. Meaning that the reflection at R2 is higher for vacuum. The vacuum measurement is therefore underestimated compared to the measurement at ambient pressure. A correction to the measurements, which lowers the air to vacuum ratio by 39 ppm, and increases the correction factor by the same amount, is applied.

The calculation is mainly sensitive to the refractive index of nitrogen. Therefore this parameter has been varied to study the impact on the result. This serves as an uncertainty estimate for this calculation.

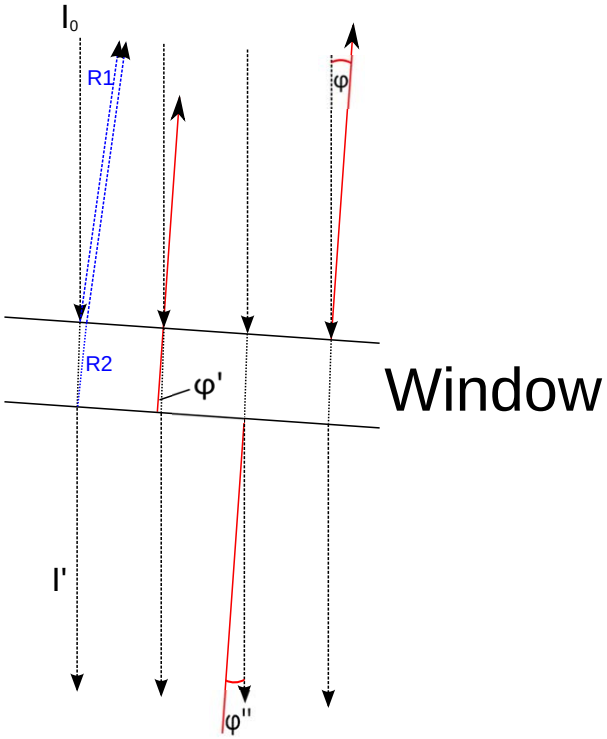

Figure 3.33: Reflections at the vacuum tank window: The blue lines refer to the reflections at the two material transitions. The red reference lines are perpendicular to the glass surface and should help to illustrate the different angles.

Symbol	Value	Remark
φ	4^o	input from geometry
$\varphi\prime$	approx 2.60^o	calculated
$\varphi\prime\prime(N_2)$	approx 4.0000^o	calculated
$\varphi\prime\prime(Vac)$	approx 4.0007^o	calculated
n_{Air}	1.000292	input (Kaye & Laby online [93])
n_{N_2}	1.000298	input (Kaye & Laby online [93])
n_{Quartz}	1.54	input (Kaye & Laby online [93])
R_1	approx 4.5%	
R_2	approx 4.5%	
Difference in R_2 $(Vac - N_2)$ relative to I'	39 ± 5 ppm	

Table 3.27: Numerical values of the window reflection at the vacuum tank.

Dust Accumulation on the Windows

A major problem in the experimental set-up is dust accumulation on the windows. As the whole experiment takes part outdoors, both windows (reference instrument and vacuum chamber) accumulate dust during the day. The dust reduces the transmission of the window. Figure 3.34 shows the ratio of the reference instrument(with window) to an instrument without window. It can be seen that the ratio decreases during the day, meaning that the apparent sensitivity of the instrument decreases. In this case it is almost 1 %.

Another example is shown in Figure 3.35. It illustrates the effect of cleaning the windows. Cleaning of a window can have an effect in the order of a percent as well, this corresponds to the finding of the accumulation of dust.

The accumulation of dust makes it challenging to evaluate the data from the air to vacuum ratio experiment. Depending on environmental conditions like wind or aerosol/pollen load the data is strongly influenced by the dust accumulation on the windows. However when determining the air to vacuum ratio, the dust accumulation on the windows is not thought to have a systematic influence, but introduces a rather high scatter to the data. An example is given in the next section.

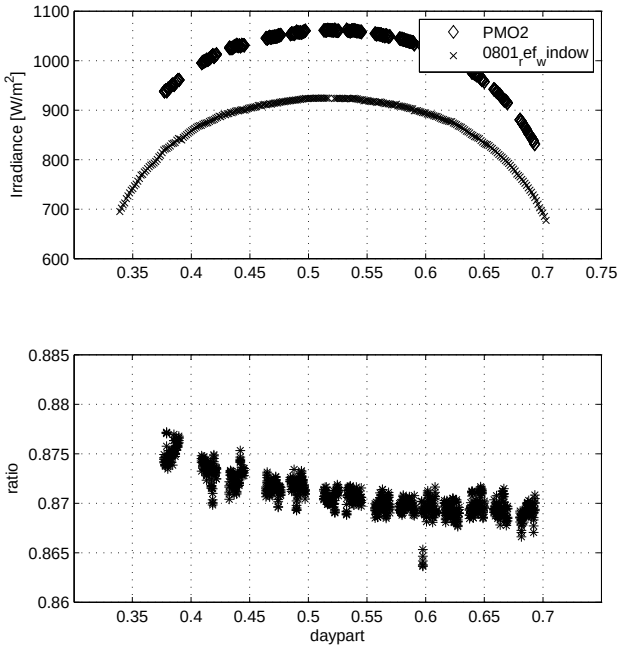

Figure 3.34: Ratio of PMO6-0801 (reference instrument with window) to PMO2 (WSG reference instrument without window)

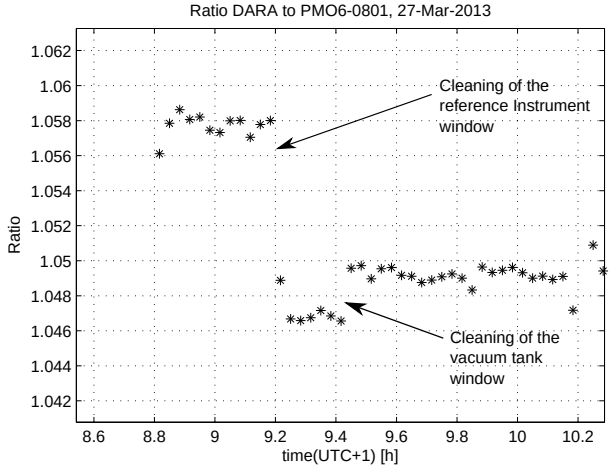

Figure 3.35: Illustration of the cleaning of the windows: Cleaning can be clearly seen in the ratio of DARA to the reference instrument.

3.7.4 Data Evaluation and Correction Factors

Measurements have been performed between August 2012 and September 2013. During this time different adjustments to improve the measurement have been made. However the measurement has been found tricky in the past [33] and it is still challenging. On each measurement day three to seven measurement blocks (vacuum or ambient pressure) have been taken. Each irradiance reading of DARA is divided by the corresponding value of the reference instrument.

The DARA data is corrected for the thermal expansion of the aperture because the DARA is usually at a higher temperature in the vacuum phase, than in the ambient air phase. Thus a systematic offset would be introduced if this was not corrected. However there is no thermal expansion correction for the aperture of the reference instrument. This is because the estimation of the temperature of the reference aperture is very difficult, and no systematic effect on the air to vacuum ratio is expected from the thermal expansion of the reference aperture.

Figure 3.36 shows two series of ratios to the reference instrument for to different days. The top figure containing 5 blocks and the bottom picture containing seven blocks. The air to vacuum difference is fitted for each sequence of vacuum-air-vacuum or air-vacuum-air. Thus for a measurement day with five blocks as shown in Figure 3.36 on top, three estimates of the air to vacuum ratio are determined.

It can be seen that the data quality is very good in the 2012 example (top), whereas in the example at the bottom the corresponding vacuum and ambient pressure data points do not agree well. This is thought to be caused by dust accumulation on the windows.

A linear fit is performed to determine the air to vacuum difference of the ratios to the reference or the actual air to vacuum ratio. As illustrated in Figure 3.36 two straight lines of the same slope are fitted, one line for vacuum and one line for ambient air data. The free parameters are the slope (equal for both lines) and two offset parameters. The difference

between these two offset parameters is the relative difference in sensitivity between air and vacuum operation. To determine the air to vacuum ratio the linear fits are evaluated at the mean value of the time axis and then the value for air is divided by the value for the vacuum.

Figure 3.37 shows all the results from these fits. Each point represents a fit. Figure 3.38 shows the corresponding histograms (in units of relative difference). These figures do not include the correction for the refraction losses at the window. An overview of the measurements is shown in Table 3.28

The resulting correction factors for non-equivalence are listed in Table 3.29. These are calculated from the results of the air to vacuum measurements and the corresponding window loss correction.

3.7.5 Uncertainty Estimation

The uncertainty of the measured air to vacuum ratios are simply determined by taking the standard deviation of the distribution. It can be seen that the measurements for cavity A have a much higher scatter than the measurements for the other cavities. The origin of this fact is not completely understood.

Furthermore the uncertainty of the thermal expansion of the aperture correction needs to be taken into account. It is assumed that the correction of one type of reading (e.g. vacuum) has a 31 ppm uncertainty with respect to the other correction (e.g. ambient).

A partly independent source of uncertainty comes from the fact that the data acquisition circuits is also inside the vacuum chamber. It means that different calibration procedures for the electronics need to be applied (Section 3.2), which introduces a further uncertainty. This calibration uncertainty is accounted for with 20 ppm, it has however only a very small effect on the overall uncertainty.

When operating in vacuum there is no correction applied, however there is a small uncertainty of 4 ppm (1σ). It is taken out of the model results from Section 3.7.2 where an upper boundary for the correction is proposed at 7ppm. The derived uncertainties for the correction factors are listed in Table 3.29.

3.7.6 Results and Discussion

The resulting correction factors for the non equivalence are listed in Table 3.29. It can be seen that the non equivalence is indeed much lower than the PMO6-type radiometers (Table 3.25). This means that one of the main design goals with DARA has been reached. Thus the uncertainties of the non equivalence correction are also significantly lower than for the PMO6. This is not only an advantage for calibrating future DARA type space experiments against the WRR, but also a benefit for future ground based radiometers based on the DARA design.

Comparison with the model calculation shows that the measured values are almost two to five times higher than predicted for an ideal cavity. The model calculation shows also, that very little misplacement of the heater element can easily double the non equivalence. The model would suggest that the heater elements of cavity A and C are placed quite accurately though not perfectly while the heater element of cavity B is misplaced in the order of a few tenth of a mm (shifted upwards along the cone).

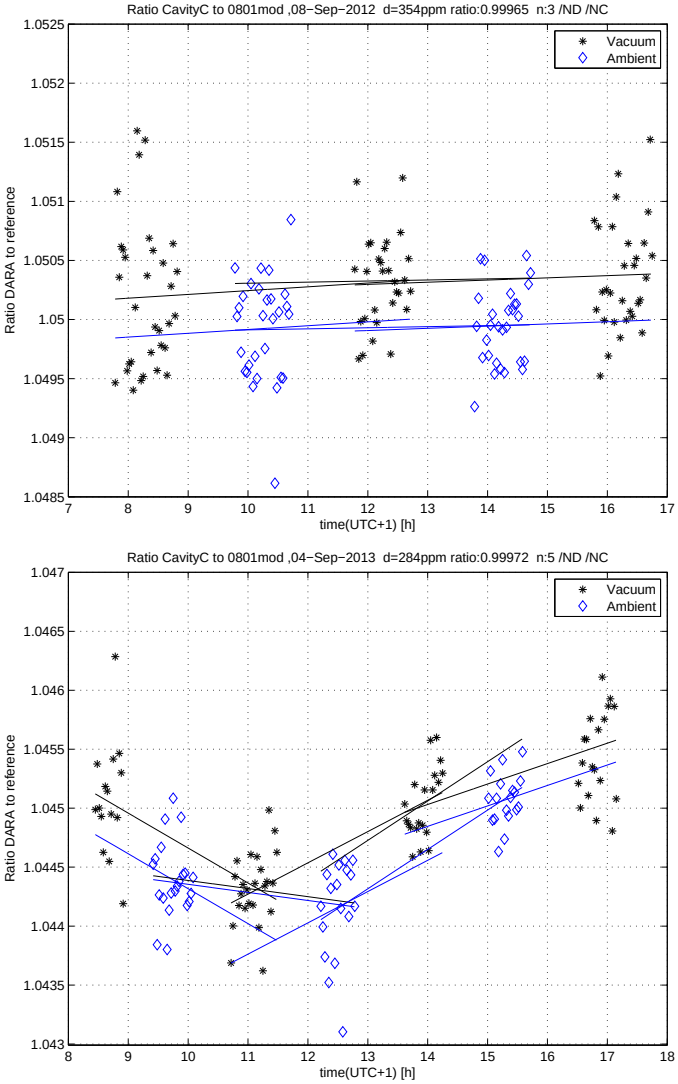

Figure 3.36: Air to vacuum determination for DARA cavity C on September 8th, 2012 (top) and on September 4th, 2013 (bottom). The air to vacuum ratio is determined for each vac/air/vac or air/vac/air set respectively. While the data on top is very nice, the data at the bottom is more difficult to interpret.

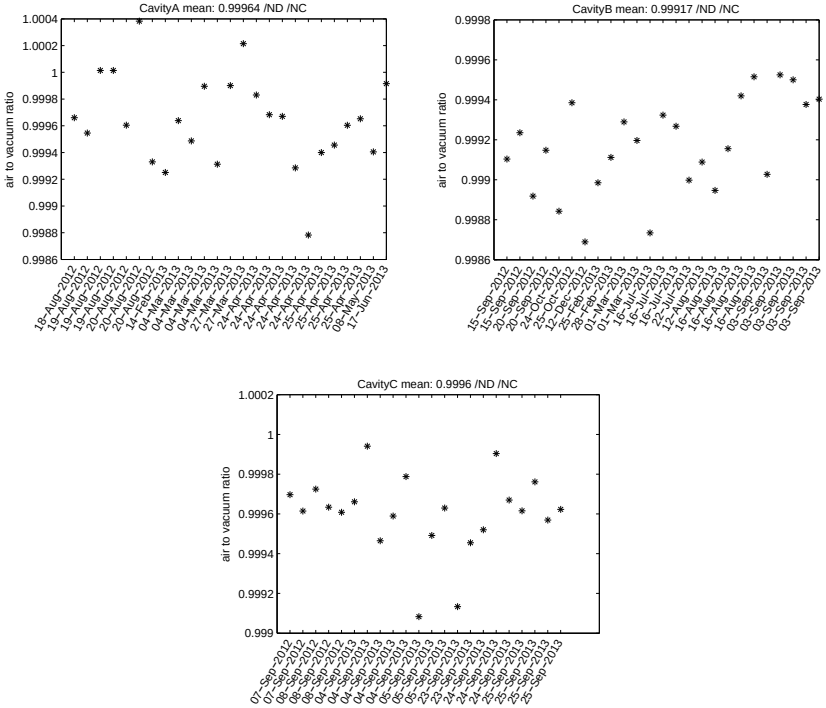

Figure 3.37: Overview of the air to vacuum ratios determined by single sequence fits.

	Cavity A	Cavity B	Cavity C
Number of measurements	27	25	22
Number of measurement days	11	13	7
mean of single measurements	0.999637	0.999167	0.999600
standard deviation of single measurements	0.000342	0.000237	0.000201
mean of daily means	0.999648	0.999099	0.999576
standard deviation of daily means	0.000252	0.000197	0.000161

Table 3.28: air to vacuum ratio, measurement results, (no correction for window losses included)

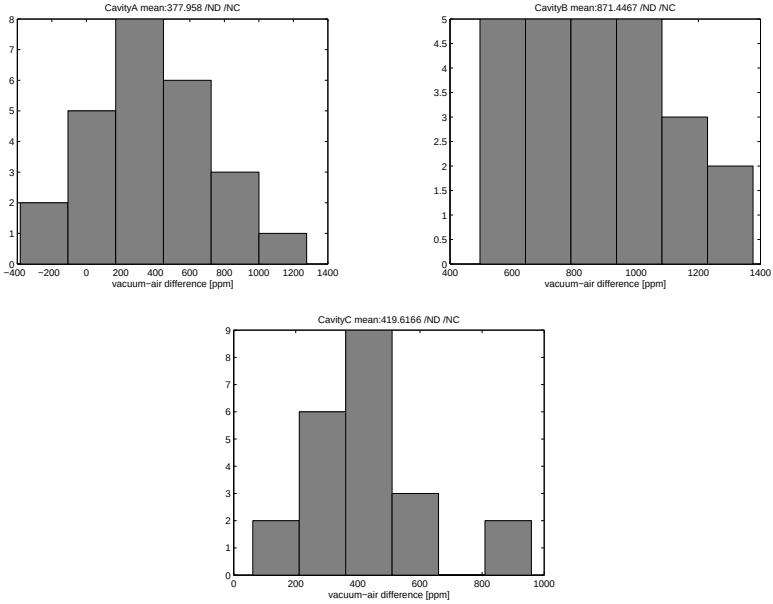

Figure 3.38: Histogram of the air to vacuum ratios determined by looking at single sequence fits.

	Cavity A	Cavity B	Cavity C
Correction Factor (at ambient pressure)	1.00040	1.00087	1.00044
Uncertainty 1σ	0.000084	0.000066	0.000071
Correction Factor (operating in vacuum)	1.000000	1.000000	1.000000
Uncertainty 1σ	$+0.000004$	$+0.000004$	$+0.000004$

Table 3.29: Correction factors for the non-equivalence

3.8 Time Constants and Temperature Difference of the Cavities

Measurements are made to evaluate the time constants of the DARA cavities. From these measurements the temperature difference between heat sink and cavity can also be estimated. A further interesting parameter is the thermal crosstalk, changing temperature at the heat sink and cavities as a response to the applied heater power in any one of the cavities.

Additionally a finite elements simulation is performed. Time constants and temperature difference is then also calculated from the simulation. The simulations are compared to the measurements.

3.8.1 Time Constants

The time constant gives a measure on how fast the cavity will react to changes in the incoming radiation, but also to a changing thermal environment. Due to the digital feed forward controller loop the time constant is less critical for the operation, as the cavity is virtually balanced at all times.

Measurement Set-up

In order to determine the cavities time constants, the instrument head is disconnected from the controller. The connector, feeding the wires from the detector to the controller electronics is connected to the measurement set-up (mobile NI-data acquisition system). The resistance of the cavity thermometer and its coresponding heat sink thermometer are read in 2-wire Ω mode. Measurements are taken every second. An electrical power is applied to the cavity heater (approx 18 mW). The power is switched on and off periodically.

Data Evaluation

The electrical resistance of the thermometer as a function of temperature is given in Equation 3.31, where α_R is the coefficient of the temperature dependency. At room temperature this relation is linear.

$$R = R_{T_0} \cdot (1 + (T - T_0) \cdot \alpha_R) \tag{3.31}$$

This can be solved for the temperature T:

$$T = T_0 + \left(\frac{R}{R_0} - 1 \right) \frac{1}{\alpha_R} \tag{3.32}$$

It follows for ΔT, the difference between the two thermometers:

$$\Delta T = T_{Cav} - T_{Sink} = \left(\frac{R_{Cav}}{R_{0_{Cav}}} - \frac{R_{Sink}}{R_{0_{Sink}}} \right) \alpha_R \tag{3.33}$$

Once $R_{0_{Cav}}$ and $R_{0_{Sink}}$ have been determined ΔT can be derived easily by measuring R_{Cav} and R_{Sink}. In order to measure the resistance temperatures at the reference temperatures, the instrument head is kept at a constant temperature with no heating applied. Then, heater power is switched on, and from the two measured resistances the temperature difference is derived.

In order to measure the time constants, heater power is applied periodically and an exponential[8] is fitted to every resulting ΔT slope. Results of the fit are listed in Table 3.30. For comparison the approximate value for the PMO6-PREMOS instrument is also listed[9].

[8] For the response of ΔT to the step function in heater power an exponential function is considered. Although this is just an approximation in order to estimate a time constant.

[9] Personal communication with André Fehlmann (PMOD/University of Hawaii)

	Cavity A	Cavity B	Cavity C	Uncertainty (2σ)	PMO6-PREMOS
Air	14.2 s	14.3 s	14.5 s	0.2 s	7.4 s
Vacuum	20.3 s	20.3 s	20.7 s	0.2 s	9.2 s
Ratio	0.7	0.7	0.7		0.8

Table 3.30: Time constants of the DARA cavities and PMO6 cavities

The uncertainty of the time constant calculation is estimated to be 0.1 s (1σ) due to the uncertainty of the resistance measurement. The impact of these uncertainties on the time constant is estimated by introducing offsets to the raw data and then performing a fit for the time constant. The value of the time constant proves to be very stable against measurement offsets. The corresponding statistical standard deviation between the individual measurements taken is of the same order.

3.8.2 Temperature Change and Coupling

The absolute temperature difference between cavity and heat sink is measured by a similar experiment as the time constants. Electrical power of 20 mW with a period of 360 s and a duty cycle of 0.5 is applied. From the measured resistance values the corresponding ΔT values are derived, in a similar way as in the previous section. The upper plot in Figure 3.39 shows a temperature difference at the heated cavity of 1 K at a heater power of 20 mW in vacuum. The heat sink and the temperature of an additional cavity are plotted below. It can be seen nicely how the heat is transferred to the heat sink and to the additional cavities. These temperatures vary around 15 mK. In this configuration the heat sink temperature leads the cavity temperature by roughly 40 s. This effect however should not influence irradiance measurements, as long as all cavities are hold in equilibrium.

The numerical results from this experiment are listed in Table 3.31.

3.8.3 Finite Element Simulation

The results from the finite elements (FE) simulation will give an idea on the value and accuracy of such a tool, for future design changes. The finite element simulation is done with the ANSYS® software [10]. The geometry is imported directly from the construction files and then simplified. Air is simulated as a solid body with the appropriate thermal properties of air. This is assuming that convection is not relevant.

Material Properties

The used values for the material properties are listed in Table 3.32, these are mostly ANSYS® default values. The crucial value is the thermal conductivity of the aluminium alloy that is not specified with high accuracy in the literature. Manufacturers specify this property to less then 10 % accuracy. Therefore this parameter has been adjusted (within boundries) to fit the measured values.

Results and Comparison between Measurements and Simulation

Both, time constants and temperature profile are good quantities for comparison. However, only a comparison that includes both parameters in the vacuum and air case can validate

[10] ANSYS® is a finite elements simulation software by ANSYS, Inc. Canonsburg PA, USA, http://www.ansys.com

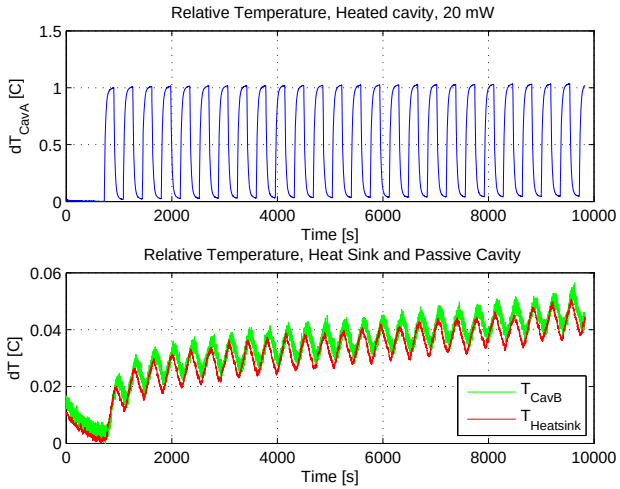

Figure 3.39: Temperature difference in vacuum (20 mW heater power applied)

	Cavity A	Cavity B	Cavity C	PMO6 *
Temperature difference air	0.7 K	0.7 K	0.7 K	0.5 K
Temperature difference vacuum	1 K	1 K	1K	

Table 3.31: Temperature difference between the heat sink and the cavities at 20 mW electrical power (* The PMO6 value has been derived by André Fehlmann with PMO6-PREMOS, personal communication)

results from the simulation. This is because the thermal conductivity of aluminium is adjusted to the optimum value. Table 3.33 shows the results of the simulation.

3.8.4 Discussion

DARA has higher time constants than PMO6 type radiometer. This means that the response of the radiometer to changes in irradiance is somewhat slower. While the analogue controller loop of a PMO6 radiometer needs to readjust after every shutter cycle a fast cavity is crucial to have a fast radiometer. With DARA's digital feed forward controller however the cavity is always in a balanced state and only needs to adjust to changes in irradiance. Therefore a slower time constant is not a disadvantage.

The temperature difference between cavity and heat sink is slightly higher than with PMO6 type radiometers. High temperature differences could be a problem if convection would be induced in the surrounding air. The results of the air to vacuum ratio determination (Section 3.7) however do not show any sign of high interaction with the surrounding air.

The absolute values of time constant measurements and simulation do agree to within

Material	Heat capacity	Thermal conductivity	Density
Air	1.005 J kg^{-1} K^{-1}	0.257 W m^{-1} K^{-1}	1.2 kg m^{-3}
Silver	235 J kg^{-1} K^{-1}	430 W m^{-1} K^{-1}	10490 kg m^{-3}
Aluminium AW6082	900 J kg^{-1} K^{-1}	160 W m^{-1} K^{-1}	2700 kg m^{-3}
Copper	385 J kg^{-1} K^{-1}	401 W m^{-1} K^{-1}	8300 kg m^{-3}

Table 3.32: Material properties at 20 °C

	Air	Vacuum
Temperature difference at 20 mW heater power	0.7 K	1 K
Time constant	13 s	18 s

Table 3.33: Results from simulation

approx. 10%. A weakness of the FE-simulation is the material junctions, as thermal behaviour is difficult to describe at these regions. To increase the value of the simulated time constant one would need to either lower the thermal conductivity of the aluminium alloy or enhance the thermal resistance of the bond between the silver cone and the heat resistor. However, both operations would rise the temperature at the cone. Nevertheless in order to get a first impression on implications of future small design changes (e.g. CLARA) it can still be a valuable tool.

3.9 Balance of the Thermometers and Readjustment Thereof

The operational principle of the DARA, that is illustrated in Figure 2.1, is based on a equal heat flow from the reference cavity to the heat sink and from the active cavity to the heat sink respectively. In order to control the heat flow of the active cavities it is important that the thermometer resistances of the measurement bridge (Figure 2.7) have an equal ratio. Otherwise these heat flows will not be equal, and the cavities are thermally not optimally balanced, which can affect the measurement result.

Dark measurements have therefore been carried out to investigate the influence of temperature changes on the DARA measurement results. It has been found that the thermal balance between the cavities is unsatisfactory. This is due to the thermometer wires whose resistance values are not ideally adjusted with respect to the other cavity thermometers.

This section describes how to readjust the thermal sensors, using dark measurement data to calculate the necessary corrections.

3.9.1 Dark Measurements

Figures 3.40 and 3.41 show the data of the dark measurements. The temperature of the heat sink (top) is varied over time, so that also the derivative of the temperature (middle) gets a distinct shape. The heater power that is applied to the cavities is shown in the bottom figures. It can be seen that the shape of the heater power of the active cavities is similar to the derivative of the temperature. Furthermore there is a difference of roughly 7 mW between the power level of cavity A and the power level of cavity C. Table 3.34 gives the approximate power level for the three cavities and the three measurements, at dT/dt=0. Figure 3.41 shows the strong correlation between the temperature change in the heat sink (dT/dt) and the heater power in the active cavities .

3.9.2 Preparation and Calculation

Using the power data from the dark measurements, the necessary data to improve the balancing of the cavities can be derived.

The bridge circuit that generates the error signal consists of two thermally sensitive resistors, for each cavity. One resistor (R_C) is attached to the cavity, whereas the second one is attached to the heat sink (R_H). The resistance depends linearly on temperature:

$$R_C(T) = R_{C0} + R_{C0} \cdot \Delta T \alpha_R \tag{3.34}$$

where R_{C0} is the resistance of R_C at the heat sink temperature, and:

$$\Delta T = P \cdot R_{Thermal} \tag{3.35}$$

thus $\Delta T \alpha_R$ can be substituted by the heater power (P) and the thermal impedance of the heat link ($R_{Thermal}$) between cavity and heat sink.

$$R_C(T) = R_{C0} + R_{C0} \cdot Pk \tag{3.36}$$

with

$$k = R_{Thermal} \cdot \alpha_R \tag{3.37}$$

For the equilibrium condition (bridge signal, see Figure 2.7) of two cavities (e.g. A and B) it can be written:

$$\frac{R_{CA}}{R_{HA}} = \frac{R_{CB}}{R_{HB}} \Leftrightarrow \frac{R_{C_0A}(1+P_Ak)}{R_{HA}} = \frac{R_{C_0B}(1+P_Bk)}{R_{HB}} \Leftrightarrow \frac{R_{C_0A}R_{HB}}{R_{HA}R_{C_0B}} = \frac{1+P_Bk}{1+P_Ak} \tag{3.38}$$

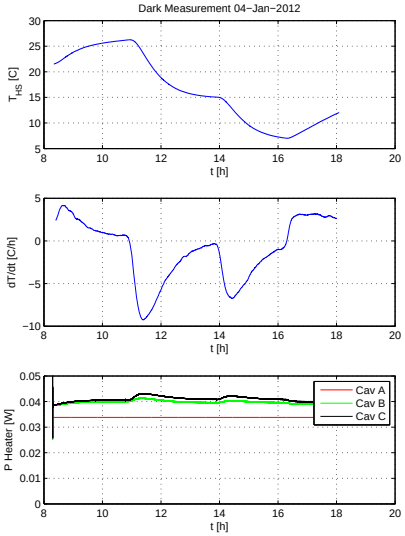

(a)

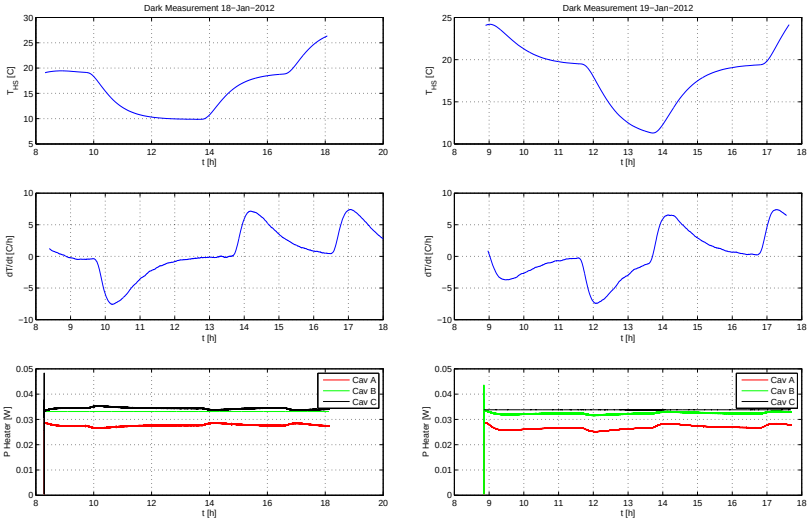

(b) (c)

Figure 3.40: Dark measurement, temperature and power, (a) Reference A, (b) Reference B, (c) Reference C

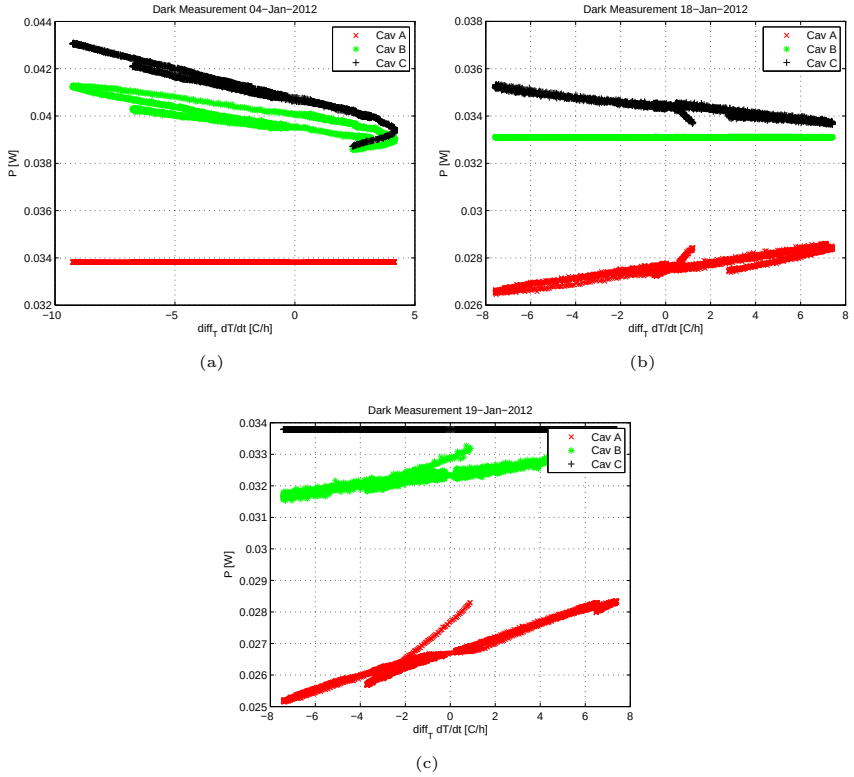

Figure 3.41: Heater power vs. temperature change, (a) Reference A, (b) Reference B, (c) Reference C

	Cavity A	Cavity B	Cavity C
Measurement Ref A	0.0339 W	0.0398 W	0.0408 W
Measurement Ref B	0.0277 W	0.0322 W	0.0344 W
Measurement Ref C	0.0267 W	0.0323 W	0.0338 W

Table 3.34: Power levels in W (at $dT/dt = 0$)

	A:B	A:C	B:C
Measurement Ref A	1.00082	1.00096	1.00014
Measurement Ref B	1.00077	1.00093	1.00017
Measurement Ref C	1.00078	1.00099	1.00021
Mean	1.00079	1.00096	1.00017

Table 3.35: Asymmetry factors

ΔR_{A_B}	ΔR_{B_A}	ΔR_{A_C}	ΔR_{C_A}	ΔR_{B_C}	ΔR_{C_B}
-0.072 Ω	+0.072 Ω	-0.087 Ω	+0.087 Ω	-0.016 Ω	+0.016 Ω

Table 3.36: Correction values for the thermometer wires $\Delta R = R - R^{new}$

B	C
8.5 mm	C 10 mm

Table 3.37: Length of the added cooper wires (R=7.23 Ω/m)

P_B and P_A are directly measured in the dark measurements, k has to be estimated from other measurements. It is known from time constant measurements (Section 3.8) that ΔT is 0.7 °C at 20 mW heater power (ambient pressure), this leads to $R_{Thermal}$=35 K W^{-1}. α_R (copper) is 0.0039 K^{-1} [66]. This leads to k=0.14 W^{-1}

The last expression in Equation 3.38 is now defined as the asymmetry factor:

$$asym_{AB} = \frac{1 + P_B k}{1 + P_A k} \tag{3.39}$$

It describes the imbalance of the branches of the bridge. In the ideally adjusted position (equal heater power in both cavities) the asymmetry factor is equal to one. That means, in the example above, the resistance R_{CA} needs to be corrected so that the asymmetry factor becomes unity:

$$R^{new}_{C_0 A_B} = \frac{R_{C_0 A_B}}{asym_{AB}} \tag{3.40}$$

The determined asymmetry factors are listed in Table 3.35. The nominal resistance of the thermometer wires is 91 Ω. Accordingly the necessary corrections of the thermometers can easily be derived. The correction needed to balance one cavity with another cavity are listed in Table 3.36.

3.9.3 Implementation

According to the calculation the cavity set up has been readjusted. The resistance of the cavity thermometers have been increased for cavity B and C. An additional short cooper wire (R=7.23 Ω/m) has been added to the thermometer wires, the lengths of these wires are shown in Table 3.37.

3.9.4 New Balance Results

Figure 3.42 shows the heater power versus the temperature change for dark measurements after the adjustment of the thermometers, from a similar measurement as performed for the

data in Figure 3.41. The balance between the cavities has improved a lot. The absolute difference has been reduced from roughly 7 mW down to 1 mW. The steep feature in Figures 3.42(b) and (c) are caused by the data of the first hour. It is highly probable that is caused by a drift in the reference cavity during warm up. The reference cavity signal can not be corrected for thermal effects, as the data acquisition is not calibrated at the voltage level of the reference cavity.

3.9.5 Impact of the Cavity Drifts on the Measurement Result

When evaluating radiometer data, it is necessary to interpolate the measurement points of the closed phase over time to the measurement points of the open phase (see also Section 2.8 and Figure 2.9). As long as the drift of the heater power signal is linear the result is not affected by the drift. However the the signal is not necessarily drifting linearly. Figure 3.44 illustrates the interpolation error that is originating from a non linear drift in closed shutter phase heater power. ΔP is underestimated in the illustrated case.

The dark measurement data (after the improvement of the balance) is used to estimated the influence of such drifts on ΔP. Therefore ΔP values are calculated according to the following formula:

$$\Delta P = \left[\frac{P\left(t + \frac{\Delta t}{2}\right) + P\left(t - \frac{\Delta t}{2}\right)}{2} \right] - P(t) \tag{3.41}$$

As this data is "dark" data, the shutter is always closed, and the ΔP is then directly the difference between the interpolated P_{closed} and the true P_{closed}. If there is no non linear drift, there is no interpolation error and ΔP will be zero.

Figure 3.43 shows the result for these calculations. It is shown only for cavity A, as cavity A shows the highest drifts and is therefore expected to have the highest interpolation error. The interpolation has been performed for a hypothetical cycle of 30 s (15/15), 60 s (30/30) and 180 s (90/90), in order to estimate the influence of the shutter cycle length. Comparing the two figures it can be seen that in the 30 s case the sharp temperature change at 14 h has small impact on the interpolation, whereas in the case of the 180s cycle, the interpolation is heavily affected at this points. Note that the scale is different by one order of magnitude. If evaluating this particular scenario for a solar power of 20 mW, it is found that the error on the measurement is in the order of 8 ppm for a 30s, 25 ppm for a 60s and 200 ppm for a 180 s cycle.

While this large abrupt thermal drifts have been artificially introduced for the measurement, in real measurements the thermal drifts will seldom reach this intensity and can really be seen as an upper limit. But it still illustrates well the advantage of fast shutter cycles. These are therefore really necessary to avoid errors due to the closed power interpolation. For long shutter cycles (e.g. 180 s) an uncertainty covering this effect needs to be taken into account.

3.9.6 Discussion

The balance of the cavities has been improved significantly. Furthermore the importance of short shutter cycles has been showed. If high thermal instabilities are present an interpolation error is introduced, that can be significant if the shutter cycle becomes too long. No uncertainty component is introduced due to this effect, as DARA measurement cycles are kept short (30 s normal, 60 s maximal).

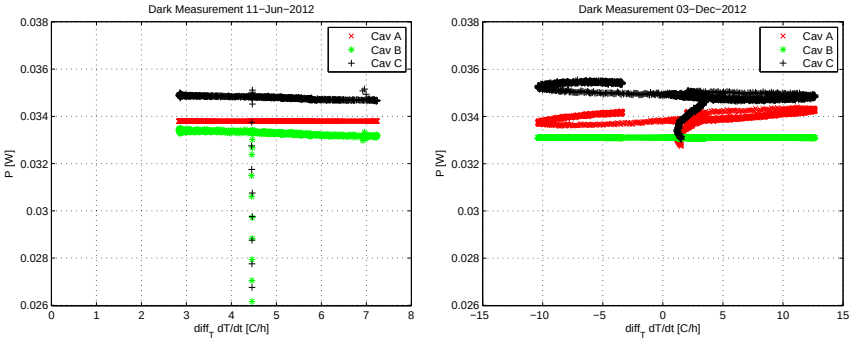

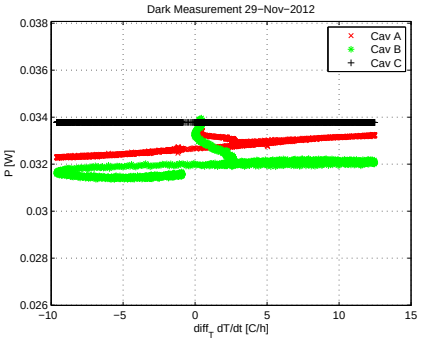

Figure 3.42: Heater power vs. temperature change after improvement, (a) Reference A, (b) Reference B, (a) Reference C

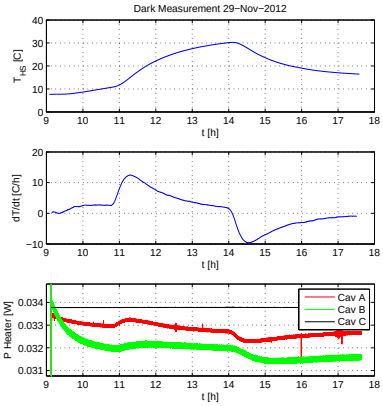

(a)

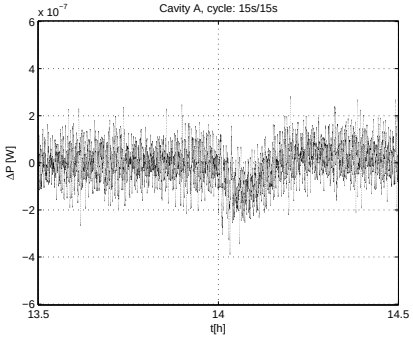

(b)

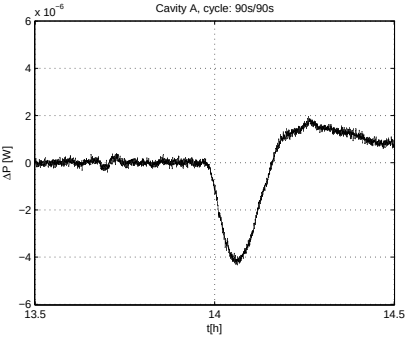

(c)

Figure 3.43: Interpolation Error: Figure (a) gives an overview of the raw data. The figures (b) and (c) show the interpolation error around t=14 where a sudden temperature change occurs. (b): 30s, (c): 180s

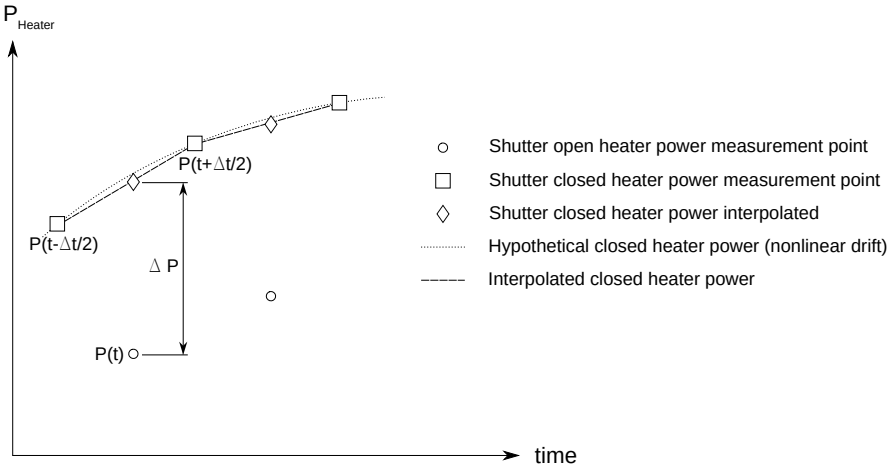

Figure 3.44: Illustration of the interpolation error: The interpolated point (diamond) does not represent the "hypothetical true value" dashed line very well. Thus ΔP is biased.

3.10 Summary of the Characterisation and Correction Factors

Table 3.38 summarises all the correction factors resulting from the characterisation of DARA. The factors are given for two conditions, namely for solar irradiance measurements at ambient pressure, and for a wavelength of 532 nm in vacuum (e.g. TRF).

The uncertainties of the characterisation, that is also the uncertainty of the DARA native scale is given in Table 3.39. Additionally to the uncertainty of the correction factors, the uncertainties of the electrical calibration and the aperture size are included also.

	Ambient/Solar (Davos)			**TRF Irradiance**		
	Cavity A	Cavity B	Cavity C	Cavity A	Cavity B	Cavity C
Absorptivity	1.00103	1.00094	1.00100	1.00094	1.00096	1.00097
Lead heating	1.00050	1.00064	1.00052	1.00050	1.00064	1.00052
Diffraction	1.00122	1.00122	1.00122	1.000724	1.000724	1.000724
Non equivalence	1.00040	1.00087	1.00044	1	1	1
Total Correction[11]	1.003153	1.003675	1.003184	1.002166	1.002326	1.002216

Table 3.38: Summary of the characterisation corrections for measurements of solar irradiance in Davos and at the TRF

	Ambient/Solar (Davos)			**TRF Irradiance**		
	Cavity A	Cavity B	Cavity C	Cavity A	Cavity B	Cavity C
Aperture area[12]	0.000042	0.000049	0.000040	0.000042	0.000049	0.000040
Electronics	0.000070	0.000070	0.000070	0.000070	0.000070	0.000070
Absorptivity	0.00016	0.00016	0.00016	0.00012	0.00012	0.00012
Lead heating	0.000025	0.000025	0.000025	0.000025	0.000025	0.000025
Diffraction	0.000043	0.000043	0.000043	0.000024	0.000024	0.000024
Non equivalence	0.000085	0.000066	0.000070	0.000004	0.000004	0.000004
Combined uncertainty	0.000205	0.000199	0.000199	0.000149	0.000151	0.000147

Table 3.39: Uncertainty budget (1σ, relative) of the characterisation, for measurements of solar irradiance in Davos and at the TRF

3.10.1 Discussion of the Uncertainty Budget

The relative uncertainties determined for measurements of solar irradiance at ambient pressure are in the order of 200 ppm at (1σ). The main contribution comes clearly from the absorptivity. A second large contributor is the data acquisition electronics. Especially the uncertainty of the electronics could be further reduced by a better traceability to of calibration equipment and the usage of more advanced components.

Compared to Brusa & Fröhlich [59] results who found an uncertainty of 560 ppm (1σ) for the PMO6 characterisation, the DARA characterisation could reduce the uncertainties by more than a factor of 2. The main improvements are more reliable air to vacuum ratio measurements, a higher confidence in diffraction correction, and more accurate aperture area measurements. The uncertainty on the absorptivity however is larger, mainly due to the fact that also the corresponding correction itself is three times larger.

[11] Does not include the temperature dependent correction for the thermal expansion of the aperture of 12 ppm per ^{o}C

[12] Including thermal expansion of the aperture

The characterisation of the PMO6-PREMOS instruments claims an uncertainty of 132 ppm at (1σ), however it does not include any calibration uncertainties of the data acquisition chain. Also the absorptivity/reflectivity of PMO6-PREMOS has not been measured, but rather taken from previous measurements of PMO6 radiometers. Therefore it is not straightforward to compare these two characterisations. On a component level the uncertainties for the DARA characterisation are comparable to or better than PREMOS, except for the absorptivity where it is not possible to compare.

The TIM characterisation by Kopp et al. [58] has an overall uncertainty of 200 ppm (1σ) which is comparable to the DARA characterisation.

Solar Irradiance Measurements in Space

If the DARA instrument would be measuring solar irradiance from a satellite platform, the uncertainty budget would include the absorptivity and diffraction correction for the full spectrum, but only the small uncertainty of vacuum non-equivalence. The uncertainty for such measurements would be about 180 ppm (1σ). However in case of a real application on a satellite platform there will be additional uncertainties that will increase the overall uncertainty by a certain amount. Reasons for this could be the thermal environment, pointing issues etc.

Chapter 4

Calibrations of the DARA Instrument and its Implications

4.1 Introduction

DARA is calibrated against the two reference standards that are described in Section 1.3.6, in order to implement these standards as scales in the DARA radiometer. These are the WRR standard and the SI cryogenic laboratory standard for irradiance. Results are compared to the DARA native scale as well as the WRR and SI cryogenic laboratory scales to each other.

To ensure the stability of the WSG several comparisons between the WRR standard and the SI cryogenic laboratory standard have been made in the past, using PMO6 solar radiometers as transfer instruments. The results of these comparisons are listed in detail in Section 4.4.1. While the first three comparisons (1991, 1995, 2005) showed good agreement between the scales, the fourth comparison (2010) found the WRR scale to read 0.34% higher than the SI scale. Another hint that there might be a difference between WRR traceable scales and SI (base units) traceable scales comes from the fact that space borne absolute radiometers tracable to the WRR showed a significant difference of 0.33% to the newer TIM/SORCE instrument that is tracable to the SI base units [41] (see also Section 1.4.3).

At the very beginning of it's commissioning phase, DARA had been participating in the International Pyrheliometer Comparison (IPC-XI) in 2010 [96]. However the results from IPC-XI could not be evaluated with high accuracy due to problems with the data acquisition. Therefore DARA was calibrated against the WSG a second time in early 2012 (next Section).

4.2 WRR Calibration

4.2.1 Measurement Set-up at PMOD/WRC

The DARA instrument has been compared against the World Standard Group (WSG) at PMOD. The WSG is representing the WRR standard for solar irradiance measurements. These measurements have been done in February 2012. The reference instrument (PMO2) and the DARA instrument measured the solar irradiance side by side at PMOD.

Four data runs, each a full day were performed. On 21 February and 24 February cavities A and B were operated actively, on 22 February and on 27 February cavities

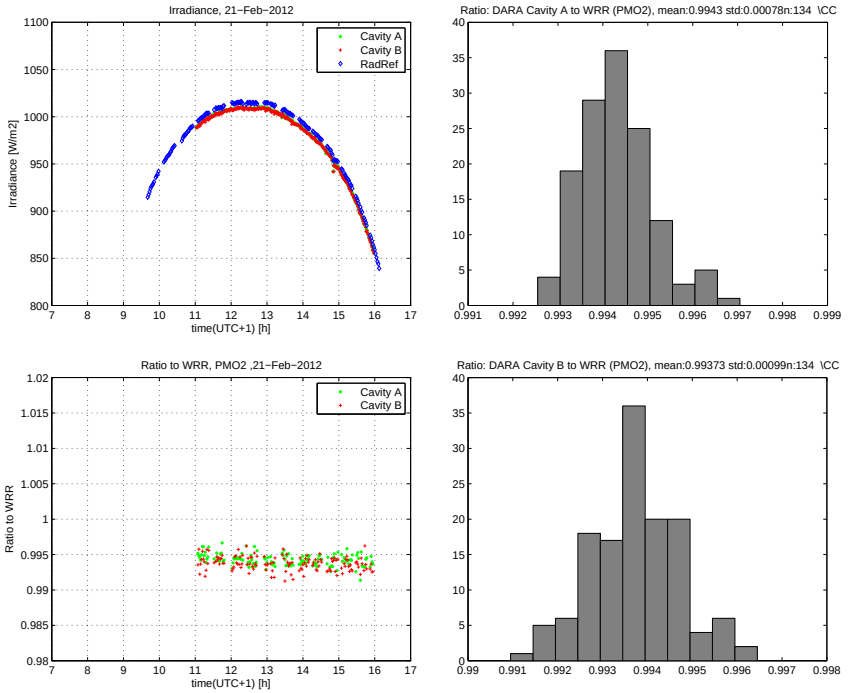

Figure 4.1: Calibration raw data 21 February 2014: Irradiance (top left) , ratio (DARA to WRR) (bottom left) and the corresponding histograms (right).

A and C were active. This yields four days of data for cavity A and two for B and C respectively.

4.2.2 Data Evaluation and Results from the WRR Comparison

Figure 4.1 shows the irradiance data and the corresponding ratios DARA to WRR (PMO2) for 21 February. A circumsolar correction has been applied to these data (as described described by Fehlmann [33]). No air to vacuum or diffraction correction has been applied to these data yet. Table 4.1 list the ratio to WRR for each measurement day.

Thermal Expansion of the Apertures

DARA measurements are corrected for the thermal expansion of the aperture. In case of the comparison with a reference instrument (in this case the PMO2) of the WSG, the data of the reference instrument also needs a correction. The aperture of the PMO2 is made of copper and has therefore a higher thermal expansion than the DARA aperture. A thermal expansion coefficient of $16.8 \cdot 10^{-6}$ K^{-1} [66] is used for the correction of the copper aperture.

The exact temperature of the aperture is not known, therefore the temperature of the nearby meteorological station is used. The most recent WRR-factor of the PMO2 radiometer was determined at the IPC-XI in 2010 at a mean temperature of 12 °C [96]. This temperature has been used as reference temperature. Table 4.1 lists the temperature (meteo station) and the resulting correction factor for the PMO2.

4.2.3 Uncertainties

The main uncertainty of the calibration is associated with the WSG reference instrument. Aspects like how an accurate representation is the reference radiometer for the WRR, the uncertainty of the WSG data acquisition, thermal expansion of the aperture etc. The corresponding standard uncertainty value is given by the WRC calibration procedures (GUM type B), it is listed in Table 4.1.

The statistical uncertainty (type A) of the ratio is also listed in Table 4.1, it is found very small against the calibration uncertainty.

For the corrected ratio in Table 4.2 (full DARA characterisation applied), the uncertainty also includes the uncertainty of the characterisation (native sacle). The uncertainty of the mean value is only slightly smaller than the uncertainties for the individual cavities. This is because most of the uncertainty originates from the WRR calibration itself, it is assumed that the calibration "error" is systematic for all three cavities. Half of the characterisation uncertainty can also be considered systematic, meaning that a possible "error" is the same for every cavity (e.g. diffraction). The independent individual uncertainty of the characterisation is estimated to be around 140 ppm which is also the order of the standard deviation of the three measurements.

Uncertainty of the WRR Scale

The WRR scale that is now implemented in the DARA can not only be compared to the DARA native scale, but also used for measurements. In that case the uncertainty of the DARA native scale does not need to be added, but some reduced uncertainties due to changes of the environmental conditions, or ageing of components need to be taken into account. Taking 31 ppm for aperture expansion, 53 ppm for the data acquisition and 20 ppm for the diffraction correction, as well as the WRR calibration uncertainty into account, a relative uncertainty of 366 ppm (1σ) is estimated for a ground based measurement at the WRR scale. For an extraterrestrial measurement, also the uncertainty of the air to vacuum ratio needs to be taken into account, which would add up to 372 ppm (1σ).

4.2.4 Corrected Results

Table 4.2 shows corrected (full DARA characterisation applied) ratios of the the DARA measurements with respect to WRR. This ratio links the WRR standard to the SI base units via the DARA characterisation. The uncertainty includes the calibration uncertainties, and the uncertainty of the DARA native scale.

The ratio can also be interpreted as the ratio between DARA's native scale and DARA's WRR scale. It means that DARA reads roughly 0.3% higher when usig the WRR scale instead of the native scale.

	n_{meas}	T_{mean}	Cavity A	Cavity B	Cavity C	PMO2 corr.
21 February	134	0.1 °C	0.99431	0.99373		1.00040
22 February	133	3.4 °C	0.99431		0.99406	1.00028
24 February	132	7.4 °C	0.99390	0.99315		1.00015
27 February	95	-1.5 °C	0.99436		0.99426	1.00045
Weighted mean			0.99390	0.99317	0.99381	corrected
Stat uncertainty(1σ)			0.00004	0.00006	0.00006	
Calib uncertainty (1σ)			0.00035	0.00035	0.00035	
Comb. uncertainty (1σ)			0.00035	0.00036	0.00036	

Table 4.1: Overview of the data from the WRR calibration: The ratios DARA to WRR for all three cavities, the number of measurements, the mean temperature of the measurement timespan, and the aperture area correction for PMO2, based on the mean temperature. (The shown data is evaluated using the basic radiometric constant $\widetilde{C}$, with only circumsolar and aperture expansion correction applied)

	Cavity A	Cavity B	Cavity C	mean
Ratio DARA to WRR	0.99703	0.99682	0.99696	0.99694
Uncertainty (1σ)	0.0004	0.0004	0.0004	0.00039
Characterisation factor used (DARA)	1.00315	1.00368	1.00318	

Table 4.2: Ratio DARA to WRR, corrected using the DARA characterisation values

4.3 TRF Calibration

The DARA instrument has been calibrated against a cryogenic radiometer at the Total solar irradiance Radiometer Facility (TRF). The TRF cryogenic radiometer is representing the SI cryogenic laboratory scale. It is located at the Laboratory for Atmospheric and Space Physics (LASP) at the University of Colorado in Boulder, USA. The facility has been built for indoor irradiance calibrations of solar radiometers with a high accuracy [31]. Previously the PMO6-PREMOS flight unit and the PMO6-VIRGO flight spare radiometers have been calibrated at the TRF. This is described in detail by Fehlmann [33]. The DARA calibration runs took place between 29 September and 5 October 2011. Figure 4.2 shows the instrument inside the TRF Vacuum chamber.

During this campaign there were several technical problems appearing. These problems did not severely impact the results of the comparison, but some notes can be found in Appendix B.

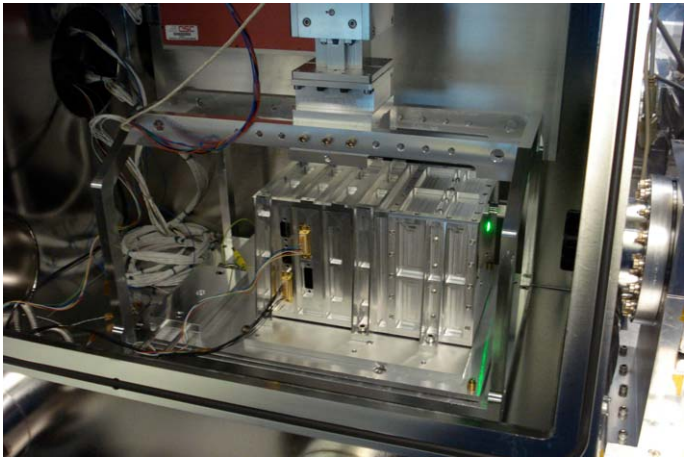

Figure 4.2: DARA package in the TRF vacuum chamber

4.3.1 Measurements

Calibration Measurements have been performed in power and irradiance mode. Power mode means the diameter of the light beam that is measured with the radiometer is smaller than the precision aperture. Whereas in irradiance mode the measured quantity is a homogeneous radiation field that overfills the instruments precision aperture.

Ideally an irradiance mode calibration is considering all components of the instrument and calibrates the instrument directly for its purpose to measure solar irradiance. A power calibration on the other hand neglects the influence of the aperture size, stray light and diffraction. Also if the absorption characteristics of the cavity is not homogeneous, a power calibration depends on the light distribution inside the cavity. Nevertheless a power calibration can be a valuable diagnostics tool.

Beam Pattern Three different beam patterns have been used to perform the calibration runs:

- 1.5 mm circular pattern (power mode)

- 2.5 mm annular Pattern (power mode)
- 7.3 mm circular Pattern (irradiance mode)

The two different power mode patterns will help to distinguish reflections from the cavity tip from reflections from the rest of the cavity. The tip is expected to contribute the most to the cavity reflection losses.

The Data runs have been performed in the following way: The cryogenic radiometer has been placed in the beam line for 20 minutes. Afterwards the instrument stage was moved so that the DARA instrument was placed in the beam for ten minutes. this switching has been performed several times. Usually four cryo sequences and 3 DARA sequences have been carried out in each data run.

4.3.2 Data Evaluation

The data has been evaluated in two different ways. In the first approach the beam power is assumed to drift linearly over the whole measurement run. Therefore a linear slope is fitted to the data in a least square sense. An additional offset parameter is introduced into this fit that allows the DARA data to have a fixed offset to the TRF data. This offset parameter is one of three degrees of freedom of the fit. Together with the absolute value, the ratio between the DARA readings and the cryogenic radiometer readings is determined. Figure 4.3 shows the power data and the irradiance data with the corresponding fit. The corresponding uncertainties of the fit are listed in Table 4.3.

Another approach as performed by Fehlmann [33] and the TRF team is to fit a single test instrument sequence to the preceding and the succeeding cryo sequence. A test with the preliminary data showed that this leads to the same results than the simple method with one linear fit for the whole measurement.

channel/ cavity	power 1.5 mm full circle	power 2.5 mm ring	irradiance 7.3 mm full circle
A	0.000045	0.000066	0.000100
B	0.000060	———	0.000068
C	0.000037	0.000044	0.000074

Table 4.3: Fit uncertainties of DARA to TRF ratios (1σ relative)

	Cavity A	Cavity B	Cavity C	mean
DARA to TRF	0.999917	1.000196	0.999958	1.000024
Uncertainty (1σ)	0.000251	0.000242	0.000241	0.000221
Characterisation factor	1.002166	1.002326	1.002216	

Table 4.4: Ratio DARA to TRF, with corrections applied (irradiance mode)

4.3.3 Results of the TRF Calibration

Irradiance Mode

After the fitting of the raw data, the correction factor for the DARA characterisation is applied to the ratio. These are the correction factors obtained in Chapter 3 and summarised in Table 3.38. This leads to an improved ratio that compares the SI traceable DARA measurement to the SI traceable TRF measurement. Table 4.4 shows the resulting DARA

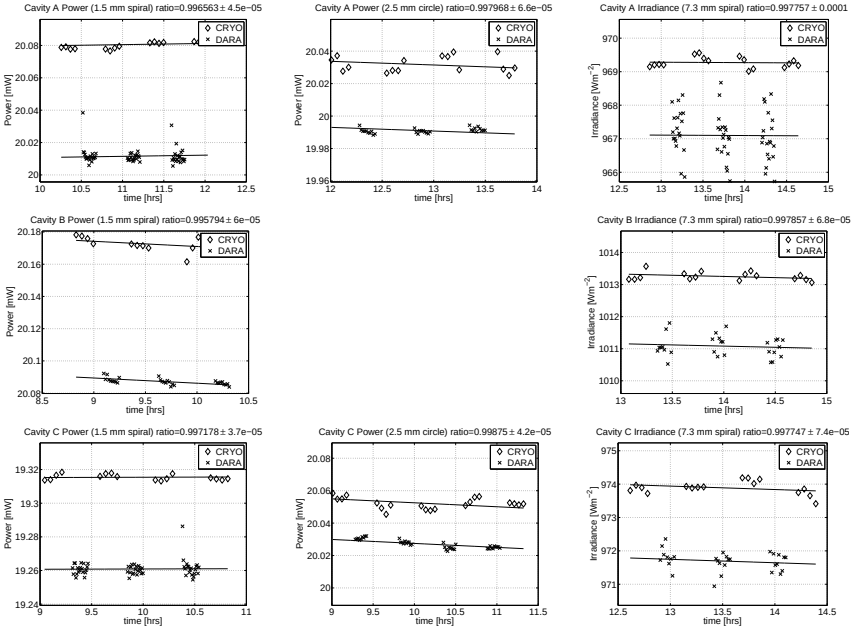

Figure 4.3: Calibration raw data from TRF calibration with simple fit applied

to TRF ratios, which are also the ratios between DARA's native scale and the DARA's SI cryogenic laboratory scale.

A good agreement is found between DARA and TRF. Cavity B shows a the largest difference between DARA and TRF of about 200 ppm which is roughly the 1σ uncertainty. Cavities A and C show even better agreement. The mean value of the DARA to TRF ratio is 1.000024.

Power Mode

In order to evaluate power mode measurements, a native power mode scale needs to be established first. When measuring in power mode the unit of measurement is the watt. The size of the aperture does not go into the calculation. Furthermore the correction factor for the DARA characterisation is different to the correction factor for irradiance measurements: There is no diffraction in power mode, and due different illuminated parts of the cavity, the absorptivity is different. While neglecting diffraction is straightforward, the absorptivity of a certain beam profile at the cavity is difficult to estimate. In Section 3.3 the absorptivity for the situations at TRF have been estimated, the values can be found in Table 3.10.

Table 4.5 shows the final results for the power mode DARA to TRF ratio. Due to the higher absorptivity correction also the uncertainty increases for the 1.5 mm full circle pattern. For the 2.5 mm ring pattern the absorptivity correction is smaller which reduces the uncertainty of the correction.

The agreement between DARA and TRF in power mode is not as good as in irradiance

Power 1.5 mm full circle	Cavity A	Cavity B	Cavity C
Ratio DARA to TRF	1.00076	1.00032	1.00211
Uncertainty of the ratio (1σ)	0.00063	0.00066	0.00071
Characterisation factor	1.00421	1.00455	1.00495
Characterisation uncertainty (1σ)	0.00060	0.00063	0.00069

Power 2.5 mm ring	Cavity A	Cavity B	Cavity C
Ratio DARA to TRF	0.99909	-	0.99985
Uncertainty of the ratio (1σ)	0.00021	-	0.00021
Characterisation factor	1.00112	1.00137	1.00110
Characterisation uncertainty (1σ)	0.00010	0.00012	0.00010

Table 4.5: Ratio DARA to TRF (power mode)

mode. For three out of the five measurements there is agreement within 2σ. For one measurement, the ratio is just at 3σ (C, 1.5 mm full circle). One ratio (A, 2.5 mm ring) is more than 4σ away from unity. It should be noted that the uncertainty for the measurements with the ring profile the uncertainties are very low. This is because the absorptivity correction itself is very low. Most probably the uncertainty of the absorptivity is underestimated, especially the uncertainty contribution resulting from the selection of the illuminated area.

4.3.4 Uncertainty Budget

The uncertainties of the ratio between the DARA native scale and the SI cryogenic laboratory scale are listed in Table 4.4, they originate from three sources: First, the general uncertainty for calibrations at TRF is 176 ppm [31]. This uncertainty describes the uncertainty of the set up at TRF, or in other words the accuracy of a calibration with respect to SI base units. The second source of uncertainty is the uncertainty of the DARA native scale (characterisation), and third the scatter from the single measurements is used to estimate an uncertainty for the fit (Figure 4.3). Table 4.6 shows the uncertainty budget for the irradiance calibration at TRF. In a similar way the uncertainties are determined for the power mode.

The estimation of the uncertainty of the mean values for all three cavities is not so easy to estimate. This is because there are uncertainties that originate from systematic offsets that are identical for all three cavities. Such uncertainty components are for example the uncertainty of the cryogenic radiometer with respect to SI base units, or the uncertainty of the diffraction correction. These uncertainty components can not be further reduced by taking mean values. All components of the characterisation and of the calibrations have partly such a common uncertainty. The uncertainty of the mean value consists of 200 ppm systematic (common) uncertainty and of a contribution of 95 ppm for individual uncertainties, which leads to a combined relative standard uncertainty (1σ) of 221 ppm for the mean value. Thus the uncertainty of the mean value is not greatly reduced compared to the uncertainties for the individual cavities.

Note on the Diffraction Corrections at TRF

As discussed in Section 3.5.8 the diffraction correction is assumed to be equal for the illumination by the TRF irradiance field and illumination by a solar like geometry. (This has also been assumed by Fehlman [33] when calibrating the PREMOS instrument.) For

	Cavity A	Cavity B	Cavity C
TRF calibration uncertainty (1σ)	0.000176	0.000176	0.000176
statistical uncertainty (1σ)	0.000100	0.000068	0.000074
DARA characterisation (1σ)	0.000149	0.000151	0.000147
Combined uncertainty of the ratio (1σ)	0.000251	0.000242	0.000241

Table 4.6: Uncertainty budget for the irradiance calibration

the comparison to the SI cryogenic laboratory standard, not only DARAs diffraction correction is relevant, but also the diffraction correction for the cryogenic radiometer. The cryogenic radiometer at TRF had been designed to have the same aperture arrangement as the TIM radiometer, which reduces the influence of an inaccurate diffraction correction for a calibration of a TIM radiometer against the cryogenic radiometer [31]. In order to compare DARA to the cryogenic radiometer, the precision front aperture ($\varnothing$= 8 mm) of the cryogenic radiometer had been replaced with a smaller, DARA like aperture ($\varnothing$= 5 mm). Thus the slope angle of the cryogenic radiometer becomes much larger than the slope angle of DARA (Section 2.4.2). This in turn leads to a much smaller diffraction correction for the cryogenic radiometer compared to the DARA, which means that the uncertainty due to wrongly calculated TRF diffraction is dominated by the uncertainty due to DARAs diffraction correction. Because of lack of a solid foundation for a reasonable estimate no additional uncertainty is added for for TRF diffraction. Nevertheless a rough estimate is made for the case of a 10 % uncertainty of the diffraction calculation at 532 nm, that would lead to an increase of the combined uncertainty values given in Table 4.6 by only 10 ppm. Thus it can be concluded that the issue is not extremely critical concerning the combined uncertainty but a correct treatment (theoretical or experimental) would be desirable for future comparisons, see also Section 3.5.8.

Uncertainty of the SI Cryogenic Laboratory Scale

If the implemented SI cryogenic laboratory scale is now directly used to take measurements, an uncertainty for such irradiance measurements with respect to the SI base units is estimated. Therefore, unlike in the chart in Table 4.6, only parts of the DARA characterisation need to be taken into account. When transferring the SI cryogenic laboratory scale into space to measure TSI, the absorptivity of the cavity needs to be extended from 532 nm to the solar spectrum, likewise the diffraction correction, furthermore the uncertainty of the thermal expansion and uncertainties of the data acquisition electronics need to be taken into account. Combining all these uncertainties, a relative uncertainty (1σ) of 220 ppm for extraterrestrial TSI measurements with the SI cryogenic laboratory scale is obtained.

4.3.5 Cavity Diagnostics

The set-up at the TRF offers the opportunity to capture a reflection image of the cavity. This is done in the following way. The TRF laser beam scans the cavity on a grid pattern. The reflections from the cavity are then re imaged to a silicon photo diode detector. With an iris baffle in the image plane, reflections originating from the aperture can be blocked. Some of this stray light however is still entering the detector. Figure 4.4 show these images. Images A and B suffer from incorrect baffling of the aperture edge stray light.

The bright tip is very obvious in all three pictures. Unlike in the reflectivity measurements in Section 3.3 only light that is scattered back out through the front aperture is

recorded. This is also not an absolute measurement. As these measurements were performed before the absorptivity measurements described in Section 3.3 it was the first hint of the high reflectivity of the tip of the cone.

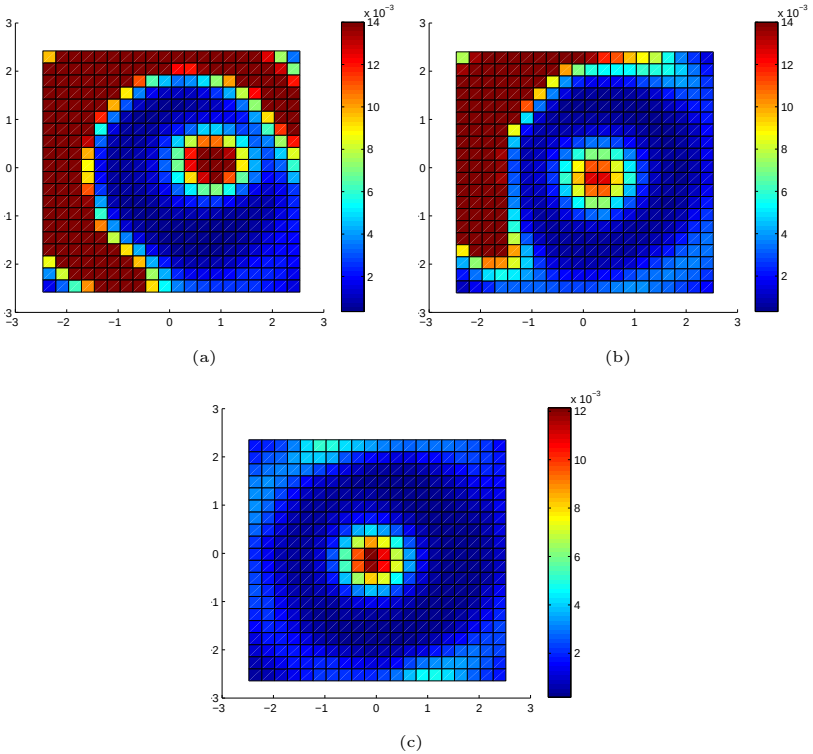

Figure 4.4: Reflectivity diagnostics pictures from TRF: The colour scale is normalized to the laser monitor current. The spatial coordinates are in mm. (a) is cavity A,(b) is cavity B, (c) is cavity C

4.3.6 Discussion

The 2011 TRF calibration campaign provided very valuable results. As an overall result it can be stated that in irradiance mode the DARA native scale and the cryogenic laboratory scale agree well within the uncertainties. In power mode the overall picture looks similar. However there is one outlier and the understanding of the measurements is not as good as in the irradinace mode.

The discrepancies between the measurement modes and the TRF diagnostics picture were the first hints for the inhomogeneous absorptivity of the cavity. The tip could be identified as the most likely source of reflected light. The subsequent more extensive studies on the absorptivity confirmed this findings, and quantitative, spatially resolved

measurements of the absorptivity (Section 3.3) led in turn to a better understanding of the TRF results.

The diffraction effects in the TRF irradiance field is not yet fully understood. With regard to future TRF calibrations such as the calibration of CLARA it would be desirable to investigate these effects further.

4.4 WRR to SI Cryogenic Laboratory Standard Comparison

Having implemented the WRR scale as well as the SI cryogenic laboratory scale to DARA it is possible to compare the two underlying standards to each other, by comparing the two scales implemented in DARA. Such comparisons between the WRR standard and the SI cryogenic laboratory standard have been performed several times in the past. Thus it is possible to compare the ratio found with DARA to values from the literature.

4.4.1 Previous Comparisons

WRR to SI cryogenic laboratory standard comparisons

Previously four WRR to SI cryogenic Laboratory standard comparisons have been carried out, starting in 1991. The 1991, the 1995 and the 2005 comparisons yielded results that were compatible with the assumption that the two standards are equal within the uncertainties of the measurements. The 2010 comparison however showed that there is a difference of 0.34 % between the scales. Unlike earlier comparisons the 2010 comparison was carried out in irradinace mode. This means that the beam in the laboratory is overfilling the radiometer apertures when doing SI cryogenic laboratory calibrations. This simulates a similar situation as the measurement of sunlight, whereas in the earlier comparisons the beam was underfilling the apertures. When doing the SI cryogenic laboratory comparison in power mode, additional transfer factors, such as the aperture area and stray light corrections need to be taken into account. Fehlmann et al. [56] suggest that in the earlier comparisons stray light was heavily underestimated. Table 4.7 shows the results from these comparisons. It can be seen that also in the 2010 comparison the power mode result is lower than the irradiance mode result.

An instrument comparison in irradiance mode became only possible when the TRF went into operation, which was mainly built for this purpose.

Looking at the uncertainties it can be seen that the first two comparisons in 1991 and 1995 would not have been able to find a significant difference between the two standards even if a ratio similar to the Fehlmann result in irradiance mode from 2010 had been found. Therefore only the 2005 result is in contradiction to the irradiance mode result from 2010 (and the result from DARA).

Year	Literature	Ratio WRR/Cryo	Instrument(s)	Remarks
1991	[97] [98]	1.0011 ± 0.003 (2σ)	PMO5/PMO6-9	Power Mode
1995	[97] [99]	1.0013 ± 0.003 (2σ)	PMO6-11	Power Mode
2005	[97]	0.9999 ± 0.0016 (2σ)	PMO6-9, PMO6-11	Power Mode
2010	[56]	1.0018 ± 0.0018 (2σ)	PMO6-PREMOS-3	Power Mode
2010	[56]	1.0034 ± 0.0018 (2σ)	PMO6-PREMOS-3	Irradiance Mode

Table 4.7: Results of the previous four WRR to SI cryogenic laboratory standard comparisons

Comparison of the WRR to the SI (base units) traceable PMO6 native scale

In order to compare the WRR standard with the SI base units, there is an additional possibility by comparing the WRR standard with the native scale of the PMO6. The native scale of the PMO6 has been established by Brusa and Fröhlich [59, 67] in the early 1980s by means of a characterisation, comparable to the characterisation of DARA.

Brusa and Fröhlich [59] also compared their native PMO6 scale to the WRR by calibrating seven characterised PMO6 radiometers against the WSG. Their result is listed in Table 4.8. Although Fehlmann et al. [56] claimed that stray light had generally been

underestimated in PMO6 characterisation efforts and therefore led to the results that suggest equality between the WRR standard and the SI base units (previous section), the result of Brusa and Fröhlich [59] is compatible with the 2010 WRR to SI cryogenic laboratory standard comparison and the results from DARA. The result is remarkable as it was an attempt at PMOD/WRC to independently link the WRR to the SI base units, e.g. the characterisation of a radiometer that was not part of the WSG. The uncertainty is smaller than the uncertainties of the later conducted WRR to SI cryogenic laboratory scale comparisons described in the previous section.

Using these results it is also possible to link the PMO6 native scale to the DARA native scale. Thus a PMO6 to DARA native scale comparison would yield a value of 1.0009 ± 0.0015 (2σ).

Ratio WRR to PMO6 native scale	1.0022 ± 0.0013 (2σ)

Table 4.8: WRR to SI base units comparison based on the PMO6 characterisation [59]

4.4.2 WRR to SI Cryogenic Laboratory Scale Comparison with DARA

The ratios between the WRR and the SI cryogenic laboratory standard as found with the three DARA cavities are listed in Table 4.9. The mean of these ratios shows a difference of roughly 0.31 % between the two standards, meaning that DARA reads 0.31% higher, using its implemented WRR scale than using its SI cryogenic laboratory scale. The values from the three cavities agree well within about 0.5σ around the mean value. This is expected, as most of the uncertainty originates from the uncertainty of the WRR calibration, rather than from individually characterised components of DARA. Therefore the uncertainty of the mean value is not greatly reduced compared to the results of the individual cavities.

Figure 4.5 illustrates the position of the WRR and SI Cryogenic Laboratory standard on the DARA native scale.

A comparison of the WRR and SI cryogenic laboratory standards based on the DARA data had been presented before at the WMO-TECO conference in 2012 [100]. The results presented in this work do not significantly differ from the 2012 result, but have smaller uncertainties.

	Cavity A	Cavity B	Cavity C	Mean
Ratio WRR to TRF	1.00289	1.00339	1.00301	1.00310
Uncertainty (2σ)	0.00086	0.00086	0.00086	0.00081

Table 4.9: WRR to SI cryogenic laboratory scale (TRF) comparison with DARA

Uncertainty Budget

The uncertainty of the WRR scale to SI cryogenic laboratory scale (TRF) comparison differs slightly from the uncertainty budgets presented for the individual calibrations. This is because certain components cancel out, or have reduced uncertainty in the ratio between the two scales. The lead heating effect and the size of the aperture is the same for both cases and therefore drop out. The ratio of the two diffraction corrections is only dependent on the spectrum used for the terrestrial solar correction. The uncertainty of the absorptivity is reduced due to the fact that the absorptivity at 532 nm is coupled to the overall

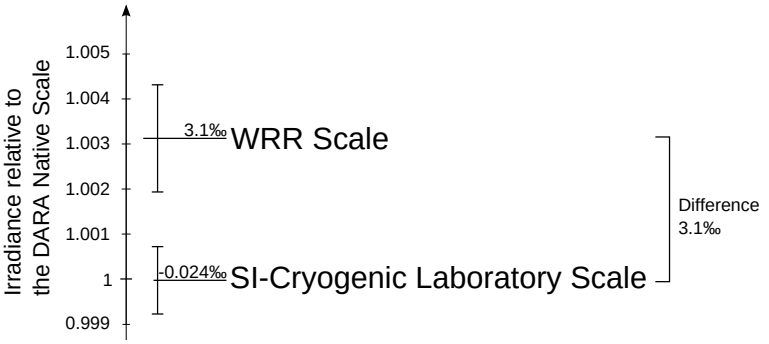

Figure 4.5: DARA's WRR scale and SI cryogenic laboratory scale expressed in the DARA native scale. The error bars represent a 3σ uncertainty, with respect to SI base units (including native scale uncertainty)

	Cavity A	Cavity B	Cavity C	contribution to mean
TRF calibration uncertainty	0.000176	0.000176	0.000176	0.000172
TRF statistical	0.000106	0.000068	0.000068	0.000056
WRR calibration uncertainty	0.000350	0.000360	0.000360	0.000350
Thermal expansion of the aperture	0.000031	0.000031	0.000031	0.000031
Diffraction	0.000036	0.000036	0.000036	0.000036
Electronics	0.000020	0.000020	0.000020	0.000014
Absorptivity	0.000100	0.000100	0.000100	0.000086
Air to vacuum ratio	0.000085	0.000066	0.000070	0.000050
Combined	0.000430	0.000427	0.000428	0.000409

Table 4.10: Uncertainty Budget (1σ) of the WRR to TRF comparison with DARA

absorptivity. For the data acquisition electronics the absolute accuracy is also not relevant, but the linearity of the PWM and the air to vacuum ratio is relevant.

Concerning the uncertainty of the mean value, the situation is similar to the situation at the individual calibrations. Most of the uncertainties are systematic to all three cavities. Only a few components can be reduced or partly reduced, due to the fact that these are individual to the cavities and independent. The uncertainty budget is shown in Table 4.10.

4.5 Conclusion and Implications

Having three irradiance scales implemented in the DARA radiometer the following conclusions can be drawn:

- The DARA native scale is compatible with the SI cryogenic laboratory standard within the uncertainties.
- The DARA native scale is not compatible with the WRR standard within the 3σ uncertainty.
- DARA's WRR scale reads roughly 0.3% higher than the DARA native scale and the SI cryogenic laboratory scale.

It is important to note that the SI cryogenic laboratory standard is a technology based standard, and therefore represents the SI base units with a certain uncertainty of the realisation, while the WRR standard as an artefact based standard can have a "fixed" error with respect to SI base units that is independent from the realisation (or calibration) uncertainty. Therefore it is crucial that the DARA native scale agrees with the SI cryogenic laboratory standard as both represent the SI base units. If the agreement was not achieved it would mean that the understanding of DARA is not satisfying.

As described in further detail in Section 1.3.6, the uncertainty of the WRR with respect to SI base units was estimated to be 0.3% at the time of establishing the WRR. The measurements with DARA do not contradict this assumtion. The measurements suggest that this "fixed" error of the WRR with respect to the SI base units is just about 0.3%.

These findings confirm the measurement of Fehlmann et al. [56] who already found a difference between WRR and SI cryogenic laboratory standard of the same order. It also supports the explanation for the discrepancies of TSI values from different satellite experiments that were either linked to WRR or SI base units (Section 1.4.3).

The uncertainty of a possible extraterrestrial measurement of TSI with the implemented scales has been estimated, under the assumption that no further correction and uncertainties due to the environment on the satellite need to be taken into account. A relative uncertainty of about 440 ppm (2σ) has been found for the SI cryogenic laboratory scale and 740 ppm (2σ) for the WRR scale respectively.

Chapter 5

Heliostat Design and Construction

5.1 Introduction

In a broad sense a heliostat is a system of two flat mirrors that can direct a solar beam into a fixed direction. It consists usually of a movable mirror and a fixed mirror. Heliostats as well as coelostats and siderostats (special cases of heliostats) have been widely used in solar astronomy to feed solar telescopes. A good description of these systems can be found in the review by A. A. Mills [101].

In a narrower sense a heliostat is a system where the first mirror directs the beam into the polar axis, thus rotating at a constant rate around the polar axis. The heliostat described in this chapter however is not a heliostat in this sense as the primary axis of rotation in our system is inclined with respect to the earth rotation axis. Nevertheless throughout this thesis our tracking system will be called heliostat.

This chapter gives some motivation and describes the design of the heliostat. Chapter 6 describes the motion control system and Chapter 7 describes the installation and the commissioning. Monetary aspects like funding and the budget can be found in Appendix E

5.2 Motivation

When doing optical experiments with solar radiometers, obviously a light source is always needed. These light sources can be lamps, lasers, or the sun. All of these light sources have their advantages and disadvantages.

An ideal light source would have a spectrum equal to the solar spectrum, it would be stable over time, and it would have the exact same geometry (divergence) and degree of (in)coherence as the solar light on earth. Unfortunately this ideal light source does not exist.

A stable light source can easily be built with lasers. Lasers however are operating at a fixed wavelength and as a further disadvantage it is not so simple to achieve a solar like beam geometry. An example where a laser source is used to simulate a solar irradiance field is the TSI Radiometer Facility (TRF) at the LASP in Boulder, USA [31]. When using lamps it is even more difficult to simulate a homogeneous irradiance field. While the sun itself has other disadvantages like stability and availability it gives us the correct beam geometry, as well as the terrestrial solar spectrum. The heliostat will provide such a solar beam in the laboratory, where experiments can be performed under controlled environmental conditions.

5.2.1 Experiments

The heliostat will allow a number of experiments with benefits for different ongoing projects in solar radiometry and possibly in other fields at PMOD/WRC. These experiments/projects include:

- Measurements of cavity reflectivity
- Measurements of reflectivity/absorptivity of front shield mirrors.
- Indoor testing of instruments under controllable environmental conditions
- Using the heliostat as a sun simulator/verifications of thermal models
- Characterisation of stray light in PMO6 radiometers
- Visualisation of diffraction effects and verification of diffraction calculations
- Determining the non equivalence of radiometers
- Characterising the *Monitor to Measure the Integral Transmittance of Windows* (MITRA) [33, 62]
- Characterising the *Cryogenic Solar Absolute Radiometer* (CSAR) [33, 32]
- Testing space equipment in the clean room

5.3 Requirement Specification

Before discussing the actual design, some basic requirement specifications are given. These specifications give some guidelines to the design process. Some of the specifications are discussed in later sections, while some of the specifications are more interesting for the technical implementation and for the selection of components.

- **Tracking accuracy/beam stability:** For most radiometric experiments the lowest tolerable value for the accuracy/beam stability is 0.1° (primary goal). The beam direction shall be stable within 0.005 degrees or better (secondary goal).

- **Field of view:** The field of view as seen from the laboratory should be ±4 degrees, so that the full field of view of a PMO6 radiometer is covered.

- **Mirror flatness / beam quality:** The flux density within the beam should vary by less than 100 ppm. In terms of mirror flatness, this is equal to a manufacturing tolerance of 25 nm rms and a self gravity deformation in the same order (Section 5.5).

- **Safety:** The system should be equipped with end switches, so that the heliostat can not rotate out of its working range and damage cables or the mirror. Furthermore an emergency stop button should be installed on the heliostat platform, as well as at the power supply located at the operating desk.

- **Storage temperature range:** −30°C to +40°C

- **Operating temperature range:** −20°C to +35°C

- **Snow and wind loads:** The heliostat structure should withstand snow and wind loads according to the applying SIA standard 261 [102].

- **Mirror protection:** In the storage position the mirrors need to be protected (with a lid etc.) from environmental influence. In order to avoid oxidation the mirrors should be purged with dry nitrogen.

Concerning the accuracy of the tracking the following aspects are considered: For the absolute minimum conditions the tracking accuracy should be comparable to the accuracy of a common solar tracker, as used for direct solar irradiance measurements. A widely spread solar tracker is the INTRA tracker from the Brusag company. Its pointing accuracy according to the data sheet is 0.1° [103]. 0.1° is therefore considered as the lowest limit for radiometric experiments at the heliostat.

If basic imaging experiments of the sun are performed a higher accuracy and stability is necessary. Considering an image of the sun (0.5° diameter) a basic criteria could be stability to within one hundredth of the image diameter. This leads to a tracking accuracy of 0.005°. For more advanced imaging experiments an even higher accuracy would be desirable, but it is not the main focus of this heliostat system.

The beam quality criteria is chosen so that if performing a radiometric calibration in the beam, e.g. a WRR calibration, the uncertainties due to the beam are smaller than the rest of the calibration uncertainties.

5.4 Baseline Design

As mentioned earlier, the heliostat consists of two mirrors. The first mirror is the tracking mirror that is rotatable in two axes, it will be called M1. The fixed mirror is called M2. Designing the heliostat, different aspects are to consider: This includes the site, the quality of the beam, the field of view of an instrument mounted in the laboratory, the technical realisation, etc. As the position of the laboratory is given in our situation, the following aspects are to be considered:

- Maximize the time of operation (minimise shading by obstacles)
- Optimize the field of view as seen from the laboratory
- Optimize the incidence angle (mirror surface)
- Optimize for "continuous" motion
- Avoid singularities in system coordinates
- Avoid shading of mirror M1 by mirror M2

5.4.1 Position of the Heliostat: Field of View Versus Unobstructed View

The time of operation is determined by the position of the tracking mirror M1. This position ideally should have an obstacle free view of all possible positions of the sun throughout the year. The field of view as seen from the laboratory is determined by the size of the mirror and the length of the ray path from the laboratory reference point to the primary mirror. The closer the mirror, the wider the field of view. The optimal position of M1 regarding the field of view would thus be as close as possible to the laboratory entrance window.

As the position of the laboratory entrance window is given, it limits the possible locations for the tracking mirror M1. Figure 5.1 shows the outline of the observatory building and possible sites for M1. Position A is as close as possible to the laboratory entrance window. It provides therefore the largest field of view as seen from the laboratory. On the downside, position A has a limited view of the sun in the afternoon. Positions B and C however have an unobstructed view of the sun but the trade-off is the narrow field of view of an instrument in the laboratory in this configuration.

As the length of the ray path would more than double from configuration A to B the diameter of mirror M1 needs also to be doubled in order to achieve the same field of view as seen from the laboratory. A reasonable field of view for radiometer experiments is ± 4 Degrees, according to the WMO standard for the limit angle of a solar radiometer (Section 2.4.2) and it is also a requirement listed in Section 5.3 . This means the beam diameter needs to have a diameter of roughly 550 mm when having a 4 m beam length, and more than a metre for 8 m beam length. This is a very strong argument for position A as the size of the mirrors should be kept as small as possible (costs, handling).

The obvious disadvantage of position A is the obstructed view due to the wall of the building. To study the amount of possible operational time that is lost due to shading while having the mirror at position A, the calibration dataset of a reference instrument from 1990 to 2010 is used. WRR calibration measurements are manually operated, whenever weather conditions allow and are therefore a good measure for possible operating time of the heliostat. For each stable measurement point of the calibration dataset, the azimuth angle is calculated. Histograms are made for these azimuth data. Figure 5.2 shows a

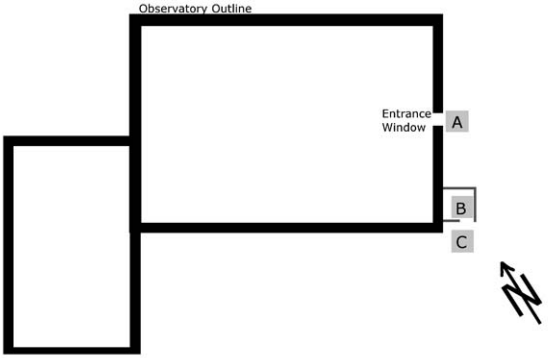

Figure 5.1: Outline of the observatory, with different positions for the heliostat primary mirror

2D histogram of the azimuth data, illustrating seasonal effects. The colour indicates the absolute number of data points per azimuth per day of the 1990 to 2010 period. Figure 5.3 shows a 1D illustration histogram on the compass rose and the corresponding cumulative diagram. Angles with an azimuth greater than 214 degrees cannot be seen by the heliostat from position A. The cumulative diagram shows the relative loss of data if cutting the field of view from one side.

The evaluation shows that only about 17% of possible operational time would be lost due to the limited view from position A. The short distance between location of the experiment in the laboratory and the primary mirror, combined with a loss of only 17% of the operational time favours the selected location A over other possible locations.

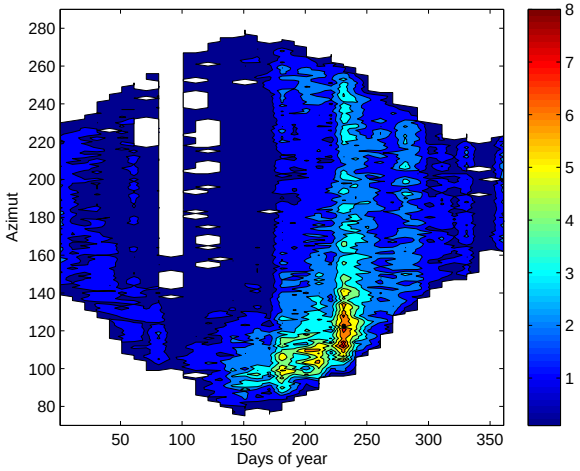

Figure 5.2: 2D-Histogram of valid pyrheliometer/pyrenometer calibration data points. The data is binned by day-of-year and azimuth. The scale represents the absolute number of data points per azimuth and day oft the period 1990 to 2010.

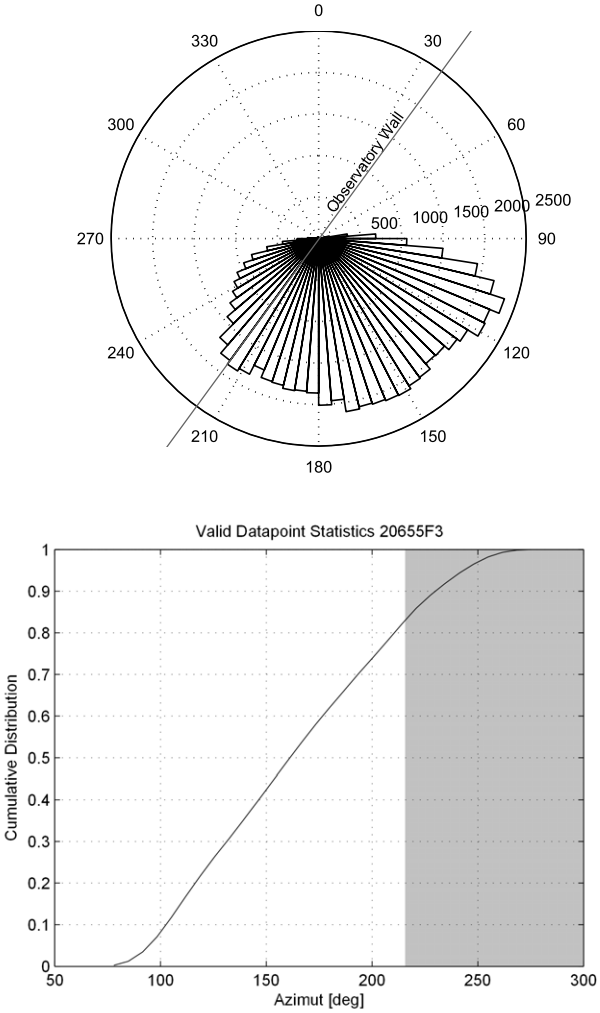

Figure 5.3: 1D-Histogram of the azimuth distribution of the WRR calibration data (left) and the corresponding cumulative diagram (right), the shaded area is the region where the field of view of the heliostat is obstructed by the observatory wall.

5.4.2 Rotation Axes and Motion of the Tracking Mirror M1

Choosing the rotation axes of the tracking mirror involves thoughts about tracking speed, coordinate transformations between the different systems, as well as practical aspects. In this section the selected motion system is presented and explained. The topic of the motion system is of course also related to the field of view and mirror size optimisation described in Section 5.4.3.

The main axis (Mirror M1 to Mirror M2) of the heliostat has been chosen to optimize incident angles at the two mirrors, while avoiding shadowing of M1 by M2. The main axis is also the primary rotation axis (azimuth axis) of the tracking mirrors. This allows to decouple the tracking offset in the two motion axes.

The orientation of the tracking mirror as a function of time is shown in Figure 5.4 for three different dates of the year. Gray lines are azimuth and zenith angles in the horizontal plane. It can be seen that the mirror approaches zenith=0 at noon in summer times. For an altitude-azimuth mount this would cause a singularity in the tracking system, which would require an extremely high dynamic range of the motion control system.

The systems main axis (M1-M2) is therefore chosen as rotation axis of the tracking system. It is inclined by 27 degrees to the vertical (Figure 5.6). This allows to operate without the problem of a singularity at vertical mirror orientation while keeping the dynamic range of the motors low. Furthermore it easily allows to decouple offset signals in the two axes. The black lines in Figure 5.4 show the corresponding orientation in the coordinate system of the M1 tracking system.

In order to avoid confusion the tilted main axis (M1 to M2) will be called the primary rotation axis, whereas the the rotation perpendicular to the primary rotation axis (pseudo zenith) will be called the secondary rotation axis.

Tracking velocities are shown in Figure 5.5. Tracking velocities in the primary axes (pseudo azimuth) varies between 13 deg/h and 18 deg/h. Whereas in the secondary axis (pseudo zenith angle) the velocity is between ± 2 deg/h.

The operation range for the heliostat secondary axis is around 30 degrees. For the primary axis rotation it is slightly less than 150 degrees.

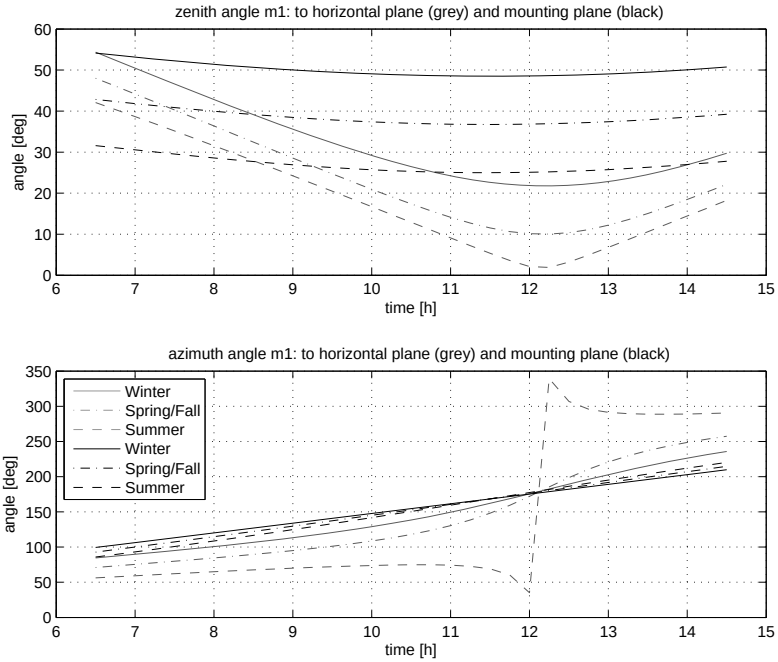

Figure 5.4: Tracking mirror orientation

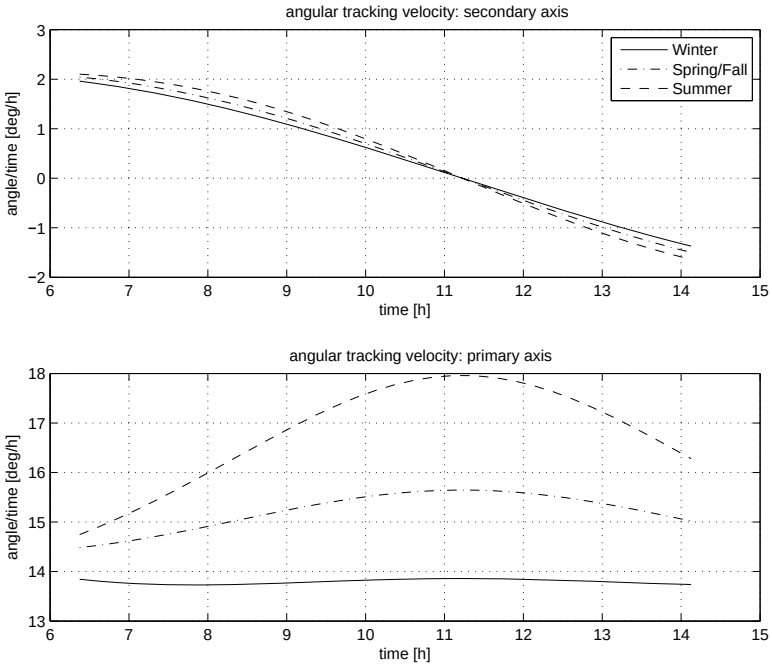

Figure 5.5: Tracking mirror velocity

5.4.3 Visualization of the Field of View

A study of the field of view of the heliostat system is performed to illustrate the heliostat's capabilities and to obtain a criteria for dimensioning the Heliostat mirrors. Figure 5.6 gives an illustration of the system.

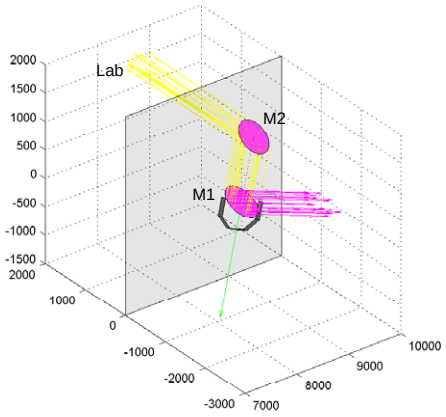

Figure 5.6: Illustration of the Heliostat Ray Path: The magenta rays represent the rays from the sun, that are reflected from M1 onto M2 and further into the laboratory (yellow). The green axis is the heliostat main axis (M1 to M2) that is also the primary rotation axis.

A ray tracing simulation is set up to visualize the field of view. The field of view is visualized for five viewpoints inside the laboratory. These points are located 1.2 m behind the outside face of the observatory wall. The first viewpoint is located in the centre of the beam. The other four viewpoints are shifted sideways $\pm$ 45 mm in x and z axis so that there is a viewpoint in each quadrant 64 mm from the centre of the beam. Figure 5.8 shows the perspective view from these side points, while Figure 5.7 (left) shows the view from the central point.

The shortest distance between the centre of the coordinate system (sun) and the respective ellipse limits the undisturbed field of view. Figure 5.9 shows the limiting angles of the undisturbed field of view as a function of time and season. Seasonal lines are computed for solstice and equinox. The colours correspond to the colours in Figure 5.8. Figure 5.7 (right) shows the view limiting angle for the location in the centre of the beam. If the black (M1) line is below the magenta (M2) line, M1 is the limiting mirror. In the reverse case mirror M2 is the view limiting mirror.

It can be seen that in winter season M1 is the view limiting mirror, whereas in summer M2 mirror is the limiting mirror. For the centre point (Fig. 5.7) the view limiting angle for the summer months is above 4 degrees (corresponds to a tangent of approx 0.07). For the 64 mm off axis viewpoints the view limiting angles vary between 2.5 and 3.5 degrees. Thus the 4 degree criteria is not fully met. In winter, the field of view is slightly smaller. This has to be kept in mind when performing experiments in winter. Therefore the heliostat

Mirror M1 radius	0.315 m
Mirror M2 radius	0.3 m
Entrance window radius	0.225 m
Distance M1-M2	1 m
Distance M2-lab	2.2 m
Angle between rotation axis and the vertical	27 deg

Table 5.1: Simulation parameter

software provides a real time illustration of the field of view, so that the operator can directly watch the evolution of the field of view during operation (Section 6.2).

The Relevant system parameters for the simulation are listed in Table 5.1.

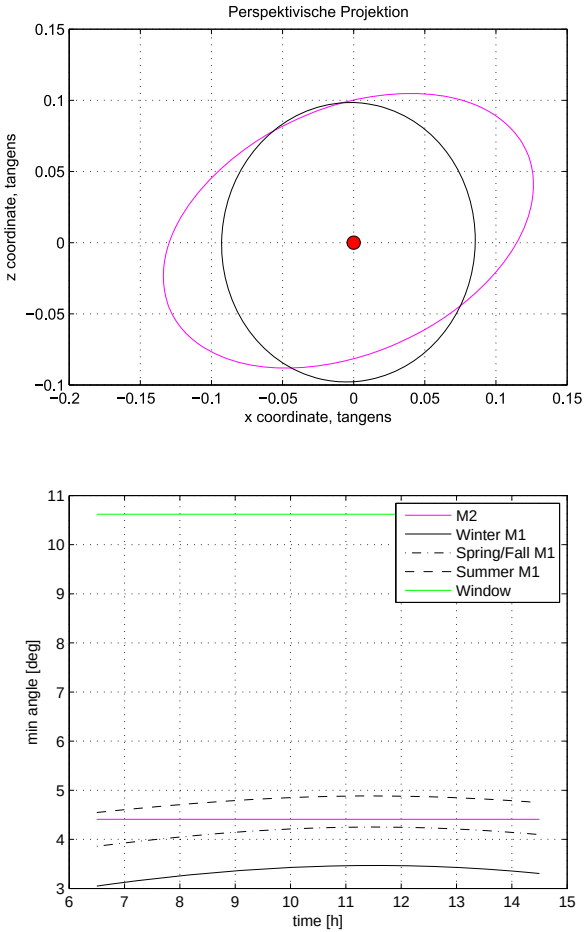

Figure 5.7: Example field of view as seen from the centre of the beam (top) and temporal dependence for the central field of view (bottom). Black: M1, magenta: M2, red: sun.

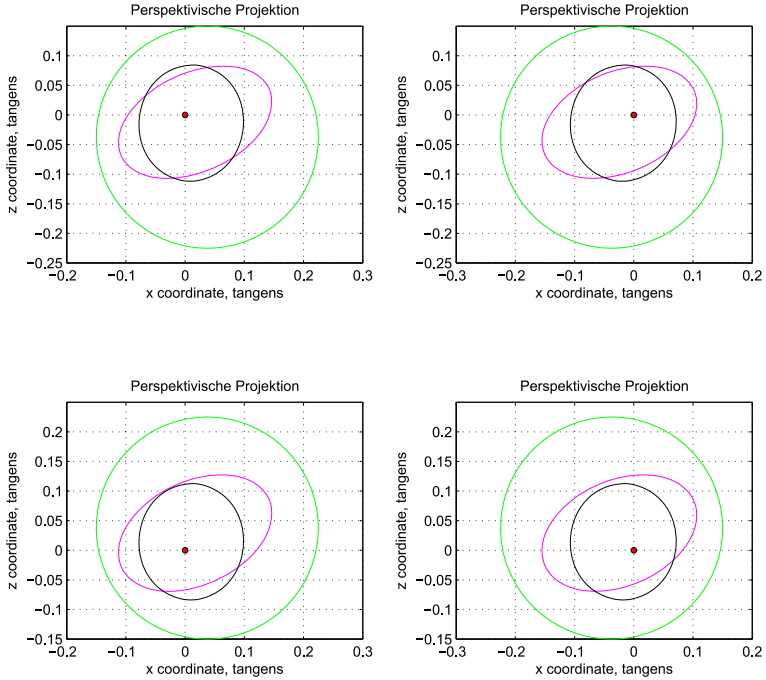

Figure 5.8: Illustration of the field of view looking outside from the laboratory (21 June at 12:00). The scale represents the tangent of their respective view angle. The black ellipse is the primary mirror, the ellipse in magenta is the secondary mirror. The green circle represents the entrance window (does not correspond to a real existing window, it represents rather an aperture that is constant in all cases and comes in handy for visual comparisons of the different situations). The size of the sun is plotted in red in the centre of the coordinate system.

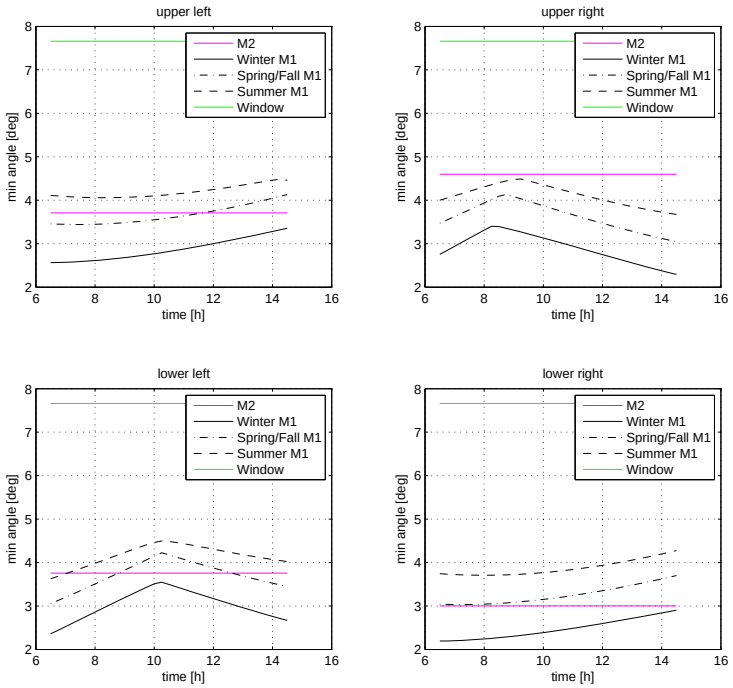

Figure 5.9: Temporal dependence of the view limiting angles

5.5 Mirrors and Beam Quality

Ideally the heliostat mirrors would be completely flat. In reality the flatness is limited by the polishing tolerances as well as the deformation of the mirror due to self gravity. The self gravity effects can be partly compensated by a sophisticated mounting, whereas the polishing is limited by manufacturing and monetary aspects. In this section the mounting of the mirrors is discussed as well as the impact of a non ideally flat mirror on the beam geometry. Furthermore the spectral properties, that influence the spectrum of the heliostat beam are examined within this section.

The mirrors are front surface mirrors and are made of circular blanks of Zerodur® and a reflective aluminium coating with a protective layer. Zerodur® is a glass ceramic that has virtually no thermal expansion. It is therefore suited best for applications with sunlight where the mirrors heat up while exposed to the solar radiation.

5.5.1 Support Frame of the Mirrors and Mounting

A customized frame with the shape of a big pan is designed for mounting the mirrors. It consists of an aluminium structure in light-weight design. It is optimised for maximal stiffness while keeping the weight as low as possible. The frames are identical for the two mirrors, and can be equipped with the appropriate interior, suiting the needs of the respective mirror M1 and M2. The mirror frame is visualised in many pictures throughout this chapter, it can be seen best in Figure 5.25.

Mounting of the Primary Mirror

The primary mirror is mounted on a *3 points on 3 points* mount (Figure 5.10). This mount equally distributes the supporting force on all nine points and thus reduces the deformation due to self gravity. Finite elements simulations are carried out to estimate the residual deformation of the mirror front surface due to self gravity. The simulation assumes an equal force distribution among the supporting points. Figure 5.11 shows the results of these simulations. It can be seen that with optimal mounting the the error (peak to valley) is in the order of 30 nm at maximum. This is the order of the manufacturing tolerance which is 25 nm rms error. This allows maximal curvatures that are in the same order of magnitude as the mounting error.

The basic design for this *3 points on 3 points* mount is adopted from the Vacuum Tower Telescope (VTT). Drawings and further information have been provided by Thomas Kentischer from the Kipenheuer Institut für Sonnenphysik (KIS) in Freiburg im Breisgau, DE.

Mounting of the Secondary Mirror

The secondary mirror of the heliostat is mounted in a much simpler way than the primary mirror. The mirror is mounted at three well defined points (Figure 5.12). The deformation that occurs due to gravity will be corrected directly when grinding and polishing the mirror. This is possible as the mirror is always in a fixed position, this means that the effect of gravity is always the same.

To simulate the effect of gravity on the mirror a finite-element simulation is also carried out for M2, using two different approaches. One calculation was carried out including the whole mounting system, and another calculation was carried out, simulating only the supporting pads and the mirror (Figure 5.12). It can be seen that the deformation of the mirror compared to the deformation of the mounting pan is relatively small. Figure 5.13 shows the result for the mirror surface for both calculations. Figure 5.14 shows the difference between the two cases. The figure is adjusted so that the mean difference is

zero. With the exception of the support points the agreement between the two simulation is within 20 nm, which is in the order of the targeted accuracy. The dependency on the element size for the simulation has also been investigated. An element size of 8 mm and 15 mm has been used. It was found that the dependence on the grid size is low and the results differ by less then 2 %.

Data Evaluation and Transfer

The output of the simulation is now re-grided on to an 1x1 mm grid, and the heights are converted into wavelength units (632.8 nm), in order to transfer the data to the manufacturer (THALES-SESO Aix-en-Provence). A mask is laid over the data to mark the elliptical area that needs to be within the specifications (Figure 5.15). The data submitted to THALES-SESO is based on the simulation visualised in Figure 5.12 on the left.

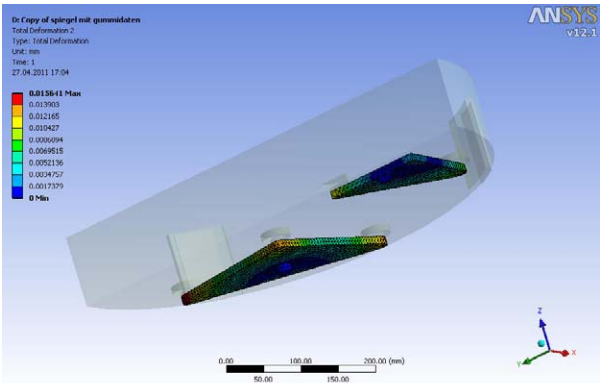

Figure 5.10: The 3 points to 3 points mirror mounting system distributes the force equally to all 9 supporting points

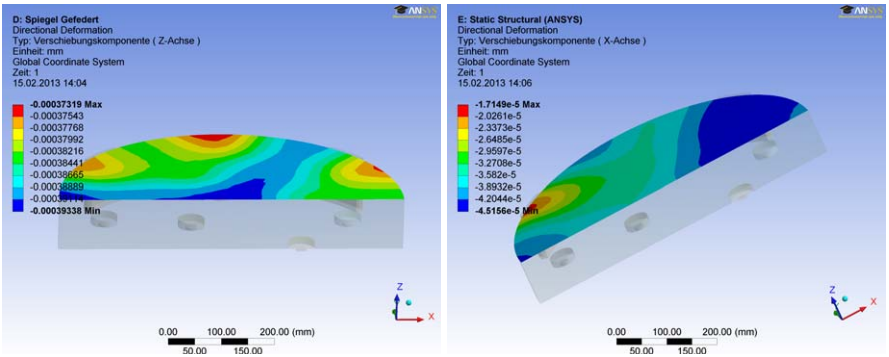

Figure 5.11: Mirror Deformation in horizontal position (left) and tilted by 42° (right)

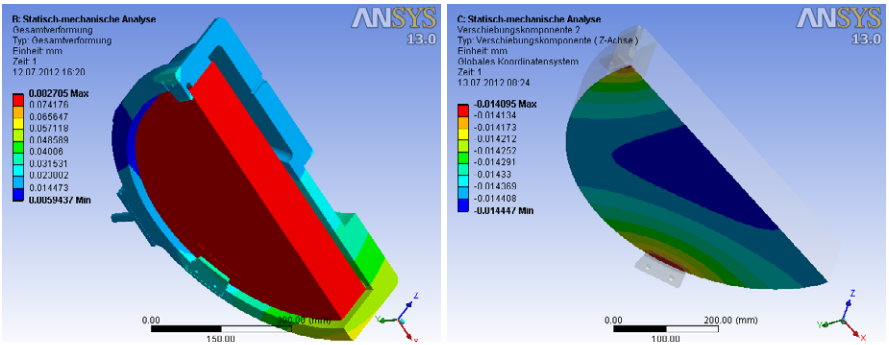

Figure 5.12: Mirror M2 with complete mounting (left) and with mounting pads only (right), the deformation of the mirror can only be seen in the right figure, as the deformation of the mirror is small compared to the deformation of the frame.

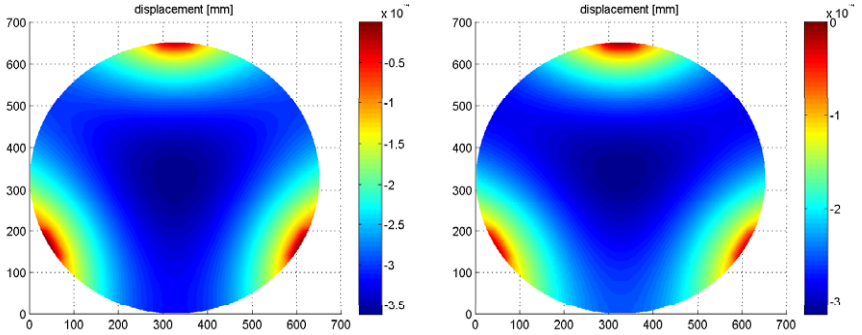

Figure 5.13: Deformation of mirror M2 due to self gravity: On the left, simulated with the complete mounting pan, on the right simulated with the mounting pads only.

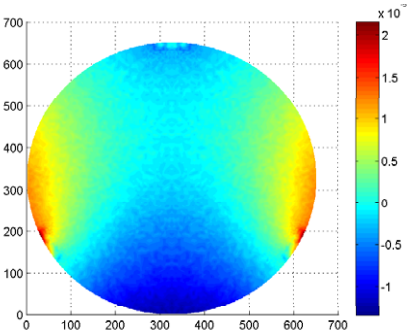

Figure 5.14: Difference between the two simulation cases (with and without frame) in mm. A subtraction is made, so that the mean difference is zero

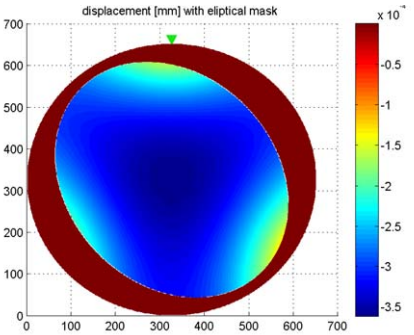

Figure 5.15: Deformation of the mirror M2 due to gravity, with mask applied. Only the area shown needs to be within the specifications

5.5.2 Impact of Deformed Mirrors on the Beam Geometry

In the previous section it was discussed how the mirrors are mounted in order to keep the mirrors as flat as possible. In this section the influence of not entirely flat mirrors on the beam density profile is estimated.
Knowing the mirror deformation that is occurring from gravity and assuming a curvature error from the manufacturing specification, an estimation of the focusing effect of non ideally flat mirrors is being performed by a 2D ray tracing.

In this sample calculation, two mirrors are irradiated with parallel rays at an incident angle of 34 degrees. Figure 5.16 shows the schematic arrangement of the two mirrors and the laboratory screen. The mirrors are assumed to have a slight convex (or concave) shape due to the manufacturing process and the self gravity deformation. The curve is approximated by a hyperbolic cosine curve. Due to its mounting the curvature of mirror M2 is assumed to be slightly higher than the deformation of M1. With this assumption the result will be more conservative and represent a worst case scenario.

For each ray passing through the system the displacement from ideal position at the lab screen is calculated. From the displacement values the ray density relative to the ideal condition is calculated. In this step the result is extended into the "missing" third dimension by assuming that the density increase is equal in both dimensions of the mirror surface. The density ratio is plotted in Figure 5.17 for all four concave/convex combinations of the two mirrors.

The beam density ratio varies from centre to edge of the beam by roughly 100 ppm assuming, both mirrors focus in the same direction. At the centre of the beam (± 100 mm), where most experiments will take place, the density ratio varies less than 50 ppm. This result matches the specifications listed in Section 5.3.

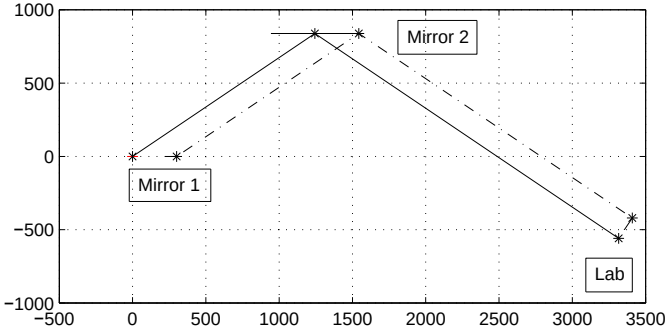

Figure 5.16: Schematic arrangement of the mirrors and the lab screen

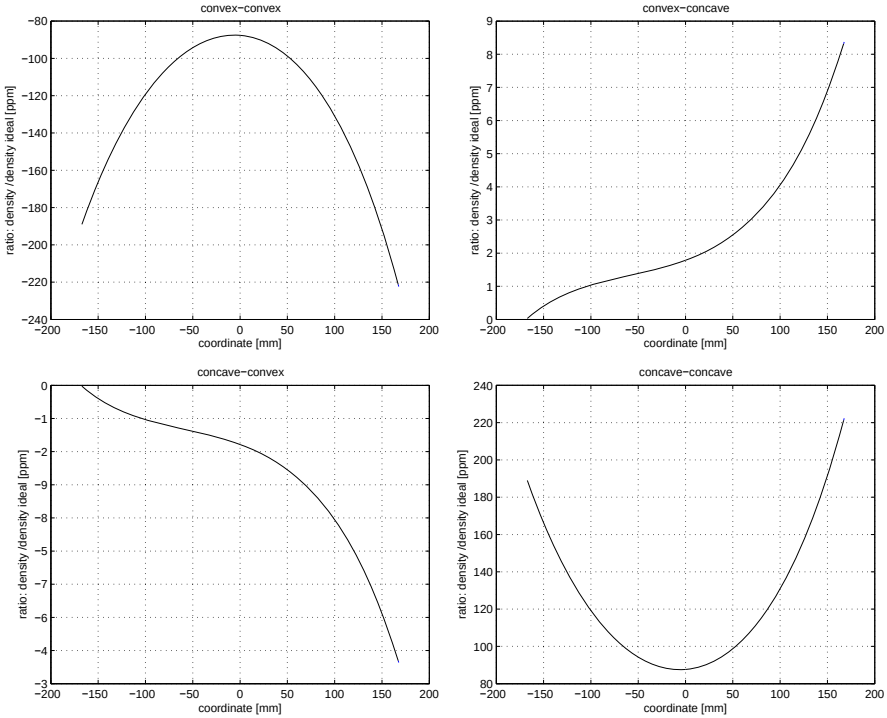

Figure 5.17: Relative beam density for different configurations, on the x-axes are the distances from the centre of the beam.

5.5.3 Spectral Properties of the Mirrors

The mirrors are front side mirrors, coated with aluminium and a protective layer. Aluminium has a high reflectance in the visible and infra red range. Figure 5.18 shows the reflectance at a heliostat mirror for wavelengths form 300 to 1800 nm for two different incidence angles. Figure 5.19 shows the incident angle at the tracking mirror during day and season (left). On the right the combined reflectivity of the two mirrors is shown for two positions of the tracking mirror, while the incident angle of the secondary mirror is constant at 39°. These calculations are based on measurement results obtained from THALES-SESO. When combining the reflectance of the two mirrors, no polarisation effects are taken into account. Therefore this result is only a rough estimation.

The spectrum of the heliostat beam will differ slightly from the solar radiation spectrum due to the losses at the mirrors which depend on the wavelength. In the visible region the total reflectivity is between 70 and 80%, it increases in the infrared region.

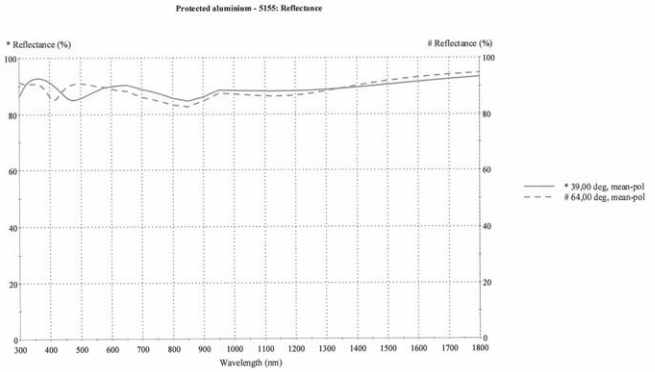

Figure 5.18: Spectral reflectance at the mirror surface for two different incidence angles (39° and 64°) (Figure from the manufacturer THALES-SESO)

5.5.4 Measured Reflectance

During commissioning of the heliostat a spectral irradiance measurement with a spectro-radiometer has been performed. This radiometer measures the absolute spectral irradiance from 300 nm to about 1000 nm. The spectro-radiometer is mounted in the heliostat beam inside the laboratory. A second identical radiometer is mounted on the roof of the observatory on a solar tracker. The data of both instruments are then compared to estimate the efficiency of the heliostat mirror configuration. Figure 5.20 shows the ratio between the measurement at the heliostat and the outside measurement. It can be compared to the values from the previous section (manufacturer data) that are also included in the graph. The measured values and the calculated values agree very well in the near infra red region. In the visible wavelength range and part of the UV however the measurements differ from the calculation by up to 5%. The uncertainty of the measurement is estimated to be in the order of 2% to 3%. A possible explanation for this discepancy might be that polarisation effects have not been taken into account when combining the reflectance of the two mirrors.

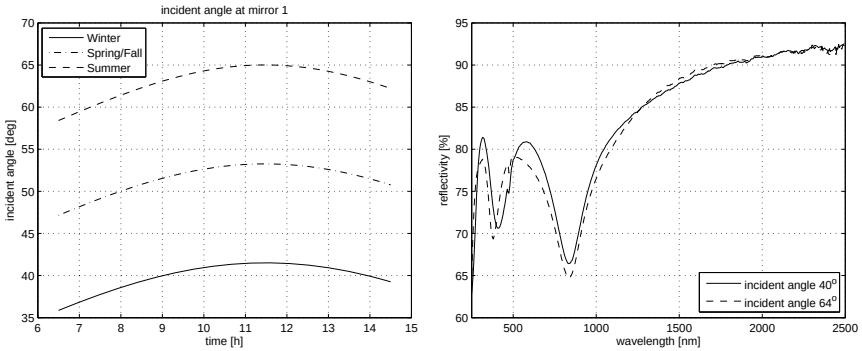

Figure 5.19: Incident angles at the tracking mirror as a function of time and season (left), combined reflectance of the two mirrors for two different positions of the tracking mirror (Incident angle of 40° and 64°)

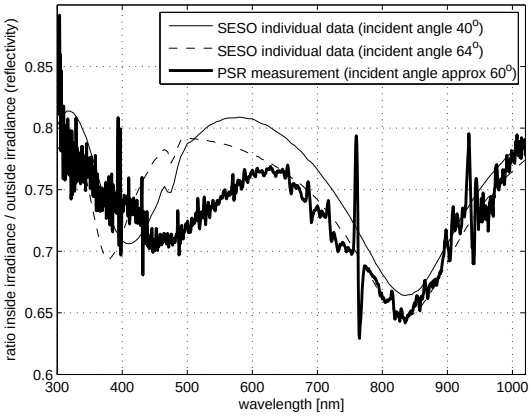

Figure 5.20: Ratio between the measured spectral irradiance in the heliostat beam and the outside measurement. The thin lines are the values, calculated from the manufacturer data.

5.6 Mechanical Set-up

The mechanical construction consists of two independent structures to support the two mirrors. The supporting structure for mirror M2 holds M2 in its fixed position. Mirror M2 is adjustable in position and tilt by hand wheels for alignment purpose. The mirror M1 on the other hand needs to move automatically, as it needs to track the sun. The structure of M1 is therefore equipped with motors and encoders.

This Section describes the mechanical structure and how it was designed in detail.

5.6.1 Support Construction for Mirror M2

The function of the support construction for the fixed mirror M2 is to keep the fixed mirror M2 in the desired position. The structure should ensure stability of the mirror while the heliostat is operated and resist external loads such as heavy wind or snow. Furthermore the fine positioning of the mirror should be adjustable in order to align the heliostat system.

Construction Space

While designing the support structure for the secondary mirror, it is important to consider that the construction is not obstructing the field of view of M1 or blocking the beam path of the installation. Therefore a construction space is defined where the structure can be designed within.

The construction space for the mounting of the secondary mirror is derived from the heliostat field of view visualisation program (Section 5.4.3). The construction space is integrated into the 3D model first, then the view as seen from the laboratory through the mirrors is computed and visualized. This visualisation allows to check whether the construction space is affecting the heliostat's field of view.

Figure 5.21 shows the modelled situation in 3D. The solar time is 6 am on 21 June, it represents an extreme situation in solar azimuth. Figure 5.22 shows the same situation in a perspective view as seen from the laboratory through the mirrors. The construction space (red boxes) is not allowed to overlap with both mirrors (black and magenta elipses) at the same time. In this particular situation the condition for the construction space is fulfilled. These figures can be watched as a motion picture over a whole day, to quickly check a particular situation.

Final Design

The final design of the structure of the mirror M2 support was done by an external company, G+P Engineering AG in Sargans. The specifications were the construction space (Figure 5.23), the mirror frame (designed in house) as well as the necessary degrees of freedom for fine adjustment of the alignment. Figure 5.24 shows the final design of the support structure for mirror M2.

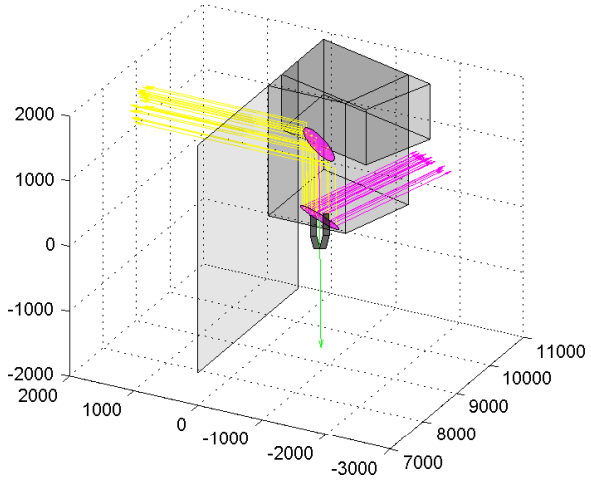

Figure 5.21: 3D view of the heliostat mirrors with two construction space boxes

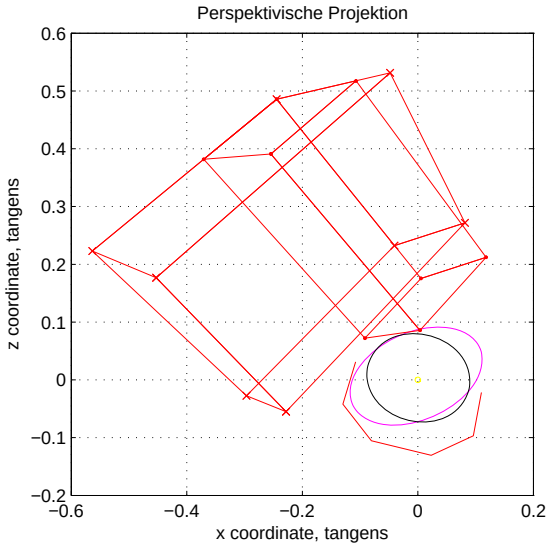

Figure 5.22: Perspective view from the laboratory position through the mirrors (corresponds to the situation in Figure 5.21)

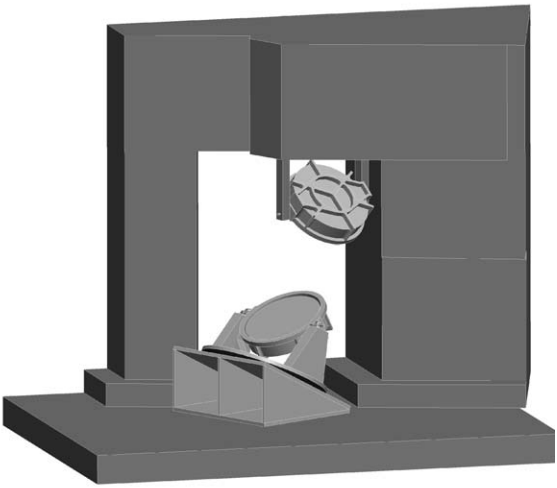

Figure 5.23: Construction space for the support construction for mirror M2

Figure 5.24: Final design of the support construction for mirror M2

5.6.2 Design of the Tracking System for Mirror M1

The tracking system is the heart of the heliostat. It needs to hold the mirror frame of mirror M1 and be able to rotate mirror M1 in two axes as described in Section 5.4.2. Furthermore, the structure needs to be mechanically stable to keep the heliostat beam stable.

Figure 5.25 shows the tracking system. The construction consists of a 27° tilted base. Attached to the base is a ball bearing of 841 mm diameter. It allows the rotation around the primary heliostat axis. On top of the bearing a welded steel support is mounted, it supports the bearings for the secondary rotation axis. The mirror frame is mounted in these two bearings, and can rotate around the secondary axis. Figure 5.26 shows the motor and gearbox of the secondary axis in detail.

The baseline of this design has been made at PMOD, whereas the detailed design work has been done by G+P Engineering AG in Sargans, the same company that did also the design of the mirror support structure. Figure 5.27 shows the complete arrangement of the heliostat structure, with primary and secondary mirrors. All main components of the structure are painted in white in order to keep the heating (and deformation) of the structure due to solar radiation low.

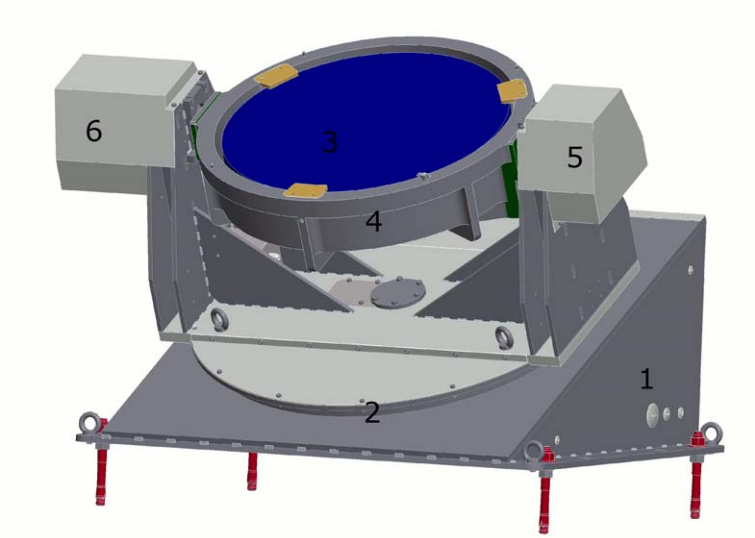

Figure 5.25: The heliostat tracking system structure, consisting of: 1 base construction, housing the electrical installation, 2 ball bearing (841 mm diameter) for primary axis, 3 mirror, 4 mirror frame, 5 housing for the rotary encoder (secondary axis), 6 housing for the motor (secondary axis)

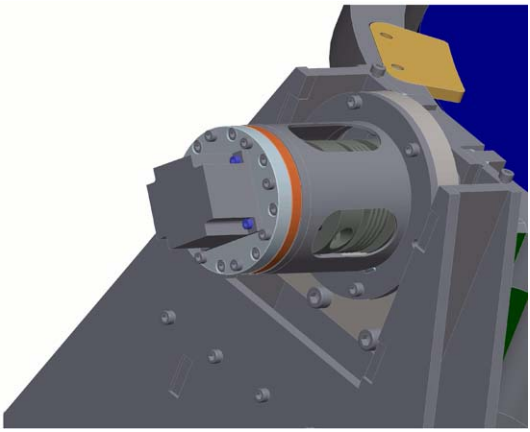

Figure 5.26: Detailed view of the motor and gearbox, connected to the secondary axis.

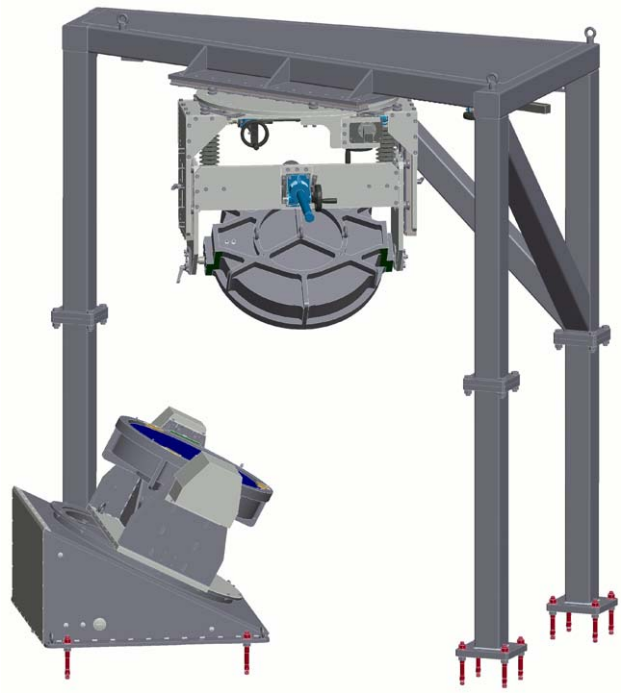

Figure 5.27: Final design of the complete heliostat construction

Chapter 6

Heliostat Motion Control

The role of the motion control hardware and software is to manoeuvre the heliostat mirror M1 into the desired position. The system therefore needs to sense the position of the mirror with sensors and it also needs to mechanically turn the mirror by means of the actuators. Furthermore, in order to track the sun accurately, the position of the sun with respect to the heliostat needs to be calculated so that the mirror M1 can be moved accordingly.

A camera is continuously monitoring the heliostat. This allows the heliostat operator in the laboratory to visually monitor the movements of the mirror M1 without having direct sight.

6.1 Hardware

The motion control hardware consists of sensors, actuators and a control computer. The devices are connected through a CAN-bus system. The following sections describe these components in further detail.

6.1.1 Actuators

Both heliostat axes are driven by stepper motors with micro stepping capability (1 microstep = 0.007°). The motor drivers are directly attached to the motors and communicate with the control computer via the CAN-Bus. The motors and drivers operate with 24V DC.

A backlash free harmonic drive gearbox with a transmission ratio of 160:1 is installed between the motor shaft and the mirror to further improve the step resolution.

6.1.2 Sensors

Rotary Encoders

Both Axes are equipped with 18 bit single turn rotary encoders. This would allow passive tracking within an accuracy below 0.01 degrees. This accuracy will be high enough for most radiometry experiments. The rotary encoders are programmed to automatically send the actual position through the CAN network. The rotary encoders are powered independently from the motors with 24V DC.

Optical Sensors

In addition to the rotary encoders an active guiding system with a sun sensor is installed. This system allows a higher tracking accuracy. The optical sensor is aligned with the experiment in the laboratory and ensures the tracking stability directly where it is needed. The active tracking system is also independent from small misalignments in the mechanical arrangement.

To date the signals from the optical sensors are acquired trough an RS232 connection. It is foreseen to replace the RS232 link at a later state and to integrate the the optical sensor into the CAN-bus network.

Limit Switches

As a safety measure each motion axis is equipped with emergency end switches. These emergency switches cut down the power supply if a certain angle is reached, so that the motors stop immediately. If an emergency switch is triggered, it needs to be bypassed in order to move the motor again.

Additionally there is also a limit switch in the heliostat primary axis in the forward direction. This limit switch is connected to the motor driver. If the limit switch is reached, the motor driver automatically stops the movement in the forward direction. It is however still possible to move the motor backwards without bypassing the limit switch. This limit switch prevents the user from arduous recovery manoeuvres with bypassing emergency switches, if the heliostat is accidentally left running at the end of the operational time.

6.1.3 Control Computer

The controller consists of a standard PC with a CAN-Bus interface, located in the laboratory. A program written in MATLAB® is used to process the sensor data and to control the motors. The program is described in detail in section 6.2

6.1.4 CAN-Bus

The CAN-bus (Controller Area Network[1]) is used as communication link between the hardware components. It runs at a frequency of 500 kbps. CAN is a multi-master system that allows every node to send messages on their own.

6.1.5 Camera

The camera is a robust outdoor camera that can stream the video signal over the LAN to the control computer. The live-stream can be watched in a standard web browser.

6.2 Program Structure

The controller program is programmed with MATLAB®, using object oriented style. The program consists of two main objects/classes: The controller object (controller class) and the IO module (IO module class).

Additional classes are a graphical user interface (GUI) and classes that can visualize the operation data. Figure 6.1 shows schematically how the objects are connected. The listing below gives a short overview of the program structure. More details about the program can be found in Section 6.3 (functional) and in Appendix D (technical).

[1] Specifications can be found at www.can-cia.org

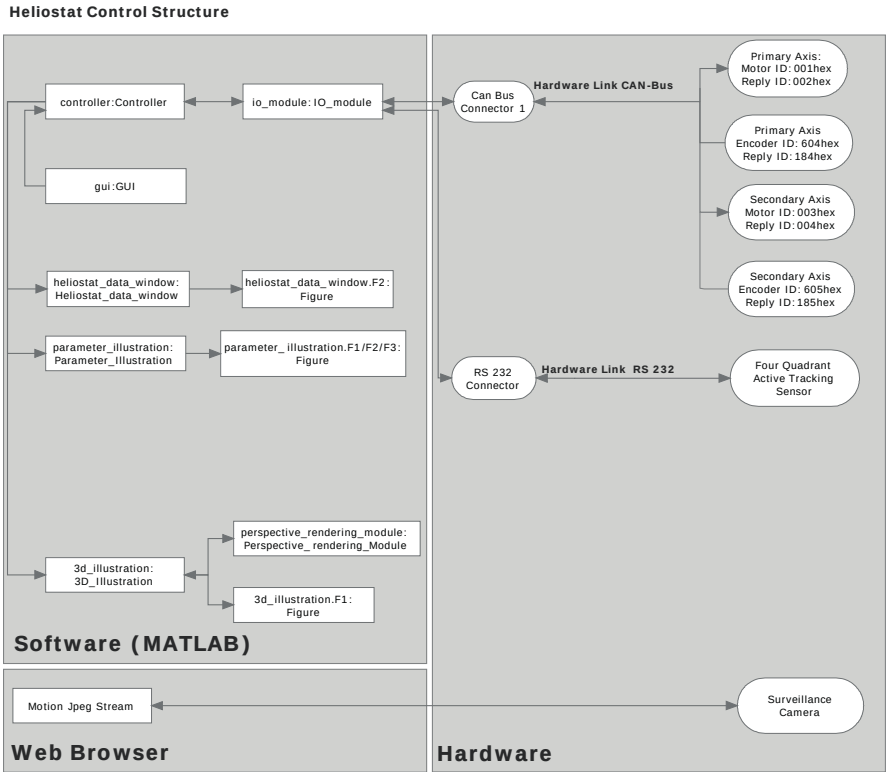

Figure 6.1: Heliostat control structure: The Illustration shows the components of the control software as well as the hardware, and the connection between the single modules. The software modules represent the instances and the underlying class.

The IO Module

The IO module handles the communication between the controller module and the hardware (CAN-bus). CAN bus properties and message structures are defined here. Message input from the bus is interrupt controlled.

The I/O module prepares the incoming data for further processing in the controller module and sends commands from the controller module to the CAN bus.

The Controller

The controller module handles the main task. The "state" variable defines the current type of operation, e.g. "go home". A timer at a defined period (2s) triggers the control routine, which executes the necessary task according to the state variable. The controller gets the latest position/tracking data from the IO module and updates the motor speed values, according to the tracking scheme. These values are sent to the motor through the

IO module.

The GUI

The graphical user interface (GUI) connects to the controller module. It allows the user to change the state of the controller by clicking buttons. The graphics output windows can also be opened using the GUI. The GUI can be closed and opened again without influencing the controller. On start up the GUI looks for the running instance of the controller module, and automatically connects to it. If there is no instance running it will instantiate a controller module.

The Perspective Rendering Module

The perspective rendering module calculates the heliostat mirror position and the actual field of view. It gets the data from the controller module and delivers the output to the graphics module that can plot a 3D view of the situation as well as an illustration of the field of view of an experiment in the heliostat beam.

6.3 Modes of Operation

The heliostat control program features the following modes of operation:

- Go Home
- Go to Position
- Passive Sun Tracking
- Active Sun Tracking

The "Go To" modes simply move the mirror to the desired position / home position. A maximal speed of 5000 micro steps per seconds is applied, this corresponds to 0.2°/s. The tracking modes require more sophisticated code and are therefore described in more detail in the next sections. The parameter that is fed to the motors is in all modes the motor speed in micro-steps/second.

6.3.1 Passive Sun Tracking Mode

In the passive mode the current position and speed of the sun with respect to the heliostat axes is calculated, using a code[2] based on Reda and Afshin [104]. If the offset between target and current position is large, the mirror is moved towards the target position with a maximum speed of 5000 micro-steps/s. When the target is reached (error smaller than 1°) the controller switches into the fine tracking mode.

In the fine tracking mode the current speed of the sun is taken as a base value to feed the motor. As only integer values can be fed to the motor, the value is rounded, before it is sent. The remainder is the added to the next value, to compensate the rounding errors.

Additionally an error signal is calculated, by taking the difference between the current position of the sun and the current position of the mirror. This error is then fed into a PI controller in order to adjust the calculated speed value.

[2]The code has been written in MATLAB® by Vincent Roy, Copyright © 2004, all rights reserved. The code *sun_position.m* can be downloaded from http://www.mathworks.com/matlabcentral/fileexchange/4605-sun-position-m

6.3.2 Active Sun Tracking Mode

In the active tracking mode the error signal is generated by an optical sensor. This signal is then used to correct the motor speed that is based on the current sun velocity. The signal generated in the optical sensor is in laboratory coordinates. Therefore it needs to be transformed into the main axes of the heliostat. This transformation is a rotation that is dependent on the position of the heliostat. The transformation matrix is therefore dynamic and needs to be recalculated for every new position.

In order to make the system reliable, the coordinates are simultaneously calculated with the algorithm used in the passive tracking mode. If the deviation between the actual heliostat position and the calculated position becomes too large, the system automatically follows the passive tracking scheme. This ensures that in case of clouds, obstructions in the ray path or malfunction of the optical sensor the heliostat stays within a certain boundary.

6.4 Test Operation

A motion test set-up has been built in order to test motor, gearbox, encoder, end switch and program functionality before the heliostat was actually built. Figure 6.2 shows this set-up. The set up consists of a motor gearbox combination, an encoder, and a shaft that connects the sensor and the actuator. Attached to the system are two limit switches. The installation box with the power supply is also part of the system. This box has later been installed at the site of the final set up.

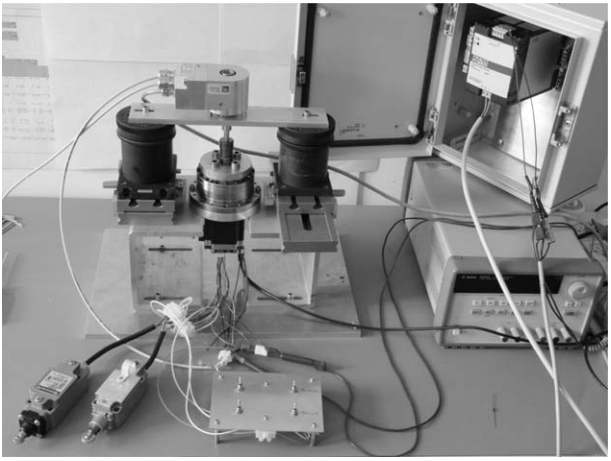

Figure 6.2: Motor/encoder test set-up: The rotary encoder sits on top of the construction and is connected through a wave to the motor/gearbox unit below. In the lower left corner are two limit switches.

The test system allowed to test the passive tracking mode, the manual mode and the "go to" modes. Intensive testing, especially of the passive tracking mode has been performed. Figure 6.3 shows the tracking data of such a test run. The graph shows the position, the motor speed and the error (difference between actual and target position). It can be seen that the error is within 3 resolution steps of the rotary encoder (1 step = 0.0014°). The

result from these test are not very meaningful with respect to the tracking accuracy as no loads or bearings have been attached to the system. But the program could be debugged in a realistic system composition.

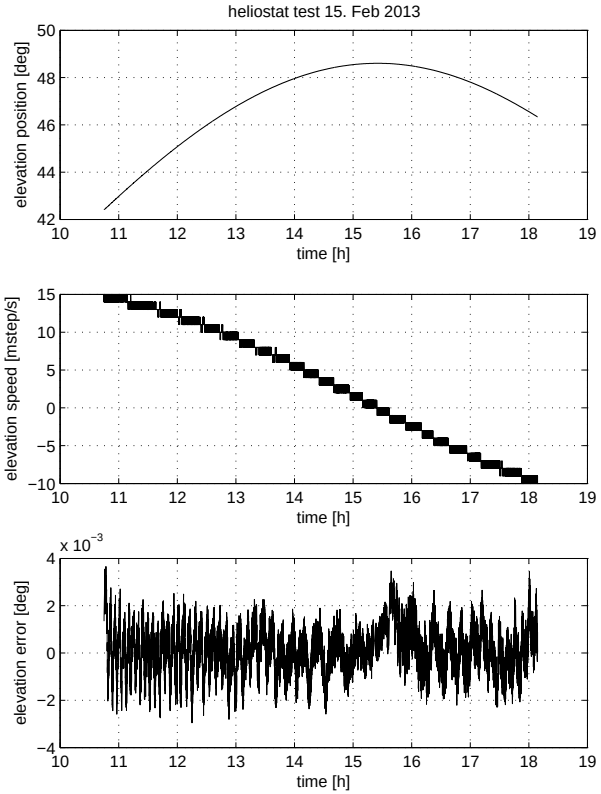

Figure 6.3: Test run data in passive tracking mode (elevation axis)

Chapter 7

Manufacturing and Commissioning

7.1 Manufacturing

Manufacturing of the mirrors started in 2012 by THALES-SESO, a French company located in Aix-en-Provence. The mirrors were delivered by January 2013.

The mirror support frames have been manufactured also by the end of 2013. These were designed fully in house and milled by Eckold AG in Trimmis.

Beginning of 2013 the manufacturing of the main structure began. This work was lead by the G+P Engineering company in Sargans, and closely accompanied by PMOD/WRC. The structure had been first installed in a assembly hall in Sargans, where also first tests of the motion control system have been carried out.

The concrete foundation has been built in the course of the renovation of the PMOD/ WRC institute building in 2011/2012.

7.2 Installation, Commissioning and First Experiments

The heliostat structure was installed on 20 June 2013. The concrete foundation had been prepared in advance. The structure of the heliostat was lifted with a "manitou" crane from the lorry to its final position. Figure 7.1 gives an impression of the installation procedure.

Thereafter the electronic wiring was conducted and dummy mirrors were installed. Basic testing took place in the months of August and September. In November 2013 the actual mirrors have been unpacked and integrated into their support frames and the heliostat became fully operational with the actual mirrors in place. The Heliostat saw "first light" on 16 November whereby the mirrors were uncovered for the first time in front of the sun (Figure 7.3). At 12:05 the beam was directed into the laboratory for the first time. Active tracking was implemented and tested thereafter. An inauguration party took place on 2 December 2013. The Heliostat was presented to the PMOD staff and cake was offered.

In December 2013 the MITRA instrument [33, 62] was frequently operated in the Heliostat beam.

In May 2014 a spectro-radiometer was installed in the heliostat beam in order to measure the spectral composition of the heliostat beam, and to compare with the outside spectrum. The results of this experiment is described in Section 5.5.4.

In June 2014 the heliostat has been used for diffraction experiments with DARA apertures (Section 3.6).

It is planned to perform an experiment in order to characterise the homogeneity of the solar light beam provided by the heliostat. This experiment will include two radiometers that are mounted on a platform that can be rotated around the axis of the heliostat beam. The radiometers will simultaneously measure the irradiance from different positions during a measurement day. Thus possible gradients in the Irradiance field can be characterised.

Figure 7.1: Impressions from the installation of the heliostat structure

Figure 7.2: Empty mirror support frame (left) and integration of the mirror into the support frame (right).

Figure 7.3: First light event: Markus Suter taking off the lid of mirror M1 for the first time (left). The laboratory is illuminated (right).

7.3 Tracking Performance

While operating the heliostat, different parameters such as speed and accuracy have been evaluated. First the Heliostat has been tested in passive mode. Figure 7.4 shows the error signals (difference between actual position and desired position) in passive mode for both axes. It can be seen that the secondary axis runs much smoother than the primary axis. The error signal of the secondary axis stays within 0.005 degrees, while the error signal of the primary axis gets as high as 0.05 degrees. This is thought to be caused by a friction problem (Section 7.3.1).

Operation of the heliostat in the active tracking mode is illustrated in Figure 7.5. The same problem as in passive mode arises in active mode: The primary axes has a lot more jitter than the secondary axes. Nevertheless tracking is still well within $\pm$ 0.1° in total. Which is tolerable for most radiometric experiments. Thus the primary axis still fulfils the minimal design goals, while the secondary axis reaches the desired accuracy (secondary design goal).

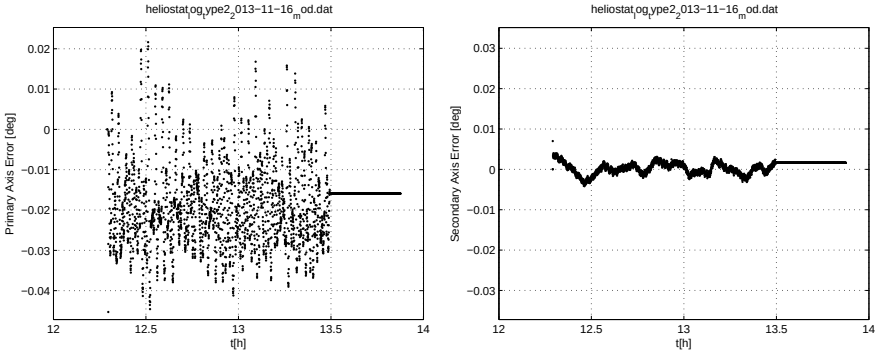

Figure 7.4: Passive mode tracking performance: Error signal of the primary axis on the left, and secondary axis on the right.

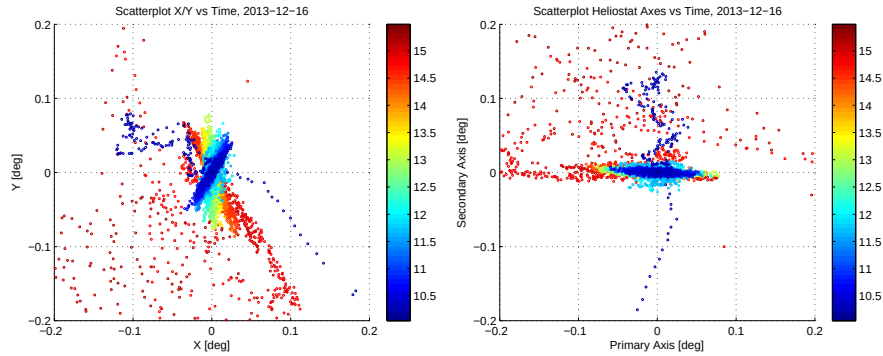

Figure 7.5: Data from the optical sensor (active tracking mode): The left figure shows the position of the sun when looking out of the laboratory through the heliostat mirrors. The

colour indicates the time. On the right figure the data is transformed into the main axes of the heliostat system. It can be seen that the jitter is associated with the primary axis, while the secondary axis is stable.

7.3.1 Friction Problem

The bearing of the heliostat primary axis is a heavy duty 841 mm diameter bearing. It is originally designed to build construction vehicles. The manufacturer however underestimated the friction in the bearing. The estimated friction under the given load conditions have been estimated to be roughly 5 Nm. Measurements however have shown, that the friction is in the order of 50 Nm.

Considering the torsional stiffness of the coupling of 2500Nm/deg, the impact of the friction can be estimated. A moment of torque of 50 Nm would lead to a torsion of 0.02 deg. This is in the order of the observed jitter and supports the assumption of the friction as the source of the problem.

In order to solve this problem, one of the rubber seals at the bearing that was thought to be a major source of friction has been removed. This however had no relevant impact on the friction.

A proposed solution is to pretension the bearing in the froward direction, in order to reduce the moment of torque that the motor needs to pass via the coupling.

7.4 Alignment

In order to calculate the required mirror position from the current sun coordinates, the alignment parameters of the system need to be evaluated. This has been done by geometrical levelling, and measurement. Operating the heliostat for longer time periods reveals slight drift between the sun-sensor guided position and the calculated position of almost 0.1 degrees per hour.

Better knowledge on the alignment parameters will improve the passive tracking accuracy. In order to gain the necessary information on the alignment parameters, the tracking data from different seasons of the year shall be evaluated in the future. The alignment parameter are listed in Table 7.1. There are two parameters for each axis. Two parameters are basically the rotary encoder calibration, whereas the others describe the orientation of the tracking platform with respect to the altitude/azimuth coordinate system.

Accurate knowledge of these parameters will not only improve the passive tracking, but also make the active tracking more robust. The program only allows active tracking if the difference between active tracking position and the calculated (passive) tracking position is smaller than a certain threshold (Section 6.3.2). Therefore inaccurate position calculation due to inaccurate alignment parameters also leads to problems in the active tracking mode.

Variable name	Description
controller.trafoA	Describes the orientation of the heliostat tracking platform in the horizontal plane with respect to north
controller.trafoE	Describes the inclination of the heliostat main axis (primary rotation axis) with respect to the horizontal.
IO_module.Enc_offset_A	Describes the rotation offset that is needed to transform the raw output of the primary axis encoder into the heliostat coordinate system.
IO_module.Enc_offset_E	Describes the rotation offset that is needed to transform the raw output of the secondary axis encoder into the heliostat coordinate system.

Table 7.1: Alignment parameter of the heliostat, the unit of all parameter is degree

Chapter 8

Ideas for Future Improvements of the Radiometer Hardware

Although the development of DARA was a considerable step forward, compared to the previous generation of PMOD's radiometers, there is still room for future improvements. This chapter gives some ideas and considerations for improvements in the future. Most of these issues will need rather long evaluation and development time, and are therefore not applicable for the upcoming CLARA radiometer.

8.1 Cavity

The Cavity as the heart of the radiometer is of course the part of the main interest. To date the manufacturing involves still a lot of handwork. So generally less hand work, better reproducibility, and well defined processes should be favoured when upgrading the design and manufacturing processes.

8.1.1 Coating

A replacement of the coating of the cavity is necessary. The Aeroglaze z302 paint that has been used to coat the DARA cavities as well as the cavities of later PMO6 series is no longer available and therefore needs to be replaced in any case. For the CLARA radiometer the Aeroglaze z302 coating had been replaced by the MAP PU1 coating (diffuse). The result is not yet very convincing, as the overall reflectivity compared to DARA more than doubles, and because the absorptivity is sensitive to the pointing of the instrument [75]. Therefore the search for a new coating will remain an important issue. Replacing the coating, different aspects should be considered:

- **Space approved:** The coating should meet specifications on out-gassing and resistivity against the space environment.
- **Manufacturing:** The shape of the cavity cone limits the possible application of coatings. The coating must be placed inside the cavity, this procedure can be much more complicated than coating a flat surface. Especially vapour deposition coatings or for example the growing of carbon nano-tubes inside the cavity could be very challenging. Therefore a lacquer that can be sprayed inside the cavity remains the simplest and most economic solution. Although with a lacquer difficulties have also

been experienced when coating the very tip of the cavity, where too much or too little of the paint will lead to higher reflectivity of the tip.

- **Degradation:** Exposition to the space environment will lead to degradation of the cavity coating. This has been described for example by Anklin et. al. [77] for the VIRGO radiometers. A future coating should be more resistant against these degradation processes, and degradation processes should be studied on ground beforehand.

- **Gloss versus diffuse:** A further issue to consider is, weather to use a coating that has a glossy or a matt surface. While the glossy surface leads to forward reflections and thus the geometry of the cavity can capture the reflected light efficiently (Section 3.3), a matt surface leads to diffuse reflections that are not captured very efficiently with the actual cavity shape. Thus the question of the coating type also rises the question of the ideal cavity shape, that is definitely different for these two cases. Another argument that has to be considered is that the degradation (decrease in cavity absorptivity) can not only be introduced by a lower absorptivity of the coating, but also by a loss of gloss, and thus increased diffuse reflectivity. This argument favours diffuse coating despite the less efficient capturing of the reflected part of the light.

- **Spectral Flatness:** A further requirement for the coating is that it has similar absorbance properties throughout the solar spectrum. Otherwise the cavity's absorptivity will become spectrum dependent and make especially ground based calibrations very difficult.

8.1.2 Cavity Shape and Heater

The question of the cavity's ideal shape has already been raised in the previous section. Furthermore, also the type of heater that is to be integrated in the cavity, is worth some thoughts.

- **Cavity shape:** If a diffuse reflecting coating is considered, then the shape of the cone could be redesigned, possibly with the application of new coatings and heater elements in mind. A new shape could also open new possibilities from the manufacturing perspective.

- **Heater resistance:** As a consequence from the lead heating studies (Section 3.4) and from the evaluation of the heater resistance (Section 3.2.9) it is recommended to increase the ohmic resistance of the cavity heater. For technical reasons a value of 400 Ω is considered, in order to avoid the voltages to become to high.

- **Design of the heater foil:** A new heater foil, for future radiometers, that consists of two segments with slightly different power dissipation per area, has been designed within this work. The new design fits the power deposited by radiation better than the non segmented heater used by DARA and thus further reduces the non equivalence (Section 3.7). This heater design however might become obsolete if the glossy coating will be replaced by a diffuse coating.

- **Embedded heater:** On the long run it might be worth to consider an embedded heater. This could be done for example by means of physical vapour deposition. In this manner a heater structure could be applied directly onto an isolating layer in the cavity. No glue would be necessary. As long as the cavity shape is conical this might be too difficult, but if the cavity shape changes the option of an embedded heater should be reconsidered.

8.1.3 Thermometers

The cavity thermometers that consist of a very thin copper wire (Section 2.4.3) are well established in PMOD's radiometer technology. They have been proven very reliable and especially the trimming to the desired resistance can be done quite easily by shortening the wires accordingly.

The downside of this thermometer technology is, that the manufacturing process is done completely by hand and therefore quite arduous. Furthermore there have been problems in PMO6 radiometers, arising from poor soldering joints, of this thin wire. Such poorly soldered joints can cause serious malfunction of the instrument at a later stage of life. While this can easily be repaired at ground based radiometers, there is no possibility to save an instrument should such an event happen in space.

A possible replacement of the copper wires would need to fulfil several requirements. It must be possible to trim the resistance and the manufacturing should be repeatable with high precision and involve less manual work. Furthermore the thermometer element should cover the cavity over the whole circumference.

8.2 Heat Sink

In order to reduce the size of the heat sink structure for the CLARA radiometer, it is considered to remove one ring in the heat link labyrinth structure. This will lower the temperature difference between cavity and heat sink and reduce the time constant slightly, but should not reduce the instruments performance. However the lower thermal mass of the heat sink will make the instrument more sensitive to changes in the thermal environment. Special care to the thermal balance of the thermometer is therefore needed, and fast shutter cycles will become more important (Section 3.9.5).

8.3 Data Acquisition

The DARA data acquisition and its characterisation that is described in Section 3.2 has certainly potential for improvement. Mainly the replacement of voltage reference with more stable and possibly pre-aged components, could improve the accuracy of the data acquisition. Furthermore also some conceptual considerations should be made, for example if it is necessary to continuously sample the voltage drop across the heater. Further details on improving the data acquisition can be found in Section 3.2.10.

Chapter 9

Conclusion and Outlook

The DARA prototype has been tested and studied extensively over the last four years. Teething troubles have been identified and fixed. New insights have been found valuable for the design of the CLARA radiometer on the upcoming NORSAT-1 mission and have already led to further design improvements.

A DARA native scale has been established that allows to perform measurements that are traceable to the SI-base units with an uncertainty of less than 400 ppm (2σ). Furthermore the WRR scale and the SI-cryogenic laboratory scale has been implemented in DARA. Thus DARA is the first radiometer having these three scales properly and consistently implemented[1].

9.1 Design Improvements and Characterisation

The characterisation of DARA has led to extensive theoretical studies which have improved the understanding of PMOD's radiometers substantially. The characterisation experiments have generally been improved compared to the experiments performed with PMO6 radiometers in earlier work, and are now well established procedures that could be applied to future radiometers.

The DARA design brought new advantages like the digital controller loop that allows much faster measurement cycles than it was possible with PMO6 radiometers. A further major advantage is lower non equivalence value compared to PMO6 radiometers and the deepening of the understanding of non equivalence. This is not only important for space radiometers but especially useful for ground based radiometry.

The absorptivity of the cavity has been identified as the component that dominates the overall uncertainty of the DARA native scale. Not only the experimental determination of the absorptivity needs to be improved, also the absorptivity itself needs to be reduced, which would automatically lead to a lower uncertainty. Furthermore the degradation process needs to be further investigated, degradation tracking and degradation prevention will be the most important follow up task to this work. Investigation on the process of degradation of the cavity coating and comparison of different coatings will be crucial to further reduce uncertainties in TSI measurements. If the uncertainty of the reflectivity

[1] The SORCE/TIM flight spare instrument that is now the TCTE/TIM had been compared to the WRR at the IPC-XI in 2010. However this measurement would have stated that the TIM's WRR scale reads lower than its native scale which is in contradiction to all other recent scale comparisons. No final conclusion has bee drawn from this comparison so far [54, 96].

can be reduced to the level of the other uncertainty components, a overall uncertainty of the DARA native scale in the order of 100 ppm (1σ) seems possible.

9.2 Comparison between the Irradiance Scales

Having three irradiance scales (native, WRR, SI-cryogenic laboratory) implemented in DARA, the scales have been compared. Good agreement has been found between the DARA native scale and SI-cryogenic laboratory scale. Between these two scales and the WRR scale a relative difference of 0.31% has been found, the instrument reading higher using the WRR scale. This is in good agrement with the findings of Fehlman et. al [56].

In connection with future comparisons at TRF it would be desirable to study the diffraction effects at TRF in detail, either theoretically ore experimentally.

9.3 Satellite Measurements

DARA has proven the concept of a light weight solar radiometer for space application. A new generation of light-weight radiometers will be valuable for TSI monitoring on a relatively "low" budget on small satellites in the future. The CLARA radiometer on NORSAT-1 will be the first of these radiometers, based on the DARA prototype to measure TSI from a small low budget satellite.

The uncertainties for the different scales implemented in DARA can be compared on the base of a hypothetical satellite based TSI measurement. The uncertainties of the scales are 180 ppm for the native, 370 ppm for the WRR (with respect to WRR) and 220 ppm for SI cryogenic laboratory scale, all on the 1σ level. These values are valid under the assumption that no further uncertainties are introduced due to environmental conditions on the satellite.

Whether this absolute accuracy is already good enough to detect a possibly upcoming grand minimum state of the sun depends on how much lower the TSI will be in such a minimum state, which is still under debate and model results differ heavily as discussed in the Introduction. The accuracy requirements of 0.01% as discussed in Section 1.1.4 are not yet met by the DARA native scale, however if the main uncertainty that results from the reflectivity can be significantly reduced in upgraded versions of DARA, this goal sems to be reachable.

9.4 Heliostat

The planning and construction of the heliostat have been finished and the heliostat has been installed, commissioned and used for first experiments. The overall performance of the heliostat is satisfactory, some problems however still need to be solved. From a bookkeepers point of view the project was very successful, the spendings were only slightly over the budget (3%).

The design study optimised the heliostat to the needs of radiometry. The optimal compromise between operational time, field of view, mirror size and tracking system could be found. Reliable industry partners made it possible to successfully realise the project.

9.4.1 Performance and Necessary Improvements

The Heliostat has been operated on several occasions. The motion control concept, as well as the software have proven reliable. The main problem that has been encountered is the high friction of the primary axis bearing that has been underestimated. It leads to a reduced accuracy of the heliostat pointing and beam stability. Thus the heliostat only

meets the basic requirements on pointing accuracy. Therefore the tracking accuracy needs to be improved, a solution with pre tensioning has been proposed.

Furthermore to improve the passive racking performance, the alignment parameters need small adjustment, these adjustments will be deduced from the positioning data collected during operation.

An experiment to check the homogeneity of the heliostat beam has been proposed in order to make the heliostat ready for upcoming experiments.

9.4.2 Experiments with the Heliostat

With the heliostat, PMODs capabilities in calibrating and characterising radiometers have been improved. The first applications have been the visualisation of diffraction effects at the DARA apertures and characterising of the MITRA instrument. The heliostat will be a valuable tool for the upcoming calibration of the CLARA space radiometer. A first experiment with CLARA will be the determining of the air to vacuum ratio, using the heliostat beam.

References

[1] D. L. Hartmann, A. M. G. Klein Tank, M. Rusticucci, L. V. Alexander, S. Brönnimann, Y. Charabi, F. J. Dentener, E. J. Dlugokencky, D. R. Easterling, A. Kaplan, B. J. Soden, P. W. Thorne, M. Wild, and P.M. Zhai. Observations: Atmosphere and Surface. In T. F. Stocker, D. Qin, G. K Plattner, M. Tignor, S. K. Allen, J. Boschung, A. Nauels, Y. Xia, V. Bex, and P. M. Midgley, editors, *Climate Change 2013: The Physical Science Basis. Contribution of Working Group I to the Fifth Assessment Report of the Intergovernmental Panel on Climate Change*. Cambridge University Press, Cambridge, UK and New York, USA, 2013.

[2] U. Cubasch, D. Wuebbles, D. Chen, M. C. Facchini, D. Frame, N. Mahowald, and J. G. Winther. Introduction. In T. F. Stocker, D. Qin, G. K Plattner, M. Tignor, S. K. Allen, J. Boschung, A. Nauels, Y. Xia, V. Bex, and P. M. Midgley, editors, *Climate Change 2013: The Physical Science Basis. Contribution of Working Group I to the Fifth Assessment Report of the Intergovernmental Panel on Climate Change*. Cambridge University Press, Cambridge, UK and New York, USA, 2013.

[3] S. K. Solanki, N. A. Krivova, and J. D. Haigh. Solar Irradiance Variability and Climate. *Annual Review of Astronomy and Astrophysics*, 51:311–351, August 2013.

[4] G. Myhre, D. L. Shindel, F. M. Bréon, W. Collins, J. Fuglestvedt, J. Huang, D. Koch, J. F. Lamarque, D. Lee, B. Mendoza, T. Nakajima, A. Robock, G. Stephens, T. Takemura, and H. Zhang. Anthropogenic and Natural Radiative Forcing. In T. F. Stocker, D. Qin, G. K Plattner, M. Tignor, S. K. Allen, J. Boschung, A. Nauels, Y. Xia, V. Bex, and P. M. Midgley, editors, *Climate Change 2013: The Physical Science Basis. Contribution of Working Group I to the Fifth Assessment Report of the Intergovernmental Panel on Climate Change*. Cambridge University Press, Cambridge, UK and New York, USA, 2013.

[5] J. A. Eddy. The Maunder Minimum. *Science*, 192:1189–1202, June 1976.

[6] M. Stuiver. Variations in Radiocarbon Concentration and Sunspot Activity. *Journal of Geophysical Research*, 66:273–276, January 1961.

[7] M. Stuiver and P. D. Quay. Changes in Atmospheric Carbon-14 Attributed to a Variable Sun. *Science*, 207:11–19, 1980.

[8] J. Beer, A. Blinov, G. Bonani, R. C. Finkel, H. J. Hofmann, B. Lehmann, H. Oeschger, A. Sigg, J. Schwander, T. Stafelbach, B. Stauffer, M. Suter, and W. Wölfli. Use of Be-10 in Polar Ice to Trace the 11-year Cycle of Solar Activity. *Nature*, 347:164–166, September 1990.

[9] M. Stuiver and T. F. Braziunas. Sun, Ocean, Climate and Atmospheric $^{14}CO_2$: An Evaluation of Causal and Spectral Relationships. *The Holocene*, 3(4):289–305, 1993.

[10] R. C. Willson, H. S. Hudson, C. Fröhlich, and R. W. Brusa. Long-Term Downward Trend in Total Solar Irradiance. *Science*, 234:1114–1117, November 1986.

[11] R. C. Willson and H. S. Hudson. Solar Luminosity Variations in Solar Cycle 21. *Nature*, 332:810–812, April 1988.

[12] J. Beer, K. McCracken, and R. von Steiger. *Cosmogenic Radionuclides : Theory and Applications in the Terrestrial and Space Environments*. Physics of Earth and Space Environments. Springer Verlag, 2012.

[13] I. G. Usoskin, S. K. Solanki, and G. A. Kovaltsov. Grand Minima and Maxima of Solar Activity: New Observational Constraints. *Astronomy and Astrophysics*, 471:301–309, August 2007.

[14] F. Steinhilber and J. Beer. Prediction of Solar Activity for the Next 500 Years. *Journal of Geophysical Research (Space Physics)*, 118:1861–1867, May 2013.

[15] G. Feulner and S. Rahmstorf. On the Effect of a new Grand Minimum of Solar Activity on the Future Climate on Earth. *Geophysical Research Letters*, 37:5707, March 2010.

[16] J. G. Anet, E. V. Rozanov, S. Muthers, T. Peter, S. Brönnimann, F. Arfeuille, J. Beer, A. I. Shapiro, C. C. Raible, F. Steinhilber, and W. K. Schmutz. Impact of a Potential 21st Century "Grand Solar Minimum" on Surface Temperatures and Stratospheric Ozone. *Geophysical Research Letters*, 40:4420–4425, August 2013.

[17] A. I. Shapiro, W. Schmutz, E. Rozanov, M. Schoell, M. Haberreiter, A. V. Shapiro, and S. Nyeki. A New Approach to the Long-Term Reconstruction of the Solar Irradiance Leads to Large Historical Solar Forcing. *Astronomy and Astrophysics*, 529:A67, May 2011.

[18] G. Kopp. An Assessment of the Solar Irradiance Record for Climate Studies. *Journal of Space Weather and Space Climate*, 4(27):A14, April 2014.

[19] Committee on Evaluating NOAAs Plan to Mitigate the Loss of Total Solar Irradiance Measurements from Space; Board on Atmospheric Sciences, Climate; Division on Earth, and Life Studies; National Research Council. *Review of NOAA Working Group Report on Maintaining the Continuation of Long-Term Satellite Total Irradiance Observations*. National Academies Press, Washington DC, USA, 2013.

[20] N. Fox, A. Kaiser-Weiss, W. Schmutz, K. Thome, D. Young, B. Wielicki, R. Winkler, and E. Woolliams. Accurate Radiometry from Space: an Essential Tool for Climate Studies. *Philosophical Transactions of the Royal Society A: Mathematical, Physical and Engineering Sciences*, 369(1953):4028–4063, October 2011.

[21] GCOS Secretariat. *Systematic Observation Requirements for Satellite-based Data Products for Climate, 2011 Update*. GCOS-154, World Meteorological Organisation (WMO), Genève CH, 2011.

[22] Commission for Instruments and Methods of Observation (CIMO). *Guide to Meteorological Instruments and Methods of Observation* . World Meteorological Organisation (WMO), Genève CH, 2008.

[23] Organisation Intergouvernementale de la Convention du Mètre. *Le Système International d'Unités (SI)*. Bureau International des Poids et Mesures, Paris FR, 2006.

[24] International Astronomical Union (IAU) Division I Working Group. Numerical Standards for Fundamental Astronomy: Astronomical Constants. http://maia.usno.navy.mil/NSFA/index.html, access: 28 July, 2014.

[25] S. Schlamminger, E. Holzschuh, W. Kündig, F. Nolting, R. E. Pixley, J. Schurr, and U. Straumann. Measurement of Newton's Gravitational Constant. *Physical Review D*, 74(8):082001, October 2006.

[26] B. N. Taylor and T. J. Witt. New International Electrical Reference Standards Based on the Josephson and Quantum Hall Effects. *Metrologia*, 26:47–62, January 1989.

[27] I. M. Mills, P. J. Mohr, T. J. Quinn, B. N. Taylor, and E. R. Williams. Adapting the International System of Units to the Twenty-First Century. *Philosophical Transactions of the Royal Society A: Mathematical, Physical and Engineering Sciences*, 369(1953):3907–3924, October 2011.

[28] C. Fröhlich. History of Solar Radiometry and the World Radiometric Reference. *Metrologia*, 28:111–115, January 1991.

[29] N. P. Fox and J. P. Rice. 2. Absolute Radiometers. In A C. Parr, R. U. Datla, and J. L. Gardner, editors, *Optical Radiometry. Series: Experimental Methods in the Physical Sciences*, volume 41, pages 35–96. Elsevier, 2005.

[30] R. Goebel, M. Stock, and R. Köhler. *Report on the International Comparison of Cryogenic Radiometers Based on Transfer Detectors*. Rapport BIPM 2000-9, Bureau International des Poids et Mesures, Paris FR, 2000.

[31] G. Kopp, K. Heuerman, D. Harber, and G. Drake. The TSI Radiometer Facility: Absolute Calibrations for Total Solar Irradiance Instruments. In J. J. Butler and J. Xiong, editors, *Society of Photo-Optical Instrumentation Engineers (SPIE) Conference Series*, volume 6677, October 2007.

[32] R. Winkler. *Cryogenic Solar Absolute Radiometer - a Potential SI Standard for Solar Irradiance*. PhD thesis, University College London UK, 2013.

[33] A. Fehlmann. *Metrology of Solar Radiometry*. PhD thesis, Universität Zürich CH, 2011.

[34] C. S. M. Pouillet. *Mémoire sur la chaleur solaire, sur les pouvoirs rayonnants et absorbants de l'air atmosphérique, et sur la température de l'espace*. Bachelier, Paris FR, 1838.

[35] K. Ångström. Über absolute Bestimmungen der Wärmestrahlung mit dem elektrischen Compensationspyrheliometer, nebst einigen Beispielen der Anwendung dieses Instrumentes. *Annalen der Physik*, 303:633–648, 1899.

[36] A. A. Kmito and Yu. A. Sklyarov. *Pyrheliometry*. Amerind Publishing, New Dehli, IN, 1987. Translated from Russian.

[37] K. L. Yeo, N. A. Krivova, and S. K. Solanki. Solar Cycle Variation in Solar Irradiance. *Space Science Reviews*, July 2014.

[38] P. Zacharias. An Independent Review of Existing Total Solar Irradiance Records. *Surveys in Geophysics*, 35:897–912, July 2014.

[39] C. Fröhlich, J. Romero, H. Roth, C. Wehrli, B. N. Andersen, T. Appourchaux, V. Domingo, U. Telljohann, G. Berthomieu, P. Delache, J. Provost, T. Toutain, D. A. Crommelynck, A. Chevalier, A. Fichot, W. Däppen, D. Gough, T. Hoeksema, A. Jiménez, M. F. Gómez, J. M. Herreros, T. R. Cortés, A. R. Jones, J. M. Pap, and R. C. Willson. VIRGO: Experiment for Helioseismology and Solar Irradiance Monitoring. *Solar Physics*, 162:101–128, December 1995.

[40] C. Fröhlich, D. A. Crommelynck, C. Wehrli, M. Anklin, S. Dewitte, A. Fichot, W. Finsterle, A. Jiménez, A. Chevalier, and H. Roth. In-Flight Performance of the Virgo Solar Irradiance Instruments on SOHO. *Solar Physics*, 175:267–286, October 1997.

[41] G. Kopp, G. Lawrence, and G. Rottman. The Total Irradiance Monitor (TIM): Science Results. *Solar Physics*, 230:129–139, August 2005.

[42] G. Thuillier, S. Dewitte, W. Schmutz, and Picard Team. Simultaneous Measurement of the Total Solar Irradiance and Solar Diameter by the PICARD Mission. *Advances in Space Research*, 38:1792–1806, January 2006.

[43] W. Schmutz, A. Fehlmann, W. Finsterle, G. Kopp, and G Thuillier. Total Solar Irradiance Measurements with PREMOS/PICARD. In R. F. Cahalan and J. Fischer, editors, *Radiation Processes in the Atmosphere and Ocean (IRS2012): Proceedings of the International Radiation Symposium (IRC/IAMAS), AIP Conference Proceedings*, volume 1531, pages 624–627, 2013.

[44] Total Solar Irradiance Calibration Transfer Experiment (TCTE). http://lasp.colorado.edu/home/tcte, access: 22 July, 2014.

[45] H. L. Kyle, D. V. Hoyt, and J. R. Hickey. A Review of the Nimbus-7 ERB Solar Dataset. *Solar Physics*, 152:9–12, June 1994.

[46] R. C. Willson. Solar Total Irradiance Observations by Active Cavity Radiometers. *Solar Physics*, 74:217–229, November 1981.

[47] R. C. Willson, S. Gulkis, M. Janssen, H. S. Hudson, and G. A. Chapman. Observations of Solar Irradiance Variability. *Science*, 211:700–702, February 1981.

[48] R. C. Willson. Irradiance Observations of SMM; Spacelab 1; UARS; and ATLAS Experiments. In J. M. Pap, C. Frohlich, H. S. Hudson, and S. K. Solanki, editors, *Proceedings from IAU Colloquium 143: The Sun as a Variable Star: Solar and Stellar Irradiance Variations*, pages 54–62, 1994.

[49] R. B. Lee, III, M. A. Gibson, N. Shivakumar, R. Wilson, H. L. Kyle, and A. T. Mecherikunnel. Solar Irradiance Measurements - Minimum Through Maximum Solar Activity. *Metrologia*, 28:265–268, 1991.

[50] R. C. Willson. ACRIM3 and the Total Solar Irradiance Database. *Astrophysics and Space Science*, 352:341–352, August 2014.

[51] G. Kopp. Greg Kopp's TSI Page. http://spot.colorado.edu/~koppg/TSI/, access: 14 July, 2014.

[52] G. Kopp, W. Ball, S. Dewitte, A. Fehlmann, A. Finsterle, C. Fröhlich, Mekaoui S., W. Schmutz, R. Willson, and P. Zacharias. An Assessment of the Accuracies and Uncertainties in the Total Solar Irradiance Climate Data Record. http://www.issibern.ch/teams/solarirradiance/, access: 10 July, 2014.

[53] G. Kopp and J. L. Lean. A New, Lower Value of Total Solar Irradiance: Evidence and Climate Significance. *Geophysical Research Letters*, 38:1706, January 2011.

[54] G. Kopp, A. Fehlmann, W. Finsterle, D. Harber, K. Heuerman, and R. Willson. Total Solar Irradiance Data Record Accuracy and Consistency Improvements. *Metrologia*, 49:29–33, April 2012.

[55] J. J. Butler, B. C. Johnson, J. P. Rice, E. L. Shirley, and R. A. Barnes. Sources of Differences in On-Orbital Total Solar Irradinace Measurements and Description of a Proposed Laboratory Intercomparison. *Journal of Research of the National Institute of Standards and Technology*, 113(4):187–203, August 2008.

[56] A. Fehlmann, G. Kopp, W. Schmutz, R. Winkler, W. Finsterle, and N. Fox. Fourth World Radiometric Reference to SI Radiometric Scale Comparison and Implications for On-Orbit Measurements of the Total Solar Irradiance. *Metrologia*, 49:34–38, March 2012.

[57] P. Brekke and M. Osmundsen. Norsat-1: Total solar irradiance, space weather and ship detection. Sorce Science Meeting 2014: http://lasp.colorado.edu/media/projects/SORCE/meetings/2013/presentations/Web_S6/07_Brekke-norsat_Update%20-%20Copy.pdf, access: 25 June, 2014.

[58] G. Kopp, K. Heuerman, and G. Lawrence. The Total Irradiance Monitor (TIM): Instrument Calibration. *Solar Physics*, 230:111–127, August 2005.

[59] R. W. Brusa and C. Fröhlich. Absolute Radiometers (PMO6) and their Experimental Characterisation. *Applied Optics*, 25:4173–4180, 1986.

[60] ISO. *Guide to the Expression of Uncertainty in Measurement (GUM)*. International Organisation for Standardization, Genève CH, 1 edition, 1995.

[61] L. Kirkup. A guide to GUM. *European Journal of Physics*, 23:483–487, September 2002.

[62] B. Walter, A. Fehlmann, W. Finsterle, R. Soder, M. Suter, and W. Schmutz. Integral Window Transmittance Measurements for a Cryogenic Solar Absolute Radiometer. *Metrologia*, Submitted, 2014.

[63] G. Kopp and G. Lawrence. The Total Irradiance Monitor (TIM): Instrument Design. *Solar Physics*, 230:91–109, August 2005.

[64] M. Suter. *Experimentelle Charakterisierung des Einflusses der Blendenerwärmung auf das Messresultat von PMO6 Absolutradiometern*. Bachelor's thesis, Universität Zürich CH, 2007.

[65] Lord Corporation. Aeroglaze Z302 Absorptive Polyurethane Black, Data Sheet (Rev.2 4/04). Lord Corporation, Erie PA, USA, 2004.

[66] DMK/DPK. *Formeln und Tafeln: Mathematik - Physik*. Orell Füssli Verlag, Zürich CH, 7 edition, 1997.

[67] R. W. Brusa. *Solar Radiometry*. PhD thesis, ETH Zürich CH, 1983.

[68] General Carbide. The Designer's Guide to Tungsten Carbide. http://www.generalcarbide.com/PDF /Designer-Guide.pdf, access: 3 July, 2014.

[69] Hewlet-Packard. 3458A Multimeter User's Guide. Hewlet Packard Company, Loveland CO, USA, February 1994.

[70] Vishay. VHP100 Data Sheet. Vishay Precision Group, Malvern PA, USA, March 2010.

[71] Analog Devices. Precision Voltage References REF01/REF02/REF03 Data Sheet. Analog Devices Inc, Norwood MA, USA, 2010.

[72] C. Brazil. *Application Note 713: The Effect of Long-Term Drift on Voltage References*. Analog Devices Inc, Norwood MA, USA, 2004.

[73] Labsphere. Technical Guide: Integrating Sphere Theory and Applications. http://www.labsphere.com/uploads/technical-guides/a-guide-to-integrating-sphere-theory-and-applications.pdf, access: 30 June, 2014.

[74] D. Meschede. *Gerthsen Physik*. Springer Verlag, 22 edition, 2004.

[75] I. Beck. *Determination of the Relative Absorbance of Cavities for a Solar Radiometer*. Bachelor's thesis, Universität Zürich CH, 2014.

[76] R. L. Kurucz. Synthetic Infrared Spectra. In D.M. Rabin, J.T. Jefferies, and C. Lindsey, editors, *Infrared Solar Physics*, volume 154 of *International Astronomical Union /Union Astronomique Internationale*, pages 523–531. Springer Netherlands, 1994.

[77] M. Anklin, C. Frohlich, W. Finsterle, D. A. Crommelynck, and S. Dewitte. Assessment of Degradation of VIRGO Radiometers on Board SOHO. *Metrologia*, 35:685–688, 1998.

[78] E. Lommel. *Die Beugungserscheinungen einer kreisrunden Oeffnung und eines kreisrunden Schirmchens theoretisch und experimentell*. Verlag der königlichen Akademie, München DE, 1 edition, 1884.

[79] E. L. Shirley. 9. Diffraction Effects in Radiometry. In A C. Parr, R. U. Datla, and J. L. Gardner, editors, *Optical Radiometry. Series: Experimental Methods in the Physical Sciences*, volume 41, pages 409–451. Elsevier, 2005.

[80] E. L. Shirley. Revised Formulas for Diffraction Effects with Point and Extended Sources. *Applied Optics*, 37:6581–6590, October 1998.

[81] W. H. Steel, M. De, and J. A. Bell. Diffraction Corrections in Radiometry. *Journal of the Optical Society of America (1917-1983)*, 62:1099–1103, September 1972.

[82] E. Wolf. Light Distribution Near Focus in an Error-Free Diffraction Image. *Royal Society of London Proceedings Series A*, 204:533–548, January 1951.

[83] C. A. Gueymard. Reference Solar Spectra: Their Evolution, Standardization Issues, and Comparison to Recent Measurements. *Advances in Space Research*, 37:323–340, 2006.

[84] D. Bolsée, N. Pereira, W. Decuyper, D. Gillotay, H. Yu, P. Sperfeld, S. Pape, E. Cuevas, A. Redondas, Y. Hernandéz, and M. Weber. Accurate Determination of the TOA Solar Spectral NIR Irradiance Using a Primary Standard Source and the Bouguer-Langley Technique. *Solar Physics*, 289:2433–2457, July 2014.

[85] C. Wehrli. *Extraterrestrial Solar Spectrum*. PMOD Report No 615, Physikalisch-Meteorologisches Observatorium & World Radiation Center (PMO/WRC) Davos Dorf CH, July 1985.

[86] C. A. Gueymard. The Sun's Total and Spectral Irradiance for Solar Energy Applications and Solar Radiation Models. *Solar Energy*, 76:423–453, April 2004.

[87] ASTM. Standard Solar Constant and Zero Air Mass Solar Spectral Irradiance Tables. http://www.astm.org/Standards/E490.htm, access: 3 July, 2014.

[88] B. Mayer and A. Kylling. Technical Note: The libRadtran Software Package for Radiative Transfer Calculations - Description and Examples of Use. *Atmospheric Chemistry and Physics*, 5(7):1855–1877, 2005.

[89] IAP Universität Bern. STARTWAVE Database. http://www.iapmw.unibe.ch/research/projects/STARTWAVE/index.html, access: 3 July, 2014.

[90] M. Troller, A. Geiger, E. Brockmann, and H.-G. Kahle. Determination of the Spatial and Temporal Variation of Tropospheric Water Vapour Using CGPS Networks. *Geophysical Journal International*, 167:509–520, November 2006.

[91] E. L. Shirley, R. Kacker, and R. U. Datla. Diffraction Corrections in Radiometry: A Proposed Method to Estimate Uncertainties. In *Proceedings of the 2002 Measurement Science Conference*, Anaheim, CA, USA, January 2002.

[92] D. M. Harber, K. F. Heuerman, G. A. Kopp, and G. Lawrence. Aperture Edge Scatter Calibration of the Cavity Radiometers for the Spaceflight Total Irradiance Monitor. In J. J. Butler, editor, *Society of Photo-Optical Instrumentation Engineers (SPIE) Conference Series*, volume 6296, September 2006.

[93] A. Wallard, N. Sené, D. Craston, J Williams, and M. Milton. Kaye & Laby Online, Tables of Pysical & Chemical Constants. http://www.kayelaby.npl.co.uk/, access: 28 July, 2014.

[94] M. J. Moran, H. N. Shapiro, Munson B. R., and DeWitt D. P. *Introduction to Thermal Systems Engineering*. John Wiley & Sons, Hoboken, NJ, USA, 1 edition, 2003.

[95] Max Born. *Optik*. Springer Verlag, 3 edition, 1972.

[96] W. Finsterle. *International Pyrheliometer Comparison (IPC-XI), Final Report*. WMO IOM Report No. 108, World Meteorological Organization, Genève CH, 2011.

[97] W. Finsterle, P. Blattner, S. Moebus, I. Rüedi, C. Wehrli, M. White, and W. Schmutz. Third Comparison of the World Radiometric Reference and the SI Radiometric Scale. *Metrologia*, 45:377–381, August 2008.

[98] J. Romero, N. P. Fox, and C. Fröhlich. First Comparison of the Solar and an SI Radiometric Scale. *Metrologia*, 28:125–128, January 1991.

[99] J. Romero, N. P. Fox, and C. Fröhlich. Improved Comparison of the World Radiometric Reference and the SI Radiometric Scale. *Metrologia*, 32:523, May 1996.

[100] M. Suter, W. Finsterle, and G. Kopp. WRR to SI Comparison with DARA. In *Proceedings of the WMO Technical Conference on Meteorological and Environmental Instruments and Methods of Observations (WMO-TECO-2012)*. WMO IOM Report No. 109, 2012.

[101] A. A. Mills. Heliostats Siderostats and Coelostats - a Review of Practical Instruments for Astronomical Applications. *Journal of the British Astronomical Association*, 95:89–99, April 1985.

[102] SIA. *SIA Norm 216 - Einwirkungen auf Tragwerke*. Schweizerischer Ingenieur- und Architektenverein, Zürich CH, 2003.

[103] INTRA Base Unit: Datasheet for Units Equipped with INTRA Controller Board V2. http://www.brusag.ch/DL/INTRA2/DS_0_BaseUnit_icb.pdf, access: 5 August, 2014.

[104] I. Reda and A. Afshin. *Solar Position Algorithm for Solar Radiation Applications*. NREL Technical Report TP-560-34302, National Renewable Energy Laboratory, Golden USA, 2008.

Abbreviations

ACRIM	Active Cavity Radiometer Irradiance Monitor
BBL	Bundesamt für Bauten und Logistik, Bern CH
BIPM	Bureau International des Poids et Mesures, Paris FR
CAN	Controller Area Network
CLARA	Compact Lightweight Absolute Radiometer
CSAR	Cryogenic Solar Absolute Radiometer
DARA	Digital Absolute Radiometer
DIARAD	Differential Absolute Radiometer, part of the VIRGO experiment
EGSE	Electrical Ground Support Equipment
ERB	Earth Radiation Budget, Experiment on the Nimbus-7 satellite
ERBE	Earth Radiation Budget Experiment, on the ERBS satellite
ERBS	Earth Radiation Budget Satellite
ESA	European Space Agency
GCOS	Global Climate Observing System
GUM	Guide to the Expression of Uncertainty in Measurement
HF	Hickey-Frieden Radiometer
IPC	International Pyrheliometer Comparison
IPCC	Intergovernmental Panel on Climate Change
IRMB	Institut Royal Météorologique de Belgique, Bruxelles BE
ISS	International Space Station
ISSI	International Space Science Institute, Bern CH
KIS	Kipenheuer Institut für Sonnenphysik, Freiburg i. B. DE

LASP	Laboratory for Atmospheric and Space Physics, Boulder USA
METAS	Eidgenössisches Institut für Metrologie, Bern CH
MITRA	Monitor to Measure the Integral Transmittance of Windows
NASA	National Aeronautics and Space Administration
NIST	National Institute of Technology, Gaithersburg USA
NORSAT-1	Norwegian Microsatellite
NPL	National Physics Laboratory, Teddington UK
PICARD	Satellite named after Jean Picard(1620-1682)
PMOD	Pysikalisch-Meteorologisches Observatorium Davos, CH
PREMOS	Precision Monitoring Sensor, radiometer on board PICARD
PROBA3	PROBA3 Satellite of ESA
PWM	Pulse Width Modulation
SI	International System of Units
SMM	Solar Maximum Mission, satellite
SNF	Schweizerischer Nationalfonds
SOHO	Solar and Heliospheric Observatory, ESA/NASA satellite
SORCE	Solar Radiation and Climate Experiment satellite
STPSat-3	U.S. Air Force Space Test Program spacecraft
TCTE	Total Solar Irradiance Calibration Transfer Experiment, on board STPSat-3
TIM	Total Irradiance Monitor, instrument on board SORCE
TRF	Total Irradiance Radiometer Facility, at LASP
TSI	Total Solar Irradiance
TSIS	Total Solar Irradiance Sensor
UARS	Upper Atmosphere Research Satellite
VIRGO	Variablilty of the Solar Irradiance and Gravity Oscillations, experiment on board SOHO
VTT	Vacuum Tower Telescope, Teneriffa ESP
WMO	World Meteorological Organisation
WRC	World Radiation Centre, Davos CH
WRR	World Radiometric Reference
WSG	World Standard Group

Appendix A

Electrical Calibration Additional Material

A.1 Calibration Figures

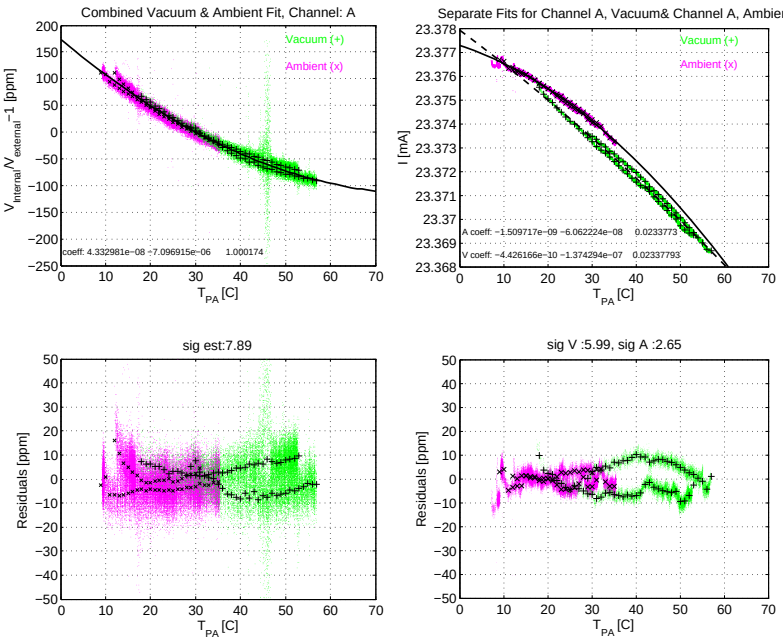

Figure A.1: Voltage (left) and current (right) calibration curves for data acquisition channel A (2011)

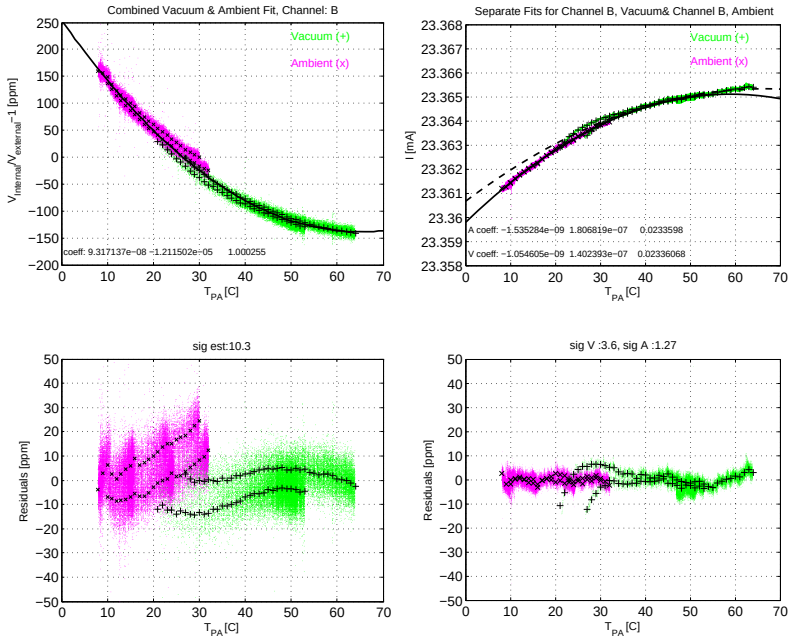

Figure A.2: Voltage (left) and current (right) calibration curves for data acquisition channel B (2011)

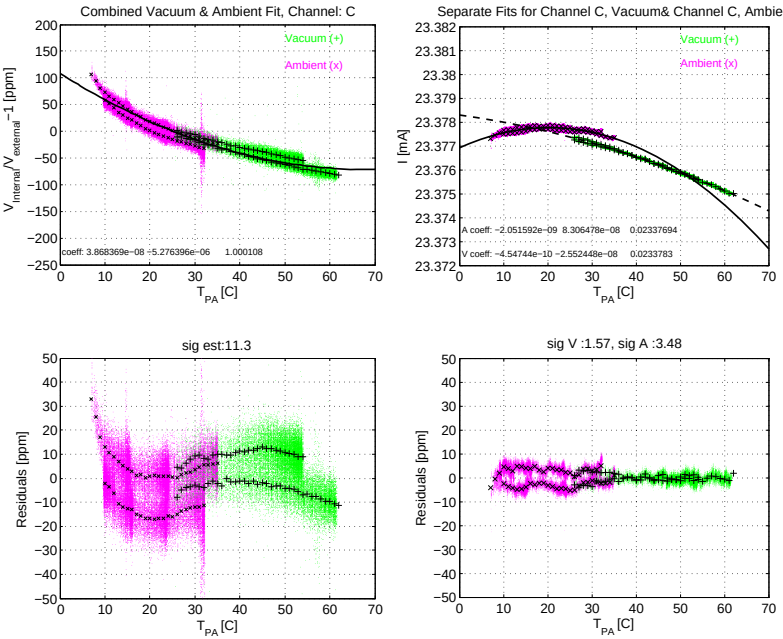

Figure A.3: Voltage (left) and current (right) calibration curves for data acquisition channel C (2011)

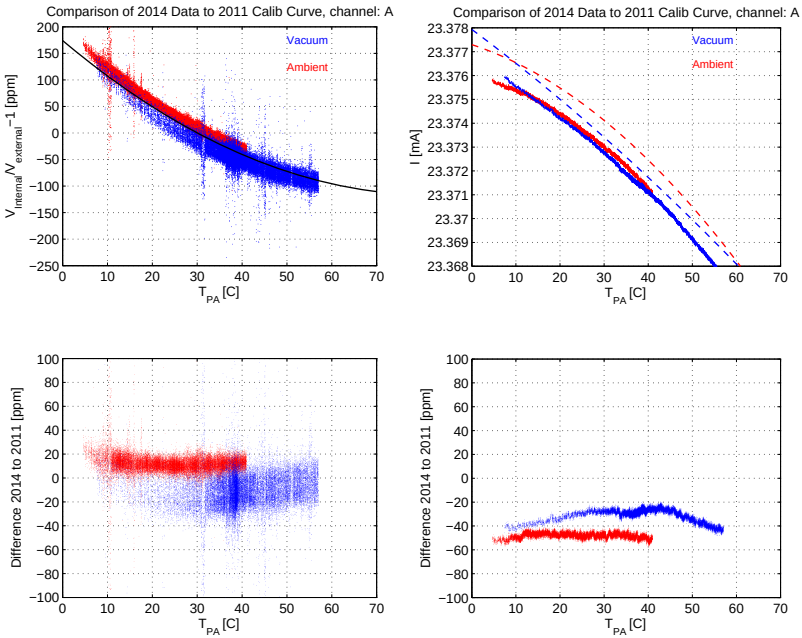

Figure A.4: Comparison of the 2014 calibration with the original implemented calibration curve from 2011 for channel A voltage (left) and current (right)

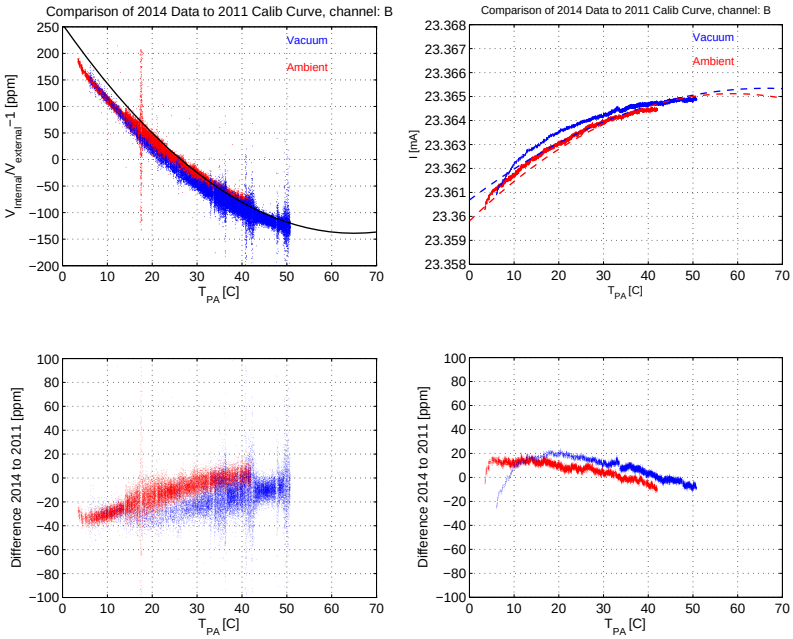

Figure A.5: Comparison of the 2014 calibration with the original implemented calibration curve from 2011 for channel B voltage (left) and current (right)

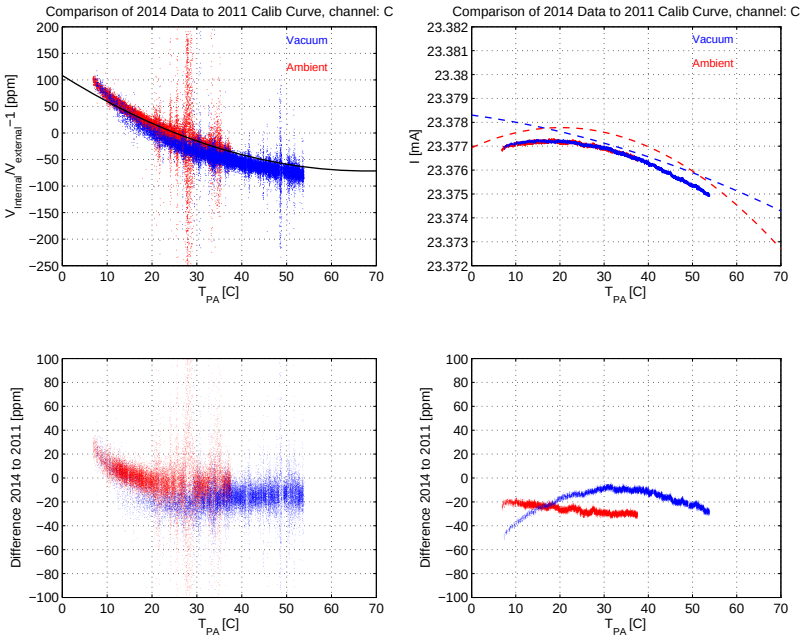

Figure A.6: Comparison of the 2014 calibration with the original implemented calibration curve from 2011 for channel C voltage (left) and current (right)

A.2 Note to the Current Measurement

DARA is designed to also make a current measurement at the very beginning of a measurement series. There is even a dedicated ADC channel for this purpose. This current value is then used to compute internally the power level at the cavity heaters. This measurement has been found very unreliable. It is even a major error source for the measurement result. In an external data analysis this measurement needs to be compensated. Thus equation 3.7 becomes:

$$C_{UI}(T) = C_U(T) \cdot \frac{I_{cal}(T)}{I_{meas}} \tag{A.1}$$

where C_U is a correction factor for the U measurement, I_{cal} is the current as measured in the calibration measurements and I_{meas} is the internal (single) measurement that needs to be compensated.

The actual application of this correction is a rather arduous task, as these internal current measurements are not stored in the DARA data structure. They need to be extracted from the log file of the serial communication.

Appendix B

Additional Notes to the Calibration at TRF

Instrument Breakdown and Repair

When the instrument was first placed in the TRF vacuum chamber it did not show any abnormal behaviour. However after several hours in vacuum (in stand-by mode) the instrument's power consumption had risen significantly. The instrument could not be operated in measurement mode and had to be taken out of the vacuum tank. A look inside the instruments electronics revealed the driver stage of the cavity heaters as the source of the additional power dissipation. All of the involved transistors have been found damaged. The transistors have been replaced, however these transistors burned as well, shortly after the next power on. This event occurred at ambient pressure. It is not yet clear why it was happening. As the first event could be explained with a heat build-up in vacuum, the second event needs another explanation.

It was then decided to remove the amplifier stage and directly drive the cavity heaters with the operational amplifier output. This has proven reliable. However we had to assume that the rise time of the PWM signal had increased due to the modification. This means that the PWM duty cycle should be kept within a certain range. Too low or too high duty cycles could lead to discrepancies between the nominal duty cycle and the applied heater power. Further investigations have been carried out later at PMOD. It has been found that the raise time is still fast enough(Section 3.2.7).

The amplifier stage was designed in a way to offer very fast rise times for the PWM signal. This however on the cost of a continuous power dissipation at the transistors, which could have led to an overheating and to permanent damage and instrument failure.

Notes to the Controller Loop Performance

The digital controller loop of the DARA heaters showed some abnormal behaviour during the TRF calibration campaign. First the controlled signal was rather nervous and showed signs of oscillations, and secondly the transition wiggles in the power signal showed very abnormal behaviour and evolved from one period to the next. The reason for this was thought first to be a change in the controlled system, that is most likely the higher time constant of the cavity in vacuum. The problem could be partly solved by adjusting the PI-parameters of the controller loop, and also by adjusting the DARA open/closed cycles from 15/15s to 30/30s.

While this procedure helped a lot to improve the measurements in power mode, the measurements in irradiance mode are still a lot noisier (see Figure 4.3). It is not obvious what could cause this noise. The only difference between power and irradiance mode is that the laser beam moves in and out of the cavity at a frequency of 24 Hz. This means that the optical signal that actually goes into the cavity is modulated at that frequency. As the controller operating/updating frequency is 20 Hz, the question is if there is a beat frequency that is stimulated by this configurations. While adjustments of the controller parameter could improve the performance, the performance level of the measurements in power mode could not be achieved, with this procedure.

Further investigation in this direction would be very interesting and helpful for future TRF comparisons. It shall be noted here that similar effects had been found earlier by Fehlmann when calibrating PMO6-PREMOS at TRF. A detailed discussion can be found in [33].

Appendix C

Heliostat Operating Instructions

C.1 Begin of Operation

The weather situation needs to be checked. The heliostat should only be operated in good weather conditions.

C.1.1 Unpacking

Removal of Snow or Water

- In Winter, remove snow from the top (1) as well as from mirror M1. In summer, remove possible rainwater.

- Shake the spindle cover (2) to get possible water out.

Figure C.1: Covered heliostat

Removal of the Rain Cover

- First the top cover is removed. Open the zippers on both sides. Then roll up the cover. Fix the cover with the designated straps (1). Then roll up the back cover on the window side in the same manner.

- Open the zipper of the mirror M1 cover. Unclamp the cover on the bottom. Roll over the cover and store it in front of the mirror socket (2).

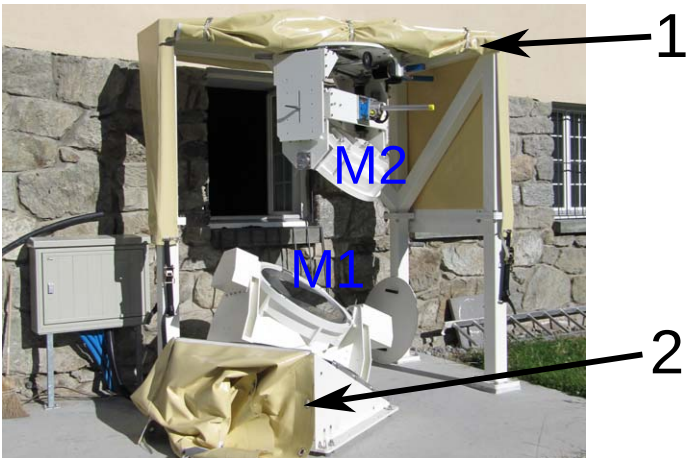

Figure C.2: Uncovered heliostat

C.2 Tracking

C.2.1 Preparation

- Start the control computer (use wsg-user account)

- Open the web browser and call the camera live-stream

- Turn on the heliostat power supply. If the power supply does not start up, check if the security button, in the control cabinet next to the heliostat, is released.

-

C.2.2 Start Tracking

- Start MATLAB. Click “Start Heliostat” in the MATLAB-toolbar.

- Select passive tracking in the GUI

- Open the real time data window to see the tracking position

C.3 Removal of the Mirror Cover

- If the heliostat has not been used for a longer period, dust has accumulated on the backside of the M2 mounting. If so, the dust should be wiped off before removing the covers.
- The mirror M2 is uncovered first.
- One person should hold the cover while a second person removes the wing nuts. Then carefully remove the cover.
- Mirror M1 is uncovered after M2. It should be done soon after uncovering M2. Otherwise M2 could fog up while not illuminated. Remove the wing nuts and lift the cover carefully.
- The covers should be stored in a safe and clean place.
- After removing the covers, turn off the nitrogen lines.

C.4 Tracking and Software

C.4.1 Active Tracking

If active Tracking is needed, active tracking can be activated. In this case the heliostat is guided by an optical sensor.

- Set up the optical sensor. (To date it is the 4Q Sensor from the WSG monitor)
- Arrange the sensor so that it has signal in all four quadrants and the offset is less than 0.2 deg. This can be checked in the real time data window, or in the data illustration windows.
- Select active tracking in the GUI main window.
- Check if the active guiding is working properly. (The tracking sensor data should indicate values around zero.

C.4.2 General Remarks

- Active tracking mode is only allowed within a certain window around the calculated value of the sun. This ensures that the heliostat will under no circumstances move to an arbitrary position. Otherwise displacement of the sensor or condensation trails in front of the sun could lead to uncontrolled movement of the heliostat.
- In the primary axes there are two hard stop end-switches. This means if the heliostat moves over a certain position this end switch is triggered and shuts down the 24V power supply for the motor. Additionally, in the direction of the afternoon position a soft stop end switch is placed. This switch is connected to the motor controller. Upon this trigger the motor can not be moved forward any further, but can still move backwards. This is to prevent the heliostat from running into the hard stop switch while in normal tracking operation.

C.5 End of Operation

C.5.1 Cleaning Procedure

- Install the nitrogen spray head. There is a nitrogen connection inside the control cabinet. After successful connection of the spry head, the green nitrogen valve (in the laboratory) needs to be opened.
- If desired mirror M1 can be adjusted so that the Surface is somewhat tilted. This can be done either by just stopping the tracking (if in a tilted position), or move the mirror to a convenient position with the "Go to Target" function.
- Clean M1 first, carefully spray away the dust that has accumulated on the mirror surface.
- Cover the mirror M1. Tighten the wing nuts.
- Clean M2 the same way, cover M2.
- Close the green nitrogen valve in the laboratory. Release nitrogen inside the spray head, remove the spray head.

C.5.2 Send Heliostat to Home Position

- Select "Go Home" in the GUI.
- Wait until the tracker has reached the home position
- Click "Stop"
- Close all program windows. Click "End Heliostat" in the tool bar, or alternatively close MATLAB.
- Shut down the power supply

C.5.3 Cover the Heliostat

- Turn on the nitrogen purging lines (in the laboratory) check the flow at the flow meter, it should be around 0.5 l/h.
- Put the rain cover onto mirror M1, check again that the power is turned off!
- Fix the rain cover of the structure.

Appendix D

Heliostat Program Documentation

In this appendix, the properties of the two main classes of the heliostat control software are described. It should complement the comments that are already in the code.

D.1 Class: controller_module

The controller module handles the main task of the program. When created it also creates an IO module (IO_module). The controller module should always be instantiated with the controller_module.getInstance method in order to avoid to have multiple instances running.

A timer at a defined period (2s) triggers the control routine. The control routine calls the appropriate controller type. The controller gets the latest position/tracking data from the IO Module and updates the motor speed values, according to the tracking scheme. These values are sent to the motor through the IO Module.

Variables

Generally, the variables are documented in the code. Therefore only the most relevant are listed here.

state mode of operation: 0=stop, 1=go home, 2=passive tracking, 3=active tracking, 4=go to position

location location of the Heliostat, with the fields: lon, lat, alt

POS current position, with fields: A, E, FQ (2x2 matrix)

M motor speed, with fields: A and E

trafoA coordinate transformation parameter (Heliostat position with regard to south)

trafoE coordinate transformation parameter (Heliostat position with regard to zenith)

Methods

go(CO) This method is called every time the Timer executes (T=2s). It runs trough the state machine an calls the appropriate function to calculate tracking speed. The tracking speed is then sent to the motors.

M=home(CO,POS) Is calling the method go_to_target with the argument of the home position.

M=passive_tracking(CO,POS) Calculates the motor speed for passive Tracking. Depending how close the mirror is to the target position, the value is determined in a different way. If the offset is larger than 1° the speed is set to the maximum speed. If the offset is between 0.01° and 1° the speed is proportional to the offset. If the offset is even smaller, a PI controller (PI_module) comes into action.

M=active_tracking(CO,POS) Calculates the motor speed for active tracking. The target position is calculated as in passive tracking mode. If the mirror is closer than 0.5° to the target position, the signal of the active tracking sensor is used to calculate the motor speed with a PI controller. Otherwise the heliostat is run in a passive way.

M=star_tracking(CO,POS) This method should calculate the motor speed for tracking astronomical objects in right ascension/declination coordinates. It is not yet implemented.

M=fixed_target(CO,POS) Is calling the method go_to_target with the argument of the desired position (target_A and target_E fields).

M=manual_control(CO) Processes the input from the manual control panel. This panel is connected to the analogue inputs of the motors that are used for this purpose.

M=go_to_target(CO,POS,TA,TE) calculates the motor speed values needed to reach a certain target position.

set_manual_speed(CO,m) with this function the speed for operation with the manual control panel can be set.

set_target(CO,az,el) sets the target position coordinates for the fixed target tracking state.

set_RADec(CO,RA,Dec) sets the right ascension/declination coordinates of the object to track in star tracking mode.

t=get_time(CO) returns the current time in hours of the current day (UTC+1).

change_state(CO,s) changes the status of the state machine, e. g. the mode of tracking.

Heli=sun2Heli(CO,sun) transforms coordinates from the altitude/azimuth system into the heliostat coordinate system (primary and secondary axes)

[DA DE]= rotate_azimut(CO,d1,d2) can rotate coordinates from the laboratory coordinate system into the heliostat coordinate system, method is obsolete in higher versions (v10 upwards)

delete(CO) executes when the controller module is deleted. It deletes the timer object and the IO_module

Static Methods

singleObj = getInstance returns the pointer of the instantiated object. If there is no instance of the object present, then an object is created. In order to avoid multiple running controller objects, an object should always be created using this function.

M=stop sets the tracking speed to zero.

D.2 Class: IO_module

Variables

A last known position primary axis

E last known position secondary axis

FQ last known 4-Qadrant data 2*2 matrix

canch1 can bus channel on hardware, pointer

scaler_enc can bus data integer scaler (2^{18}/-360)

L_bit length of data (can message) 32 bit

data_type can bus data type as MATLAB® expression: 'int32'

endian_Motor Endianness of motor messages: 'BigEndian'

endian_Enc Endianness of encoder messages: 'LittleEndian'

can_bus_speed speed of can bus 500000 mbps

good_to_send communication status of the respective motor, is set to 1 if an answer for the last command has been received, otherwise 0 -> error wait before sending the next message (fields A and E)

N_no_answer number of missed answers from the motor ((fields A and E)

Enc_offset_A encoder offset parameter: Describes the rotation offset that is needed to transform the raw output of the primary axis encoder into the heliostat coordinate system.

Enc_offset_E encoder offset parameter: Describes the rotation offset that is needed to transform the raw output of the secondary axis encoder into the heliostat coordinate system.

motor_ID_A message ID for messages to the primary axis motor: 001_{dec}

motor_ID_E message ID for messages to the secondary axis motor: 003_{dec}

motor_reply_ID_A message ID for messages from the primary axis motor: 002_{dec};

motor_reply_ID_E message ID for messages from the secondary axis motor: 004_{dec};

enc_SID_A message ID for messages to the primary axis encoder: 604_{hex}

enc_SID_E message ID for messages to the secondary axis encoder: 605_{hex}

enc_ID_A message ID for messages from the primary axis encoder: 184_{hex}

enc_ID_E message ID for messages from the secondary axis encoder: 185_{hex}

M_status Motor reply acknowledge status, 100 if command is acknowledged (fields A and E)

M_rep_C special motor reply message (command) (fields A and E)

M_rep_M special motor reply message (fields A and E)

status_reply special motor reply message (fields A and E)

M4Q 4Q interface module

drehwinkel_2d_fix angle for rotation matrix (static)

drehmatrix_2d_fix rotation matrix for optical sensor data (dynamic)

Methods

IO = IO_module() is the constructor method. It prepares CAN-bus settings, and defines the interrupt routine. Also it creates a Q4_com_module that handles the communication with the four quadrant sensor.

send_data(IO,M) sends the motor speed on the CAN-bus. The speed variables M.E and M.A are packed into a CAN-bus message. If the bus is clear to send the message is sent out.

recieve_fcn(IO) is an interrupt triggered function, that reads data from the CAN-bus input buffer. The data is stored and interpreted. Encoder position messages are stored in the corresponding variable fields. Acknowledge messages from the motors are interpreted, if everything is clear, the clear to send variable is set to true (1).

request_manual_input(IO) requests the status of the motor's input pins.

request_motor_data(IO) requests motor status data.

data=getdata(IO) is returning the latest data from the rotary encoders and the four quadrant sensor. The structure has the fields A, E, FQ.A, FQ.E, FQ.X, FQ.Y.

FQ_out=get_4Q_data(IO) requests the four quadrant data from the Q4_com_module and returns the angular offset in laboratory and heliostat coordinates.

d=data_conv(IO,data) converts numbers into the data type specified in the 'data_type' variable. It is used to prepare data so that it can be sent on the CAN-bus.

initialize_encoder(IO,enc_SID) initialises the encoders to send data at a continuous rate.

stop_encoder(IO,enc_SID) stops the encoders, so that they don't send signals any more.

initialize_motor_end_switches(IO,motor_ID) initialises the motor drivers, and activates soft end switches where necessary.

delete(IO) executes when the controller IO_module is deleted. It deletes the Q4_com_module, stops the encoders and disconnects from the CAN-bus.

Appendix E

Heliostat Budget

The Heliostat project involved costs of roughly 450'000 Swiss Francs. This involved not only the costs of the heliostat itself but also laboratory equipment for preparation of the laboratory and instruments for the experimental set-up inside the laboratory. Not included in this budget are man power provided by PMOD.

Funding

The project had been funded by three sponsors: The Swiss National Science Foundation (SNF), a Switzerland based foundation that would like to stay anonymous and the Bundesamt für Bauten und Logistik (BBL). The BBL contribution was provided as a non-cash benefit in the form of the concrete foundation, that was built during the renovation of the PMOD institute building. Table E.1 lists the sponsors and their contribution to the budget.

Costs

Table E.2 lists the spendings for the heliostat. The overall agreement is quite good, the cost have been over budget by only 3%. There have been some shifts between budgetary items: So was the mechanical construction more expenive than budgeted, and on the other hand less money was spent on the motion control. This is also due to the fact, that some parts of the motion control system have been directly paid within the mechanical construction budget. The spendings on laboratory equipment has been reduced in order to finance the deficit araising from the mirrors.

Sponsor	Amount [CHF]
National Science Foundation (SNF)	228300
Anonymous sponsor	169700
Bundesamt für Bauten und Logistik (BBL)	*54000
Total	452000

Table E.1: Heliostat funding: The heliostat has been funded by three sponsors. * The contribution of the BBL is provided as a non-cash benefit in the form of the concrete foundation.

Component	Budget [CHF]	Spendings [CHF]
Mirrors	195000	205550
Mechanical construction	124200	161913
Motion control	40500	12461
Protection cover	5000	8424
Laboratory equipment	33300	20296
Miscellaneous	0	1566
Concrete foundation*	(54000)	(54000)
Total 1 (without foundation)	398000	410210
Total 2 (including foundation)	(452000)	(464210)

Table E.2: Heliostat budget: The table shows the budget and the actual spendings. * The Concrete foundation has been built within the renovation of the PMOD institute building and was directly paid from the renovation budget.